

https://dspace.org/

Prediction of residual stresses due to laser shock peening using eigenstrain methods

Omar, Ridwaan

2019

https://hdl.handle.net/10539/29064

Omar, Ridwaan, (2019). Prediction of residual stresses due to laser shock peening using eigenstrain methods, University of the Witwatersrand, https://hdl.handle.net/10539/29064

Downloaded from a DSpace repository. https://dspace.org/

Prediction of Residual Stresses Due to Laser Shock Peening Using Eigenstrain Methods

Ridwaan Omar

Student Number: 601525
Supervisor: Prof. C Polese
Co-supervisor: Mr. F Pietra

A dissertation submitted to the Faculty of Engineering and the Built Environment, University of the Witwatersrand, Johannesburg, in fulfilment of the requirements for the degree of Master of Science in Engineering.

Johannesburg, July 2019

Declaration

I declare that this dissertation is my own, unaided work, except where otherwise acknowledged. It is being submitted for the degree of Master of Science in Engineering in the University of the Witwatersrand, Johannesburg. It has not been submitted before for any degree or examination at any other university.

Signed this 24th day of July 2019



Ridwaan Omar

Acknowledgements

I would like to thank the following people and entities:

- My supervisors at the University of the Witwatersrand, Prof. Claudia Polese and Mr Francesco Pietra for their guidance and assistance throughout the project.
- Dr Daniel Glaser at the CSIR, for his assistance in defining the project.
- Mr Sean van Staden for his excellent work in building up a database measured residual stresses in peened samples, without which this work would not have been possible.
- My colleagues at the University of the Witwatersrand, Mr Nicholas Stiekema, Mr Oluwadamilola MacGregor, and Mr Constantin Schulte-Brader for their advice and assistance.
- The generous financial support of the DST-NRF Centre of Excellence in Strong Materials (CoE-SM) towards this research is hereby acknowledged.
- I would like to acknowledge the support of the South African Centre for Scientific and Industrial Research National Laser Centres (CSIR NLC) Rental Pool Program (RPP), funded by the Department of Science and Technology (DST).
- This work is based on research supported in part by the National Research Foundation (NRF) of South Africa Incentive Funding for Rated Researchers (IFRR) for Prof. Claudia Polese (Grant Number: 109200)

Opinions expressed and conclusions arrived at are those of the author and not necessarily to be attributed to the CoE-SM or to the NRF.

Abstract

Laser Shock Peening (LSP) is a surface treatment used to enhance the fatigue life of components. To realise the full potential of LSP, a method for predicting residual stresses arising from this process is required. Eigenstrain methods can meet this requirement in a computationally effective way. At the same time they could allow one to use residual stress data measured in simple geometries to predict the residual stress fields in complex geometries.

Five eigenstrain methods were validated and compared in terms of their predictive power. A database of laser peened Aluminium Alloy 7075 flat plates was used to validate the methods. Three methods actually yielded results. Although none of these methods was categorically found to be the best, Coratella's method was rated as the best, based on its performance statistics. In addition, it is the simplest and quickest method from those tested. This method was used in the second part of the project.

The insensitivity of eigenstrains to geometry was also tested, using simple benchmark geometries, representative of features commonly encountered in engineering. These benchmark samples were previously generated in a research collaboration with the US Air Force Research Laboratory, University of Dayton Research Institute, and Wright-Patterson Air Force Base. Generally, the assumption was found to hold, except when the peened surface is a sharp edge.

The second part of the project aimed to study the effects of component geometry on LSP-induced residual stresses, in commonly encountered geometric features in engineering. The geometries selected were cuboid samples, spheres, cylinders, fillets, structural angles, and channels. A sample was chosen from the database of peened AA7075 samples to be the basis of this study. The eigenstrain distribution was extracted from this sample and imposed on various parameter combinations of the aforementioned geometries. The aim was to study the effects of specifically chosen geometric parameters on the residual stresses due to LSP.

A critical assumption made in the second part of the project was that LSP-induced eigenstrains are insensitive to geometric parameters. This assumption was based on the Principal of Transferability of Eigenstrain. Concern was raised regarding whether this principal holds

for thin or small samples. It was hypothesised that for thin/small samples, the attenuation of the LSP-induced shock wave might be modified, leading to a different eigenstrain distribution. This concern is not universal, but limited to some specific parameters. Nevertheless, a study was conducted confirming the Principle of Transferability of Eigenstrain, showing that the assumption of insensitivity of eigenstrain to geometry holds, at least in some circumstances. Similar studies in literature affirm this.

The method has a weakness in predicting residual stresses through peened edges. This was attributed to the overlapping of different peened zones that occurs when peening over an edge, as well as the effect of the edge on the underlying eigenstrain distribution.

It was found that the residual stresses arising from LSP are insensitive to size in larger components. For smaller geometries, the residual stresses vary with changing size of the geometry but they tend to converge to specific values. It was also found that the maximum tensile stresses decrease with increasing size, and maximum compressive stresses tend to increase with increasing size, though this is not always the case. These two facts seem to indicate that LSP has a more positive effect on larger components than smaller ones.

At the outset, it was envisaged that eigenstrain methods would be used to optimise the LSP process for actual components in industrial applications. While in principle, the method studied in this project may meet this need, there are some weaknesses that need to be overcome before it is fit for such a purpose. Recommendations are made on some steps that may overcome these weaknesses and on how this method could possibly be used in conjunction with other methods to achieve this purpose.

Contents

Declaration i

Acknowledgements ii

Abstract iii

Contents v

List of Figures xii

List of Tables xx

1 Introduction 1

1 Background and Motivation 1

2 Research Questions 2

3 Objectives 2

2 Literature Review 4

1 The Laser Shock Peening Process 4

2 Physics of LSP 6

2.1 Laser-Material Interaction 6

2.2 Shock Wave Propagation . . . 7
2.3 Plastic Deformation . . . 8
2.4 Formation of Residual Stress . . . 8
3 Properties of Metals . . . 10
3.1 Material Property Relationships . . . 11
3.2 Plane Stress Assumption . . . 12
3.3 Von Mises Yield Criterion . . . 12
3.4 Hugoniot Elastic Limit . . . 12
4 Eigenstrains . . . 13
4.1 What is Eigenstrain? . . . 13
4.2 Eigenstrain Methods . . . 15
4.2.1 Direct Problem of Eigenstrain . . . 16
4.2.2 Inverse Problem of Eigenstrain . . . 17
4.3 Korsunsky's Method . . . 19
4.3.1 Development of Equation 2.16 . . . 21
5 Residual Stress Measurement . . . 23
5.1 Incremental Hole Drilling . . . 23
5.2 Diffraction Techniques . . . 24
5.2.1 X-ray diffraction . . . 24
5.2.2 Neutron Diffraction . . . 24
6 Inverse Problems . . . 25
6.1 Ill-Posed Problems . . . 25

7 Optimisation . . . 26
7.1 Nelder-Mead Method . . . 26
7.2 Powell's Method . . . 27
7.3 Broyden-Fletcher-Goldfarb-Shanno Method . . . 27
8 Curve Fitting . . . 27
8.1 Regression Analysis . . . 28
8.2 Parsimony . . . 30
8.3 Goodness of Fit Metrics . . . 31
9 Effects of Geometry on Residual Stresses due to LSP . . . 32
9.1 Effect of Thickness on Residual Stress . . . 33
9.2 Effect of Curvature on Residual Stress . . . 35

3 Validation of Models **38**

1 Benchmark Data . . . 38
2 Direct Problem of Eigenstrain . . . 41
3 Inverse Problem of Eigenstrain . . . 45
3.1 Coratella's Method . . . 45
3.1.1 Method . . . 45
3.1.2 Results and Discussion . . . 46
3.2 Korsunsky's Method . . . 49
3.2.1 Method . . . 49
3.2.2 Results and Discussion . . . 52
3.3 Korsunsky's Method with FEM to Generate Elastic Strain Matrix . . . 56

3.3.1 Method . . . 57
3.3.2 Results and Discussion . . . 60
4 Comparison of Methods . . . 62
5 Failed Methods . . . 66
5.1 Polynomial Fit Method . . . 66
5.1.1 Discussion . . . 68
5.2 Trapezoid Method . . . 69
5.2.1 Discussion . . . 71
6 Confirming the Principle of Transferability of Eigenstrain . . . 72
7 Conclusions . . . 80

4 Effect of Rectilinear Geometric Parameters on Residual Stresses in Cuboid Samples 82

1 Residual Stress Distribution in Base Sample . . . 82
2 Effect of Thickness on Residual Stress Distribution . . . 88
3 Effect of Size of Peened Area . . . 91
4 Effect of Sample Size . . . 96
5 Discussion . . . 100
6 Conclusions . . . 101

5 Effect of Curvilinear Geometric Parameters on Residual Stresses in Cylinders and Spheres 102

1 Residual Stresses in Spheres . . . 102
1.1 Base Model . . . 102
1.2 Varying Radius . . . 105

2 Residual Stresses in Cylinders . . . 110
2.1 Base Model . . . 110
2.2 Varying Radius . . . 112
2.3 Varying Length . . . 115
3 Discussion . . . 120
4 Conclusions . . . 121

6 Residual Stresses in Common Engineering Geometries 123

1 Residual Stresses in Fillets . . . 123
1.1 Base Model . . . 123
1.2 Varying Radius of Fillet . . . 126
1.3 Varying Size of Filleted Bar . . . 129
1.4 Varying Length of Filleted Bar . . . 132
2 Residual Stresses in Equal Angles . . . 137
2.1 Base Models . . . 137
2.2 Small Angles . . . 142
2.2.1 Varying Thickness of Small Equal Angles . . . 142
2.2.2 Varying Size of Small Equal Angles . . . 144
2.2.3 Varying Length of Small Equal Angles . . . 147
2.3 Large Angles . . . 150
2.3.1 Varying Thickness of Large Equal Angles . . . 150
2.3.2 Varying Size of Large Equal Angles . . . 153
2.3.3 Varying Length of Large Equal Angles . . . 156

3 Residual Stresses in Channels . . . 161
3.1 Base Models . . . 161
3.2 Varying Size of Channel . . . 164
3.3 Varying Length of Channel . . . 166
4 Discussion . . . 171
5 Conclusions . . . 172

7 Discussion **174**

8 Conclusions **177**

9 Recommendations **178**

10 Research Contributions **179**

References **180**

A Benchmark Sample Parameters **185**

B Extra Results **187**

1 Coratella's Method . . . 187
2 Korsunsky's Method . . . 191

C Scripts **197**

1 Korsunsky's Method Script . . . 197
2 Korsunsky's Method With FEM: Main Script . . . 205
3 Korsunsky's Method With FEM: ANSYS Journal File Script . . . 213

D Thickness Study – Results in y Direction **219**

E Research Contributions **228**

List of Figures

2.1 *Typical LSP process*[4] 5

2.2 *Plastic deformation of surface layer during peening process* 9

2.3 *Formation of residual stresses due to LSP* 9

2.4 *Typical residual stress profile due to LSP*[23] 10

2.5 *Visual representation of the stress tensor*[25] 11

2.6 *Elastic recovery of a component subjected to plastic deformation* 14

2.7 *Statically indeterminate bar*[21] 14

2.8 *Stress strain diagram of Figure 2.7*[21] 15

2.9 *Predicting residual stresses in complicated geometries using eigenstrain methods* 16

2.10 *Method of obtaining eigenstrains from residual stress plots* 18

2.11 *Elastic beam used to formulate a solution to the Direct Problem of Eigenstrain* 22

2.12 *Example of a least squares fitted line* 28

2.13 *Example of overfitting and underfitting* 30

2.14 *Measured residual stresses in 316L samples of varying thickness: (a) measured using contour method, (b) measured using slitting method, (c) plot showing the laser peening affected depth as a function of material thickness for each set of measurements* 33

2.15 *Eigenstrain distribution under an (a) edge pulse (b) central pulse (c) eigenstrain depth profile at the centre point of an edge pulse and a central pulse (F = Free plane S = Symmetry plane)* 35

2.16 *Descriptions of various specimen families used for laser peening residual stress geometry study: (a) convex fillets, (b) concave fillets, (c) round bars, and (d) thick-walled pipes* 36

3.1 *One of the benchmark samples* 38

3.2 *Pattern of peening* 39

3.3 *Residual stress measurements using various techniques* 40

3.4 *Coordinate system used in this dissertation* 41

3.5 *Sample B15 split into layers* 42

3.6 *Path used to extract residual stresses through centre of peened area* 44

3.7 *Unprocessed result for Sample B15: Residual stresses in the x direction* 44

3.8 *Residual stresses in x direction through depth of Sample B15* 45

3.9 *Coratella's Method: Prediction vs measured residual stress in Sample B15 - x direction* 47

3.10 *Coratella's Method: Prediction vs measured residual stress in Sample B15 - y direction* 48

3.11 *Flow chart outlining implementation of Korsunsky's Method* 52

3.12 *Optimisation framework applied to Korsunsky's method* 53

3.13 *Korsunsky's Method: Prediction vs measured residual stress in Sample B15 - x direction* 54

3.14 *Korsunsky's Method: Prediction vs measured residual stress in Sample B15 - y direction* 55

3.15 *Korsunsky's Method with FEM: Prediction vs measured residual stress in Sample B15 - x direction* 60

3.16 *Korsunsky's Method with FEM: Prediction vs measured residual stress in Sample B15 - x direction* 61

3.17 *Ranks of different methods in predicting residual stress in different samples* . 65

3.18 *Average Standard Error of the different methods* 66

3.19 *Three peened geometries in which residual stresses were measured*[57] 73

3.20 *Three peened geometries in which residual stresses were measured*[57] 73

3.21 *FEM models of the three samples* 74

3.22 *Predicted vs Measured residual stress in convex corner* 75

3.23 *Predicted vs Measured residual stress in concave corner* 76

3.24 *Predicted vs Measured residual stress in sharp corner* 76

3.25 *Schematics depicting peening over an edge* 77

3.26 *Intersection of peened regions in sharp corner model* 77

3.27 *FEM Model used to superimpose eigenstrains* 78

3.28 *Co-ordinate system to define superposition of eigenstrains* 79

3.29 *Predicting residual stresses by superimposing eigenstrains* 80

4.1 *Comparison between layers in: a.) chapter 3 and b.) chapter 4* 83

4.2 *Residual Stress distribution through thickness of Sample B15 – x direction* . . 84

4.3 *Residual Stress distribution through thickness of Sample B15 – y direction* . . 84

4.4 *Contour plots of residual stress field in Sample B15 – x direction (a) Top view, (b) Cross section (c) Bottom view* 86

4.5 *Contour plots of residual stress field in Sample B15 – y direction (a) Top view (b) Cross section (c) Bottom view* 87

4.6 *Residual stress distributions in samples with varying thickness – x direction* . 89

4.7 *Variation of some critical stresses with respect to thickness – x direction* . . . 90

4.8 *Effect of scale on residual stresses: (a) Original size, (b) Half size* 92

4.9 *Residual stress distributions in samples with varying peened squares – x direction* 93

4.10 *Comparison between residual stress fields in samples with various peened areas: (a)* 5 mm×5 mm *(b)* 15 mm×15 mm *(c)* 25 mm×25 mm 94

4.11 *Variation of some critical stresses with respect to peened area – x direction* . . 95

4.12 *Residual stress distributions in various sample sizes – x direction* 97

4.13 *Comparison between residual stress fields in samples of various sizes: (a)* 30 mm×30 mm *(b)* 70 mm×70 mm *(c)* 100 mm×100 mm 98

4.14 *Variation of some critical stresses with respect to sample size area – x direction* 99

5.1 *Base CAD model of the sphere* 103

5.2 *FEM model of the base sphere* 103

5.3 *Comparing spherical co-ordinate system to spherical* 104

5.4 *Residual stresses in base sphere* 106

5.5 *Residual stress distributions in spheres of varying radius – x direction* 107

5.6 *Variation of some critical stresses with respect to diameter of sphere – x direction* 109

5.7 *Base CAD model of the cylinder* 110

5.8 *FEM model of the base cylinder* 110

5.9 *Comparing cylindrical co-ordinate system to Cartesian* 111

5.10 *Residual stresses in base cylinder* 113

5.11 *Residual stress distributions in cylinders of varying radius – x direction* . . . 114

5.12 *Variation of some critical stresses with respect to diameter of cylinder – x direction* 116

5.13 *Residual stress distributions in cylinders of varying lengths – x direction* . . . 117

5.14 *Variation of some critical stresses with respect to length of cylinder – x direction* 119

6.1 *Base CAD model of the filleted bar* 124

6.2 *FEM model of the base filleted bar* 124

6.3 *Co-ordinate systems used to implement eigenstrains in filleted bar* 125

6.4 *Residual stresses in base filleted bar* 126

6.5 *Residual stress distributions in fillets of varying radius – x direction* 128

6.6 *Variation of some critical stresses with respect to radius of fillet – x direction* 130

6.7 *Residual stress distributions in filleted bars of varying size – x direction* . . . 131

6.8 *Variation of some critical stresses with respect to size of filleted bars – x direction* 133

6.9 *Residual stress distributions in filleted bars of varying lengths – x direction* . . 134

6.10 *Variation of some critical stresses with respect to length of filleted bar – x direction* 136

6.11 *Base CAD model of the equal angle* 137

6.12 *FEM model of the base equal angle* 138

6.13 *Co-ordinate systems used to implement eigenstrains in equal angles* 139

6.14 *Residual stresses in small base equal angle* 141

6.15 *Residual stresses in large base equal angle* 141

6.16 *Residual stress distributions in small equal angles of varying thickness – x direction* 143

6.17 *Variation of some critical stresses with respect to thickness of small equal angles – x direction* 145

6.18 *Residual stress distributions in small equal angles of varying size – x direction* 146

6.19 *Variation of some critical stresses with respect to size of small equal angles – x direction* 148

6.20 *Residual stress distributions in small equal angles of varying lengths – x direction* 149

6.21 *Variation of some critical stresses with respect to length of small equal angles – x direction* 151

6.22 *Residual stress distributions in large equal angles of varying thickness – x direction* 152

6.23 *Variation of some critical stresses with respect to thickness of large equal angles – x direction* 154

6.24 *Residual stress distributions in large equal angles of varying size – x direction* 155

6.25 *Variation of some critical stresses with respect to size of large equal angles – x direction* 157

6.26 *Residual stress distributions in large equal angles of varying lengths – x direction* 158

6.27 *Variation of some critical stresses with respect to length of large equal angles – x direction* 160

6.28 *Base CAD model of the c-channel* 161

6.29 *FEM model of the base channel* 162

6.30 *Co-ordinate systems used to implement eigenstrains in channels* 162

6.31 *Residual stresses in base channel* 164

6.32 *Residual stress distributions in channels of varying size – x direction* 165

6.33 *Variation of some critical stresses with respect to size of channels – x direction* 167

6.34 *Residual stress distributions in channels of varying lengths – x direction* . . . 168

6.35 *Variation of some critical stresses with respect to length of channels – x direction* 170

B.1 *Coratella's Method: Prediction vs measured residual stress in sample 05 - x direction* 187

B.2 *Coratella's Method: Prediction vs measured residual stress in sample 05 - y direction* 188

B.3 *Coratella's Method: Prediction vs measured residual stress in sample 38 - x direction* 188

B.4 *Coratella's Method: Prediction vs measured residual stress in sample 38 - y direction* 189

B.5 *Coratella's Method: Prediction vs measured residual stress in sample 70 - x direction* 189

B.6 *Coratella's Method: Prediction vs measured residual stress in sample 70 - y direction* 190

B.7 *Korsunsky's Method: Prediction vs measured residual stress in sample 05 - x direction* 191

B.8 *Korsunsky's Method: Prediction vs measured residual stress in sample 05 - y direction* 191

B.9 *Korsunsky's Method: Prediction vs measured residual stress in sample 38 - x direction* 192

B.10 *Korsunsky's Method: Prediction vs measured residual stress in sample 38 - y direction* 192

B.11 *Korsunsky's Method: Prediction vs measured residual stress in sample 70 - x direction* 193

B.12 *Korsunsky's Method: Prediction vs measured residual stress in sample 70 - y direction* 193

B.13 *Korsunsky's Method with FEM to Generate Elastic Strain Matrix: Prediction vs measured residual stress in sample 05 - x direction* 194

B.14 *Korsunsky's Method with FEM to Generate Elastic Strain Matrix: Prediction vs measured residual stress in sample 05 - y direction* 194

B.15 *Korsunsky's Method with FEM to Generate Elastic Strain Matrix: Prediction vs measured residual stress in sample 38 - x direction* 195

B.16 *Korsunsky's Method with FEM to Generate Elastic Strain Matrix: Prediction vs measured residual stress in sample 38 - y direction* 195

B.17 *Korsunsky's Method with FEM to Generate Elastic Strain Matrix: Prediction vs measured residual stress in sample 70 - x direction* 196

B.18 *Korsunsky's Method with FEM to Generate Elastic Strain Matrix: Prediction vs measured residual stress in sample 70 - y direction* 196

D.1 *Residual stress distributions in samples with varying thickness – y - direction* 220

D.2 *Variation of some critical stresses with respect to thickness – y - direction* . . 221

D.3 *Comparison between residual stress fields in samples with various peened areas: (a)* $5 \times 5mm$ *(b)* $15 \times 15mm$ *(c)* $25 \times 25mm$ 222

D.4 *Variation of some critical stresses with respect to thickness – y - direction* . . 223

D.5 *Variation of some critical stresses with respect to peened area – y - direction* . 224

D.6 *Residual stress distributions in various sample sizes – y - direction* 225

D.7 *Comparison between residual stress fields in samples of various sizes: (a)* $30 \times 30mm$ *(b)* $70 \times 70mm$ *(c)* $100 \times 100mm$ 226

D.8 *Variation of some critical stresses with respect to sample size area – y - direction* 227

List of Tables

3.1 Range of values 40

3.2 Goodness of Fit metrics for Coratella's Method 49

3.3 Goodness of Fit metrics for Korsunsky's method 55

3.4 Goodness of Fit metrics for Korsunsky's method with FEM to Generate Elastic Strain Matrix 61

3.5 Comparison of Goodness of Fit metrics for different methods in Sample B15 . 62

3.6 Comparison of Goodness of Fit metrics for different methods in Sample 05 . . 63

3.7 Comparison of Goodness of Fit metrics for different methods in Sample 38 . . 63

3.8 Comparison of Goodness of Fit metrics for different methods in Sample 70 . . 64

3.9 Corner samples vs Sample B15 72

A.1 Key to Table A.2 185

A.2 Parameters of benchmark samples 186

Chapter 1 Introduction

1 Background and Motivation

Laser Shock Peening (LSP) is a technique used to enhance the surface characteristics of a material. Typically it is used to improve fatigue life by inducing beneficial compressive residual stresses near the surface of the material. It has been shown to have numerous advantages over traditional shot peening and is envisaged as a substitute for shot peening[1].

Although LSP has enormous potential, the complex nature of the process has inhibited its growth in the local industry. In order to realise the full potential of this technology, the process parameters of LSP have to be optimised. The LSP initiative in South Africa aims to develop and optimise this process, so that it can be transferred to local industries.

Experimental parameter studies are possible, and have been conducted before, but they are expensive and time consuming[1]. Therefore, in order to optimise the LSP process, a reliable predictive model that can be used in parametric studies is required. Due to the complex nature of the LSP process, it is usually modelled using the Finite Element Method (FEM). Predicting residual stresses is usually done in one of two ways:

- **Process modelling** The physics of the residual stress formation by shock wave propagation are modelled. This firstly requires determination of the laser-material interaction, which leads to plasma formation. The shock wave that results from the plasma pressure is modelled and used along with the constitutive model of the material to determine the plastic deformation of the material, and hence the residual stresses induced.
- **Eigenstrain methods** The residual stress field throughout the body is calculated using residual stress measurements through the depth at a single location. The plastic strain distribution that caused the residual stress is inferred from the residual stress distribution itself. The plastic strain distribution is then enforced on a model of the

sample and solved for equilibrium. In this manner, the entire residual stress field can be determined from a few measurements of residual stress.

Process modelling is more complicated and computationally expensive than eigenstrain methods. In addition, the inputs to the model are not always easy to determine. The true power of eigenstrain methods, however, lies in the fact that eigenstrains are insensitive to part geometry, and depend only on material properties and LSP parameters[2]. Thus, residual stress data obtained from a simple geometry can be used to predict residual stress fields in more complex geometries, ceteris paribus. This gives eigenstrain methods a strong advantage in modelling complex geometries.

The insensitivity of eigenstrains to geometry also presents the opportunity to study the effects of geometric parameters on residual stresses in laser peened specimens.

2 Research Questions

1. How do different eigenstrain methods compare in predicting residual stresses due to laser shock peening?
2. What is the relationship between the geometry of a sample and residual stresses induced by laser shock peening?

3 Objectives

- To evaluate the accuracy of various eigenstrain models available in literature, by comparing their predictions to experimentally determined residual stresses.
- To determine the effect of the following geometric parameters on residual stresses induced by laser peening in cuboid samples:
  - Thickness
  - Size of peened area
  - Size of sample
- To determine the effect of the following geometric parameters on residual stresses in spheres and cylinders:
  - Radius of spheres and cylinders
  - Length of cylinders

- To study the effects of parameters listed below on residual stresses, in the following common engineering geometries:
  - Filleted bars
    - Radius of fillet
    - Length of filleted bar
    - Size of filleted bar
  - Structural equal angles
    - Thickness of equal angle leg
    - Length of equal angle
    - Size of equal angle
  - C-channels
    - Size of channel
    - Length of channel

Chapter 2 Literature Review

1 The Laser Shock Peening Process

A laser peening system typically consists of the following components[1]:

- A pulsed laser beam
- A confining medium (typically water)
- A surface coating (ablative layer)
- The peened object
- Some configurations use a lens to focus the laser beam on the target

The process is typically carried out in the following fashion[1]:

1. A pulsed laser beam is directed at the target. If a lens is being used it will pass through the lens, which focuses the beam.
2. The laser beam passes through the confining medium, which must be transparent to the wavelength of the laser being used.
3. The laser beam is absorbed by the surface coating, which must be opaque to the wavelength of the laser being used. In the absence of a coating, the ablative layer is the surface of the material itself.
4. The ablative layer heats up rapidly and forms a plasma. The transformation from solid to plasma causes rapid expansion of matter.
5. The rapid expansion of plasma leads to the formation of a shock wave, which propagates into the material.
6. The high stresses induced by the shock wave, cause plastic deformation of the material.

7. The shock wave attenuates as it propagates into the material, limiting the plastic deformation to a thin layer near the surface.

8. Once the shock wave has dissipated, the material recovers the elastic portion of the strain and residual stresses form in the material.

9. Compressive residual stresses form near the peened surface and tensile stresses form deeper in the material to balance out the compressive stresses.

Figure 2.1 depicts a typical LSP setup[3].

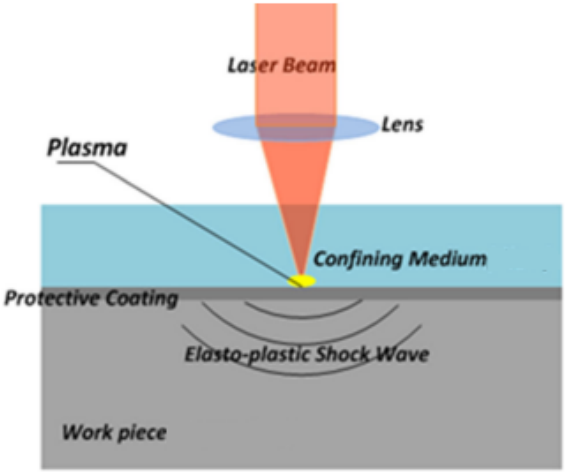

Figure 2.1: *Typical LSP process*[4]

The induction of residual stresses in the material is the main objective of LSP. It is well known that compressive residual stresses near the surface of the material retard growth of surface cracks[5]. This proves useful in mitigating against phenomena such as fatigue failure, wear and corrosion, which are usually initiated and/or accelerated by surface cracks[6]. On the other hand, the tensile stresses deeper in the material can lead to accelerated growth of sub-surface cracks, which could negatively impact fatigue life of the component[7]. Thus, LSP should not just be applied indiscriminately, but after careful consideration of the application[8]. The compressive residual stresses can be termed as beneficial and the tensile stresses as parasitic[9]. In LSP, it is desired to maximise the compressive residual stresses and minimise the tensile residual stresses[10].

The following should be noted with regards to the aforementioned process:

- The energy of the laser pulse is typically low (a few Joules) compared to the thermal energy of the material, so the affected region does not extend very far beyond the peened area.

- The confining medium must be transparent, so that it absorbs a minimum amount of energy from the laser. The purpose of the confining medium is to prevent the shock wave from weakening by dissipating into the air. It has been found that the use of a confinement medium increases the pressure by an order of magnitude[6].
- If a surface coating is used, it must be opaque, so as to absorb the maximum amount of energy from the laser[1].
- It is apparent that the process is dominated by mechanical effects rather than thermal effects[1]. The purpose of the surface coating is to prevent thermal effects on the material. When a surface coating is not used, there might be thermal effects in a small region near the peened surface[11].

The depth and magnitude of the residual stresses in the material are dependent on the configuration (type of confinement medium used, sacrificial medium used, etc.), process parameters (laser spot size and shape, power and energy of laser pulse, etc), and material. It is also dependent on the geometry of the peened component.

2 Physics of LSP

2.1 Laser-Material Interaction

The LSP process makes use of a pulsed laser. Since only the effects of the pulsed laser are of interest here, a discussion on the physics of producing laser light will be foregone. A laser, in this context, refers to a highly coherent, focussed, and usually monochromatic beam of light[12].

Like all electromagnetic waves, lasers can be viewed as consisting of particles called photons. The energy of a photon is inversely proportional to the wavelength of the beam[13]. This is important when considering the interaction of lasers with materials, as it determines how the energy is absorbed by the material. Lasers have high intensity, meaning there is a relatively large amount of energy in a small amount of space. They are also powerful, meaning they transfer a relatively large amount of energy in a short span of time[14].

When the laser beam strikes a material surface, some of the light is absorbed, some is reflected, and some is transmitted. The proportion of light which is absorbed, reflected or transmitted depends on the characteristics of the material. Some of the absorbed energy is converted into sensible energy (the kinetic energy of the particles of the material increase). This causes the temperature of the material to increase. If it reaches the melting point, it changes phase

to liquid and then continues to increase in temperature. This continues until the material becomes a gas and then a plasma[12].

In the LSP process, this conversion of the surface coating to plasma is the desired outcome. The rapid transformation to plasma causes a rapid increase in local pressure, which creates a shock wave[6]. For a plasma to form, the intensity (power per unit area) of the laser needs to be high. If the intensity is not high enough, the energy of the pulse will be absorbed by a larger body of matter, and the local increase in specific internal energy will not be large enough to transform the solid to plasma.

The rationale behind a pulsed laser for LSP can now be explained: A pulsed laser beam occurs over a very short time (usually nanoseconds in LSP). It has high power and is intense. However, its energy is relatively low due to the short time over which it acts. This is exactly what is needed. The high intensity and short duration of the laser confines the energy in space and time, mitigating diffusion of the energy and ensuring the absorption of energy by a very small body of matter. The small amount of matter undergoes a large increase in specific internal energy, leading to plasma formation.

When an ablative coating is used, the thermal effects on the peened component are minimal[6]. When a confinement medium is used, the confinement material has to be transparent to the wavelength of light used, to be effective. When a very high powered laser is used, the confinement medium may suffer dielectric breakdown, absorbing some of the laser energy and reducing the efficacy of the peening[15][16].

2.2 Shock Wave Propagation

It was mentioned in the above section that the laser pulse occurs over a very short duration. This leads to formation of plasma, which is accompanied by rapid expansion of matter. Due to the rapid expansion of the plasma, a shock wave is formed. Essentially, this is due to the disturbance travelling faster than the speed of sound in the medium[1].

A shock wave is characterised by almost discontinuous changes in the pressure, density, and temperature of the medium. A stronger shock wave has a larger change in properties across it. The amplitude of a shock wave is related to its speed. As a shock wave propagates into a medium it attenuates due to increase in entropy[17]. As long as the speed of the wave is higher than the speed of sound in the medium, the shock wave will be sustained. As soon as the speed drops below the speed of sound in the medium, the wave will become an ordinary sound wave[17].

The confining medium ensures that much more of the shock wave propagates into the peened component, rather than dissipating into the air. Confined ablation leads to the generation of pressures that are at least an order of magnitude greater than direct ablation (no confinement medium). The generated pressure also lasts much longer under confined ablation[6][18]. However, the pressure generated using confined ablation saturates at a certain power intensity level. This is due to some energy being lost in dielectric breakdown of the confinement medium. The threshold depends on the wavelength and duration of the pulse, as well as the characteristics of the confinement medium[18].

2.3 Plastic Deformation

The shock wave propagates into the peened material. As long as the peak pressure of the shock wave exceeds the dynamic yield stress of the material, the material will yield and deform plastically[1]. As soon as the pressure is below the yield limit, the wave will only deform the material elastically. The shock wave creates uniaxial compression transverse to the peened surface and tension in the peened layer of the material, as shown in Figure 2.2[6][19], which is a simplified schematic of the plastic deformation resulting from the shock wave. The translucent grey area represents the plastic deformation of the red area that occurs during peening.

The amount of plastic strain induced depends on the strength of the shock wave. Due to attenuation of the shock wave, plastic deformation is confined to a small region around the origin of the shock[6]. The depth of plastic distribution depends on the strength of the generated shock wave, as well as the rate of attenuation. The plastic deformation leads to strain-hardening near the surface and residual stresses in the material[6].

The plastic strain also depends on certain properties of the material, which influence the propagation and attenuation of the shock wave in the material. These include the acoustic properties (such as the speed of sound in the material), the yield strength of the material under dynamic conditions, and the elastic properties of the material[20].

2.4 Formation of Residual Stress

The schematic in Figure 2.2 shows the results of the shock wave. The plastically strained volume (grey block) of the material pushes against the green block. The green block represents the non-plastic part of the material. Since the green part of the sample is elastic, it resists the expansion of the grey block and pushes back against it. This leads to compressive stresses near the surface of the material[6]. The formation of residual stresses is described in more

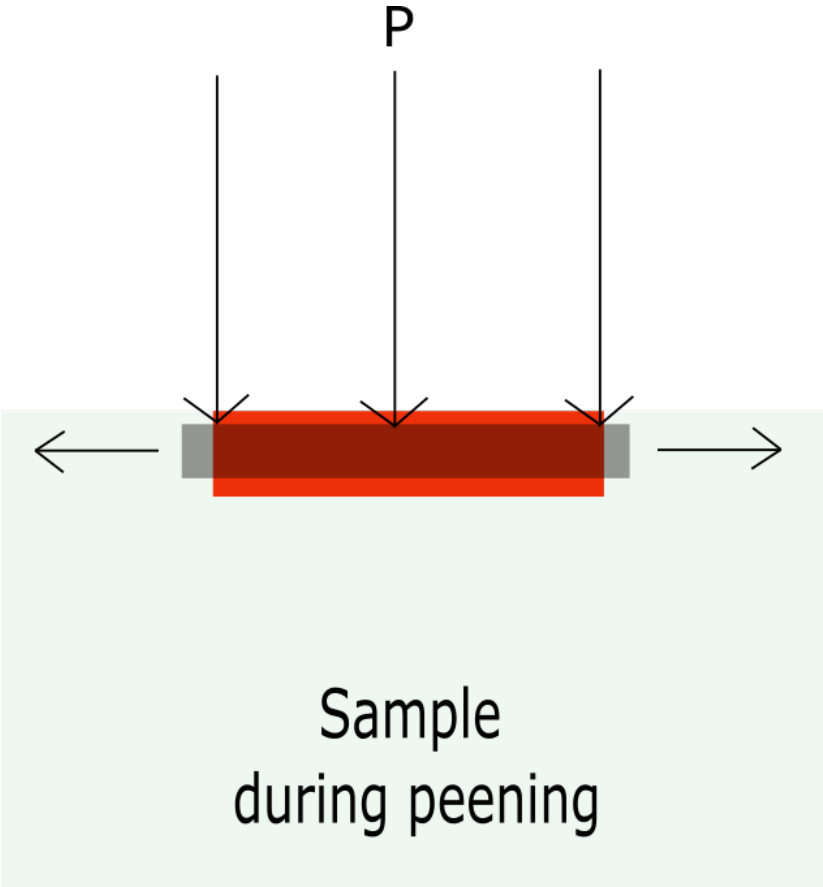

Figure 2.2: *Plastic deformation of surface layer during peening process*

detail in subsection 4.1. Figure 2.3 depicts the formation of residual stresses after peening. The blue block represents the shape of the plastically deformed area (the translucent grey block) after equilibration of the stresses occurs.

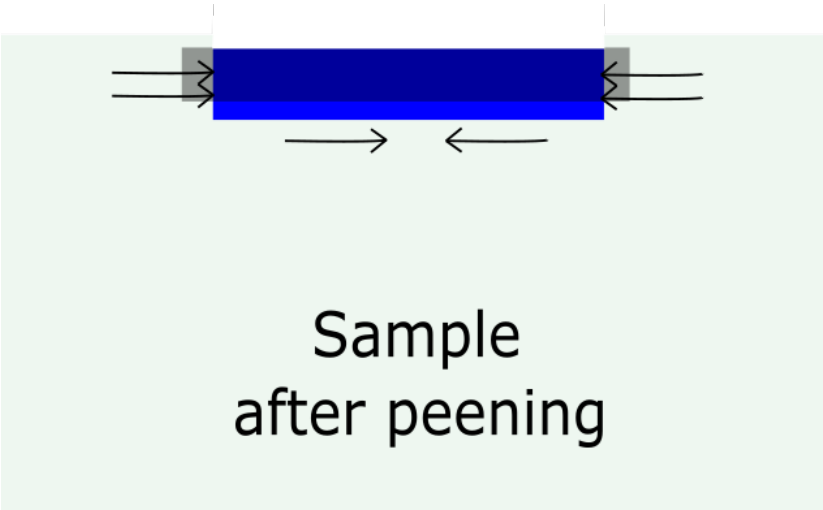

Figure 2.3: *Formation of residual stresses due to LSP*

In reality, the plastic deformation and residual stresses due to LSP are more complicated than shown in Figure 2.2 and Figure 2.3. The plastic and elastic blocks used in the schematic contrast with the reality of a continuously varying plastic distribution, which gradually transitions to a non-plastic zone. However, the process of residual stresses described above roughly matches the reality. Two principles that must hold in all cases of residual stress formation are the equilibrium condition and the compatibility condition[21]. Once again, this is explained further in subsection 4.1.

To meet equilibrium requirements, the integral of the residual stress over the cross section has to equal zero[22]. This means that beyond the plastically deformed layer, part of the stress distribution has to be tensile to balance out the compressive residual stresses near the surface. Figure 2.4 shows a typical residual stress profile due to LSP.

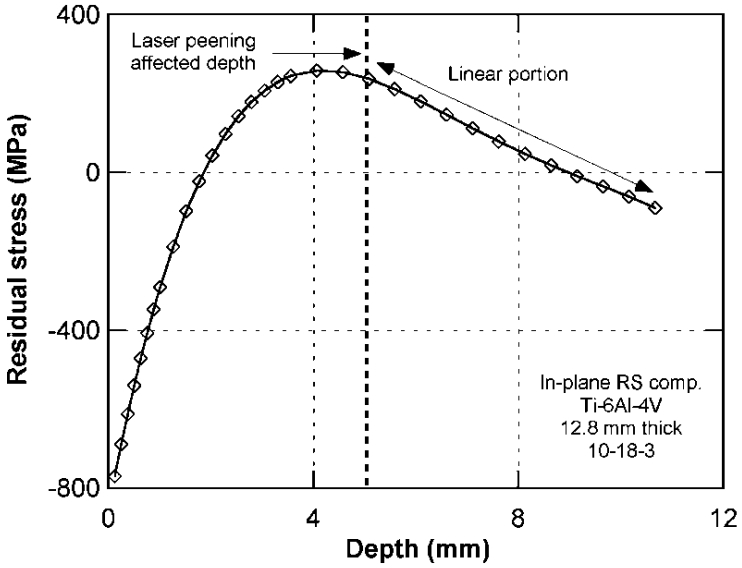

Figure 2.4: *Typical residual stress profile due to LSP*[23]

3 Properties of Metals

Many metals, including Aluminium alloys, are modelled as being homogeneous and linearly isotropic[21]. This is often true of polycrystalline metals[24]. They exhibit linear elastic behaviour for small strains. Furthermore, metals generally exhibit ductile and malleable behaviour. This means that they can be plastically deformed beyond the yield point. Metals also exhibit strain-hardening, which means that once a material is plastically deformed, a greater stress is required to cause yielding again[24].

When reviewing metal stress-strain behaviour, it is generally assumed that the behaviour is invariant with respect to strain rate. While this may be a reasonable approximation at low strain rates (static and quasi-static cases), it does not generally hold at higher strain rates. Since the strain rate due to the LSP process is high, the variation of properties with respect to strain rates has to be considered[1].

3.1 Material Property Relationships

The stress at any point in a body can be represented by a second order tensor, as demonstrated by Figure 2.5. Strain can also be represented in a similar way. Due to Poisson's effect, a normal stress not only causes a strain in the same direction as the stress, but also in the transverse directions. Thus, the normal strains in the x, y, and z directions can be related to the normal stresses using the Young's Modulus, E, and Poisson's ratio, υ, as demonstrated in Equation 2.1 to Equation 2.3[21].

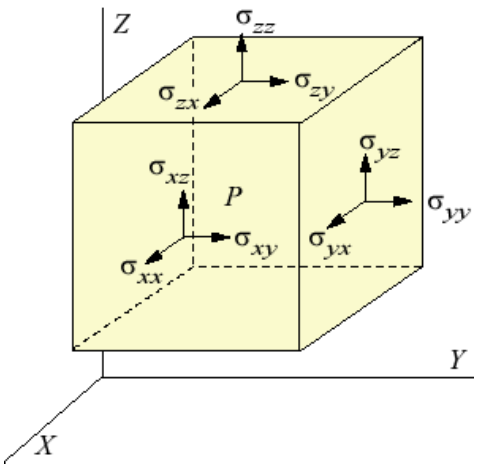

Figure 2.5: *Visual representation of the stress tensor*[25]

$$\epsilon_{xx} = \frac{1}{E}[\sigma_{xx} - \upsilon(\sigma_{yy} + \sigma_{zz})] \tag{2.1}$$

$$\epsilon_{yy} = \frac{1}{E}[\sigma_{yy} - \upsilon(\sigma_{xx} + \sigma_{zz})] \tag{2.2}$$

$$\epsilon_{zz} = \frac{1}{E}[\sigma_{zz} - \upsilon(\sigma_{yy} + \sigma_{xx})] \tag{2.3}$$

3.2 Plane Stress Assumption

The plane stress assumption applies when the principle stress in one direction is much smaller than the other stresses. The small principle stress can be assumed to be zero, reducing the stress-state to two dimensions[26]. Due to the Poisson effect, the strain in the z direction will not be zero. The following stress strain relationships apply:

$$\sigma_{zz} = 0 \tag{2.4}$$

$$\epsilon_{xx} = \frac{1}{E}(\sigma_{xx} - \upsilon\sigma_{yy}) \tag{2.5}$$

$$\epsilon_{yy} = \frac{1}{E}(\sigma_{yy} - \upsilon\sigma_{xx}) \tag{2.6}$$

$$\epsilon_{zz} = \frac{-\upsilon}{E}(\sigma_{yy} + \sigma_{xx}) \tag{2.7}$$

The plane stress assumption is usually invoked in Eigenstrain analyses[2][27].

3.3 Von Mises Yield Criterion

Metals usually obey the von Mises yield criterion, which states that yielding occurs when the distortion energy in the material equals the distortion energy due to a uniaxial loading. Thus, for any stress state, a scalar quantity called the equivalent stress can be used to determine whether the material has failed or not. This is given by Equation 2.8 in terms of the principal stresses[28].

$$\sigma_{\text{eq}} = \sqrt{\frac{(\sigma_1 - \sigma_2)^2 + (\sigma_2 - \sigma_3)^2 + (\sigma_1 - \sigma_3)^2}{2}} \tag{2.8}$$

3.4 Hugoniot Elastic Limit

A wave travelling through a material can be separated into an elastic and plastic component. The property that determines whether a wave is elastic or plastic is known as the Hugoniot Elastic Limit (HEL). Waves that have a peak stress below the HEL are elastic, else they are plastic. The HEL depends on the properties of the material, as well as the strain rate[29].

The yield stress of the material also changes at different strain rates. The yield strength at high strain rates is known as the dynamic yield stress and may differ significantly from the yield stress at low strain rates. The HEL and dynamic yield stress (${\sigma_y}^{dyn}$) can be related by Equation 2.9[29]

$$\sigma_{HEL} = \frac{1-\nu}{1-2\nu}{\sigma_y}^{dyn} \tag{2.9}$$

In LSP applications, the dynamic yield stress has to be taken into account and the static yield stress cannot be used[30].

4 Eigenstrains

4.1 What is Eigenstrain?

An eigenstrain is defined as any permanent strain induced in a material by a non-elastic process[2]. Other terms for eigenstrain are inherent strain or incompatible strain. Thus, eigenstrain can include plastic strain, thermal strain, creep strain, etc. The total eigenstrain incorporates the strain due to all these phenomena[27].

In the context of LSP, the material is plastically deformed, which leads to eigenstrain. It is reasonable to assume that plastic deformation is the only source of Eigenstrain[2]. Other strains, such as creep strains and thermal strains, do not usually occur in LSP.

Eigenstrains can be viewed as a source of residual stresses[31]. Residual stresses occur in materials due to incompatible strains. To understand this, consider an axially loaded bar that is fixed at one end. The moment the force is released, the material recovers elastically. If the stress exceeds the yield stress of the material, the material will have a permanent strain which is equivalent to the plastic strain minus the elastic recovery strain, as shown in Figure 2.6[21]. In this case there is no residual stress because the bar recovers fully to zero stress (point O' in Figure 2.6).

Now consider the case of a statically indeterminate bar, as in Figure 2.7[21]. The load, P, creates plastic strain in AC and elastic strain in BC. When elastic recovery occurs, residual stresses arise due to the redundant constraints. This can be seen in the stress strain diagram of Figure 2.8[21]. Bar BC moves to point A' on the stress-strain diagram, while bar AC moves to point B'. After elastic recovery, BC moves to point C', while AC moves to point D'.

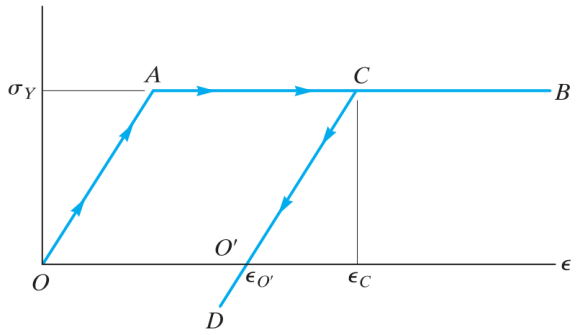

Figure 2.6: *Elastic recovery of a component subjected to plastic deformation*

The reason for this situation is that no other state of stress and strain would meet the equilibrium and compatibility conditions simultaneously. If bar BC remained at state A' and AC at state B', the compatibility requirement would be met (there would be no gaps or overlaps), but the equilibrium requirement would not be met, due to the different states of stresses in bars AC and BC. If both bars moved to zero-stress state, BC would be at state O and AC at state E, and the equilibrium condition would be met. However, such a situation cannot exist because it would lead to a gap between AC and BC, which together form one continuous, homogeneous bar (the length of the entire bar has to remain constant at 400mm). Thus, the final state of the bar has to be as shown in Figure 2.8, to meet the compatibility requirement: $\epsilon_{\text{ACFinal}} = -\epsilon_{\text{BCFinal}}$. In meeting this requirement, the equilibrium requirement is also met.

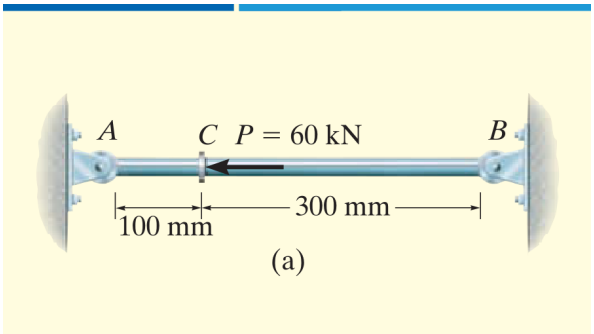

Figure 2.7: *Statically indeterminate bar*[21]

It can be seen from the above situations that not all permanent strains lead to residual stresses. It is only when a zero-stress situation fails to meet compatibility requirements that residual stresses arise. In brief, all residual stresses occur due to inelastic strains, but not all inelastic strains lead to residual stresses[32]. While the aforementioned case is much simpler than LSP, it does demonstrate a general rule: residual stresses are caused by misfits between different parts, regions, or phases of a body[33][34].

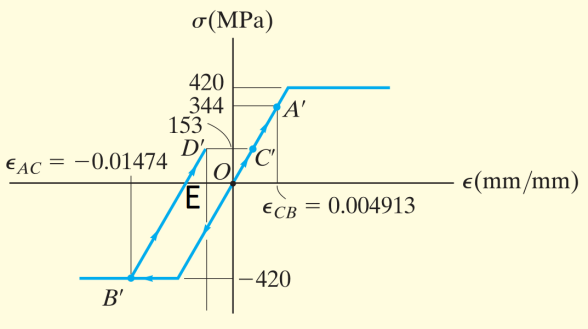

Figure 2.8: *Stress strain diagram of Figure 2.7*[21]

In the case of the bar described above, the misfit is caused by the reaction of the redundant constraints. In the case of LSP, the misfit is caused by the elastic part of the material reacting against the plastic part. In the case of the bar, there are two regions of constant strain: elastic and plastic. In the case of LSP, the strain varies continuously below the peened region. For these reasons, the residual stresses due to LSP are more complicated than those found in the bar. However, the basic principles are the same.

4.2 Eigenstrain Methods

The purpose of eigenstrain methods is to determine the residual stress and/or strain fields, given residual stress measurements at a few locations. This can essentially be achieved by solving two problems. The first is to obtain the induced eigenstrains given residual stress or residual strain. This is termed in literature as the inverse problem of eigenstrain. The second is to determine residual strain or stress from given eigenstrains. This is termed in literature as the direct problem of eigenstrain[27]. The first problem exhibits the characteristics of inverse problems in general (see section 6) and is the more difficult and complicated problem to solve.

A very important characteristic of eigenstrains is that they are insensitive to geometric parameters[23]. They depend only on the material and the peening parameters. This means that a geometrically simple specimen can be used to determine residual stresses in a complex geometry that is made of the same material and subjected to the same LSP treatment. This can be advantageous, considering that it is often difficult to directly measure the residual strains in a complex specimen.

Figure 2.9 shows a generic strategy for predicting residual stresses due to LSP in a complicated geometry. The red coloured step represents the Inverse Problem of Eigenstrain. The specifics of each step can be achieved in a variety of ways. However, most of the variety in eigenstrain methods stems from the different methods of solving the inverse problem[32][27][23]. Focus

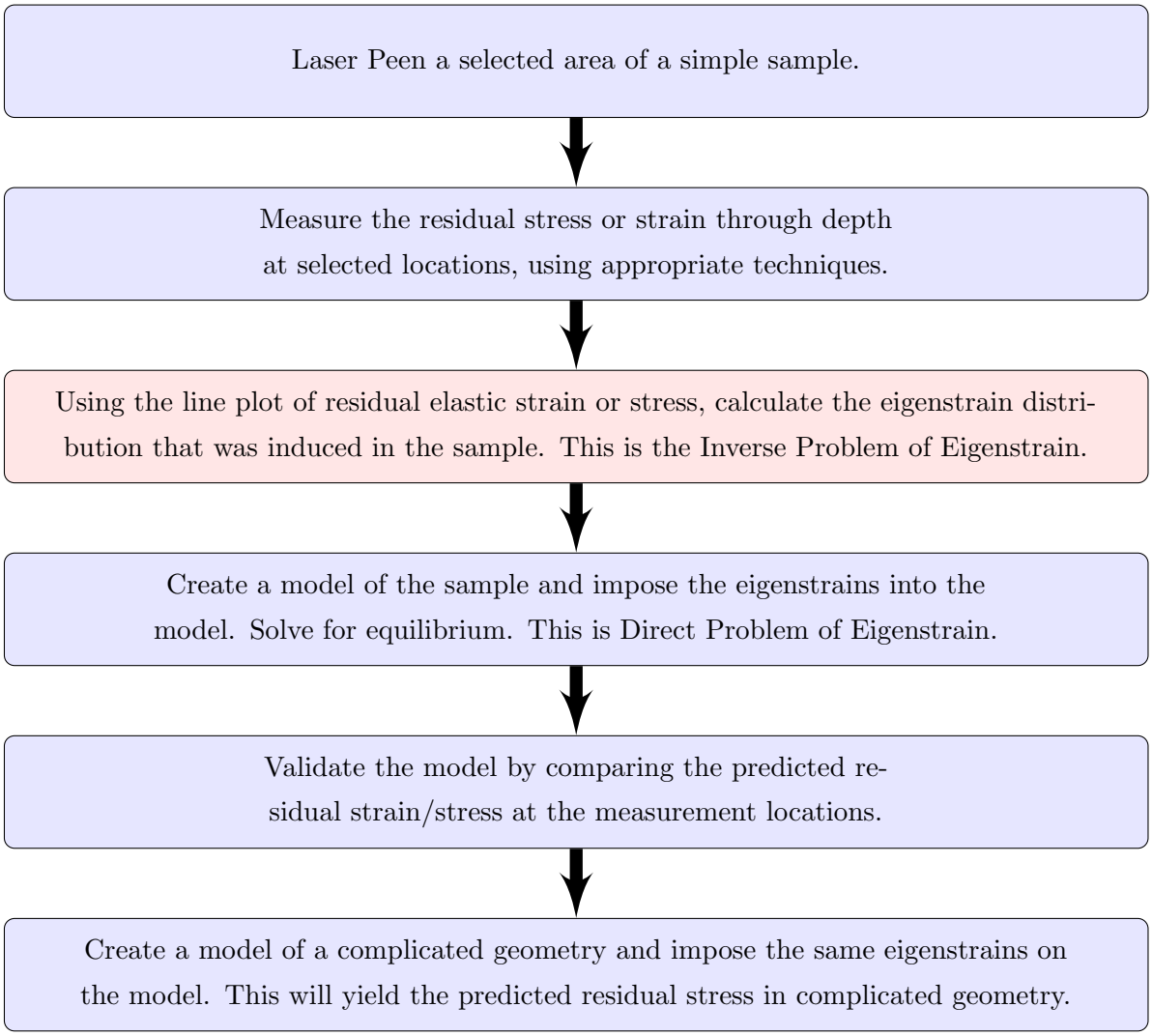

Figure 2.9: *Predicting residual stresses in complicated geometries using eigenstrain methods*

will now shift to explaining the direct and inverse problems of eigenstrain as they have been dubbed by Korsunsky[27].

4.2.1 Direct Problem of Eigenstrain

The Direct Problem of Eigenstrain involves calculating the residual stress or strain from available eigenstrain data. The total strain is given by Equation 2.10. ϵ^* represents eigenstrain and e represents residual elastic strain[27].

$$\epsilon_{\text{tot}} = \epsilon^* + e \tag{2.10}$$

The direct problem can thus be represented by Equation 2.11.

$$e = \epsilon_{\text{tot}} - \epsilon^* \tag{2.11}$$

For a complex geometry, the most obvious and common way to solve the direct problem is to create an FEM model and impose the eigenstrains on the model. As the model stands, the equilibrium and compatibility requirements are not met. In solving the model, residual elastic strain is generated. One way to impose the eigenstrains on the model is to separate the model into layers and impose the appropriate eigenstrains on each layer[2]. Another way is to impose the eigenstrains directly on the nodes[23]. The eigenstrains can be input as thermal strains. This seems to be the standard manner of doing this[2][23][35].

The residual stresses are not a direct result of LSP, itself, but are caused by the interaction of the eigenstrains with the specific geometry of the peened component. It is the eigenstrains that are a direct result of LSP. The residual elastic strain is thus sensitive to the geometry and the LSP parameters. The eigenstrain is not sensitive to geometric parameters, but sensitive to LSP parameters[2].

Once residual strain is known, the constitutive relations can be used to calculate residual stress.

Although there are minor differences in the literature concerning the details of solving the direct problem, the general approach seems to be relatively invariant, as described above[2][23][35].

4.2.2 Inverse Problem of Eigenstrain

The Inverse problem of Eigenstrain involves calculating the eigenstrains from known residual elastic strains. As with all inverse problems, this is more complicated than the direct problem. Questions over the existence of the solution and its uniqueness are common to all such problems[27].

However, in a practical situation, it is expedient to assume that the solution does exist, and that it is unique. Equation 2.10 can be manipulated to represent the Inverse Problem of Eigenstrain, as shown in Equation 2.12.

$$e = \epsilon_{\text{tot}} - \epsilon^* \tag{2.12}$$

Unlike the direct problem, there are numerous methods of solving the inverse problem available in the literature. In fact, most of the differences between different eigenstrain methods are due to differences in the inverse problem. A few methods for solving the inverse problem will be summarised hereunder. More detail can be found in the succeeding subsections.

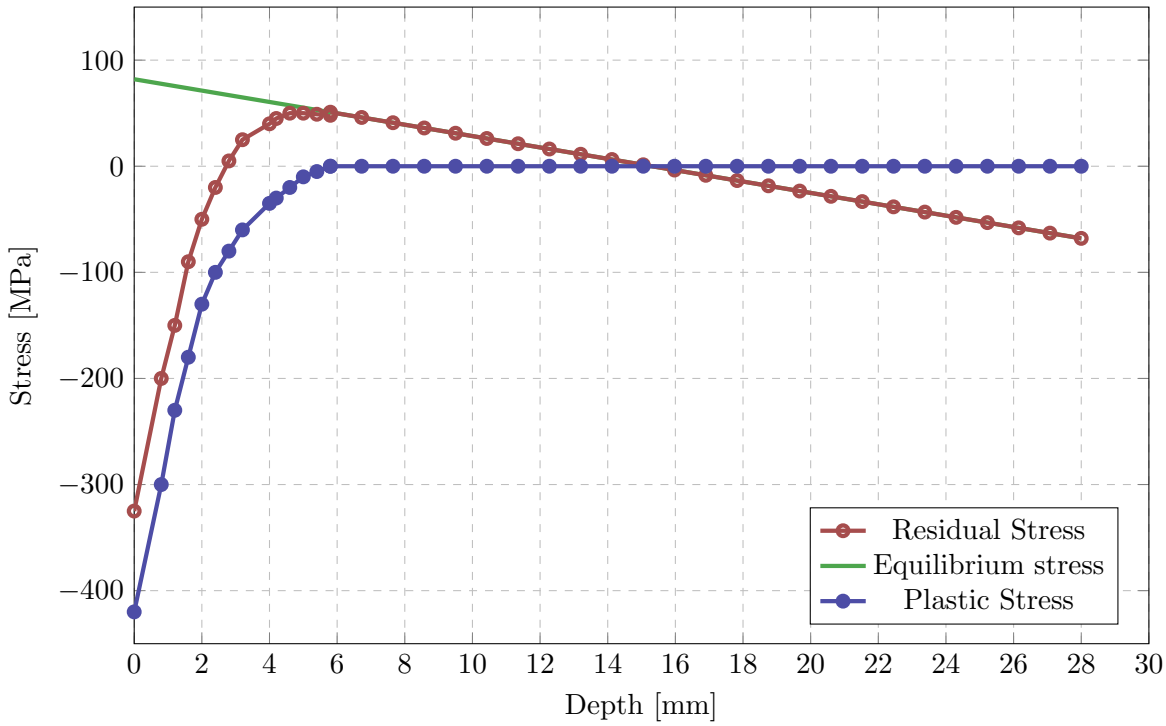

Figure 2.10: *Method of obtaining eigenstrains from residual stress plots*

The simplest method of obtaining the eigenstrains from residual stress is demonstrated by Figure 2.10. This method is based on the assumption that the peened depth is less than the thickness of the component. The method is outlined below[2].

1. Using the graph of residual stress, identify the plastically affected depth. This can be done by identifying where the curve transitions to a straight line. For example, in Figure 2.10 the plastically affected depth is around 6 mm.

2. Extrapolate the straight line through the thickness of the material. This represents the component of stress or strain that arises due to equilibrium and compatibility requirements. This is depicted by the green line in Figure 2.10.

3. Subtract the straight line from the original residual stress curve (the red curve in Figure 2.10).

4. A distribution of stresses (the blue curve in Figure 2.10) results. Use constitutive relations to convert these stresses to strains.

5. The resulting strains are the eigenstrains that produced the residual stress distribution (the red curve in Figure 2.10).

6. The eigenstrain distribution can be imposed on an FEM model of the sample to yield the residual stress field in the sample.

The above method is simple, but does not give the eigenstrain distribution in the form of an equation. Rather it yields discrete data points of the distribution. Korsunsky[27] has developed a method of solving the inverse problem that is outlined in general below. This is based on the assumption that the direct problem is a linear one. The method yields the eigenstrain distribution in the form of an equation.

1. Assume that the solution (unknown eigenstrain distribution) can be represented by a truncated sum of basis functions(ζ_i), with each function of the basis multiplied by a coefficient(c_i), as shown in Equation 3.3.

$$\epsilon^* = \sum_{i=1}^{N} c_i \zeta_i \tag{2.13}$$

2. Formulate a method of solving the direct problem, yielding residual elastic strain given an eigenstrain distribution. Korsunsky[27] presents an analytical method that is derived in subsubsection 4.3.1 that can quickly solve the direct problem. Alternatively, FEM can be used.

3. Using the method chosen above, solve the direct problem for each basis function, ζ, in turn. Due to linearity of the problem, the total predicted residual stress is the sum of all these solutions.

4. The result of the above step is a formulation of the eigenstrain in terms of the unknown coefficients of the basis distributions.

5. Determine the values of the coefficients, which will minimise the error between the predicted and measured residual elastic strain. This can be done, for example, by defining a least squares criterion between the predicted and measured residual elastic strain.

6. Since the coefficients have been solved, the eigenstrain distribution can now be expressed in terms of the basis functions and coefficients.

7. The eigenstrain distribution can be imposed on an FEM model of the sample to yield the residual stresses in the sample.

This is explained in further detail in subsection 4.3.

4.3 Korsunsky's Method

The basis of this method is the fact that the eigenstrains will be used to predict residual stress. The aim is to find the eigenstrain distribution given residual stress. According to

Korsunsky[27], the solution is the eigenstrain distribution which best predicts residual stress. The eigenstrain is assumed to be equal to a truncated set of basis functions (ζ) with unknown coefficients (c), as shown in Equation 3.3. Korsunsky proposes a set of functions of the form represented by Equation 2.14. x is the depth below the peened surface. The number of basis functions is N. x_0 is the depth of the eigenstrain distribution. ϵ^* is assumed to be invariant with all other dimensions besides x.

$$\zeta_i(x) = (x - x_0)^{i+2}, \qquad i = 1, 2, \ldots, N \tag{2.14}$$

Determining the eigenstrain becomes a matter of determining the unknown coefficients (c_i) of the basis distributions. To fix the unknown coefficients, a criterion for determining how well the predicted result fits the measured results is required. This is provided by the function J, defined in Equation 2.15.

$$J = \sum_{j=1}^{m} (y_j - e_j)^2 \tag{2.15}$$

where y_j represents the j_{th} measurement of residual stress at a depth of x_j ($j = 1, 2, \ldots, m$), and e_j represents the corresponding prediction of residual stress. Smaller values of J indicate better predictions. It is now obvious that the goal should be to seek the set of coefficients, c_i, that minimise J. To determine the predictions e_j, a linear formulation of the Direct Problem of Eigenstrain is required. This will allow us to determine e_j as the superposition of responses to each of the basis functions in turn. Korsunsky proposes a beam-bending formulation of the direct problem, which results in Equation 2.16. The full development of Equation 2.16 is outlined in subsubsection 4.3.1.

$$\begin{aligned} e(x) = \frac{1}{(x_{\mathrm{R}} - x_{\mathrm{L}})^2} \times \{ & 6\Gamma_1 (x_{\mathrm{R}} - x_{\mathrm{L}})(2x - x_{\mathrm{R}} - x_{\mathrm{L}}) \\ & + 2\Gamma \left[({x_{\mathrm{R}}}^2 + x_{\mathrm{R}} x_{\mathrm{L}} + {x_{\mathrm{L}}}^2) - 3x(x_{\mathrm{R}} + x_{\mathrm{L}}) \right] \} - \epsilon^*(x) \end{aligned} \tag{2.16}$$

The significance of Equation 2.16 is that it takes an eigenstrain, ϵ^*, as an input and outputs Residual Elastic Strain, e. For each depth at which measurements were taken, x_j, the basis functions, ζ_i, can be entered into Equation 2.16 in turn. This yields a matrix of residual elastic strain value, e_{ij}. The predicted strain at each depth, e_j is then determined from Equation 2.17.

$$e_j = \sum_{i=1}^{N} c_i e_{ij} \tag{2.17}$$

This can now be substituted into Equation 2.15 to yield Equation 2.18.

$$J = \sum_{j=1}^{m} \left(\sum_{i=1}^{N} c_i e_{ij} - e_j \right)^2 \tag{2.18}$$

As mentioned previously, the correct values of c_i are the ones which minimise J. It should be noted that J is positive definite in terms of c_i. This means that a minimum for each c_i definitely exists. The function is also quadratic, which means each c_i can have one minimum at most. Thus, a unique set of c_i can be found by satisfying Equation 2.19.

$$\begin{aligned} \frac{\partial J}{\partial c_i} &= 2 \sum_{j=1}^{m} e_{ij} \left(\sum_{k=1}^{N} c_k e_{kj} - y_j \right) \\ &= 2 \left(\sum_{k=1}^{N} c_k \sum_{j=1}^{m} e_{ij} e_{kj} - \sum_{j=1}^{m} e_{ij} y_j \right) \\ &= 0 \end{aligned} \tag{2.19}$$

Since the system of equations presented above is linear, the set of c_i can easily be solved by matrix inversion. This can be computed fairly easily without iteration. The matrix notation represented in Equation 2.20 will be used.

$$\mathbf{E} = \{e_{ij}\} \qquad \mathbf{y} = \{y_i\} \qquad \mathbf{c} = \{c_i\} \tag{2.20}$$

Equation 2.19 can be rewritten as Equation 2.21.

$$\mathbf{E}\mathbf{E}^T\mathbf{c} = \mathbf{E}\mathbf{y} \tag{2.21}$$

Letting $\mathbf{A} = \mathbf{E}\mathbf{E}^T$ and $\mathbf{b} = \mathbf{E}\mathbf{y}$, the final equation can be written as in Equation 2.22.

$$\mathbf{A}\mathbf{c} = \mathbf{b} \tag{2.22}$$

4.3.1 Development of Equation 2.16

The analysis will be conducted on the elastic beam shown in Figure 2.11. The aim of the analysis is to arrive at an expression that allows obtaining eigenstrain, ϵ^*, from residual elastic strain, e. The total strain in the body is given by the sum of the elastic and plastic strains.

Kirchoff's hypothesis of straight normals is assumed. This means that the total strain must vary linearly through the thickness of the material as shown in Equation 2.23. $h = x_{\mathrm{R}} - x_{\mathrm{L}}$ is the thickness of the beam.

$$\epsilon = a + \frac{bx}{h} \tag{2.23}$$

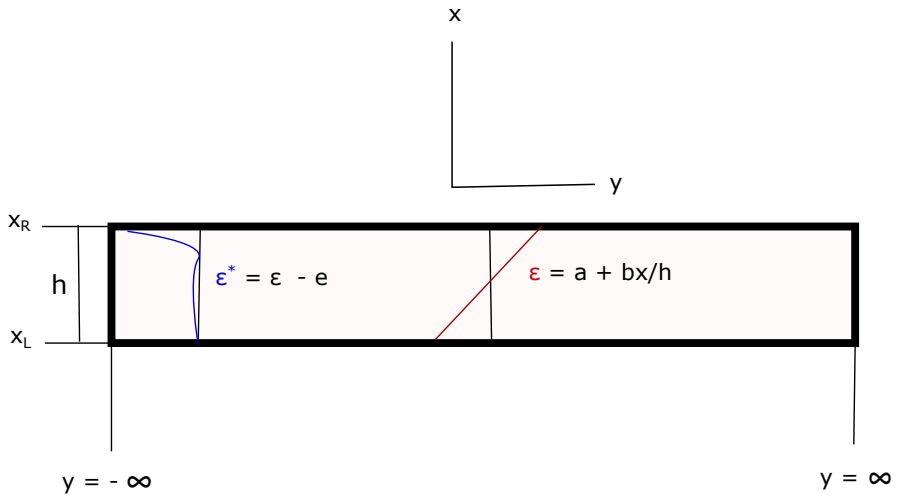

Figure 2.11: *Elastic beam used to formulate a solution to the Direct Problem of Eigenstrain*

The elastic strain can be given in terms of Equation 2.24.

$$e = a + \frac{bx}{h} - \epsilon^*(x) \tag{2.24}$$

The dependence of a and b on ϵ^* is required to make Equation 2.24 useful. The force and moment balances outlined in Equation 2.25 and Equation 2.26 can be used to obtain the necessary relationships.

$$F = \int_{x_{\mathrm{L}}}^{x_{\mathrm{R}}} \left[a + \frac{bx}{h} - \epsilon^*(x) \right] dx = 0 \tag{2.25}$$

$$M = \int_{x_{\mathrm{L}}}^{x_{\mathrm{R}}} x \left[a + \frac{bx}{h} - \epsilon^*(x) \right] dx = 0 \tag{2.26}$$

Two integral parameters that are dependent on ϵ^* can be defined as in Equation 2.27 and Equation 2.28.

$$\Gamma = \frac{1}{h}\int_{x_L}^{x_R} \epsilon^*(x)dx \tag{2.27}$$

$$\Gamma_1 = \frac{1}{h^2}\int_{x_L}^{x_R} x\epsilon^*(x)dx \tag{2.28}$$

Solving Equation 2.25 and Equation 2.26 and making use of the parameters defined in Equation 2.27 and Equation 2.28 results in Equation 2.29 and Equation 2.30.

$$a = \frac{6\Gamma_1({x_R}^2 - {x_L}^2) - 4\Gamma({x_R}^2 + x_R x_L + {x_L}^2)}{(x_R - x_L)^2} \tag{2.29}$$

$$b = \frac{12\Gamma_1(x_R - x_L) - 6\Gamma(x_R + x_L)}{(x_R - x_L)} \tag{2.30}$$

Substituting Equation 2.29 and Equation 2.30 into Equation 2.24 results in Equation 2.16.

5 Residual Stress Measurement

5.1 Incremental Hole Drilling

Incremental hole drilling is predicated on the fact that drilling a hole in an object relieves any residual stresses in the material. It is considered a semi-destructive technique, as the damage to the material is localised[22]. The technique involves drilling a small hole at the location the stresses have to be measured. The hole is drilled incrementally, and measurements are taken at each interval. This allows the stress profile through the depth to be obtained.

The stress relief around the hole manifests as a strain around the hole. This strain can be measured using a strain gauge. The residual stresses can then be calculated using the measured strains, along with calibration constants specific to the strain gauge[22].

The incremental hole drilling method is applicable to a diverse array of materials. However, certain conditions need to be met. The materials should be isotropic and the elastic properties must be known. Another important factor is that the measured strain must not be influenced by the hole-drilling process[22].

5.2 Diffraction Techniques

When a high-energy beam of a particular wavelength strikes crystallographic planes of a material at a certain angle, constructive interference occurs. This angle can be calculated by Braggs law, represented by Equation 2.31 [24]. θ is the half angle between the incoming and diffracted ray, λ is the wavelength of the incoming ray, and d is the interplanar spacing.

$$sin(\theta) = \frac{\lambda}{2d} \tag{2.31}$$

Given knowledge of the half angle and the wavelength of incident radiation, the interplanar spacing can be calculated from Equation 2.31.

When a material undergoes elastic deformation, the interplanar spacing changes from the stress-free value. Using x-ray diffraction, the interplanar spacing in a sample can be determined in the stress-free and stressed sample. The difference in interplanar spacing can be used to determine the strain that the sample is subjected to. This is the basis of diffraction techniques for measuring residual stress.

Diffraction techniques are non-destructive, as they cause no damage to the material.

5.2.1 X-ray diffraction

As the name suggests, x-ray diffraction makes use of x-rays to determine interplanar spacing between materials. In order for x-rays to penetrate deep into a thick sample (order of magnitude in cm), the energy has to be very high. This is why synchrotron sources of x-rays are needed when measuring residual stress through the thickness of a sample[22]. The low penetration depth of laboratory x-rays means that in thick samples, they can only be used to determine surface stresses.

The advantages of synchrotron diffraction are speed of data collection and high spatial resolution lateral to the beam. On the other hand, the spatial resolution varies a lot in different directions. It is excellent in the direction lateral to the beam, but much poorer in the direction parallel to the beam[22].

5.2.2 Neutron Diffraction

Neutron diffraction makes use of neutrons instead of x-rays. The principles of neutron diffraction are similar to x-ray diffraction, but here the wave nature of neutrons is being invoked.

The wavelength of massive particles is known as the de Broglie wavelength and can be determined by Equation 2.32, with h being Planck's constant, c being the speed of light in a vacuum, and m being the mass of the particle.

$$\lambda = \frac{h}{mc} \tag{2.32}$$

The de Broglie wavelength can then be used in Equation 2.31.

Neutrons have a much higher penetration depth than x-rays, and are thus much better suited to measuring residual stresses in thick samples than x-rays. The main disadvantage is that it is expensive and not highly accessible, as it requires a nuclear reactor as the source of neutrons[22].

6 Inverse Problems

Inverse problems are a class of problems in which unknown causes are determined from known effects. In a direct problem, a set of model parameters, A, is used to obtain a set of results B. The corresponding inverse problem asks the question: "Given a set of results B, what set of parameters, A, caused it?"[36][37]

6.1 Ill-Posed Problems

A well posed problem is one which the solution has the following characteristics[38]:

- The solution exists.
- The solution is unique. In other words, there is no more than one solution.
- The solution is continuous with respect to its input data. In other words, the solution is stable.

A problem with a solution that does not have any of the above characteristics is termed ill-posed. Inverse problems are mostly ill-posed problems[38]. Ill-posed problems present difficulties in solving because the solution may not exist, may not be unique, or may not be stable (A small change in initial conditions of the problem leads to large changes in the solution). Due to the instability of ill-posed problems, they require regularization to make them more stable[38].

7 Optimisation

Optimisation, in general, means finding the best object from a range of objects, according to some pre-defined criterion. Mathematical optimisation involves maximising or minimising a function or functions of one or more variables, subject to a set of constraints[39]. Minimising or maximising a function means finding the set of variables that yield a minimum or maximum value of the function.

The functions that are sought to be minimised are known as the objective functions. The independent variables of the objective function are known as design variables. If more than one objective is to be minimised at once, it is known as multi-objective optimisation[40]. Constraints are limitations on the values of the design variables. If there are no limitations on the design variables, the problem is an unconstrained problem, as opposed to constrained optimisation. Optimisation problems can also be classified as being discrete versus continuous, and deterministic stochastic.

Continuous problems are usually easier to solve than discrete problems because the smoothness of the function allows us to obtain information about neighbouring points to any particular point, x. Calculus methods can be used to calculate local minima and maxima. In deterministic problems, it is assumed that the data given is exact. In stochastic problems, uncertainty in data is taken into account[41]. There are numerous optimisation algorithms available, each tailored to suit different problems. Some algorithms will be reviewed here.

7.1 Nelder-Mead Method

Nelder-Mead is a simplex algorithm for unconstrained optimisation of multidimensional functions without derivatives. It can therefore be used for problems with discontinuous functions[42]. A simplex is the generalisation of a triangle to arbitrary dimensions. A simplex in n dimensions has $n + 1$ vertices. For example, a triangle exists in two dimensions and has three vertices[43].

The method works by evaluating the function at each vertex of the simplex, and rejecting the worst vertex. The worst vertex is then replaced by a new vertex. Thus, a new simplex is generated after each iteration. As the process continues, the vertices get closer and closer to the optimum value, and the simplex gets smaller and smaller. Eventually, the simplex converges on the solution[43].

7.2 Powell's Method

Like Nelder-Mead, Powell's method can also be used for unconstrained minimisation of multidimensional functions without derivatives.

Let $\mathbf{X}_0 = (a_1, a_2, \cdots, a_N)$ be an initial guess of the location of the minimum to the function $f(x_1, x_2, \cdots, x_N)$. Let $\mathbf{p}_1, \mathbf{p}_2, \mathbf{p}_3, \cdots, \mathbf{p}_N$ be a set of vectors called search vectors. The next approximation $\mathbf{X}_1$, can be obtained by minimising of f along each of the set of search vectors in turn, which yields a linear combination of the search vectors. $\mathbf{X}_1$ is set equal to this linear combination. $\mathbf{X}_1$ is also added to the end of the list of search vectors. The most successful search vector is deleted from the list, and the process continues until the criterion for convergence is reached[43].

7.3 Broyden-Fletcher-Goldfarb-Shanno Method

This method, commonly known as the BFGS algorithm can be used to solve unconstrained non-linear optimisation problems. It is a gradient-based method, which seeks to find local minima by finding the point at which the gradient of the function is zero. The method uses the function values and gradient values. The Hessian is not required, as it is approximated using the gradient[44].

8 Curve Fitting

Curve fitting is the process of selecting a curve which best fits a set of data points[45]. There is a distinction between curve fitting and interpolation. In interpolation, a curve which runs through all the data points is sought. The assumption is that the data points are distinct and accurate. Interpolation is useful in situations where the scatter or uncertainty in the data is small, there are few data points, and/or a causal relationship between the variables is known to exist[46].

In contrast, regression analysis seeks a smooth curve that approximates the relationship between two variables. In this case, the curve does not necessarily have to pass through any of the data points. It merely has to capture the trend of the data as closely as possible. This is useful in situations where there is large uncertainty or scatter in the data, there are many data points, and/or a stochastic relationship between the variables is sought[46].

In some cases one method is obviously more suitable than the other. At other times, both methods may be applicable and it is left to the modeller to decide between the two.

8.1 Regression Analysis

Since the aim of regression analysis is to find the best-fit curve, it is pertinent to ask: "What is the best fit?" This leads to the formulation of a criterion, J, called the Goodness of Fit, which measures how well the curve fits the data. The most popular criterion is the Least Squares criterion, which defines the best-fit curve to be the one which minimises the sum of squared residuals, as shown in Figure 2.12[46]. The least squares function is defined in Equation 2.33.

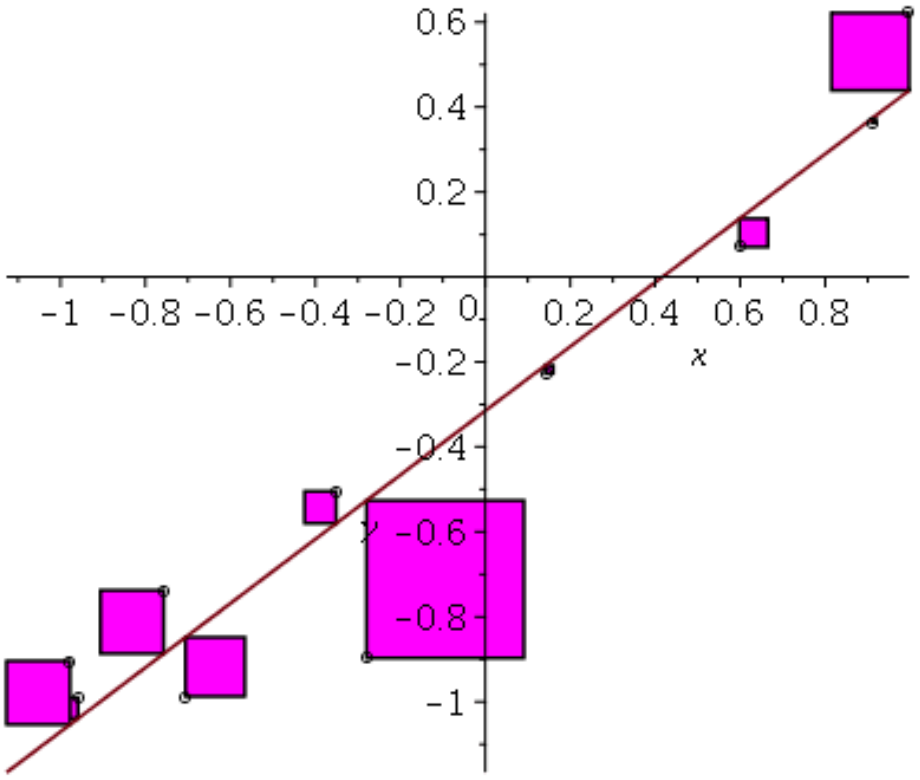

Figure 2.12: *Example of a least squares fitted line*

$$J = \sum_i (y_i - f(x_i))^2 \tag{2.33}$$

The objective of the Least Squares Analysis is to minimise J.

Besides the least squares criterion, there are other criteria that could be used, such as:

- Least Absolute Deviations, which aims to minimise the sum of absolute values of the deviations between predicted and actual values.
- Maximum Absolute Error, which aims to minimise the absolute value of the maximum deviation between predicted and actual values[47].

Having defined a Goodness of Fit criterion, the next step is to define a set of functions, differentiated by mutable parameters. This is formally expressed in Equation 2.34, where y is the dependent variable, x_i is the set independent variables, and c_i is the set of parameters. The goal is then to seek the values of parameters which best meet the criterion. In the case of least squares, the solution would be the parameters which yield a minimum of J[46]. A distinction can be made between linear and non-linear regression. In linear regression, the dependent variable is linear in terms of the parameters c_i (not the independent variables x_i). Linear regression problems are simpler to solve than non-linear problems.

$$y = f(c_i, x_i) \tag{2.34}$$

The choice of function depends on the context of the problem. For example, if the data exhibits large rates of change in the dependent variable, an exponential function might be most appropriate. A common choice is a polynomial, as polynomials are versatile and can be used in a large variety of problems. In the case of a single independent variable and linear regression, the polynomial can be defined as in Equation 2.35.

$$y = \sum_{i=0}^{N} c_i x^i \tag{2.35}$$

The parameters that need to be determined are the coefficents to the polynomial. The number of coefficients is equivalent to the number of terms, $N + 1$, in the polynomial. It is important to note that a problem with m different data points will only have a unique solution if $N < m$[46]. This is because the maximum number of equations that can be generated is m. If there are more regression coefficients than equations, there is no unique solution to the regression coefficients.

Since the least squares function in Equation 2.33 is positive definite, it has at most one minimum, and thus the solution is guaranteed to be unique.

8.2 Parsimony

Increasing the value of N does not diminish the Goodness of Fit and might increase it[27]. However, a caveat must be stated here. While increasing the terms may lead to a better goodness value, this does not necessarily imply that the approximation is more desirable. This is because adding more terms increases the order of the first derivative of the function, which increases the number of potential maxima and minima. This can lead to oscillatory behaviour of the approximation, which is undesirable, as it captures 'noise' and thus defeats the whole purpose of the regression analysis. This phenomenon is known as overfitting.

Overfitting occurs when the number of parameters is high relative to the number of data points. The opposite happens when the number of parameters is too low. In this case the polynomial does not curve enough to fully capture the shape of the data. Therefore a balance must be sought in choosing the correct value of N. Figure 2.13 is an illustration of the differences between overfitting and underfitting.

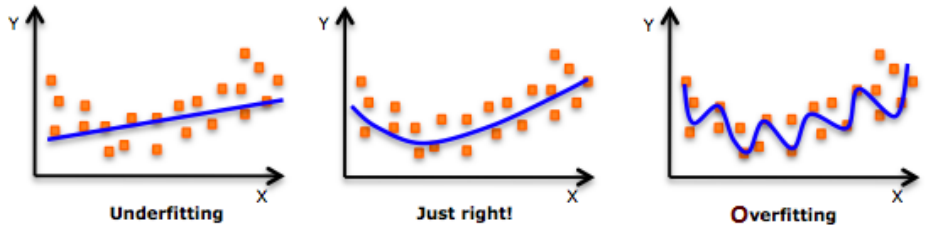

Figure 2.13: *Example of overfitting and underfitting*

It is clear from the above explanation that the Goodness of Fit criterion only tells part of the story, and cannot replace a visual examination of the predicted curve. However, while a visual examination is not a concern when testing a single model, it may prove burdensome when selecting the best model from a large number of models. In such cases, one often wishes to automate the selection process with the aid of a computer. One cannot have confidence that the Goodness of Fit criterion will yield the best model in such cases because one cannot visually examine the output of every model. For this reason another criterion specifically for comparing different regression models is needed. This criterion is called parsimony[48].

The concept of parsimony arises from the need to balance complexity with Goodness of Fit. In this context complexity is defined as the number of regression coefficients[48]. There are many measures of model parsimony, but two measures seem to be more popular than the rest: AIC (Akaike's Information Criterion) and BIC (Bayes's Information Criterion)[49].

AIC is defined in Equation 2.36, where n is the number of data points, J is the Goodness value, and p is the number of parameters[48].

$$AIC = n \log J + 2p \tag{2.36}$$

The AIC criterion is not very consistent. In particular, it fails to select a good model when the number of data points is very large[49]. It tends to select models that overfit the data[48].

BIC is defined in Equation 2.37. The symbols are consistent with Equation 2.36. The BIC criterion remains consistent as the number of data points increases. This is because the penalty term for model complexity, $p \log n$ increases with increasing n[49]. BIC tends to be conservative in allowing complex models[48]. It tends to choose models that underfit data[49].

$$BIC = 2 \log J + p \log n \tag{2.37}$$

8.3 Goodness of Fit Metrics

Although the sum of squared residuals, J, is a good criterion for Goodness of Fit, it does not give a lot of information as a metric. Firstly, it is not possible to tell, simply from looking at the value of J, whether a fit is good or not. Therefore, it cannot be used to compare Goodness of Fit between two samples with different regression coefficients. Secondly, a sample with more data points might have a larger value of J, even though the fit is as good as one with fewer data points. Thus, it cannot be used to compare the Goodness of Fit between two samples with different numbers of data points.

The Goodness of Fit criterion, however, can be used as a basis for other Goodness of Fit measures, which have better properties for comparison purposes. One such measure is the Standard Error, defined in Equation 2.38, where f is the predictive function, y_i are the measured data and n is the number of data points[50].

$$SE = \sqrt{\frac{\sum_i (y_i - f(x_i))^2}{n - 2}} \tag{2.38}$$

The numerator is equivalent to J. The minimum value of SE is 0. It has no upper limit. It is clearly not sample specific as it is not affected by the number of data points. It can thus be used to compare samples with different numbers of data points[50]. SE is an estimate of the average deviation of the predicted values from measured data. SE has the same weakness as J as an independent measure. Since it has no upper limit, there is no indication from SE on its own whether the fit is good or bad[50]. It can only be used to compare different samples.

Another metric is the Coefficient of Determination, commonly known as r^2. This metric is defined in Equation 2.39. The symbol $\overline{y}$ represents the mean of the set y_i. The numerator of the fraction is equivalent to the sum of squared residuals J. The denominator is known as the Total Sum of Squares. This metric can be interpreted as the proportion of total variance that is explained by the predictive function[50].

$$r^2 = 1 - \frac{\sum_i (y_i - f(x_i))^2}{\sum_i (y_i - \overline{y})^2} \tag{2.39}$$

The major advantage of r^2 is that it has an upper and lower limit. The upper limit is 1, which corresponds to a perfect fit, and the lower limit is 0, which corresponds to no fit. Thus, r^2 immediately gives an idea of the the fit, unlike SE. However, it is sample specific, so it cannot be used to compare between samples with different data points[50].

From the above discussion, it should be apparent that no single metric of Goodness of Fit is better than the others. They each have their advantages and disadvantages, and each conveys different information. In some cases, the different metrics can lead to different results. This is due to the fact that SE is unaffected by accidental differences in the independent variable, while r^2 is[50].

9 Effects of Geometry on Residual Stresses due to LSP

The Principle of Transferability of Eigenstrain states that, while the eigenstrains (plastic strains) induced by LSP are highly dependent on the LSP parameters, they are insensitive to the geometry of the peened specimen[2][23][51]. However, it is known that residual stresses differ according to the geometry of the specimen, despite the eigenstrain distribution being the same. The reason is that the residual stresses depend on two effects:

1. The plastic strain induced by LSP
2. The equilibration of stresses, which depends on the geometry of the peened specimen

Thus, as stated previously, knowing the eigenstrains in a specimen, one can predict what effect the same LSP process would have on a specimen with a different geometry. Such studies have already been conducted by Coratella[51] and De Wald[23][52].

9.1 Effect of Thickness on Residual Stress

De Wald[23] has conducted a study, wherein residual stresses – in 316L stainless steel samples of varying thickness – were measured. The results of this study are depicted in Figure 2.14. He noticed initial discrepancies between residual stress profiles predicted assuming the Principle of Transferability of Eigenstrain. This prompted him to conduct the currently-mentioned study. He found that, in actual fact, the depth of peening changed in specimens with differing thickness, as can be clearly seen in Figure 2.14.

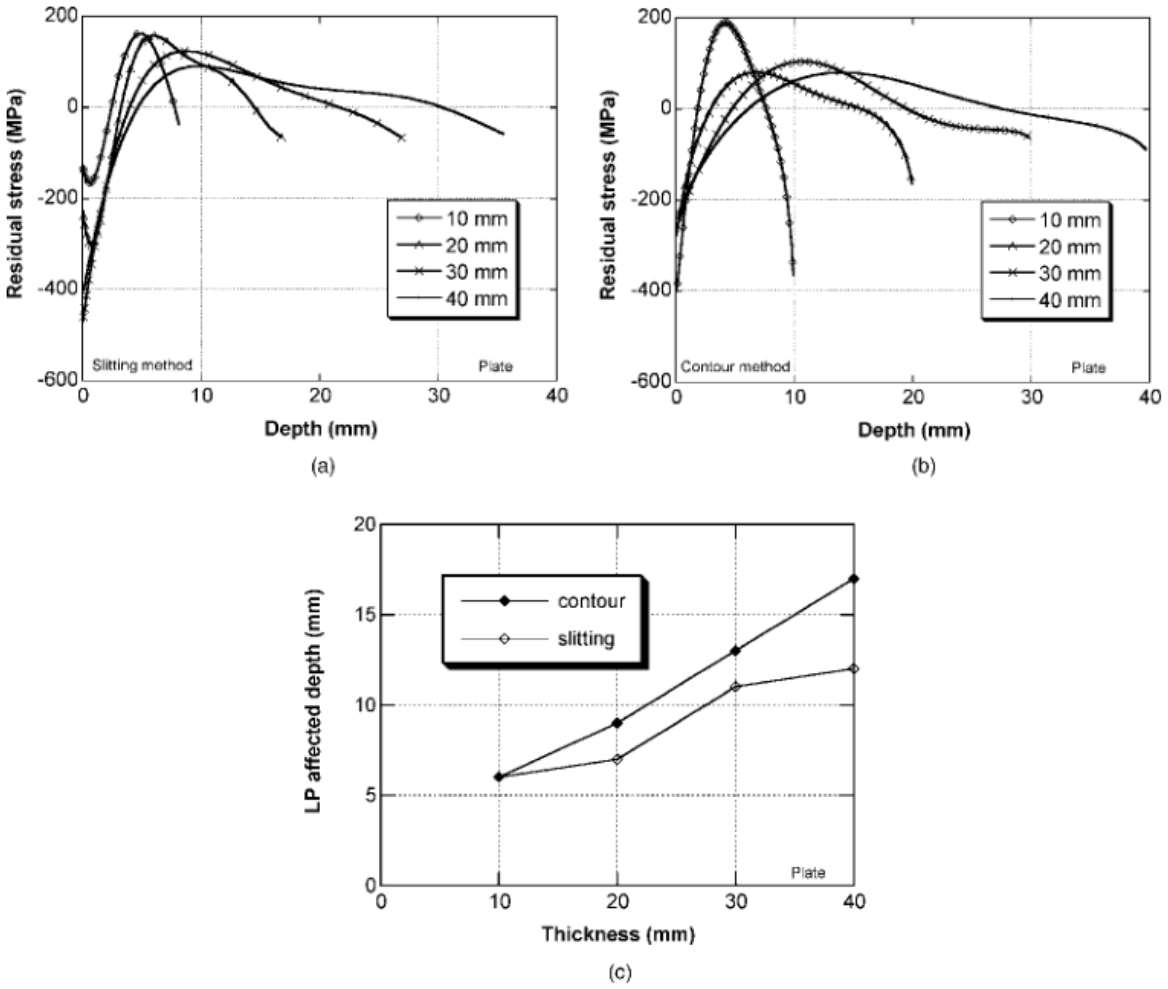

Figure 2.14: *Measured residual stresses in 316L samples of varying thickness: (a) measured using contour method, (b) measured using slitting method, (c) plot showing the laser peening affected depth as a function of material thickness for each set of measurements*

This presents a conundrum because it contradicts what many of the proponents of the Eigenstrain method claim; eigenstrains are independent of geometry[2][27][32]. De Wald[23] attributes this discrepancy to differences in shock wave propagation in different samples. In thick samples, the shock wave has a chance to dissipate before reaching the bottom of the

sample. In thin samples, the shock wave might not dissipate; leading to reflection of the shock wave and leading to tensile stressing[23].

It seems that there is a way of reconciling this apparent contradiction if one considers the Principle of Transferability of Eigenstrain to be a general rule that is not absolute. It only applies when the geometry does not affect the formation of eigenstrains.

In the above case, illustrated by De Wald, it seems that the Principle of Transferability of Eigenstrain applies more to thick samples, and less to thin samples. As the thickness increases, the shock wave has more room to dissipate. The effect of this dissipation does not change much with increasing thickness. The incremental difference in eigenstrain distribution decreases with increasing thickness, and converges to a value at infinite thickness.

One more thing to mention in this regard is that, at present, there is no way of saying with certainty, at what thickness the eigenstrain distribution can be said to be independent of thickness, or what the discrepancy is between the actual and assumed eigenstrains in thin samples. Thus, many questions remain.

Considering the above, it would not be appropriate to say that eigenstrains are independent of geometry, but rather they are insensitive to geometry. Besides the above scenario there may be other scenarios where geometry does have an effect on the process and thus eigenstrains induced.

Besides the effect of thickness on the eigenstrain distribution, there is other information that can be extracted from Figure 2.14. From the slitting method results, which seem to be more accurate near the surface, it appears that the maximum compressive residual stress increases as thickness increases. The maximum tensile residual stress also seems to increase with increasing thickness. The linear portion of the curve (note that the waviness of this portion should be ignored and attributed to measurement uncertainty) becomes less steep in thicker samples.

Achintha and Nowell[53] have conducted a study on the effects of edges on eigenstrain distribution and residual stresses in laser peened components. An important finding concerning the eigenstrain distribution next it and edge is dubbed the 'edge effect'. When peening adjacent to an edge, a narrow strip of the peened zone next to the edge is affected by the edge, leading to a different eigenstrain distribution in this narrow strip, compared to the rest of the peened region. This can be seen in Figure 2.15[53]. As can be seen, the effects of the edge do not extend into the bulk of the peened region.

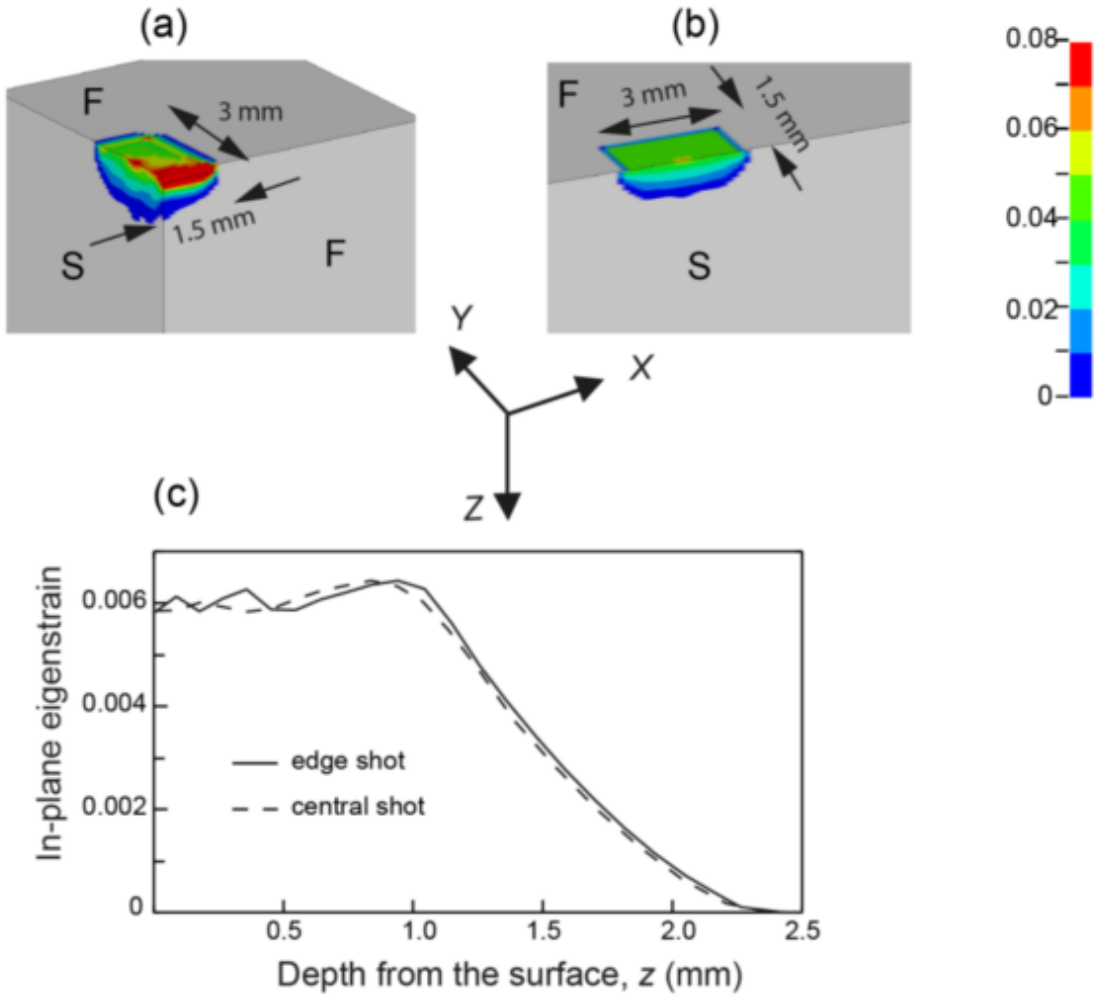

Figure 2.15: *Eigenstrain distribution under an (a) edge pulse (b) central pulse (c) eigenstrain depth profile at the centre point of an edge pulse and a central pulse (F = Free plane S = Symmetry plane)*

Achintha and Nowell have also investigated the effect of arrays of LSP shots on eigenstrain distribution. Importantly, they have shown that, ignoring edge effects, the eigenstrains induced by peening do not vary much in the plane of peening. For the purposes of eigenstrain methods, this means that one can safely assume that the eigenstrains vary only in the depth direction and not in the other directions[53][54].

9.2 Effect of Curvature on Residual Stress

DeWald and Hill[52] have conducted a study in which residual stresses in various geometries were measured and compared to eigenstrain model predictions. They focussed specifically on cylinders and fillets. The specific components they analysed are shown in Figure 2.16. Overall, they found a fair amount of agreement between predicted and measured results.

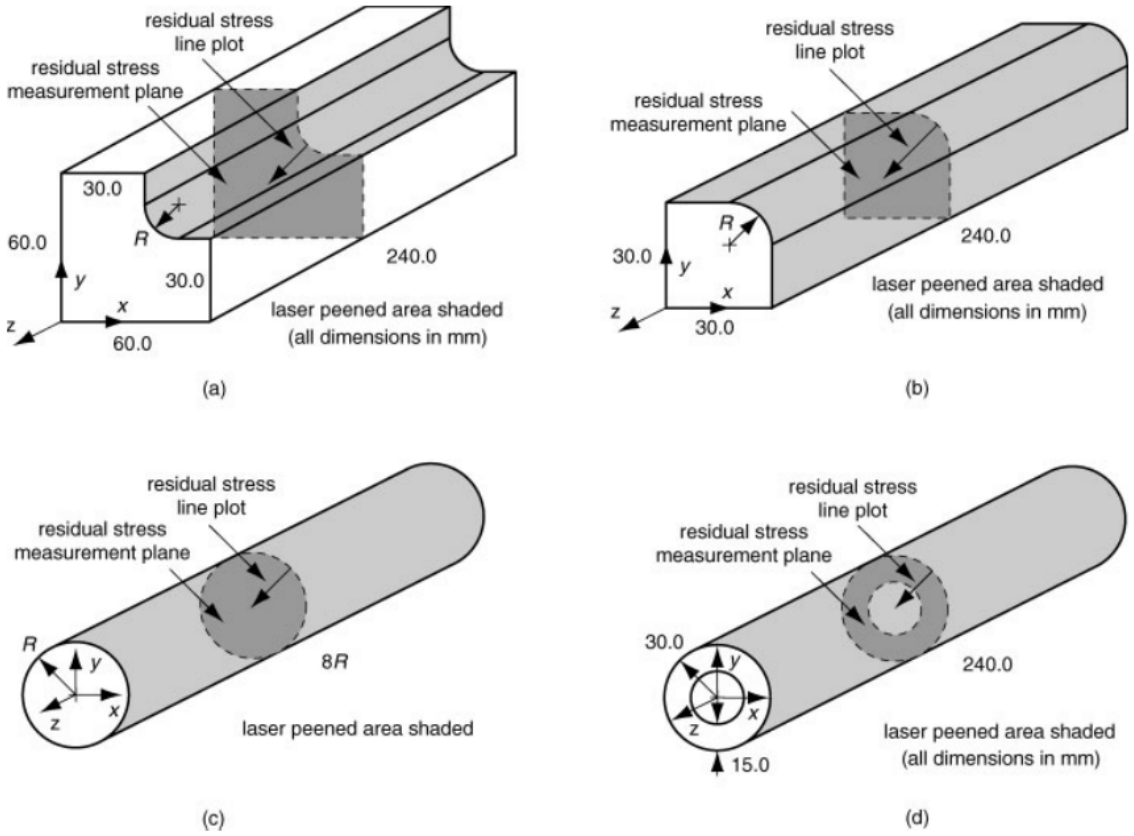

Figure 2.16: *Descriptions of various specimen families used for laser peening residual stress geometry study: (a) convex fillets, (b) concave fillets, (c) round bars, and (d) thick-walled pipes*

They found that for both cylinders and fillets, radius has an important effect on residual stresses. Increasing the radius of a convex fillet tends to decrease the depth of compressive residual stress. The opposite is true for concave fillets. For concave and convex fillets, increasing the radius increases the magnitude of the surface stress. For small fillet radii, discrepancies between measured and predicted results were found around the vicinity of the fillet. However, this discrepancy was much smaller for larger radii. This discrepancy is probably due to the geometry affecting the eigenstrain distribution. DeWald[52] postulates that for convex radii, the curvature might focus the shock, leading to a more intense plastic distribution compared to a planar shock. In concave radii, the eigenstrains at certain points might be affected by adjacent peening, modifying the eigenstrains from what is expected in a flat sample.

Increasing the radius of cylinders increases the depth of compression, but decreases the magnitude of the surface residual stress[52].

Achintha and Nowell[53] have compared residual stresses in straight edges and rounded edges. They found that while the straight edge leads to a greater depth of compression, the large radius fillet leads to a greater magnitude of compressive stress near the surface and greater maximum compressive residual stress. The stress field of a rounded edge approaches that of a straight edge as the radius decreases.

They also found that peening over a sharp edge leads to an eigenstrain distribution that is difficult to predict. This is because the peening of the second region overlaps with the first peened region[53]. They propose using superposition to estimate the final eigenstrain. Comparing the prediction of eigenstrain methods with superposition to process modelling prediction, they found good agreement[53]. However, this should not be taken as an indication that superposition can be used in general, as plastic deformation is a non-linear process in general. Achintha and Nowell used an elastic and perfectly plastic material model.

Vasu and Grandhi[55] have compared concave and convex plates with flat plates, using process modelling. Their model predicts that compressive residual stresses decrease with increasing radius in concave geometries, and increase in convex geometries.

Chapter 3 Validation of Models

This chapter deals with the first objective of the project. Various eigenstrain models are tested against previously obtained benchmark samples, and compared to each other. The Principle of Transferability of Eigenstrain is also tested.

1 Benchmark Data

This section discusses the benchmark data used to validate the various models tested in this section. The benchmark data was generated by Van Staden[56] and collated into a database. Cuboid AA 7075 samples of various dimensions were subjected to laser peening, as shown in Figure 3.1. As can be seen from the figure, the peened areas are rectangular. Some of the samples were peened over four areas (Like the sample in Figure 3.1), while others were peened on one.

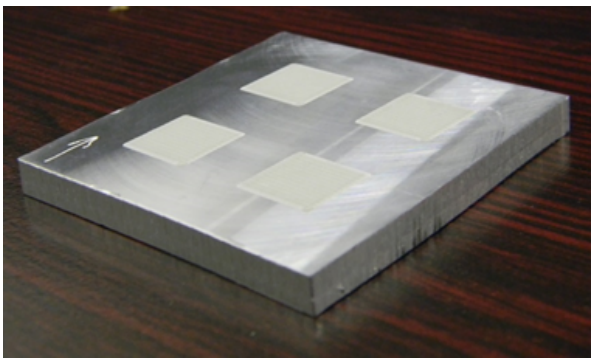

Figure 3.1: *One of the benchmark samples*

Figure 3.2 shows that the spot shape is circular and that peening was done in a raster pattern. A variety of spot sizes, power intensities, and spot coverages were used. The range of values for the different parameters is shown in Table 3.1. Details of the parameters of the samples used in this study are given in Appendix A. The nomenclature of samples in this dissertation is based on Table A.2. A number of measurement methods were used to obtain line plots of residual stresses through the centre of the samples. These are listed below:

- Incremental Hole Drilling
- Synchrotron X-ray Diffraction
- Neutron Diffraction
- Laboratory X-ray Diffraction

Figure 3.3 is an example of residual stress data collected using the techniques listed above. An important feature to note is that the residual stress beyond a depth of around 5 mm becomes non-linear with respect to depth, which implies that the eigenstrains near the bottom of the sample are non-zero. This is not a feature that is expected from laser shock peening, as it only induces plasticity close to the peened surface. It can be assumed that wherever this feature occurs, it is a result of machining or some other process that occurred before peening. This assumption is corroborated by the black line in Figure 3.3 (The neutron diffraction data), which shows that there is residual near the bottom of the sample even prior to peening.

It was decided that the validation of the various models would be conducted using the neutron diffraction data because it spans the entire sample and has less noise than the synchrotron X-ray diffraction.

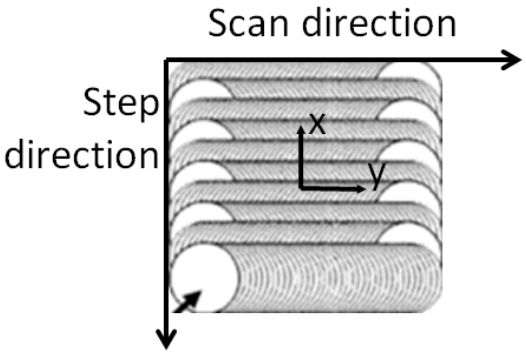

Figure 3.2: *Pattern of peening*

Although validation of the models was done with more than one sample, Sample B15 will be used to illustrate the methodology used and results. Results for other samples can be found under Appendix B. The geometric and peening parameters for Sample B15 are recalled hereunder for convenience:

- Size: 60×60
- Thickness: 6 mm
- Number of peened areas: 4

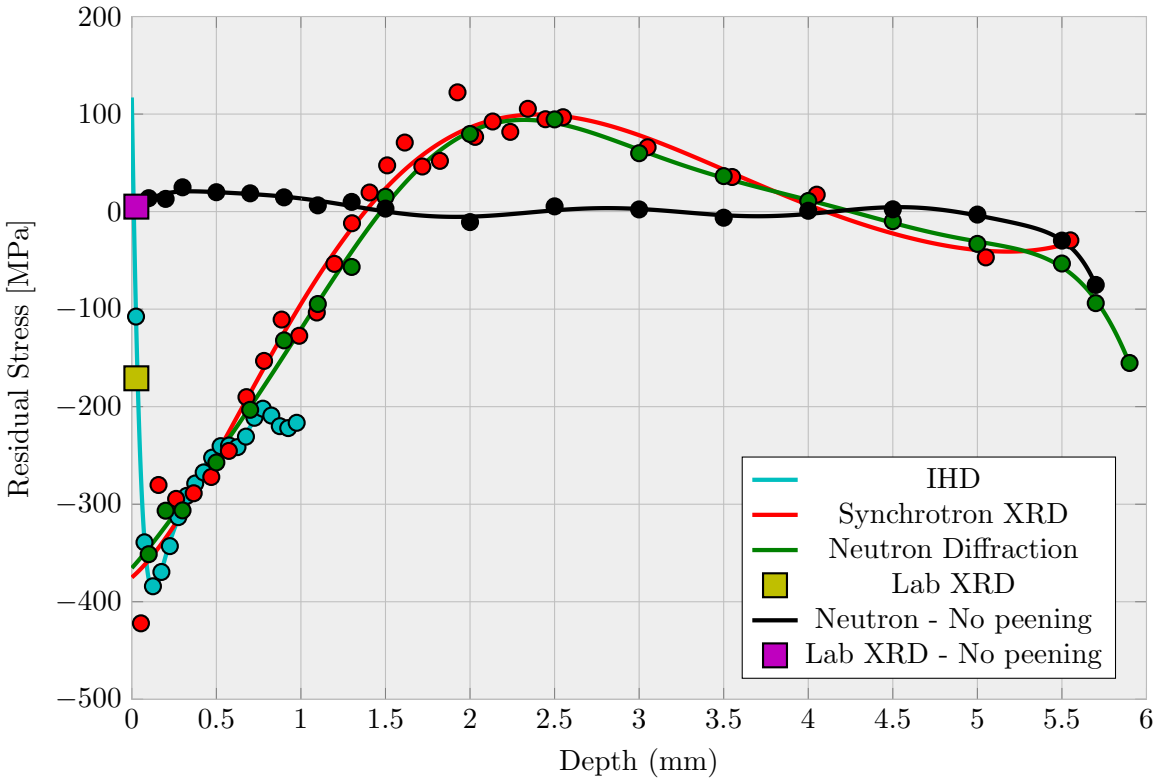

Figure 3.3: *Residual stress measurements using various techniques*

Table 3.1: Range of values

Parameter	**Range of values**
Size [mm×mm]	28 × 28; 60 × 60; 100 × 100
Thickness [mm]	1.6; 3.0; 6.0; 10.0
Number of peened areas	1; 4
Power intensity [GW/cm^2]	1.5; 3.0; 4.5; 6.0
Spot size [mm]	0.5; 1.0; 1.5; 2.0
Coverage[spots/mm^2]	2.8125; 5.0; 14.51; 21.88; 50.38; 67.1
Young's Modulus [MPa]	71 700
Poisson's Ratio	0.33

- Power intensity: $3\,\mathrm{GW/cm^2}$
- Spot size: $1.5\,\mathrm{mm}$
- Coverage: $5\ \mathrm{spots/mm^2}$

The co-ordinate system used when measuring the residual stresses in the samples is defined in Figure 3.4. The scan and step directions are defined relative to the pattern of peening, in Figure 3.2. The normal direction is the normal to the plane of peening. Throughout this dissertation, the x co-ordinate will refer to the step direction, the y co-ordinate to the scan direction and z to the normal direction, unless stated otherwise.

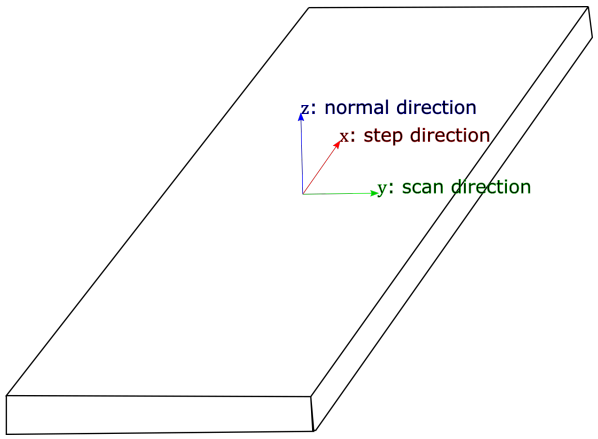

Figure 3.4: *Coordinate system used in this dissertation*

2 Direct Problem of Eigenstrain

Since the Direct Problem of Eigenstrain was conducted in the same way for all the methods tested, the approach that was used will be elucidated in this section.

The direct problem involves the determination of residual stress or strain from a known eigenstrain distribution. In this project, it was done using ANSYS Workbench. The following procedure was used:

1. A CAD model of the sample was created in Autodesk Inventor, replicating the geometry of the actual sample.
2. The peened area of the sample was measured and reproduced in the CAD model by splitting away a block of material representing the volume under the peened area. The model was thus split into a peened part and an unpeened part.

3. The peened part was split into layers corresponding to the depths at which measurements were taken, as shown in Figure 3.5.

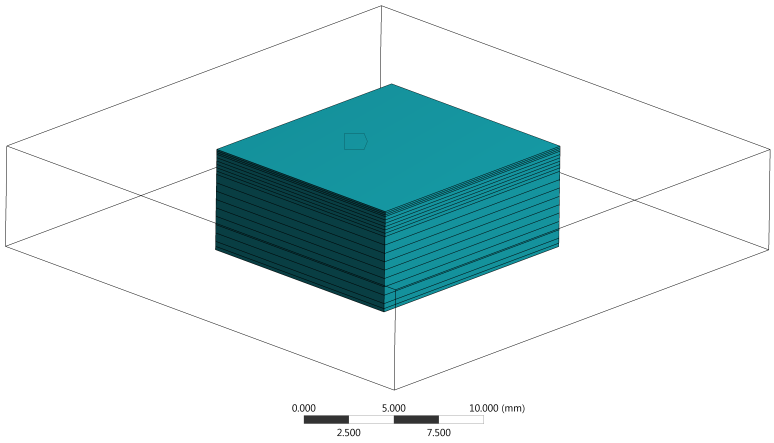

Figure 3.5: *Sample B15 split into layers*

4. Since the elastic recovery is purely a linear elastic process and occurs over a long period of time relative to the response rate of the material, ANSYS Static Structural was deemed sufficient to conduct the analysis.

5. The Inventor model was imported into ANSYS Design Modeller.

6. The sample has four peened areas, but is symmetrical about two planes. Using the symmetry tool in ANSYS Design Modeller, the geometry was reduced to a quarter of its original size, with only one peened area.

7. Since plasticity cannot be directly introduced into a model, a trick has to be used to introduce eigenstrains into the model. A simple, but effective, way of doing this, is to introduce the eigenstrains as thermal strains. For each layer of the model, a material was created with three properties: Young's Modulus, Poisson's Ratio, and Orthotropic Coefficient of Thermal Expansion.

8. For the unpeened part of the material, only Young's Modulus and Poisson's Ratio were used. For all the materials created, the Young's Modulus and Poisson's Ratio were set to 71 700 MPa and 0.33, respectively, which are the values for Aluminium Alloy 7075.

9. The eigenstrains in each direction were input as Coefficients of Thermal Expansion in the corresponding directions.

10. For each part of the model, the relevant material was assigned.

11. The mesh was generated.

12. A unit temperature rise was applied to the entire model. This applied all the eigenstrains to their respective layers in the model. No other boundary condition or loading was required, as elastic recovery process is an internal mechanism to reach equilibrium.

13. Upon solving the model for equilibrium, the residual stresses were generated.

There are some important issues to consider in the above procedure. Firstly, it is important to note that the unit temperature rise applied to the model does not reflect any physical reality of the process. It is merely a proxy to introduce the eigenstrains into the model by making use of thermal expansion. This non-physical process can be used to apply eigenstrains because the actual physical cause of the eigenstrain is irrelevant to the solution of this problem. It is the values of the eigenstrains themselves which are important. Thus, eigenstrains can be modelled as the result of a thermal expansion process and give the same results as LSP induced eigenstrains, as long as the value of the eigenstrains is the same in both cases.

The second important thing to note is that when applying the eigenstrains to the model, the eigenstrain was applied to the whole layer. The implicit assumption is that the eigenstrains do not vary in planes parallel to the peened area. In other words, ϵ^*_{xx}, ϵ^*_{yy}, and ϵ^*_{zz} are all functions of the thickness only, and not of other dimensions. This assumption greatly simplifies the analysis. This assumption is based on research by Achintha and Nowell[54] (see subsection 9.1 of chapter 2).

Similarly, by applying the eigenstrain to the entire layer, the variation of eigenstrain through the thickness is assumed to be discrete. In reality, the variation is continuous, but any continuous function can be approximated by discrete elements, as long as the elements are small enough. In this case, if the layers are thin enough, the results should be close enough to results obtained using a continuous variation of eigenstrain. It is pertinent to mention here, that FEM itself is a discretised model of continuous variables.

To validate the model, the residual stress distribution through the centre of the peened area (where residual stress measurements were originally taken), was extracted. This was done by creating a nodal path in the model, as shown in Figure 3.6. The normal stresses in the x and z directions, along the path, were retrieved and processed further.

The aforementioned results displayed discontinuities at interfaces between the layers, as shown in Figure 3.7. This can be attributed to the discretisation of the eigenstrain. In reality, the eigenstrain distribution varies continuously, but in the model, the eigenstrain is made to vary discontinuously by assuming that the eigenstrain is constant throughout each layer.

To refine the results, only the residual stress at the bottom node of each layer (corresponding roughly to the depths at which the original data were measured) was extracted. It was

presumed that the results at the bottom nodes were the most accurate because this is the most accurate position for each of the eigenstrains. In other words, the calculated eigenstrains rightfully belong to the bottom of each layer, but they were applied to the entire layer to ease setup of the model. This was done to ensure that the measured and predicted data occur at roughly the same depth, which makes it easier to compare the two datasets.

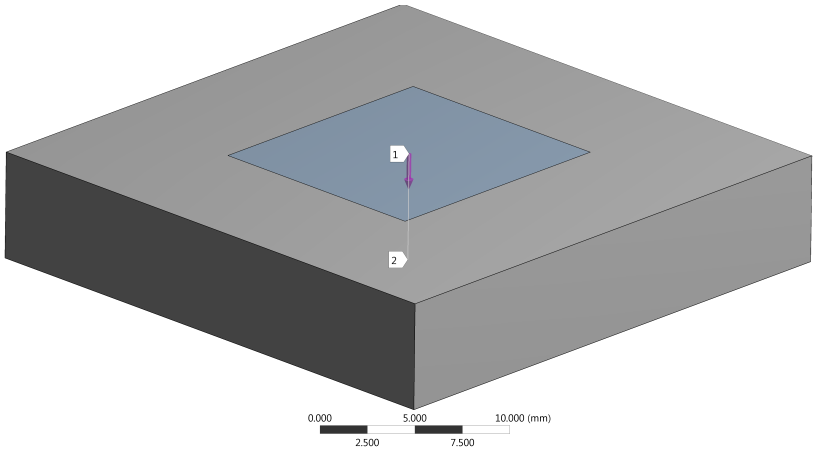

Figure 3.6: *Path used to extract residual stresses through centre of peened area*

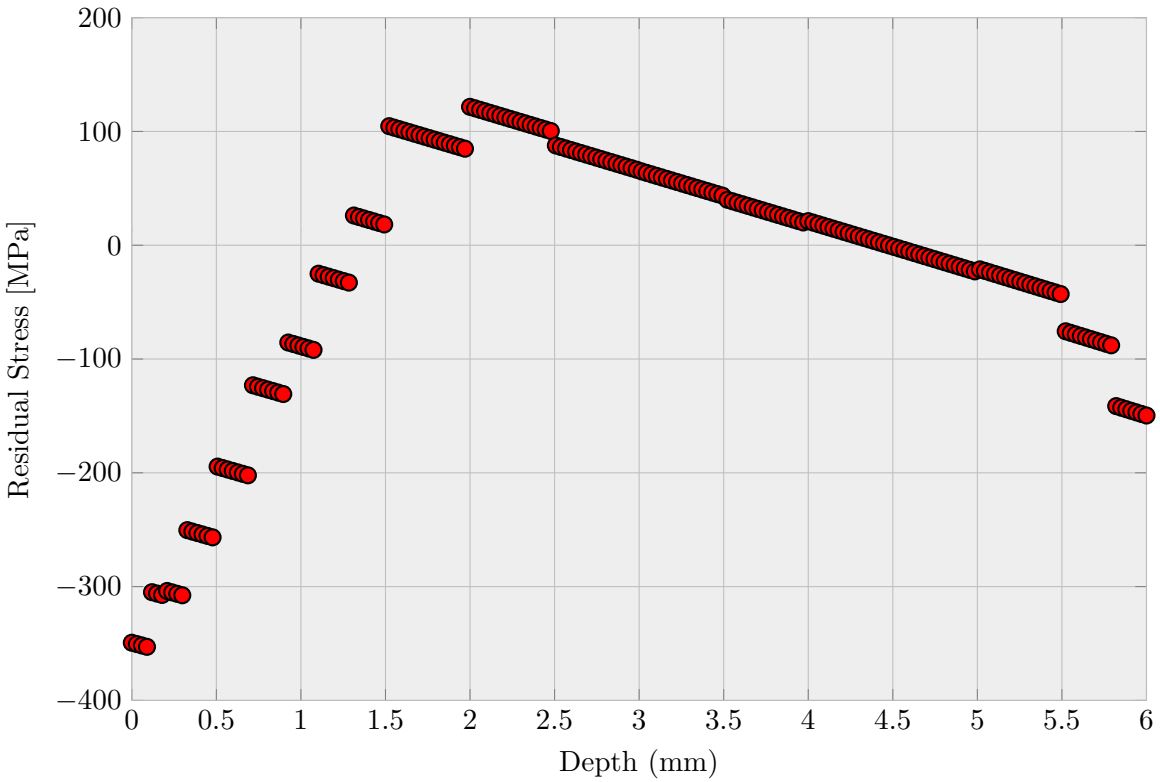

Figure 3.7: *Unprocessed result for Sample B15: Residual stresses in the x direction*

3 Inverse Problem of Eigenstrain

3.1 Coratella's Method

This method is based on the method outlined by Stefano Coratella in his Phd thesis[51] and a journal paper[2].

3.1.1 Method

This method requires a plot of the residual stress, σ_{res} through the depth of the sample. The residual stress in the x direction, through the depth of Sample B15 is shown in Figure 3.8. A similar profile for the y direction exists. The discrete data represented by dots in Figure 3.8 were copied into a spreadsheet. The next step is to determine the eigenstrain distribution

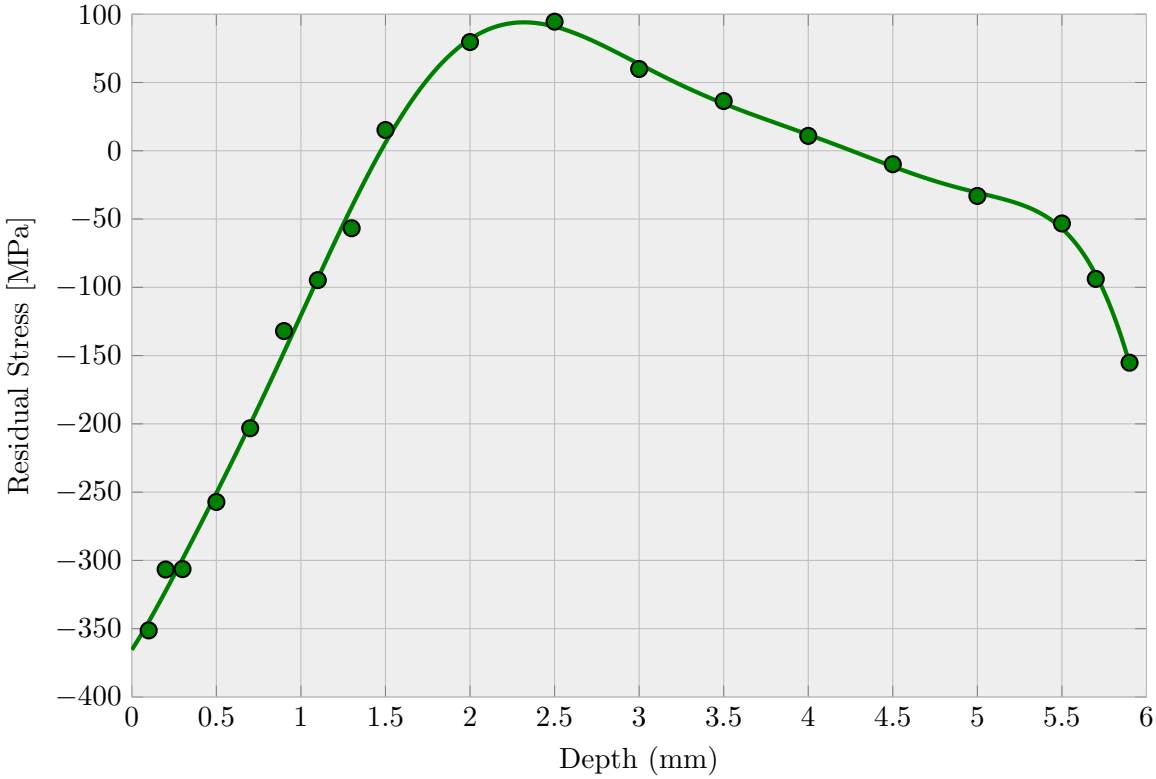

Figure 3.8: *Residual stresses in x direction through depth of Sample B15*

from the residual stress plot. This was done by firstly identifying the depth affected by peening. This is the point at which the graph becomes approximately linear. It can be seen that for Sample B15, this occurs at approximately 2.5 mm. The gradient and y-intercept of the straight line were determined and the straight line was extrapolated to span the entire

depth of the sample. The stress represented by this line will be called the equilibrium stress, σ_{eq}. This step requires the assumption that the peen affected depth is less than the thickness of the sample. The next step is represented by Equation 3.1.

$$\sigma_{\text{pl}} = \sigma_{\text{res}} - \sigma_{\text{eq}} \tag{3.1}$$

It is important to note that σ_{pl} is a fictitious stress and has no physical reality. It is the plastic stress that would have arisen from peening if the plastic behaviour was equivalent to the linear elastic behaviour of the material. In reality, the plastic behaviour is not linear. However, σ_{pl} has utility in allowing us to determine the eigenstrains in the sample, by simply using the Young's Modulus and Poisson's ratio of the material.

When measuring the residual stresses in the samples, a state of plane stress was assumed. This assumption is retained here. This means that the plastic stress in the z direction is zero, since it is normal to the plane of stress (see subsection 3.2 of chapter 2). Coratella[2] makes the further assumption that the plastic strains in the x and y directions are equal. This assumption was not made here, because peening here was done in a raster pattern, using a circular spot shape, whereas Coratella[2] used a square spot shape with no overlap. The overlap leads to anisotropy in the induced plasticity and hence the residual stresses imparted by the peening. σ_{pl} in the x and y directions were used together with Equation 2.5, Equation 2.6, and Equation 2.7 to obtain the eigenstrains ϵ^*_{xx}, ϵ^*_{yy}, and ϵ^*_{zz}. An implicit assumption is being made in this procedure, that the residual strain in each direction depends only on the eigenstrain in that respective direction and not on the eigenstrains in the other directions. This allows us to conduct the analysis separately for the each of the orthogonal directions.

Once the eigenstrains were obtained, the procedure described in section 2 was used to obtain the residual stresses in the sample.

3.1.2 Results and Discussion

Figure 3.9 shows the predicted against measured residual stress in the x direction. The prediction appears to be excellent, particularly near the peened surface of the material. Beyond the peened depth, the predicted curve diverges slightly from the measured curve.

Figure 3.10 shows the predicted against measured stress in the y direction. Although the shape of the predicted curve matches that of the measured one, the prediction is not as good as in the x direction. The residual stress near the surface of the sample appears to be close

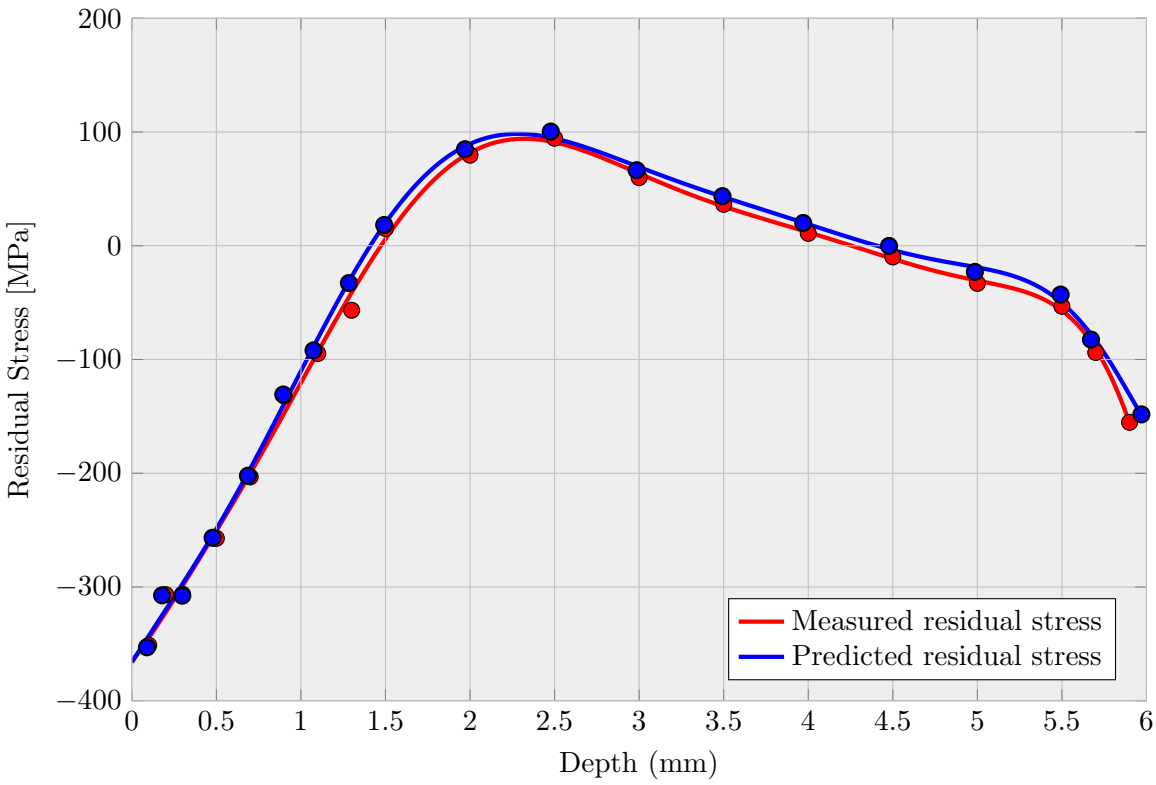

Figure 3.9: *Coratella's Method: Prediction vs measured residual stress in Sample B15 - x direction*

enough, but the predicted curve then diverges slightly away from the measured one. Beyond the peened depth, it underestimates the stresses.

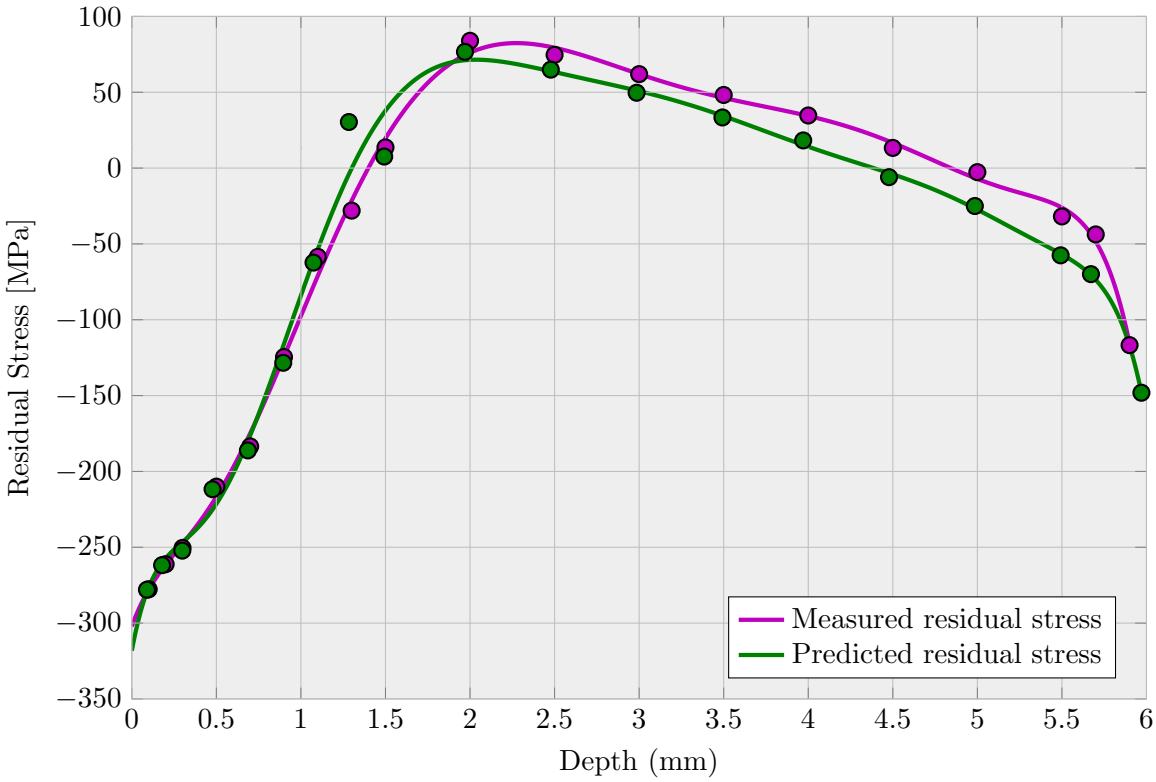

Figure 3.10: *Coratella's Method: Prediction vs measured residual stress in Sample B15 - y direction*

Appendix B shows shows predictions for other samples. Overall, this method seems capable of reasonable predictions. The predictions in some samples are better than in others. The predictions in the x direction seem to be consistently better than in the y direction.

Table 3.2 gives important information about the predictions in various samples. The Goodness of Fit criterion J, is dependent on sample size and cannot be used to compare between different samples. Therefore, it was decided to calculate the Standard Error for each sample, which is not affected by sample size. This allows us to compare samples of different sizes. The Coefficient of Determination, r^2, indicates how good the prediction is. The closer, it is to unity, the better the prediction. These three metrics can be used to complement each other and allow us to better analyse the predictive capabilities of the model in different samples. More information on these metrics is given in subsection 8.3 of chapter 2.

Comparing the Standard Errors in the different samples, it becomes apparent that the predictions in Sample B15 and Sample 38 are definitely superior to the predictions in the other two samples. This is supported by the high values of r^2 in these samples, which are very

Table 3.2: Goodness of Fit metrics for Coratella's Method

Sample	**J** (MPa^2)		**Standard Error** (MPa)		r^2	
Direction	x	y	x	y	x	y
SamB15	1316.19	7479.97	8.8	20.98	0.9962	0.9711
Sam05	32 113.62	36 290.29	36.88	38.89	0.7536	0.6369
Sam38	248.4	16 496.29	3.22	26.22	0.9989	0.9082
Sam70	12 745.24	44 632.81	23.04	43.12	0.962	0.909

close to one. Looking at these metrics, it is once again clear that the predictions in the x direction are consistently better than in the y direction.

Several factors may impact the accuracy of the prediction:

- The accuracy of the extrapolation of σ_{eq}
- The accuracy of the Young's Modulus and Poisson's Ratio used
- The number of data points measured in the residual stress plot. If more data points are measured in the peened zone, one can create more layers, which are thinner. Intuitively, it is expected that the thinner the layers, (and therefore the more layers there are) the more accurate the prediction will be.
- The assumption that residual strain in each direction depends only on the eigenstrain in that respective direction and not the eigenstrains in the other directions. How well does it hold in reality?

3.2 Korsunsky's Method

This method is based on the method outlined by Alexander Korsunsky in a journal paper[27].

3.2.1 Method

The analytical basis for obtaining eigenstrain from residual stress data is already outlined in chapter 2, subsection 4.3. This section will focus on modifications made to the basic method. The first modification made was to generalise the set of basis functions used by Korsunsky (Equation 2.14). The exponent $i+2$ can be replaced by $i+a$, where a is an integer. This allows a wider range of basis functions to be considered in the solution. The modified set of basis functions is shown in Equation 3.1.

$$\zeta_i(x) = (x - x_0)^{i+a}, \qquad i = 1, 2, \ldots, N \tag{3.2}$$

In an attempt to increase the accuracy of the method, three parameters of the basis functions were identified:

- The number of basis functions N
- The depth of the eigenstrain distribution, x_0
- The parameter, a, introduced above.

These three parameters can be varied to yield different sets of basis functions. The results for each set of basis functions are different. The aim is to find the set of parameter values which yield the best results (which minimise the sum of squared residuals, J). A Python script (shown in section 1) was thus written to perform the following fundamental tasks:

1. Choose a value for each of the parameters, a, N, and x_0, from a predefined range.
2. Implement Korsunsky's method for the chosen parameters.
3. Use the implementation of Korsunsky's method, together with a BFGS optimisation algorithm, to find a local minimum to J, with respect to a, N, and x_0.
4. Record the corresponding value of J.
5. Repeat the process for other values of a, N, and x_0, within the predefined range.
6. From the recorded values of J, identify the set of values for the parameters, which yielded the smallest value of J.
7. Using the parameter values from the previous step, implement Korsunsky's method one last time.
8. Record the output eigenstrains.

It should be noted from the aforementioned process, that a two tier optimisation process is used. In Step 3, the local minimum around the input values of a, N, and x_0, is found. To accomplish this, the Nelder-Mead method, Powell's method and BFGS method were tested (See section 7 of chapter 2). The BFGS method gave the best results consistently. However, it was found that the results still varied depending on the input parameter values. It was postulated that there are numerous minima of J with respect to a, N, and x_0. It was thus decided to find a global minimum within set bounds. This provides the rationale for Step 6.

Through trial and error, the following bounds for the parameters were determined:

- $10 < N < number\ of\ data\ points$
- $5 < a < 15$
- $1.5 < x_0 < t$ where t is the thickness of the sample.

It was found that values of N less than 10 leads to underfitting the data (see subsection 8.2 of chapter 2). The value of N cannot exceed the number of data points, as a unique solution cannot be obtained for such values of N (See subsection 8.1 of chapter 2).

The value of a used by Korsunsky was 2. This ensures that the eigenstrain and its first two derivatives turn to zero at $x = x_0$. Korsunsky starts i at a value of 1. However, since Python has a starting index of zero, $i+a$ has to be translated as $i+1+a$ in Python. It was decided to incorporate the $+1$ in the parameter a. Thus, the lowest value a tested in Python was 3. It was found that for values of a less than 5, the eigenstrains produced were entirely inaccurate, resulting in a spurious prediction of residual stress. On the other hand, very large values of a did not seem to have a much more positive effect. They only seem to force the regression coefficients to be very small, introducing greater computational inaccuracy.

The ideal value of x_0 is as close to the depth of the eigenstrain distribution as possible. Obviously, the depth of the eigenstrain distribution cannot exceed the depth of the sample. On the other hand, the depth of the eigenstrain distribution cannot be zero, as that would mean the sample is unpeened. Looking at the residual stress profiles from the database of peened samples (see Figure 3.1), it seems as if the peened depth was no less than 2mm in any sample. A value of 1.5mm was chosen as a lower bound to be safe.

Figure 3.11 shows the flow of data in Korsusnky's method, as outlined in subsection 4.3 of chapter 2, and implemented in the script shown in section 1. Figure 3.12 shows the implementation of Korsusnky's method (Figure 3.11) under the optimisation framework used to select the best basis functions. The outlined methodology applies to eigenstrains in one of the orthogonal directions. This methodology was applied separately to the residual elastic strain in x, y, and z directions. The implicit assumption in this method is that the residual strain in each direction is a function only of the eigenstrain in the same direction and not a function of eigenstrains in the other directions.

The resulting eigenstrains were imposed on an FEA model of the sample, in the same manner as was done for Coratella's Method (subsubsection 3.1.1). The direct problem was solved and the predicted residual stresses were extracted for comparison to the measured values.

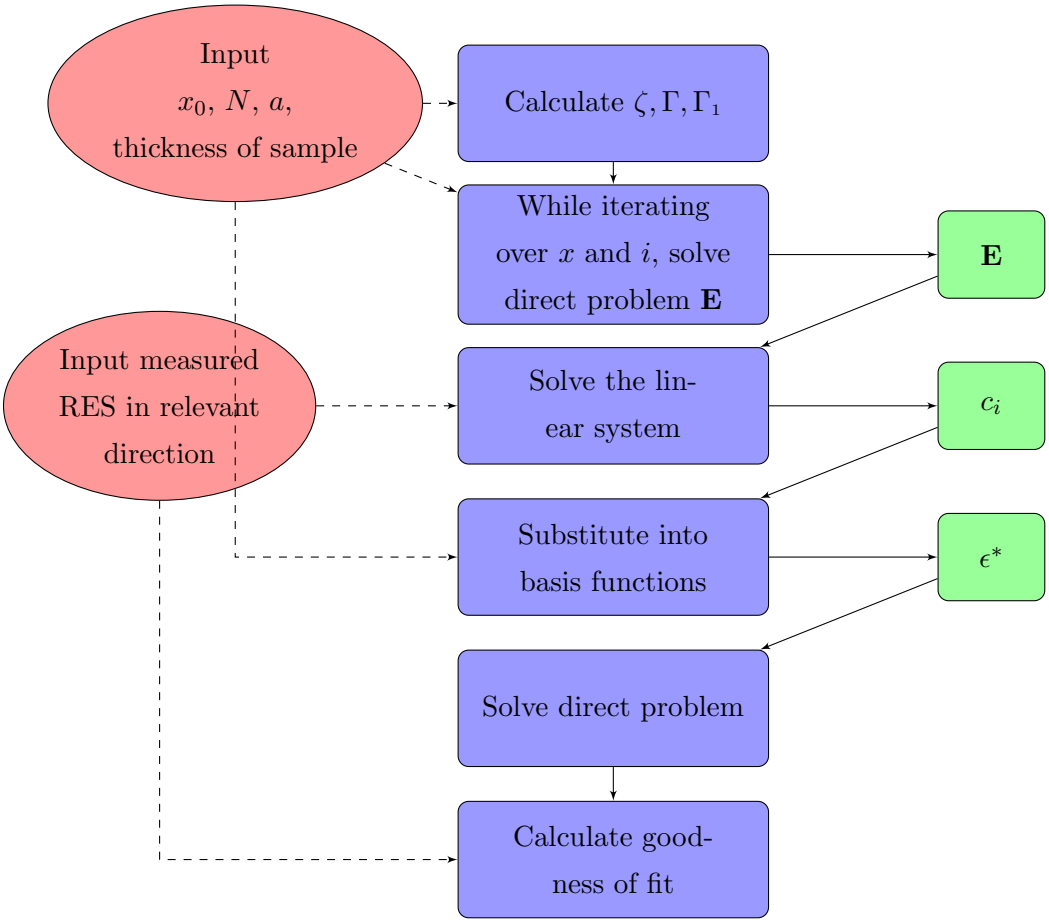

Figure 3.11: *Flow chart outlining implementation of Korsunsky's Method*

3.2.2 Results and Discussion

Figure 3.13 shows the results in the x direction. The predicted curve fits the general shape of the measured curve quite closely. The predictive curve slightly overestimates the magnitude of compressive residual stresses near surface of the peened sample. Compared to Coratella's Method, the prediction around the turning point of the curve is much better. The predicted curve tends to diverge slightly towards the bottom of the sample.

Figure 3.14 depicts the results in the y direction. The shapes of the two curves are similar, but prediction is not as good as in the x direction. The magnitude of the compressive residual stress near the surface is underestimated. The prediction also diverges from the measured curve beyond the peened depth and is very poor at the bottom of the sample.

Graphs for the other samples can be viewed in Appendix B. Table 3.3 provides various Goodness of Fit metrics for the residual stress predictions in different samples. The predictions for Sample B15 and Sample 38 are excellent, as evidenced by the lower standard errors and higher r^2 values, which are close to one. It should be noted that these were the same two

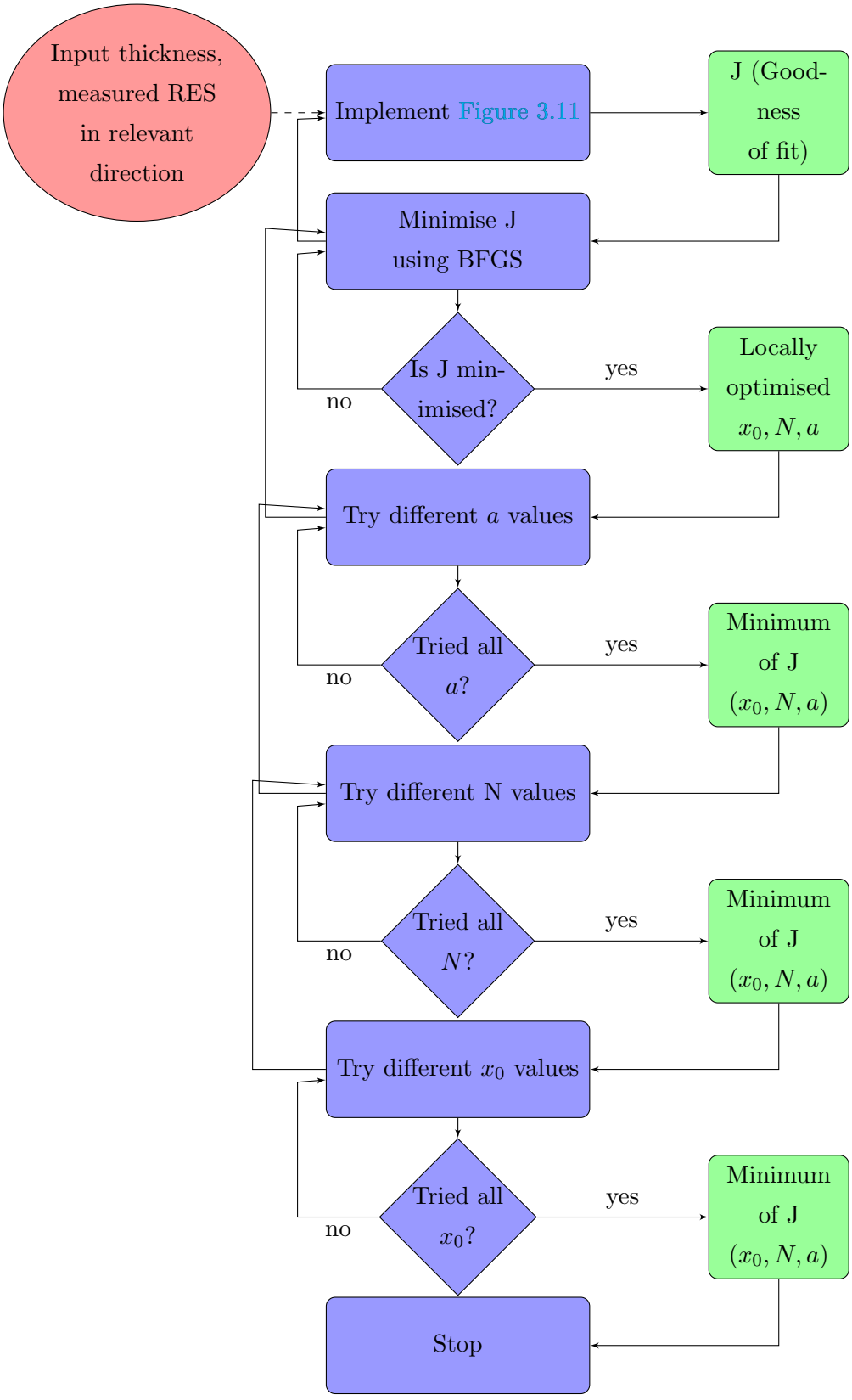

Figure 3.12: *Optimisation framework applied to Korsunsky's method*

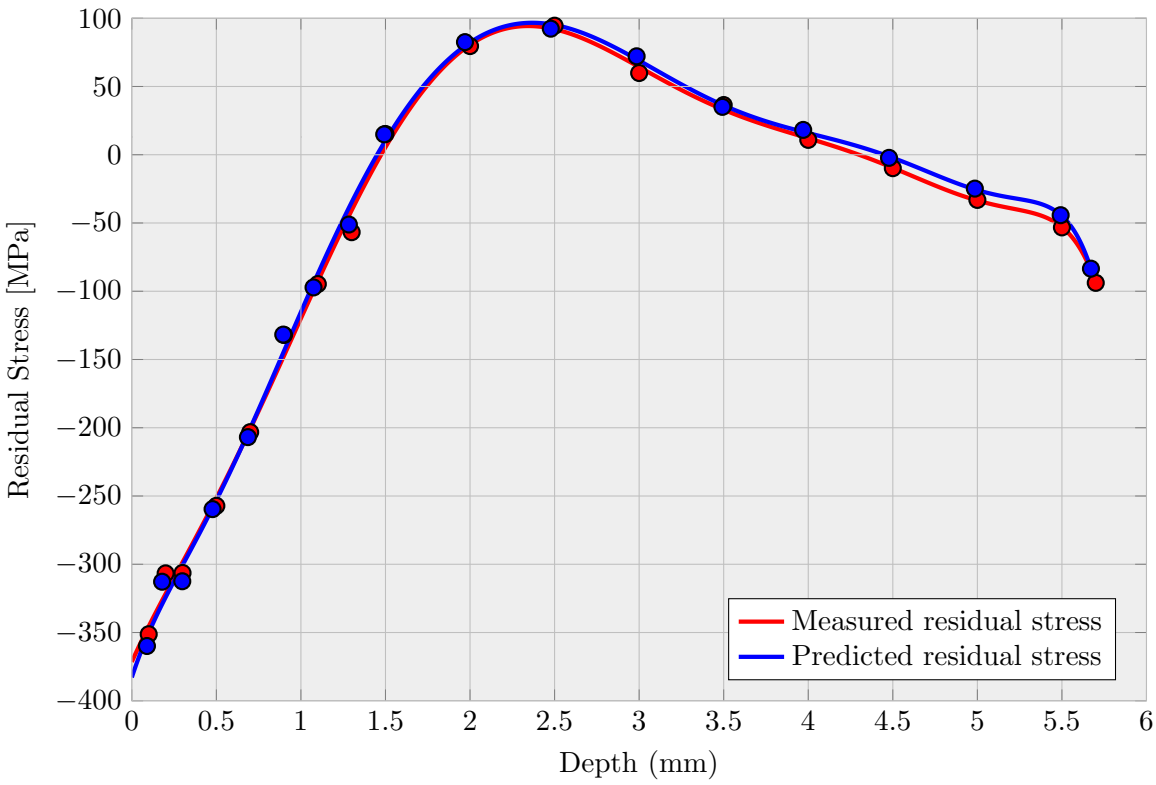

Figure 3.13: *Korsunsky's Method: Prediction vs measured residual stress in Sample B15 - x direction*

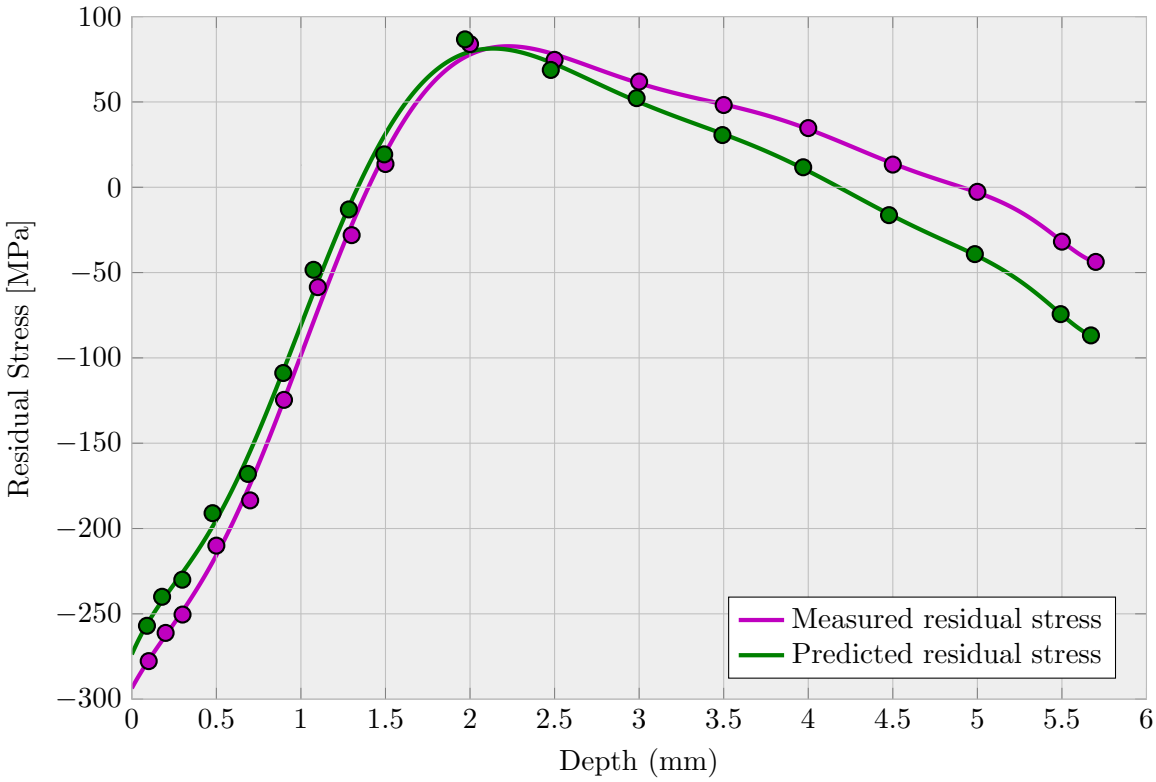

Figure 3.14: *Korsunsky's Method: Prediction vs measured residual stress in Sample B15 - y direction*

samples that yielded good predictions using Coratella's method. This may indicate that the goodness of the prediction is more dependent on the sample than on the specific method used.

Table 3.3: Goodness of Fit metrics for Korsunsky's method

Sample	**J** (MPa^2)		**Standard Error** (MPa)		r^2	
Direction	x	y	x	y	x	y
SamB15	738.2	9 350.74	6.79	24.17	0.9978	0.9635
Sam05	21 022.04	47 859.49	29.6	44.66	0.8387	0.5211
Sam38	9 238.19	13 617.12	19.62	23.82	0.9582	0.9242
Sam70	90 319.05	33 626.13	61.35	37.43	0.7306	0.9314

The method outlined here involves selecting the best model (defined by N, x_0, and a) from a range of models. As stated in subsection 8.2, The Goodness of Fit criterion, J, cannot completely replace a visual examination of the curve. A curve with a small value of J can lead to a poorly fit curve. However, with a computer doing the selection, there is no opportunity to visually examine every model. Measures of model parsimony were presented in subsection 8.2

of chapter 2 as a possible way to overcome this issue. Attempts were made to use the AIC and BIC criteria separately. It was found that the AIC criterion tends to give false results and the BIC criterion tends to under-fit the data (Value of N too low). It was therefore decided to keep the Goodness of Fit Criterion to discriminate between different models and visually examine the final model, upon completion of the algorithm. If the results are not satisfactory, the range of the parameters (N, x_0, and a) can be tweaked and the algorithm rerun.

An important question arises concerning the stability and uniqueness of the solution (See section 6). As pointed out by Korsunsky, the least squares methodology is guaranteed to produce a unique solution, due to the positive definiteness of J. However, it was found in rare instances that the algorithm yielded incorrect values of eigenstrain, despite the value of J being quite low. This seems to indicate that the solution is not unique.

There is a need to address this apparent contradiction. In Korsunsky's original method, the eigenstrains are assumed to be equivalent to one set of basis functions:

$$\epsilon^* = \sum_{i=1}^{N} c_i \zeta_i \tag{3.3}$$

What should be understood is that the uniqueness of the solution is in terms of the coefficients of the basis functions. In other words, there is only one set of coefficients, c_i, that describe the eigenstrains such that when the eigenstrains are input into the direct problem (Equation 2.14), the sum of squared errors between the prediction and measured values is minimised. Since in Korsunsky's original method, the basis functions are preset, this is equivalent to saying there is only one eigenstrain distribution, expressed using the current basis functions, that is a solution. This does not mean that in general there are no other eigenstrain distributions, which if substituted into Equation 2.14 would yield an equivalently low value of J. In the current method, a variety of bases are tried instead of one basis. It is possible that one basis leads to one eigenstrain distribution as a solution, while another basis may lead to another solution. Thus, the solution is not necessarily unique in the framework of Figure 3.12. It should be noted that while both solutions satisfy Equation 2.14, only one solution solves the direct problem when carried out using FEM.

3.3 Korsunsky's Method with FEM to Generate Elastic Strain Matrix

In subsection 4.3 of chapter 2 the basic procedure of Korsunsky's Method was outlined. The method includes a formulation of the Direct Problem of Eigenstrain, which is used together

with the basis functions to generate the elastic strain matrix, **E**. In subsection 4.3 of chapter 2 and subsection 3.2 of this chapter, the direct problem was formulated in terms of an analytically derived beam equation. However, Korsunsky's Method is flexible and is not constrained to this formulation of the direct problem. In fact, any formulation of the direct problem can be used in conjunction with this method, provided it can accurately generate **E**.

Keeping in mind that the final implementation of the direct problem is done using the Finite Element Method (FEM), it was posited that using FEM for the direct problem in Korsunsky's Method would generate a more accurate elastic strain matrix.

3.3.1 Method

The same basic method that was outlined in subsection 3.2 was used. However, the script was modified to accommodate the use of FEM for the Direct Problem of Eigenstrain. Some of the differences are outlined below:

- The optimisation framework summarised in Figure 3.12 was not used here, as it is time consuming. A consequence of this is that the range of basis functions that are possible solutions is limited.
- The direct problem was solved for all three directions simultaneously rather than separately. Due to this, the data handling had to be done differently here.
- Functions to write data to the ANSYS project file and extract residual strain data had to be created.
- Functions to calculate the integral parameters Γ and Γ_1 (see chapter 2, subsection 4.3) were not required here, as Equation 2.16 was not used.
- The thickness of the model was not required as an input, as this information is contained in the FEM model.

Having already created the script in section 1, the task was mainly to integrate the procedure for the direct problem from section 2 into the Python script. ANSYS Workbench has scripting capability via Iron Python, an implementation of Python in the .NET framework. Scripts are stored as .wbjn files and can be run directly from the Workbench environment.

It was initially envisaged that the script would be entirely written in Iron Python and run from Workbench. However, Iron Python cannot run C-based Python packages like Numpy. Since Numpy was required to solve the linear system, this presented a problem. It was decided

that the generation of the elastic strain matrix would be scripted in Iron Python and run by Workbench, while the solution of the linear system and overall data processing would be done using Python.

The main script is shown in section 2. The following procedure was implemented by the Python script:

1. Take inputs x_0, N, a, as well as sample data.
2. Write a Windows batch file which will open the relevant Workbench project file in batch mode, pass x_0, N, a to the Workbench, and run the Iron Python script (section 3 of Appendix A) from Workbench. The Iron Python script is summarised below.
3. Run the above batch file. The final result of this is a csv file (RES.csv) containing the residual elastic strain matrices ($\mathbf{E}$) in the x, y, and z directions.
4. Read the $\mathbf{E}$ matrices from RES.csv file.
5. For each orthogonal direction, solve the linear system to generate the coefficients c_i.
6. Substitute c_i back into the basis functions to generate the eigenstrains.
7. Substitute the eigenstrains into the FEM model to solve the direct problem and write the residual elastic strains to RES.csv.
8. Read the residual elastic strains from RES.csv file and calculate the Goodness of Fit.

The Iron Python script to generate the ($\mathbf{E}$) matrices implemented the following procedure successively to each basis function:

1. Evaluate the function for each layer of the sample, and write the value to the Engineering Data under the Orthotropic Coefficient of Thermal Expansion property. The same value must be written in the x, y, and z directions.
2. Solve the FEM problem.
3. Write the results to export.csv file from CFD Post.
4. Read the results from export.csv, and append to the elastic strain matrix.

Once the above procedure was applied to all the basis functions, the $\mathbf{E}$ matrices were written to RES.csv file.

There are a few issues in the above procedure that need to be discussed. Evaluating the basis functions often leads to a large number. This posed a problem because the strains resulting from such high values were unrealistically high, leading to excessive warping of the sample, and thus violating basic assumptions. In most cases, inversion of elements occurred due to highly negative eigenstrain values. This prevented the problem from being solved. To counter this, a function was written to generate a moderating coefficient that was universally applied to all the basis functions. Due to linearity of the problem, this technique did not alter the results.

The moderating coefficient was generated by identifying the largest possible value that could be generated by the set of basis functions, and successively multiplying this number by 0.1 until the value of the number was in an acceptable range. If the number was multiplied by 0.1 n times, the coefficient was set as 0.1^n. All the basis functions were then scaled by this number.

The next issue to be dealt with is CFD Post. CFD Post is a post-processing application that was designed to process results from CFD applications in ANSYS (CFX, Fluent), but can be used in conjunction with Mechanical as well.

The reason for using CFD Post is that it allows journalling in Iron Python using the `SendCommand` function. Journalling is an ability of Workbench that allows the recording of GUI actions in the form of an Iron Python script. The journal script contains the recorded commands in Python syntax and can be replayed to replicate the actions. The journal file can also be modified.

While Workbench is scripted in Iron Python, the data integrated applications (such as Mechanical, Design Modeller, and CFD Post) are scripted in different languages, like JScript for Mechanical and Design Modeller, and CCL for CFD Post. The `SendCommand` function allows one to send commands to data-integrated applications from an Iron Python script file. While it is possible to create a set of JScript commands to Mechanical to execute the necessary tasks and extract the results, this would require knowledge of the commands needed to produce specific outputs. Since Mechanical does not support journalling, it is very difficult to determine the commands needed.

By contrast, CFD Post does support journalling, so actions taken in CFD Post can be recorded in the journal file. Thus, the tasks necessary for extracting the data were performed manually and recorded in the journal file. The commands generated from this were then used in Iron Python script to automate the process of result extraction.

3.3.2 Results and Discussion

Figure 3.15 shows the results in the x direction. While the predicted curve seems accurate near the peened surface, it diverges from the measured curve up to a depth of around 2mm. The overall accuracy is not as good as the results for the method presented in subsection 3.3, especially near the turning point of the graph.

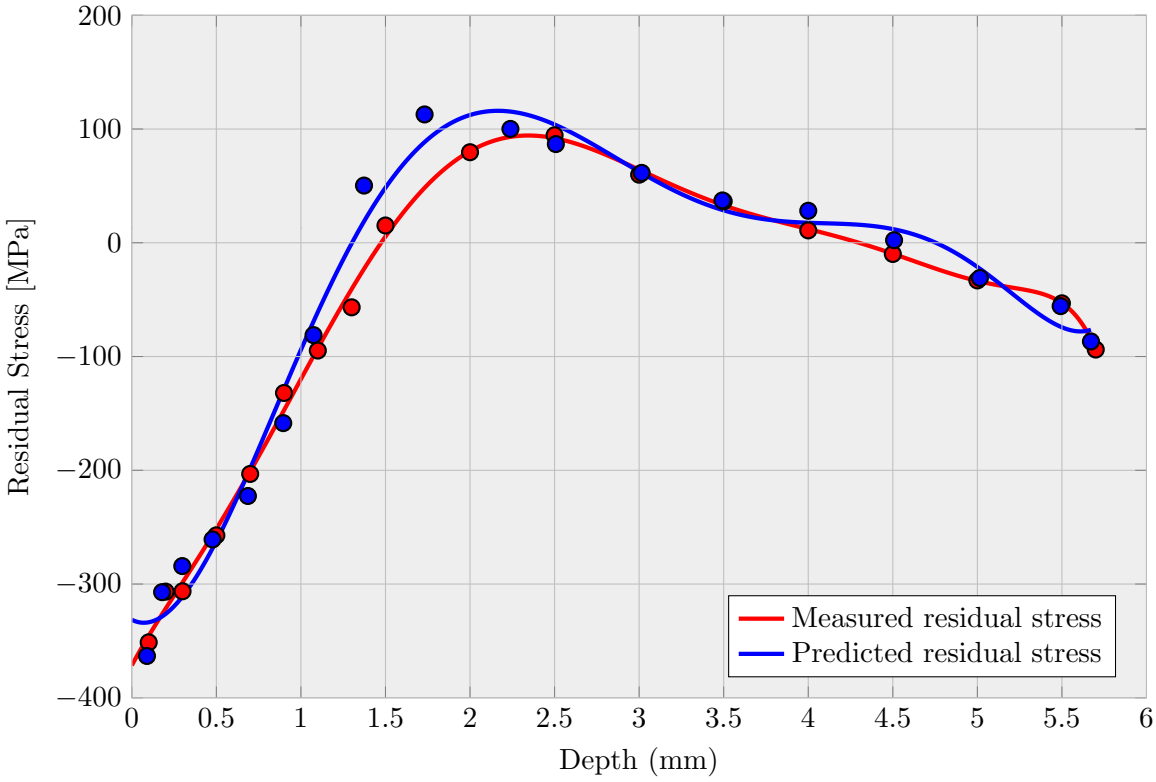

Figure 3.15: *Korsunsky's Method with FEM: Prediction vs measured residual stress in Sample B15 - x direction*

The results in the y direction are shown in Figure 3.16. Like the results for the x direction, the predicted curve is accurate near the peened surface and then deviates from the measured curve.

Graphs for the other samples can be viewed in Appendix B. Table 3.3 provides various Goodness of Fit metrics for the residual stress predictions in different samples. In the previous two methods, the best predictions were achieved in Sample B15 and Sample 38. With this model, the predictions in Sample 38 and Sample 70 are the best, with r^2 values close to one in both the x and y directions. The standard errors for Sample 38 are much better than for Sample 70, which indicates that the prediction in Sample 38 is the best. While the prediction in Sample B15 is good, as evidenced by r^2 value of over 0.9 in both the x and y directions,

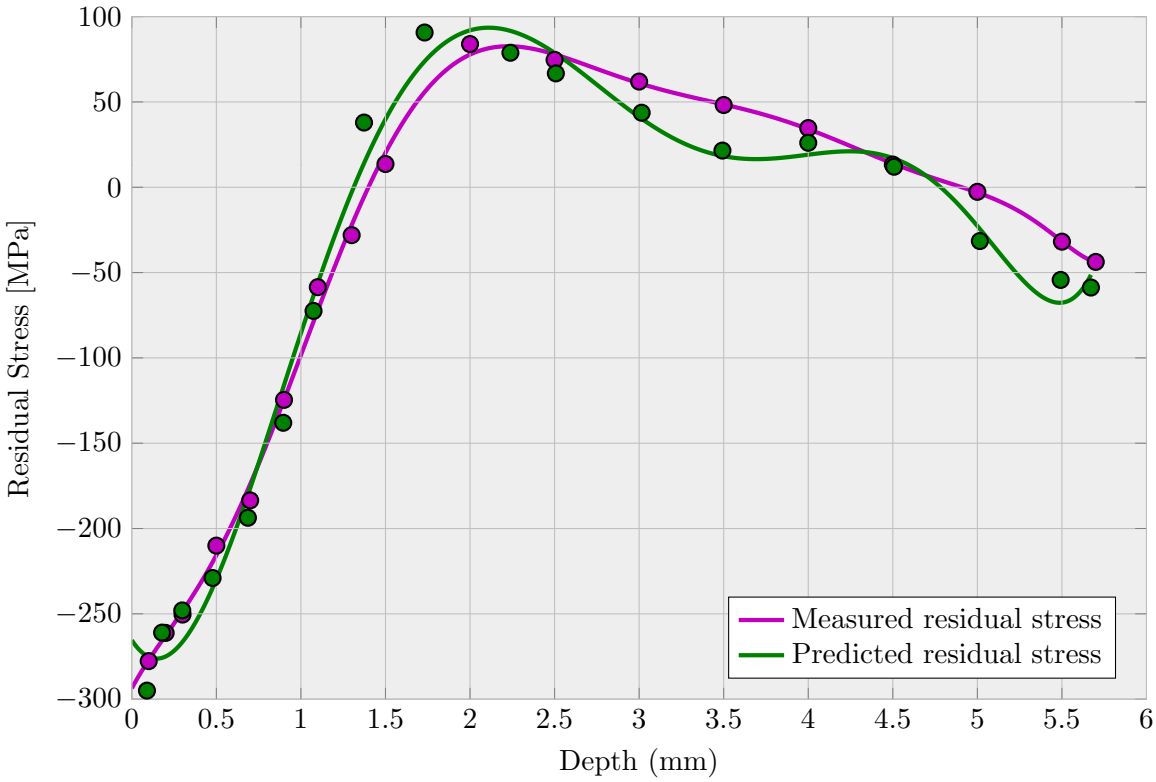

Figure 3.16: *Korsunsky's Method with FEM: Prediction vs measured residual stress in Sample B15 - x direction*

it is poor in comparison to the previous two methods, as stated previously. Like the other methods, the predictions in the y direction for this method are generally lower than for the x direction. For Sample 05, the prediction in the y direction is poor. Examining Figure B.14, the overall fit does not look too bad. However, the prediction near the surface (first three data points) is particularly inaccurate, which contributes to an r^2 value close to zero.

Table 3.4: Goodness of Fit metrics for Korsunsky's method with FEM to Generate Elastic Strain Matrix

Sample	**J** (MPa^2)		**Standard Error** (MPa)		r^2	
Direction	x	y	x	y	x	y
SamB15	23 885.59	14 207.16	38.64	29.80	0.9296	0.9446
Sam05	18 415.16	91 327.45	27.70	61.69	0.8587	0.0862
Sam38	4 477.91	18 434.12	13.66	27.71	0.9797	0.8974
Sam70	9 366.36	49 151.64	19.76	45.25	0.9721	0.8998

As mentioned in subsubsection 3.2.2, the solution is unique due to the positive-definiteness of the least squares criterion, J. There is only one set of coefficients c_i that solves the problem for

a particular set of basis functions. Unlike subsection 3.2, this method does not test different bases. Therefore, the solution to the inverse problem in this method is unique. The resulting eigenstrain distribution is guaranteed to give the correct residual elastic strain distribution when substituted into the direct problem. This is due to the fact that FEM was used for the inverse problem, rather than Equation 2.16.

Since FEM is used in both the inverse and direct problems, it was expected that this method would provide better results than the one outlined in subsection 3.2. This expectation is based on the fact that the same tool (FEM) used to solve the direct problem, is being used to minimise J, unlike subsection 3.2, where a different tool (analytical method) is used in the inverse problem. What needs to be borne in mind, though, is that the method in subsection 3.2 made use of an optimisation framework which allowed a much wider range of possible solutions to the inverse problem. Thus, there is a greater possibility of finding a lower value of J in subsection 3.2 than in this method.

It is obviously possible to implement the same optimisation framework used in subsection 3.2 in this method and get even better results. However, an exorbitant amount of time would be required to obtain the solution. The duration required to solve the inverse problem using FEM is much larger than the duration required for Equation 2.16. In addition, the exact duration required for the solution depends on the number of iterations required to perform the optimisation, which is difficult to predict prospectively. This makes it difficult to know the solution time before performing the method.

4 Comparison of Methods

The previous section outlined various methods for implementing the Inverse Problem of Eigenstrain. The methods were compared across different samples. This section will compare the different methods to each other for each sample. Since the comparison occurs over the same sample, it is meaningful to compare J values from different methods.

Table 3.5: Comparison of Goodness of Fit metrics for different methods in Sample B15

Method	**J** (MPa^2)		**Standard Error** (MPa)		r^2	
Direction	x	y	x	y	x	y
Coratella	1 316.19	7 479.20	8.8	20.98	0.9962	0.9711
Korsunsky	738.20	9 350.74	6.79	24.17	0.9978	0.9635
Korsunsky with FEM	23 885.59	14 207.16	38.64	29.8	0.9296	0.9446
Average	8646.66	10345.70	18.08	24.98	0.9745	0.9597

Table 3.5 compares the Goodness of Fit metrics, J, r^2, and Standard Error for the different methods in Sample B15. The best prediction in the x direction is due to Korsunsky's method, followed by Coratella's method. In the y direction, Coratella's method is the best. Korsunsky's method with FEM gives a much worse prediction than the other two methods, in both directions. Looking at the averages of all the metrics, it can be seen that the metrics in the x direction are generally better than in the y direction. Korsunsky's method with FEM is an exception to this rule. The average values for r^2 in both directions show that the predictions in this sample are very good.

Table 3.6: Comparison of Goodness of Fit metrics for different methods in Sample 05

Method	**J** (MPa^2)		**Standard Error** (MPa)		r^2	
Direction	x	y	x	y	x	y
Coratella	32 113.62	36 290.69	36.58	38.89	0.7536	0.6369
Korsunsky	21 022.04	47 859.49	29.6	44.66	0.8387	0.5211
Korsunsky with FEM	18 415.15	91 327.45	27.7	61.69	0.8587	0.0862
Average	23 850.27	58 492.54	31.29	48.41	0.8170	0.4147

Table 3.6 compares different methods in Sample 05. Korsunsky's method with FEM gives the best prediction in the x direction, but the worst, by far, in the y direction. Coratella's method is the worst in the x direction, but the best in the y direction. The average value of r^2 is good in the x direction, albeit not as good as Sample B15. In the y direction, the average value of r^2 is poor. Although Korsunsky's method with FEM is responsible for lowering the average, it cannot be denied that the predictions in this direction are poor in general. Even Coratella's method only yields an r^2 value of 0.6369.

Table 3.7: Comparison of Goodness of Fit metrics for different methods in Sample 38

Method	**J** (MPa^2)		**Standard Error** (MPa)		r^2	
Direction	x	y	x	y	x	y
Coratella	248.40	16 496.92	3.22	26.22	0.9989	0.9082
Korsunsky	9 238.19	13 617.12	19.62	23.82	0.9582	0.9242
Korsunsky with FEM	4 477.91	18 434.12	13.66	27.71	0.9797	0.8974
Average	4 654.83	16 182.72	12.17	25.92	0.9789	0.9099

Table 3.7 compares different methods in Sample 38. Coratella's method far outstrips the other methods in the x direction. Korsunsky's method gives the worst prediction in this direction. In the y direction, Korsunsky's method is slightly better than the other two,

followed by Coratella's method. The high average values of r^2 indicate that the predictions in this sample are good.

Table 3.8: Comparison of Goodness of Fit metrics for different methods in Sample 70

Method	**J** (MPa^2)		**Standard Error** (MPa)		r^2	
Direction	x	y	x	y	x	y
Coratella	12 745.24	44 623.81	23.04	43.12	0.9620	0.9090
Korsunsky	90 319.05	33 626.13	61.35	37.43	0.7304	0.9314
Korsunsky with FEM	9 366.36	49 151.64	19.76	45.25	0.9721	0.8998
Average	37 476.88	42 467.19	34.72	41.93	0.8882	0.9134

Table 3.8 compares the various methods in Sample 70. Korsunsky's method with FEM gives the best prediction in the x direction, but the worst in the y direction. Korsunsky's method gives a very poor prediction in the x direction, but the best prediction in the y direction. The average r^2 values indicate that the predictions are generally good in both directions. This is the first sample in which the average r^2 value in the x direction is lower (albeit slightly) than the average r^2 value in the y direction. This can be attributed to the anomalously low r^2 from Korsunsky's method.

Considering the results as a whole, it immediately becomes apparent that no method is categorically better than the rest. Even within a single sample, a method that is best at predicting residual stresses in one direction, might be the worst at predicting in another direction. The data has to be further analysed to come to a conclusion. One way of analysing the predictive capabilities of the models is to look at the number of times each model is best (1st), second best (2nd), or worst (3rd).

Figure 3.17 shows the frequency of the ranks attained by different methods. It should be noted that for the purposes of this graph, the x and y directions are considered together, rather than separately. In other words, a rank of first in the x direction is considered equivalent to a rank of first in the y direction.

The results indicate that Coratella's and Korsunsky's methods rank first equally often, but Coratella's method ranks second the most often. Korsunsky's method with FEM ranks the worst most often. Therefore, it would seem that Coratella's method is the best, followed closely by Korsunsky's method. The average ranks of the different methods is given below:

- Coratella's method: 1.75
- Korsunsky's method: 1.875
- Korsunsky's method with FEM: 2.375

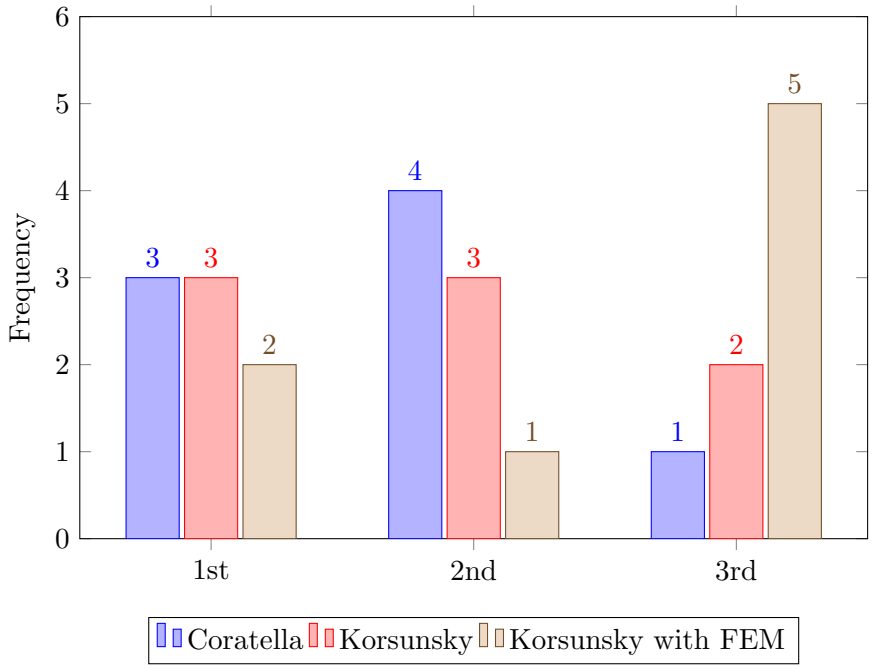

Figure 3.17: *Ranks of different methods in predicting residual stress in different samples*

This confirms the analysis of the bar graph, that Korsunsky's method is close behind Coratella's method in predictive capability. The disadvantage of this analysis is that it only takes into account the rank of each method relative to the other methods, and does not take into account how good the prediction is compared to other methods. Another way of analysing the data — that takes into account the goodness of the prediction relative to the other methods — is to look at the average Standard Error for each method. Since the Standard Error is not dependent on the sample, the average SE can provide meaningful information. Average SE values in the different directions are displayed in Figure 3.18.

Once again, Coratella's method surpasses the other methods in both directions, as well as overall. Korsunsky's method is second best overall, but Korsunsky's method with FEM is better than it in the x direction. This shows that Korsunsky's method with FEM is worst overall due to very poor predictions in the y direction.

A general trend that is observed is that the predictions in the scan (y) direction are generally worse than in the step (x) direction (see Figure 3.1 for definitions). Exceptions to this trend are rare.

While none of the methods can be proven categorically superior to the others, it is clear that within the current dataset, Coratella's method surpasses the others. Additionally, Coratella's method is the simplest and the quickest to execute. Therefore, it was chosen to complete the remaining three objectives of this project.

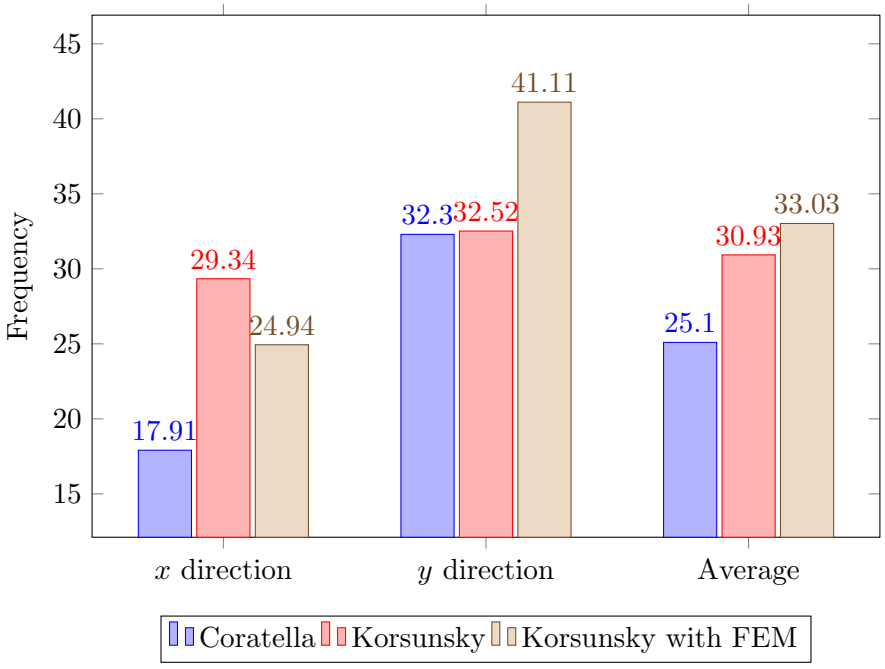

Figure 3.18: *Average Standard Error of the different methods*

5 Failed Methods

5.1 Polynomial Fit Method

The idea for this method arose from Korsunsky's method. This method made use of Equation 2.16 (recalled below) to determine a least squares solution to the problem. The eigenstrain distribution is represented by a set of basis functions with N coefficients, where N is less than the number of data points. The determination of the coefficients leads to an eigenstrain distribution, which if substituted into Equation 2.16, gives a close approximation to the measured strain. Since the number of coefficients is less than the number of equations, an exact solution (where the predicted and measured data points are exactly equal) does not exist. Thus, the predicted curve does not pass through all the data points.

$$e(x) = \frac{1}{(x_{\mathrm{R}} - x_{\mathrm{L}})^2} \times \{6\Gamma_1(x_{\mathrm{R}} - x_{\mathrm{L}})(2x - x_{\mathrm{R}} - x_{\mathrm{L}}) + 2\Gamma\left[({x_{\mathrm{R}}}^2 + x_{\mathrm{R}}x_{\mathrm{L}} + {x_{\mathrm{L}}}^2) - 3x(x_{\mathrm{R}} + x_{\mathrm{L}})\right]\} - \epsilon^*(x) \quad \text{(Equation 2.16)}$$

Given a set of $n+1$ data points, it is always possible to find a polynomial, with a degree of at most n, which passes through every data point. This is known as polynomial interpolation. Similarly, in this case, there is a unique polynomial, which if substituted as the eigenstrain distribution in Equation 2.16, will lead to a residual strain distribution, which fits all the

data points exactly. The eigenstrain distribution thus can be expressed as in Equation 3.4, where n is the number of data points, hence number of equations.

$$\epsilon^*(x) = c_0 + c_1 x + c_2 x^2 + \ldots + c_{n-1} x^{n-1} \tag{3.4}$$

By substituting Equation 3.4 into Equation 2.16, the following relations result:

$$\begin{aligned}
\Gamma_1 &= \frac{1}{h^2} \int_{x_\mathrm{L}}^{x_\mathrm{R}} \epsilon^* x dx \\
&= \frac{1}{h^2} \int_{x_L}^{x_R} \left(c_0 + c_1 x + c_2 x^2 + \ldots + c_{n-1} x^{n-1} \right) x dx \\
&= \frac{1}{h^2} \left[c_0 \frac{x^2}{2} + c_1 \frac{x^3}{3} + c_2 \frac{x^4}{4} + \ldots + c_{n-1} \frac{x^{n+1}}{n+1} \right]_{x_\mathrm{L}}^{x_\mathrm{R}} \\
&= \frac{1}{h^2} \left[\frac{c_0}{2} \left({x_\mathrm{R}}^2 - {x_\mathrm{L}}^2 \right) + \frac{c_1}{3} \left({x_\mathrm{R}}^3 - {x_\mathrm{L}}^3 \right) + \frac{c_2}{4} \left({x_\mathrm{R}}^4 - {x_\mathrm{L}}^4 \right) + \ldots + \frac{c_{n-1}}{n+1} \left({x_\mathrm{R}}^{n+1} - {x_\mathrm{L}}^{n+1} \right) \right]
\end{aligned} \tag{3.5}$$

$$\begin{aligned}
\Gamma &= \frac{1}{h} \int_{x_\mathrm{L}}^{x_\mathrm{R}} \epsilon^* dx \\
&= \frac{1}{h} \int_{x_L}^{x_R} \left(c_0 + c_1 x + c_2 x^2 + \ldots + c_{n-1} x^{n-1} \right) dx \\
&= \frac{1}{h} \left[c_0 x + c_1 \frac{x^2}{2} + c_2 \frac{x^3}{3} + \ldots + c_{n-1} \frac{x^n}{n} \right]_{x_\mathrm{L}}^{x_\mathrm{R}} \\
&= \frac{1}{h} \left[c_0 \left(x_\mathrm{R} - x_\mathrm{L} \right) + \frac{c_1}{2} \left({x_\mathrm{R}}^2 - {x_\mathrm{L}}^2 \right) + \frac{c_2}{3} \left({x_\mathrm{R}}^3 - {x_\mathrm{L}}^3 \right) + \ldots + \frac{c_{n-1}}{n} \left({x_\mathrm{R}}^n - {x_\mathrm{L}}^n \right) \right]
\end{aligned} \tag{3.6}$$

Substituting Equation 3.4, Equation 3.5, and Equation 3.6 into Equation 2.16, for all x_i, and factoring out the n unknown coefficients c_j, results in the linear system shown in Equation 3.7.

$$\begin{pmatrix}
k_{11} & k_{12} & k_{13} & \cdots & k_{1n} \\
\vdots & \ddots & & & \vdots \\
k_{i1} & & k_{ij} & & k_{in} \\
\vdots & & & \ddots & \vdots \\
k_{n1} & & \cdots & & k_{nn}
\end{pmatrix}
\begin{pmatrix}
c_0 \\ c_1 \\ c_2 \\ \vdots \\ c_{j-1} \\ \vdots \\ c_{n-1}
\end{pmatrix}
=
\begin{pmatrix}
y_1 \\ y_2 \\ y_3 \\ \vdots \\ y_i \\ \vdots \\ y_n
\end{pmatrix} \tag{3.7}$$

where $y_1, y_2, y_3, \ldots, y_n$ are the measured residual elastic strains. The factors k_{ij} are defined in Equation 3.8.

$$k_{ij} = \frac{6}{h^3}\left(2x_i - x_{\mathrm{R}} - x_{\mathrm{R}}\right)\frac{{x_{\mathrm{R}}}^{j+1} - {x_{\mathrm{L}}}^{j+1}}{j+1} + \frac{2}{h^3}\left[\left({x_{\mathrm{R}}}^2 + x_{\mathrm{R}}x_{\mathrm{L}} + {x_{\mathrm{L}}}^2\right) - 3x_i\left(x_{\mathrm{R}} + x_{\mathrm{L}}\right)\right]\frac{{x_{\mathrm{R}}}^{j} - {x_{\mathrm{L}}}^{j}}{j} - x_i^{j-1} \tag{3.8}$$

This can be written in short as:

$$\mathbf{Kc} = \mathbf{y}$$

The method outlined results in n equations in n unknowns. Theoretically, the solution to Equation 3.7, if substituted into Equation 2.16, will yield predicted values of residual elastic strain, which exactly match the measured values of elastic strain.

5.1.1 Discussion

This method was applied to Sample B15, in the form of a Python script. The results generated were not usable. The eigenstrains resulting from Equation 3.7 were ludicrously high (on the order of 10^6). Theoretically, Equation 3.7 should yield a unique solution if the matrix $\mathbf{K}$ is non-singular. However, computationally, the results of a linear system will be very inaccurate if the matrix is close to being singular. Accordingly, the condition number of the matrix $\mathbf{K}$ was calculated, and indeed, it was found to be very large. (on the order of about 10^{23}). This indicates that the matrix is ill-conditioned, and thus, the solution is unreliable.

The condition number can be decreased using some methods. A matrix is ill-conditioned because there is not sufficient independence between the rows of the matrix. In other words, there is a high degree of parallelism between the rows. One method for solving such systems is to generate a new system that is equivalent to the original system, but with a lower degree of parallelism. This is done by replacing the problematic rows with orthogonal vectors. The new system is represented in Equation 3.9.

This can be written in short as:

$$\mathbf{K}'\mathbf{c} = \mathbf{y}' \tag{3.9}$$

After applying this method, the condition number of $\mathbf{K}'$ was reduced to the order of around 10^{13}. Although much lower than the original matrix, $\mathbf{K}$, it was still too high to trust the results. It became clear that this method was not computationally feasible, and it was abandoned.

5.2 Trapezoid Method

In the previous methods where Equation 2.16 was used, the eigenstrains were represented by basis functions with unknown coefficients. In that case, the problem reduces to finding the correct values of the coefficients. However, by searching for an eigenstrain distribution from a set of basis distribution, the solution is restricted to that set. Thus, the eigenstrains imposed on each layer might not be the most accurate eigenstrain to achieve the least error between the predicted and measured residual strain.

A method was conceived based on numerical integration, that would allow the solution of the Inverse Problem, without assuming a distribution for the eigenstrains. Recall Equation 2.16:

$$\begin{aligned} e(x) = \frac{1}{(x_{\mathrm{R}} - x_{\mathrm{L}})^2} \times \{6\Gamma_1(x_{\mathrm{R}} - x_{\mathrm{L}})(2x - x_{\mathrm{R}} - x_{\mathrm{L}}) \\ + 2\Gamma\left[({x_{\mathrm{R}}}^2 + x_{\mathrm{R}}x_{\mathrm{L}} + {x_{\mathrm{L}}}^2) - 3x(x_{\mathrm{R}} + x_{\mathrm{L}})\right]\} - \epsilon^*(x) \end{aligned} \qquad \text{(Equation 2.16)}$$

Consider a case where one has eigenstrains at discrete points, and wants to solve the direct problem. The obstacles in the way of achieving this are the integral parameters Γ and Γ_1. They, notionally, require a continuous eigenstrain distribution in order to be evaluated. However, this apparent issue can be resolved by using numerical integration. The simplest numerical integration technique is the trapezoid method, which approximates the integral as the area under a series of trapezoids. Using the trapezoidal rule, we can rewrite the definitions for Γ and Γ_1, as demonstrated in Equation 3.10 and Equation 3.11.

$$\Gamma_1 = \frac{1}{h^2}\sum_{i=0}^{n-1}\left[\epsilon^*(x_i)x_i + \epsilon^*(x_{i+1})x_{i+1}\right]\left(\frac{x_{i+1} - x_i}{2}\right) \tag{3.10}$$

$$\Gamma = \frac{1}{h}\sum_{i=0}^{n-1}\left[\epsilon^*(x_i) + \epsilon^*(x_{i+1})\right]\left(\frac{x_{i+1} - x_i}{2}\right) \tag{3.11}$$

The trapezoids are defined by the function values, along with their corresponding abscissas. Thus, it is not necessary to know the function, as long as the function values at discrete points are known. This allows one to solve the direct problem with the aforementioned information. It is now desired to invert this method.

For the inverse problem, the eigenstrains are unknown, but residual elastic strains at discrete points are known. We can rewrite Equation 2.16 for each known residual elastic strain value, e_i.

$$
\begin{aligned}
e(x_i) = \frac{6}{h^3}(2x_i - x_{\mathrm{R}} - x_{\mathrm{L}}) \sum_{j=0}^{n-1} \left[\epsilon^*(x_j)x_j + \epsilon^*(x_{j+1})x_{j+1}\right] \left(\frac{x_{j+1} - x_j}{2}\right) \\
+ \frac{2}{h^3}\left[({x_{\mathrm{R}}}^2 + x_{\mathrm{R}}x_{\mathrm{L}} + {x_{\mathrm{L}}}^2) - 3x_i(x_{\mathrm{R}} + x_{\mathrm{L}})\right] \sum_{j=0}^{n-1} \left[\epsilon^*(x_j) + \epsilon^*(x_{j+1})\right] \left(\frac{x_{j+1} - x_j}{2}\right) \\
- \epsilon^*(x_i)
\end{aligned}
\tag{3.12}
$$

By factoring out the unknown eigenstrains and further manipulating Equation 3.12, the linear system shown in Equation 3.13 results.

$$
\begin{pmatrix}
t_{00} & t_{02} & t_{03} & \cdots & t_{0n} \\
\vdots & \ddots & & & \vdots \\
t_{i1} & & t_{ij} & & t_{in} \\
\vdots & & & \ddots & \vdots \\
t_{n1} & & \cdots & & t_{nn}
\end{pmatrix}
\begin{pmatrix}
\epsilon_0 \\ \epsilon_1 \\ \epsilon_2 \\ \vdots \\ \epsilon_j \\ \vdots \\ \epsilon_{n-1}
\end{pmatrix}
=
\begin{pmatrix}
y_0 \\ y_1 \\ y_2 \\ \vdots \\ y_i \\ \vdots \\ y_n
\end{pmatrix}
\tag{3.13}
$$

$$
\mathbf{T}\epsilon = \mathbf{y}
$$

The elements of the matrix $\mathbf{T}$ are defined in Equation 3.14, where $R_i = \frac{6}{h^3}(2x_i - x_{\mathrm{R}} - x_{\mathrm{L}})$ and $S_i = \frac{2}{h^3}\left[({x_{\mathrm{R}}}^2 + x_{\mathrm{R}}x_{\mathrm{L}} + {x_{\mathrm{L}}}^2) - 3x_i(x_{\mathrm{R}} + x_{\mathrm{L}})\right]$.

$$
t_{ij} = \begin{cases}
\dfrac{(R_i x_j + S_i)(x_{j+1} - x_j)}{2} & \text{for } j = 0;\ i = 1, 2, \ldots, n \\
\dfrac{(R_i x_j + S_i)(x_{j+1} - x_j)}{2} - 1 & \text{for } j = i = 0 \\
\dfrac{(R_i x_j + S_i)(x_{j+1} - x_{j-1})}{2} & \text{for } i = 0, 1, 2, \ldots, n;\ j = 1, 2, \ldots, n-1; i \neq j \\
\dfrac{(R_i x_j + S_i)(x_{j+1} - x_{j-1})}{2} - 1 & \text{for } i = j = 1, 2, 3 \ldots, n-1 \\
\dfrac{(R_i x_j + S_i)(x_j - x_{j-1})}{2} & \text{for } j = n;\ i = 0, 1, 2, \ldots, n-1 \\
\dfrac{(R_i x_j + S_i)(x_j - x_{j-1})}{2} - 1 & \text{for } j = i = n
\end{cases}
\tag{3.14}
$$

The aforementioned method was written in a Python script. Solving Equation 3.13 results in the eigenstrains at discrete points, corresponding to the depths at which measurements were taken. An important consideration, is the accuracy of the numerical integration. In general, the accuracy of numerical integration over an interval increases the more segments there are. Since the number of segments in this case is fixed at the number of measurements, this aspect of accuracy cannot be controlled.

To overcome this weakness of the method, it was decided that polynomial interpolation of the residual elastic strains would be used to increase the number of data points that can be used in the analysis. This was done by adding a function to fit a polynomial to the measured data and return interpolated residual elastic strains at equal intervals. The number of intervals is input by the user and taken in by the function as an argument. Thus, the accuracy of the eigenstrains can be controlled by the user changing the number of intervals.

5.2.1 Discussion

Although the results seemed reasonable initially, the eigenstrains produced using this method are not correct. When substituted into the direct problem, the resulting residual elastic strains are completely inaccurate.

To further investigate this phenomenon, the direct problem was solved using Equation 3.13. To do this, the eigenstrain distribution was assumed equivalent to some random polynomial. This polynomial was used in conjunction with Equation 2.16 to generate a $\mathbf{y}$ vector of length n, which represents the residual elastic strains that should result if the eigenstrain distribution was described by the chosen polynomial. The polynomial was then used to generate n eigenstrains at the appropriate depths. The eigenstrain vector was multiplied by matrix $\mathbf{T}$. It was reasoned that if the problem was formulated correctly, $\mathbf{T}\epsilon$ should not be too different from the aforementioned vector, $\mathbf{y}$. Indeed, it was found that there was not much difference between the two vectors and that the error decreases with increasing n. This indicated that the problem was formulated correctly.

The inverse problem was then tested using the same $\mathbf{y}$. It was expected that multiplying $\mathbf{T}^{-1}$ by $\mathbf{y}$ should yield the same eigenstrain vector as was calculated using the aforementioned polynomial. The result was surprising. While $\mathbf{T}^{-1}\mathbf{T}\epsilon$ yielded the correct vector ϵ – as expected – $\mathbf{T}^{-1}\mathbf{y}$ yielded a totally different and incorrect ϵ vector. This is despite the fact that the error between $\mathbf{T}\epsilon$ and $\mathbf{y}$ is very small. Increasing n did not improve the situation.

It is clear from the situation described above that the unreliability of this method is related to ill-posedness of the inverse problem (see section 6). Thus, this method was abandoned.

6 Confirming the Principle of Transferability of Eigenstrain

Thus far, various methods of predicting residual stress fields in laser peened samples have been validated. However, the validation was conducted for FEM models which were identical to the original sample. In chapter 1, it was mentioned that the true potential of the eigenstrain method lies in its ability to use residual stress data from a simple geometry to predict residual stresses in complex geometries. This is possible under the assumption that the plastic strain induced by LSP is insensitive to the geometry of the peened component. This assumption is based on the Principle of Transferability of Eigenstrain (See section 9).

Several studies have been conducted to confirm this principle in practice[23][52][2]. However, since the particular peening process used in this study is different to those used by others, it was considered prudent to confirm that the known eigenstrain distribution of Sample B15 could be used to predict residual stresses in other geometries.

To achieve this, the residual stresses in three physically peened samples with different geometries were compared to predictions obtained using Coratella's method. Figure 3.19 depicts the three peened geometries[57]. All three geometries have different types of corners which were peened: convex corner, concave corner, and sharp corner. The residual stresses in the samples were measured using a variety of techniques, but a mixture of synchrotron x-ray diffraction and neutron diffraction were used to validate the eigenstrain method. The residual stresses were measured along the diagonal line of each sample. This was achieved in a previous collaboration with US Air Force Research Laboratory, University of Dayton Research Institute, and Wright-Patterson Air Force Base.

Table 3.9: Corner samples vs Sample B15

	Corner Samples	**Sample B15**
Sample material	Aluminium Alloy 7075	Aluminium Alloy 7075
Spot shape	Circular	Circular
Spot size	1.5 mm	1.5 mm
Peening pattern	Raster pattern	Raster pattern
Coverage	5 spots/mm^2	5 spots/mm^2
Power Intensity	2.6 GW/cm^2	3 GW/cm^2

The details of the samples and peening parameters are compared to the parameters of Sample B15 in Table 3.9[57]. All the parameters are identical, with the exception of the power intensity, which is slightly different. This is important because eigenstrains are only transferable across geometries, not over other parameters. The other parameters affect the eigenstrain

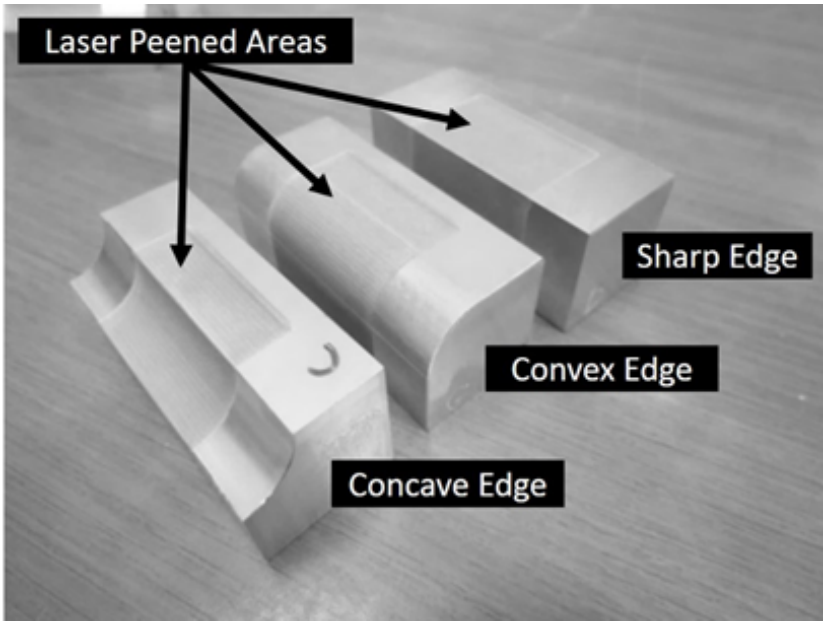

Figure 3.19: *Three peened geometries in which residual stresses were measured*[57]

distribution induced. Hence it is necessary for the material and process parameters to be similar, if not identical to each other, in order for the Principle of Transferability of Eigenstrain to hold.

Figure 3.20 shows the dimensions and peening directions of the samples. The scan direction was along the length of the samples, while the step direction was transverse to the length. The concave and convex corners were both 10mm in radius.

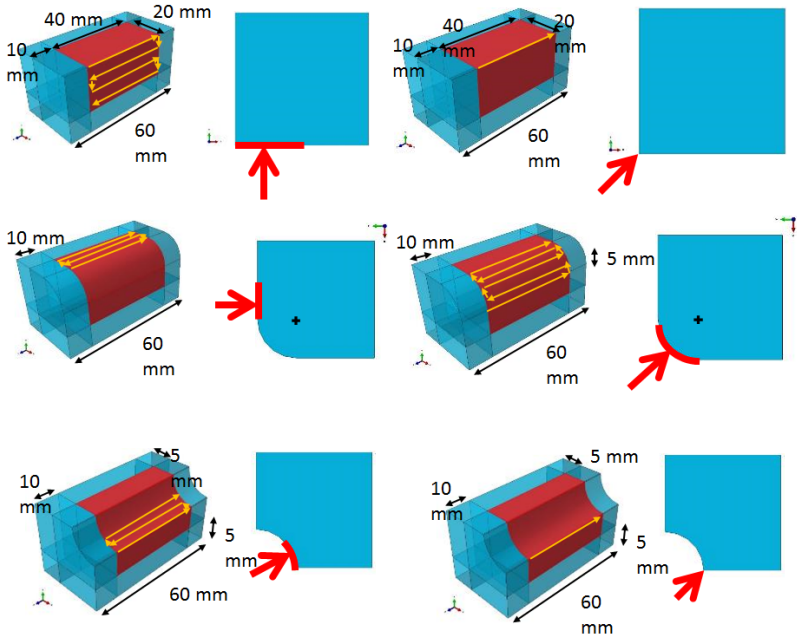

Figure 3.20: *Three peened geometries in which residual stresses were measured*[57]

For each of the corner specimens, an FEM model was created. Layers were created near the surface to impose the eigenstrains at the relevant depths. For the concave and convex corners, a separation was created between the straight and curved layers. This was to allow the application of a cylindrical co-ordinate system to the curved layers, which was essential to ensure the eigenstrains were applied in the correct directions. All the models have two planes of symmetry, and were thus reduced to a quarter of the original sizes. The FEM models are depicted in Figure 3.21.

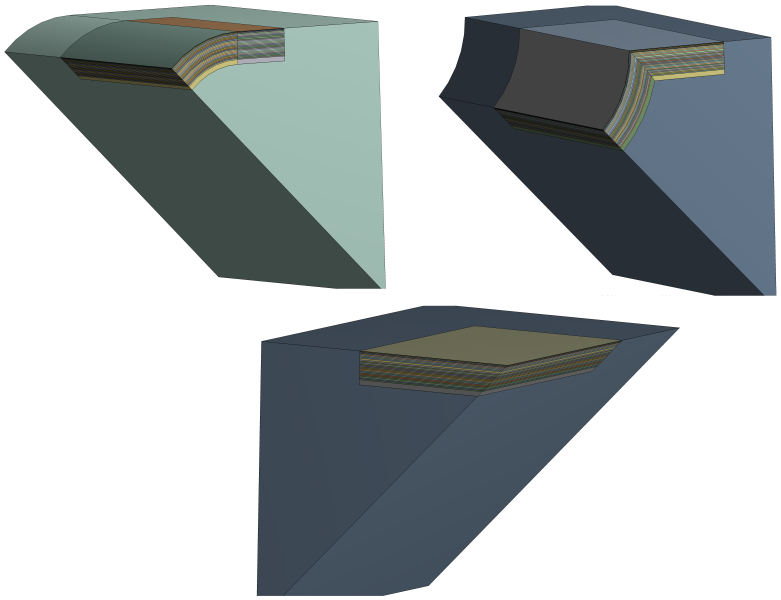

Figure 3.21: *FEM models of the three samples*

Figure 3.22, Figure 3.23, and Figure 3.24 compare the predicted residual stresses to the measured residual stresses along the diagonals of the convex, concave, and sharp corner, respectively. The prediction for the convex corner is excellent and well within the uncertainty bounds of the residual stress. The predicted residual stress curve follows the polynomial fit to the measured data (the red line) quite closely, throughout most of the depth. While the prediction for the concave corner is not as accurate as for the convex one, it is still mostly within the uncertainty bounds. The predicted curve slightly underestimates the value of the stresses, compared to the polynomial fit to the measured data. The prediction for the sharp corner is the least accurate and out of the uncertainty bounds of the residual stress in the peened region. The predicted curve overestimates the value of the residual stresses in the peened region.

It should be remembered that the power intensity of the laser was slightly different when peening the corner samples, compared to Sample B15. Despite this, the predictions in the convex and concave corners are quite good. Essentially, residual stresses in these two specimens – which were subjected to almost identical peening processes – were predicted using only measured data from Sample B15 and elastic properties as inputs. No measured data

from the corner samples were used as inputs for the prediction. This adds weight to the assumption that eigenstrains are insensitive to geometry, at least in some instances.

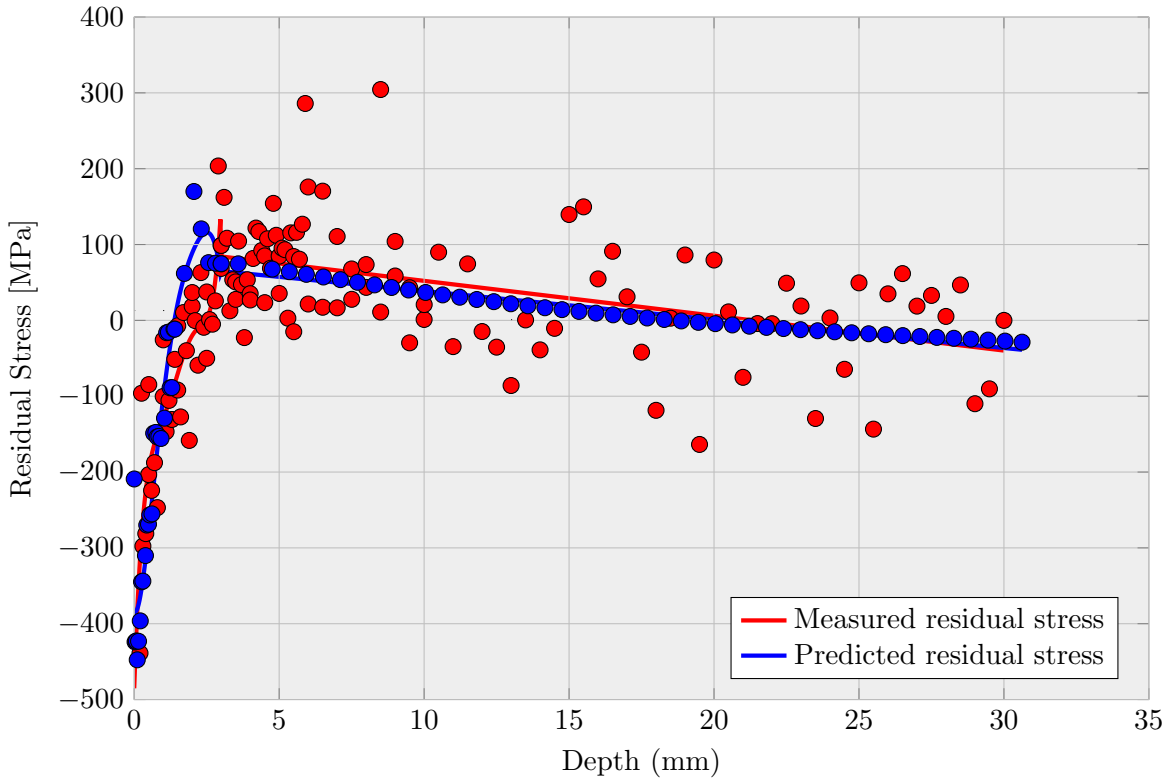

Figure 3.22: *Predicted vs Measured residual stress in convex corner*

A question that remains to be answered is why the prediction in the sharp corner is not as accurate as it is in the other samples. In short, the answer is due to the effects of peening around a corner. To understand this, consider the schematics in Figure 3.25. Diagram (a) shows a hypothetical sample to be peened. The arrows show the regions of the sample to be peened. First, the top of the sample is peened, which leads to the peened red zone in diagram (b). Next the corner is peened, as shown in diagram (c). Assuming a finite size of the corner, the green line represents the peened zone that should arise from the peening. Finally, the side is peened, which should lead to the blue peened region in diagram (d).

The problem is illustrated in the purple region in diagram (d). This represents the intersection of the peened regions from peening of the side and top. How can the plastic strains in this region be expressed? Due to non-linearity of plastic strain, one cannot simply assume it to be the superposition of the eigenstrains due to the individual peened regions. Once the top is peened, the peening of the edge and side will not result in the same eigenstrains in the purple region. This is due to the fact that the material in that region is already plastically strained and will not react to the shock wave in the same way as a strain-free material. Without more information there is no way to know what the resulting eigenstrains will be.

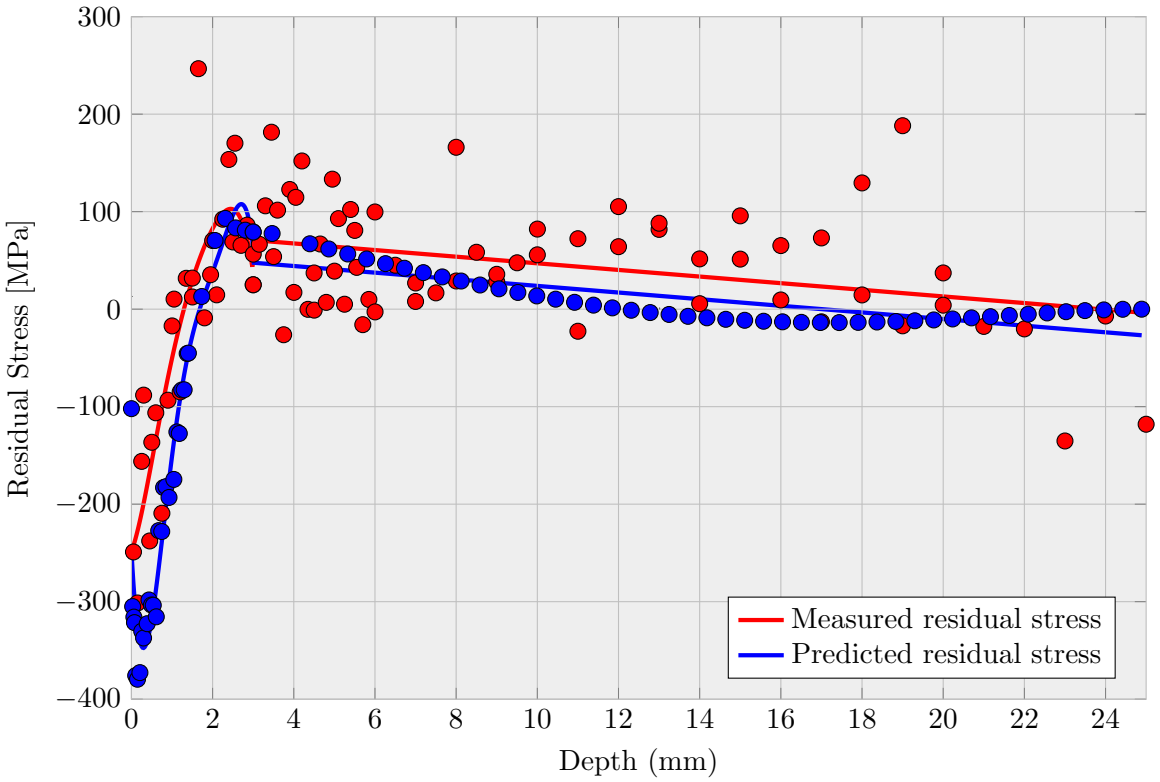

Figure 3.23: *Predicted vs Measured residual stress in concave corner*

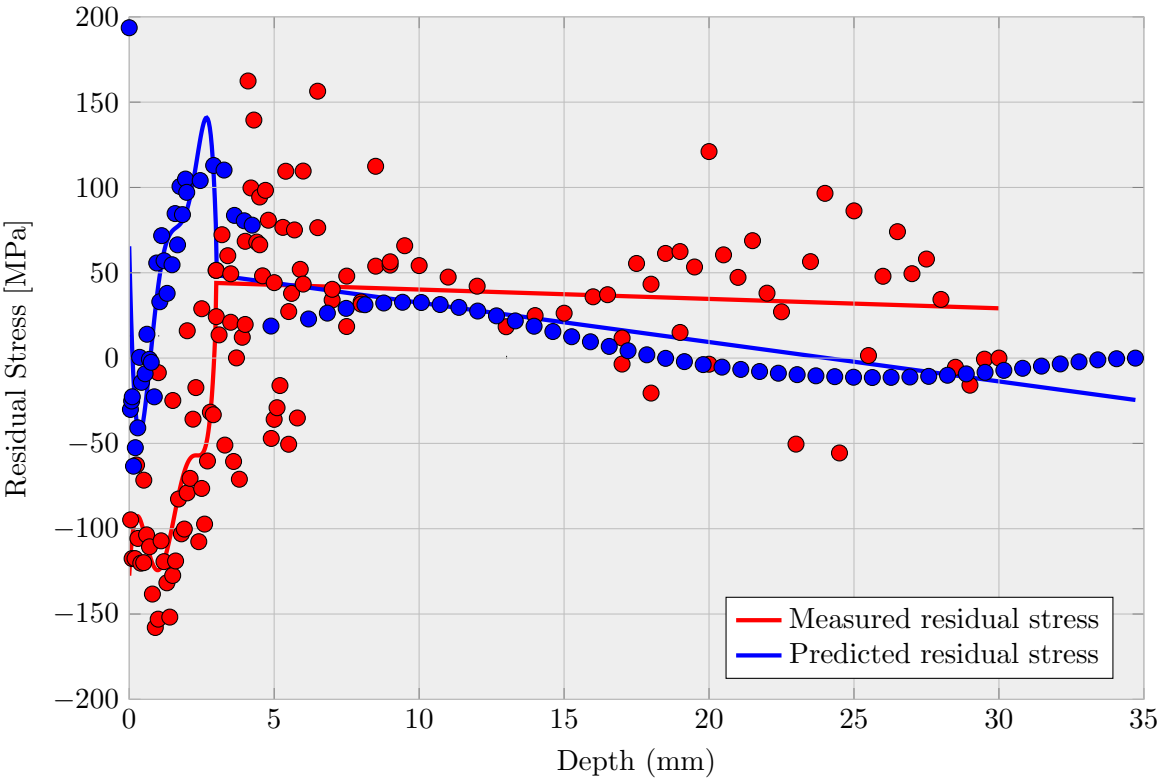

Figure 3.24: *Predicted vs Measured residual stress in sharp corner*

In the model for the sharp corner, this intersection of different peened regions was not taken into account. Instead, the intersection of peened regions was dealt with as shown in Figure 3.26, where the colours hold the same meaning as Figure 3.25. This explains some of the discrepancy between the predicted and measured results for the sharp corner.

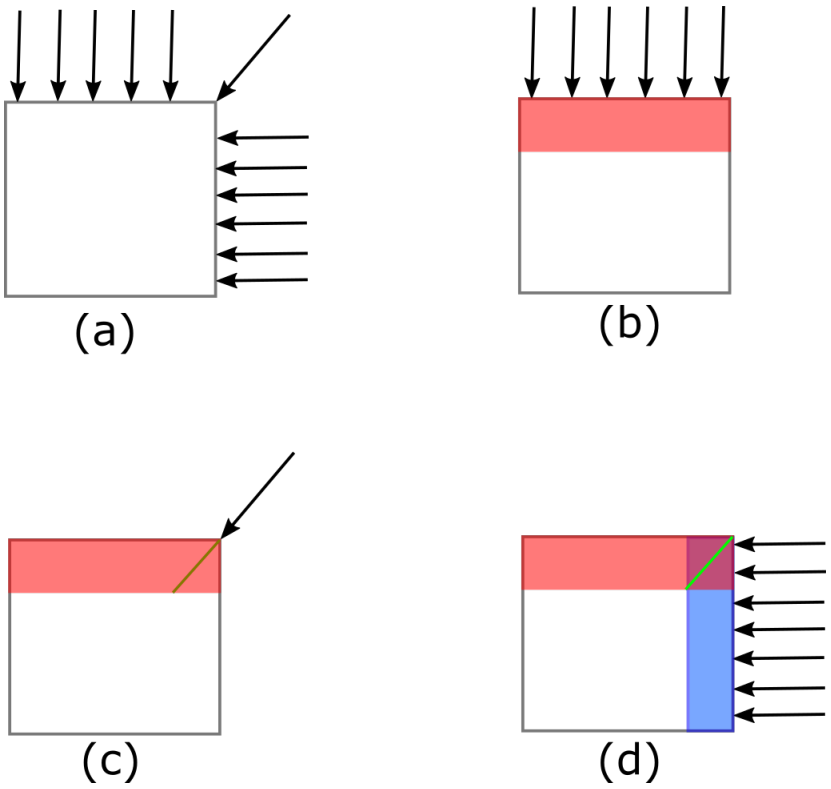

Figure 3.25: *Schematics depicting peening over an edge*

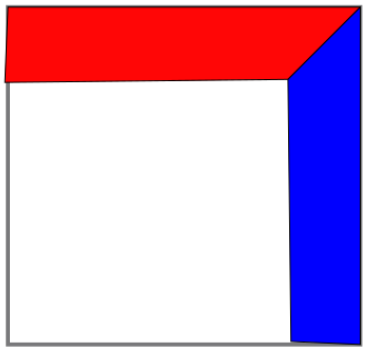

Figure 3.26: *Intersection of peened regions in sharp corner model*

This exposes a general weakness of the proposed method in dealing with peening around edges and sharp changes in geometry. Achintha[53] has proposed estimating the eigenstrain distribution by superimposing the eigenstrains that would have arisen from peening each side of the edge separately (see subsection 9.2 of chapter 2).

It was decided to test the superposition method and ascertain its effectiveness in predicting residual stresses. This required some changes to the model depicted in Figure 3.21.

Firstly, it should be noted that the layers used in the current model are inadequate to deal with superposition of eigenstrains. Consider Figure 3.25 (d) once again. For the red zone, eigenstrains are defined at particular intervals, which manifest as layers in the FEM model. There are as many layers as there are known eigenstrains. Let $(\epsilon_k^*)_i$ represent the k-direction $(k = x, y, z)$ component of eigenstrain in layer number i. Running the index i from 1 to the number of layers in the red zone leads to an algebraic vector of the defined eigenstrains in the red zone.

Similarly, for the blue region, we can define $(\epsilon_k^*)_j$ to be the k-direction component of eigenstrain in the layer number j of the blue zone. Now the purple zone represents the intersection of red and blue. If there are m defined eigenstrains in the blue zone, then for every $(\epsilon_k^*)_i$ in the purple zone, there are m eigenstrains defined at intervals corresponding to the layers in the blue zone. Thus, the eigenstrains in the purple region can only be completely described by a tensor, $(\epsilon_k^*)_{ij}$. Instead of layers, the model has to be broken into blocks, which represent the intersection of layers in the blue and red zones. This is depicted in Figure 3.27.

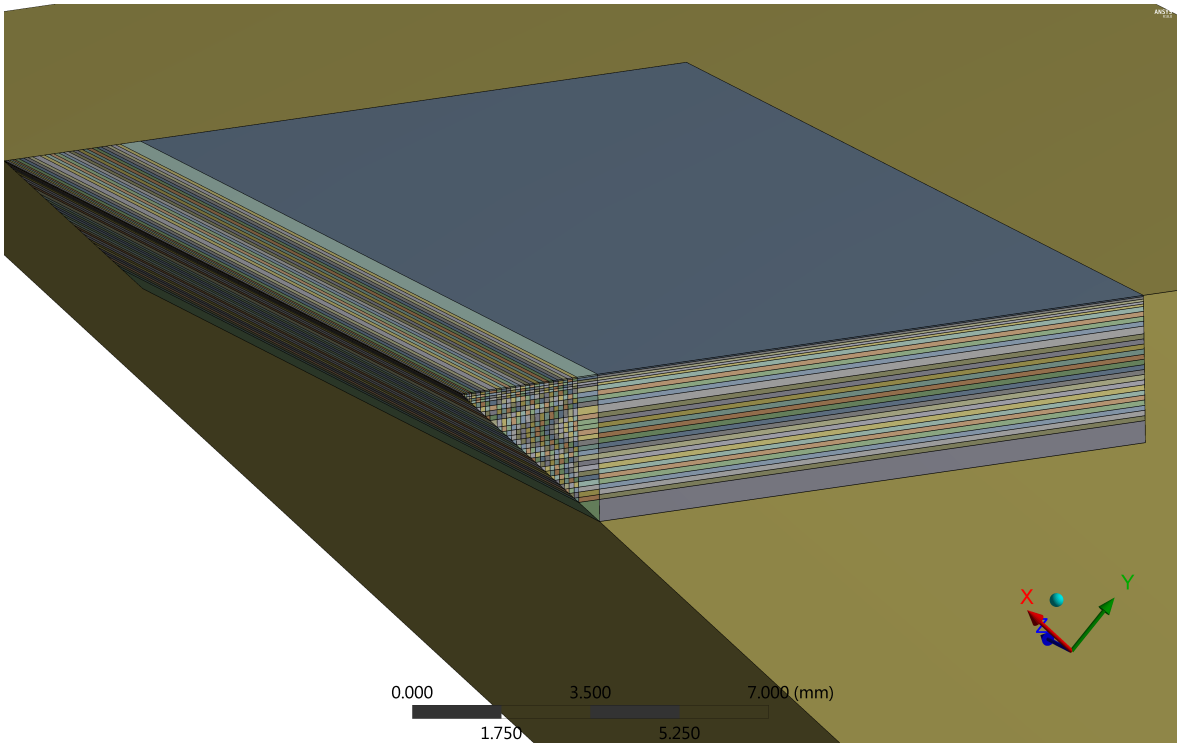

Figure 3.27: *FEM Model used to superimpose eigenstrains*

For each block in Figure 3.27, a corresponding material was created. The eigenstrains, $(\epsilon_k^*)_{ij}$, were input as outlined in section 2. $(\epsilon_k^*)_{ij}$ can be defined with reference to Figure 3.28. Using the definition of x, y, and z as being the step, scan and normal directions respectively, the

co-ordinate systems shown on each side of the edge result. The top co-ordinate system is associated with $(\epsilon_k^*)_i$, while the side co-ordinate system is associated with $(\epsilon_k^*)_j$. It is clear that on either side of the edge, the normal and step directions are inverted. Thus, using the reference co-ordinate system, the superposition of the eigenstrains can be expressed in terms of the $(\epsilon_k^*)_j$ and $(\epsilon_k^*)_i$ as follows:

$$(\epsilon_x^*)_{ij} = (\epsilon_x^*)_i + (\epsilon_z^*)_j \tag{3.15}$$

$$(\epsilon_y^*)_{ij} = (\epsilon_y^*)_i + (\epsilon_y^*)_j \tag{3.16}$$

$$(\epsilon_z^*)_{ij} = (\epsilon_z^*)_i + (\epsilon_x^*)_j \tag{3.17}$$

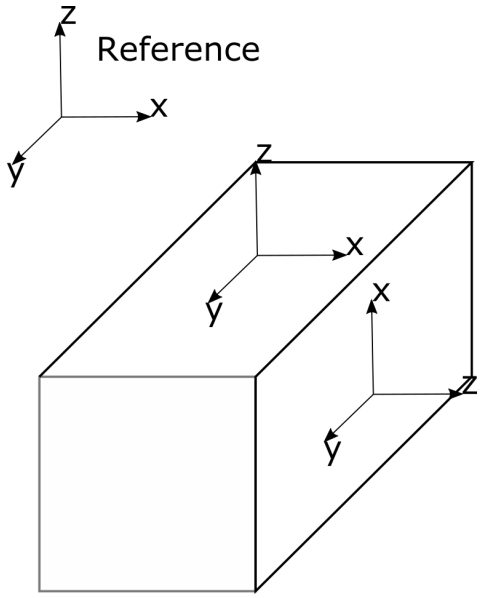

Figure 3.28: *Co-ordinate system to define superposition of eigenstrains*

Figure 3.29 compares the results from the superposition method with the previous results. With superposition of eigenstrains, the prediction is better, but only slightly. It still over-estimates the value of stresses within the peened depth. This is not entirely unexpected, considering that plastic deformation is non-linear. The principle of superposition should not be expected to hold.

Besides the overlapping of peened regions, there are other factors that affect the accuracy of prediction. One notable factor is the edge effect (see subsection 9.1). According to research by Achintha[53], the eigenstrains in a peened region adjacent to an edge are affected by the edge. Specifically, the surface eigenstrains in a narrow band adjacent to the edge, are higher

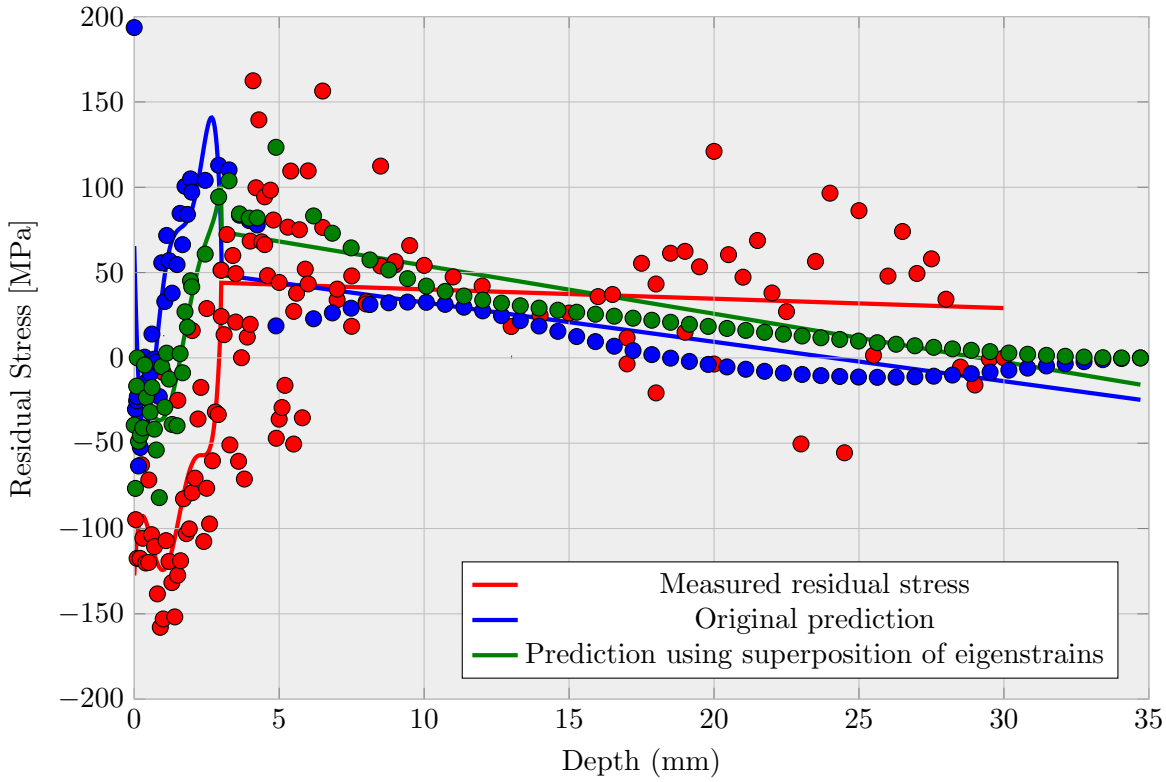

Figure 3.29: *Predicting residual stresses by superimposing eigenstrains*

than in the rest of the peened zone. In the above analysis, the edge effect was not taken into account and the eigenstrains were assumed to be uniform throughout the peened region. If the true eigenstrains near the edge are assumed to be higher than the rest of the peened zone, like in Figure 2.15, one would expect the true residual stress to be more highly compressive than the prediction, and it is clear from Figure 3.29 that this is indeed the case.

One final noteworthy matter, is that the concave corner also has sharp edges. Why is the prediction in the concave corner not as bad as the sharp corner? The major difference between the sharp corner and the concave corner, is that the line plot for the concave corner does not pass through the sharp edges, while the line plot for the sharp corner does. The fact that results far away from the edge are not much affected by the edge is consistent with Saint Venant's principle.

7 Conclusions

- Five different eigenstrain methods were tested and compared to find a model that can best predict residual stresses due to LSP. These are:

  - Coratella's method
  - Korsunsky's method
  - Korsunsky's method with FEM to generate elastic strain matrix
  - Polynomial fit method
  - Trapezoid method

- Three methods were found to be viable predictors of residual strains and stresses in components subject to LSP, viz:
  - Coratella's method
  - Korsunsky's method
  - Korsunsky's method with FEM to generate elastic strain matrix

- These three methods were applied to four different peened samples. The residual stresses through the depth had been measured in these samples. The measured data was used to obtain the eigenstrains in the sample and ultimately to calculate the residual stresses in the sample and compare them to the measured values.

- No single method was proven to be categorically better than the other methods. However, discretion was used to select Coratella's method over the others.

- Two methods were found not to be viable, viz.:
  - Polynomial fit method
  - Trapezoid method

- The polynomial fit method failed due to an ill-conditioned matrix.

- The trapezoid method failed due to ill-posedness of the inverse problem.

- The assumption of insensitivity of eigenstrains to geometry was tested: the residual stresses in peened concave, convex, and sharp corners were predicted using the eigenstrain method and compared to available measured data.

- Good agreement was found between predicted and measured results in concave and convex corners, justifying the assumption in general.

- The proposed eigenstrain method evinces a weakness in predicting residual stresses over sharp changes in geometry. This is attributed to the complex eigenstrain distribution that arises when peening over an edge.

Chapter 4 Effect of Rectilinear Geometric Parameters on Residual Stresses in Cuboid Samples

This chapter deals with the second objective. Eigenstrain methods allow one to approximate the global residual stress field in a sample, using local measurements of residual stress through the depth. It also allows the prediction of residual stresses in samples with different geometric parameters to the original sample, without additional measurements. This chapter takes advantage of this characteristic of eigenstrain methods to study the effects of different geometric parameters on the residual stresses in samples treated with Laser Shock Peening.

1 Residual Stress Distribution in Base Sample

Since eigenstrain methods require measurements of residual stress or strain to determine the eigenstrains, a base sample was required to study the effects of geometry on residual stresses. Figure 3.1 in chapter 3 outlines the benchmark samples, in which residual stresses were measured. It was decided that Sample B15 (refer to Appendix A for charcteristics of this sample) will be used as a base sample in this chapter. The reason is that this sample had been subjected to a variety of measuring techniques. Every measuring technique has its own advantages and disadvantages. To get an accurate representation of the residual stresses, a variety of complementary measuring techniques is required[56].

In chapter 3, emphasis was placed on validating different eigenstrain models. Therefore, not much attention was paid to accuracy of residual stresses in the sample. In this chapter, there is interest in gaining an accurate picture of the residual stresses in the samples being studied. For that reason, the approach used in this chapter is slightly different to that presented in chapter 3.

Unlike chapter 3, the measured residual stress distribution through the depth was characterised using Incremental Hole Drilling, Energy Dispersive XRD, and Neutron Diffraction; rather than relying solely on Neutron Diffraction. Laboratory XRD was used close to the surface, Incremental Hole Drilling results were used up to intermediate depths, and Energy Dispersive XRD along with Neutron Diffraction used at intermediate distances up to the bottom of the sample. This is in accordance with the relative strengths of each measurement technique[56].

Another crucial difference between the approach used here, compared to chapter 3, is the depth to which eigenstrains were calculated and imposed on the model. In chapter 3, the eigenstrains were calculated throughout the depth of the sample. In this chapter, the eigenstrains are only calculated up to the depth of peening, as displayed in Figure 4.1. It is assumed that the eigenstrain beyond the peened depth is zero in all directions. A corollary of this is that the residual stresses are linear beyond the peened depth. Thus, the non-linear residual stresses near the bottom of the sample (see Figure 3.3) – which are due to machining – are ignored. This approach also allows the thickness of the sample to be changed without changing the number of layers.

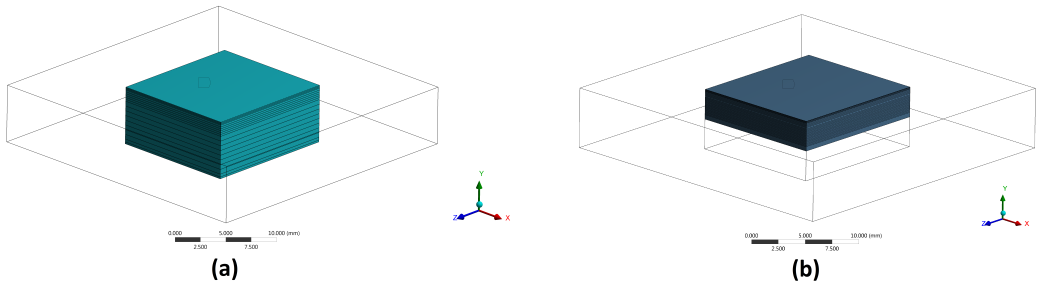

Figure 4.1: *Comparison between layers in: a.) chapter 3 and b.) chapter 4*

The newly synthesised residual stress data in Sample B15 was subjected to Coratella's method (Refer to subsection 3.1). Figure 4.2 and Figure 4.3 show the predictions of this method in the x and y directions, respectively. The predictions roughly correspond to the measured data. As mentioned, the residual stresses due to machining were ignored, hence the discrepancy between predicted and measured curves near the bottom of the sample.

The above results affirm that the method used is capable of handling the new measured data. The next step is to explore the residual stress fields in Sample B15, beyond the simple line plots provided by measurements. Contour plots of the residual stress fields in the x and y directions are displayed in Figure 4.4 and Figure 4.5. It should be noted that the co-ordinate system used in ANSYS is not the co-ordinate system used throughout the dissertation. The co-ordinate system used in this dissertation is such that the z axis is normal to the top surface of the sample. Thus, the z and y axes have to be interchanged.

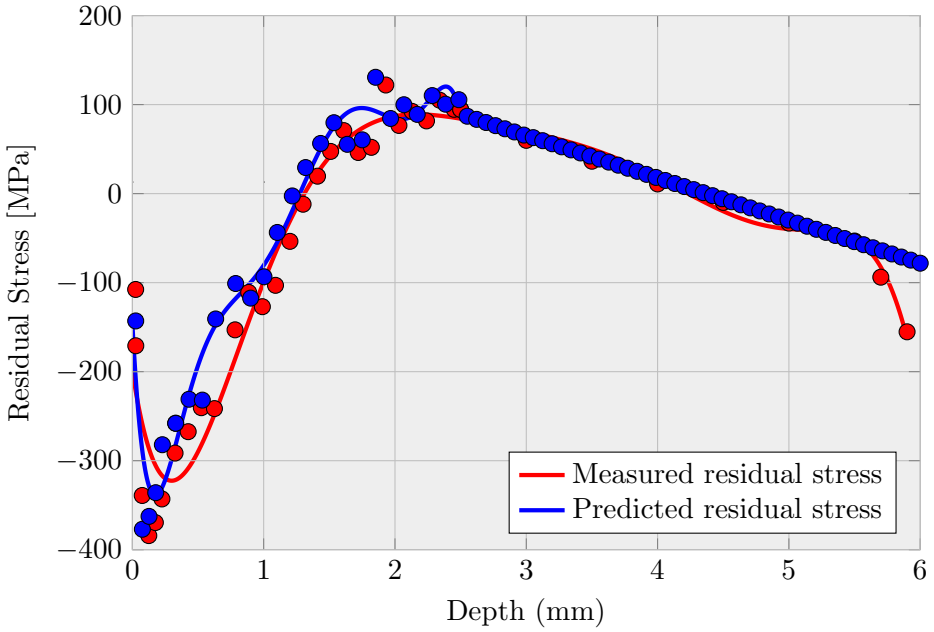

Figure 4.2: *Residual Stress distribution through thickness of Sample B15 – x direction*

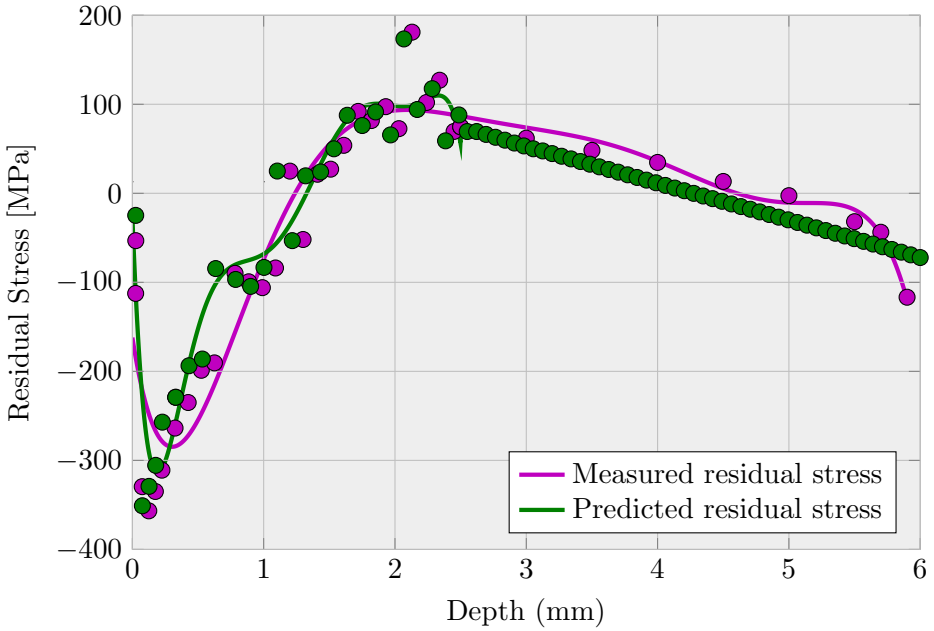

Figure 4.3: *Residual Stress distribution through thickness of Sample B15 – y direction*

The first thing that is apparent is that the stresses in the bulk of the material are close to zero. This is to be expected because the bulk of the material has not been plastically deformed. Secondly, while the eigenstrains were assumed to be invariant with regards to the x and y directions, it is apparent from Figure 4.4 and Figure 4.5 that the residual stresses do vary in the $x-y$ plane of the peened region, even if the eigenstrains do not. This is especially evident at the surface of the peened region, where the stresses near the centre are more compressive than the rest of the peened region.

The pattern of stresses in Figure 4.5 is similar to that of Figure 4.4, but rotated by 90°. The peened region is surrounded by two regions where the stresses are tensile in the y direction and compressive in the x direction and two regions where the stresses are tensile in the x direction and compressive in the y.

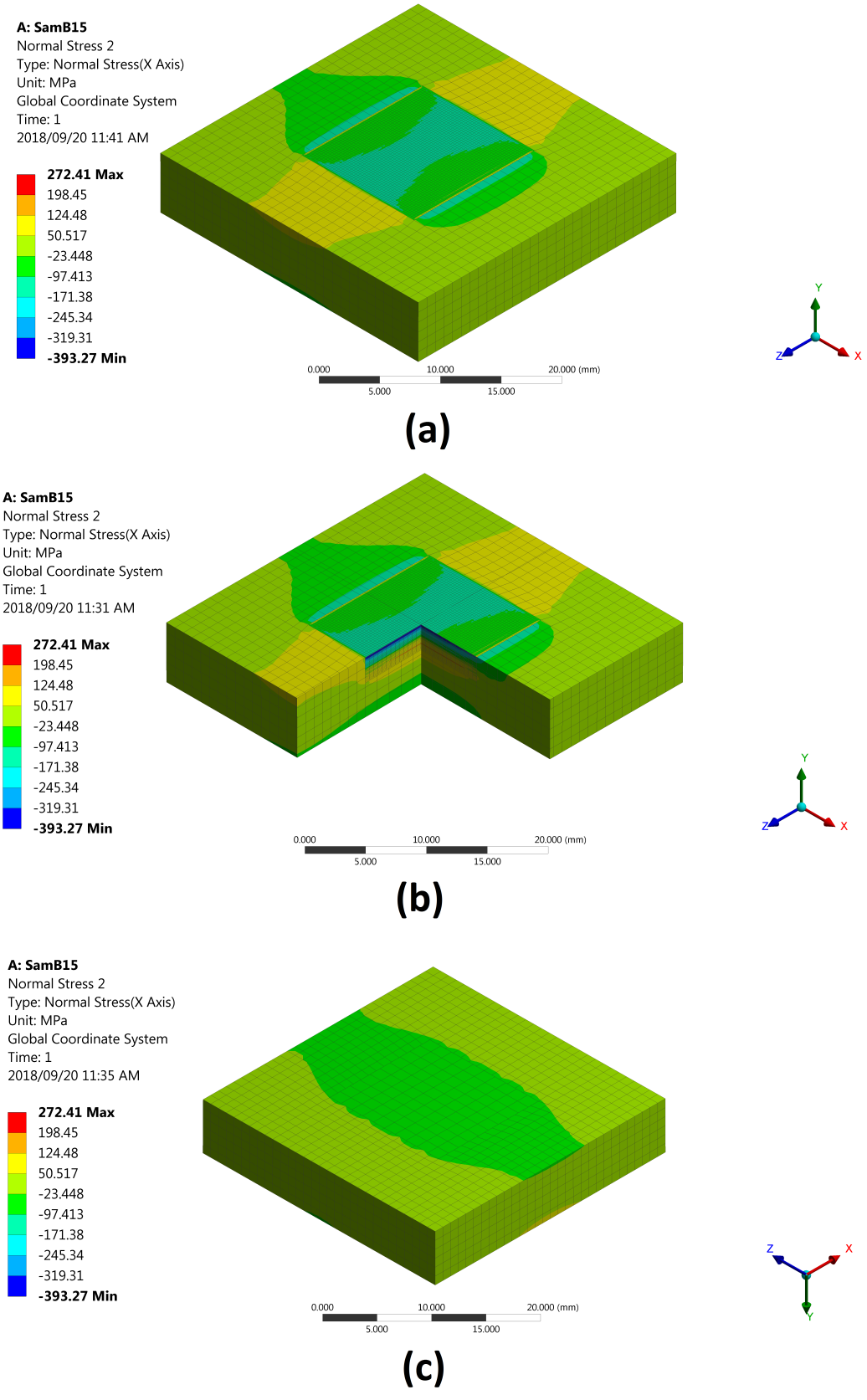

Figure 4.4: *Contour plots of residual stress field in Sample B15 – x direction (a) Top view, (b) Cross section (c) Bottom view*

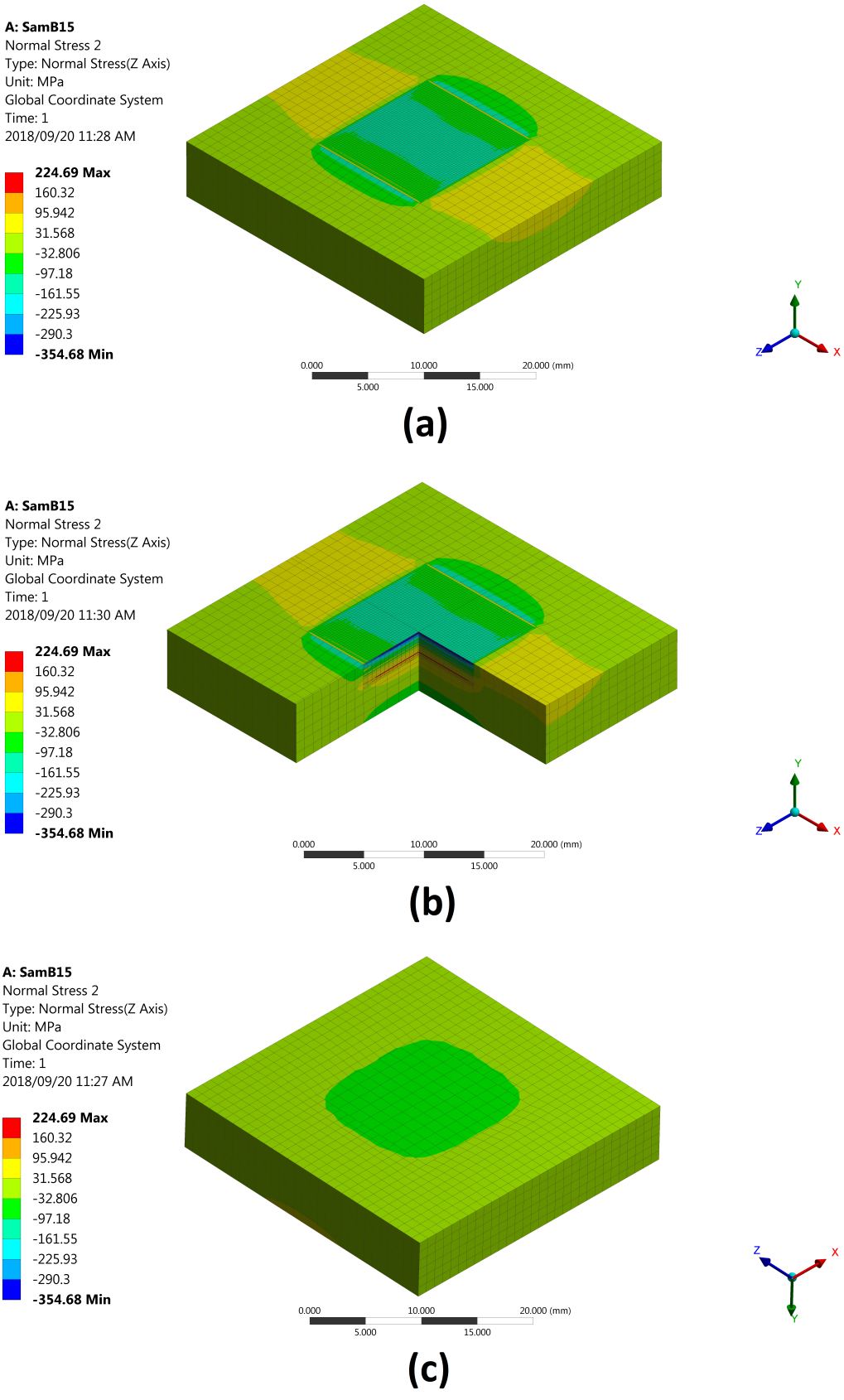

Figure 4.5: *Contour plots of residual stress field in Sample B15 – y direction (a) Top view (b) Cross section (c) Bottom view*

2 Effect of Thickness on Residual Stress Distribution

The approach outlined in section 1 was applied to models of Sample B15 with varying thickness. The rest of the geometry was kept the same as Sample B15. The same eigenstrain distribution was imposed on all the models. There is a very important assumption that requires mention here: the eigenstrain distribution was assumed to be the same, no matter the thickness of the material. This assumption is based on the Principle of Transferability of Eigenstrain (see subsection 4.2 of chapter 2) and without it, this study could not have been performed.

The resulting residual stress distributions in the x direction for the different thickness is given in Figure 4.6. The plots were obtained by fitting a polynomial to the non-linear portion of the data (up to the peened depth) and a best-fit line to the linear portion (beyond the peened depth).

Generally, the surface residual stress and maximum compressive residual stress increase with increasing thickness. The gradient of the linear portion of the graph becomes less steep as the thickness increases. The thickness does not seem to affect the depth of maximum compression or the peen-affected depth. This should be viewed as a consequence of the assumption that the eigenstrain distribution is invariant with respect to thickness.

Figure 4.7 shows how some stresses in the material vary with changing thickness. The absolute maximum and absolute minimum stresses are the highest tension and compression stresses, respectively, in the entire sample. The centre of the sample is where the measured line plot of residual stresses was extracted.

The stresses all seem to be converging to steady values as thickness increases. Also, the absolute maximum and minimum tend to converge towards the local maximum and minimum through the centre. The minimum stresses decrease monotonically and resemble logarithmic curves. The surface stress at the centre also decreases monotonically for thickness greater than 5mm. Below that thickness, the variation in the surface residual stress is erratic. The maximum tensile stress through the centre changes the least from all the stresses. It reaches a steady value very quickly. The absolute maximum appears the most erratic, but eventually settles down and converges towards the local maximum through the centre.

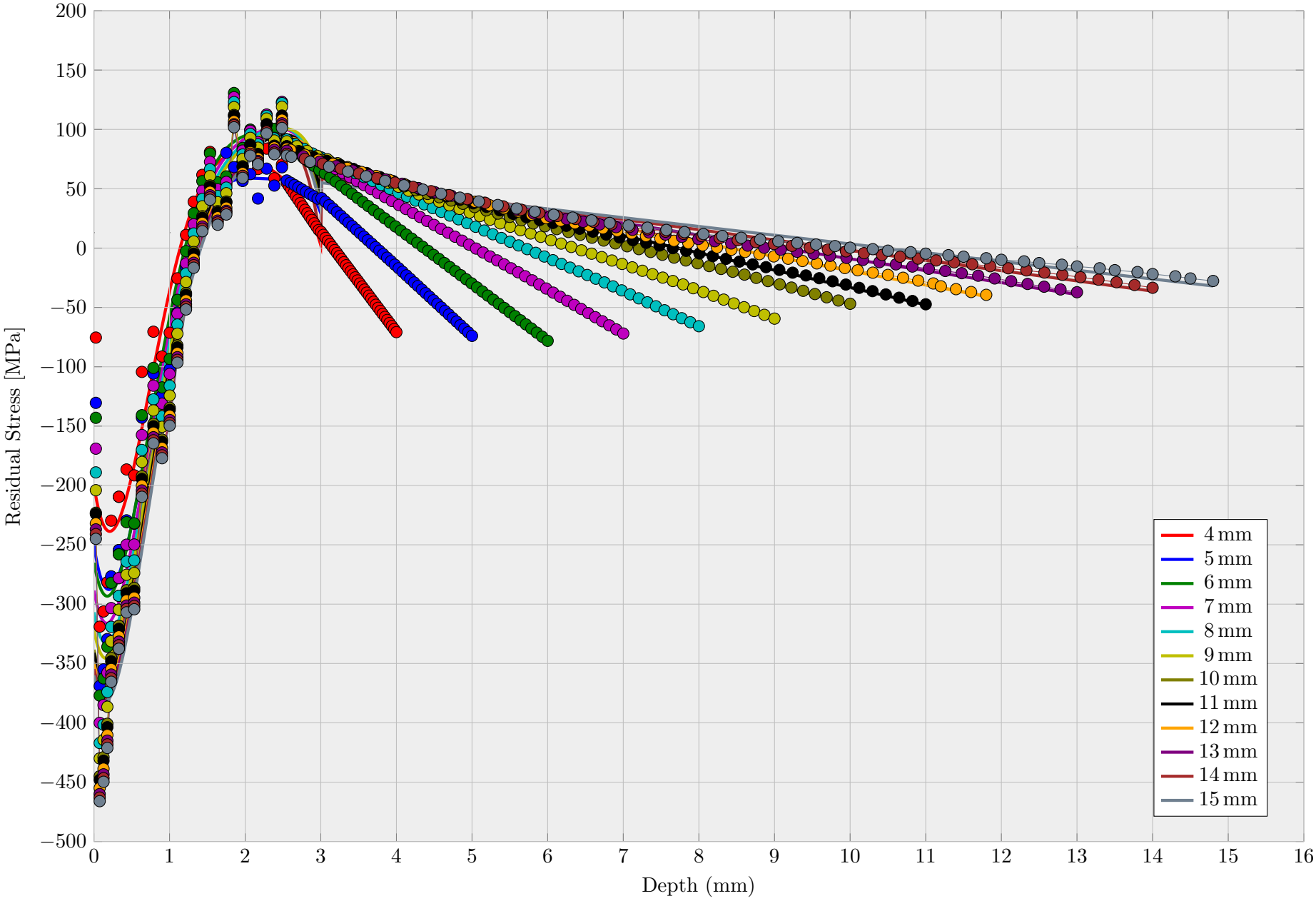

Figure 4.6: *Residual stress distributions in samples with varying thickness – x direction*

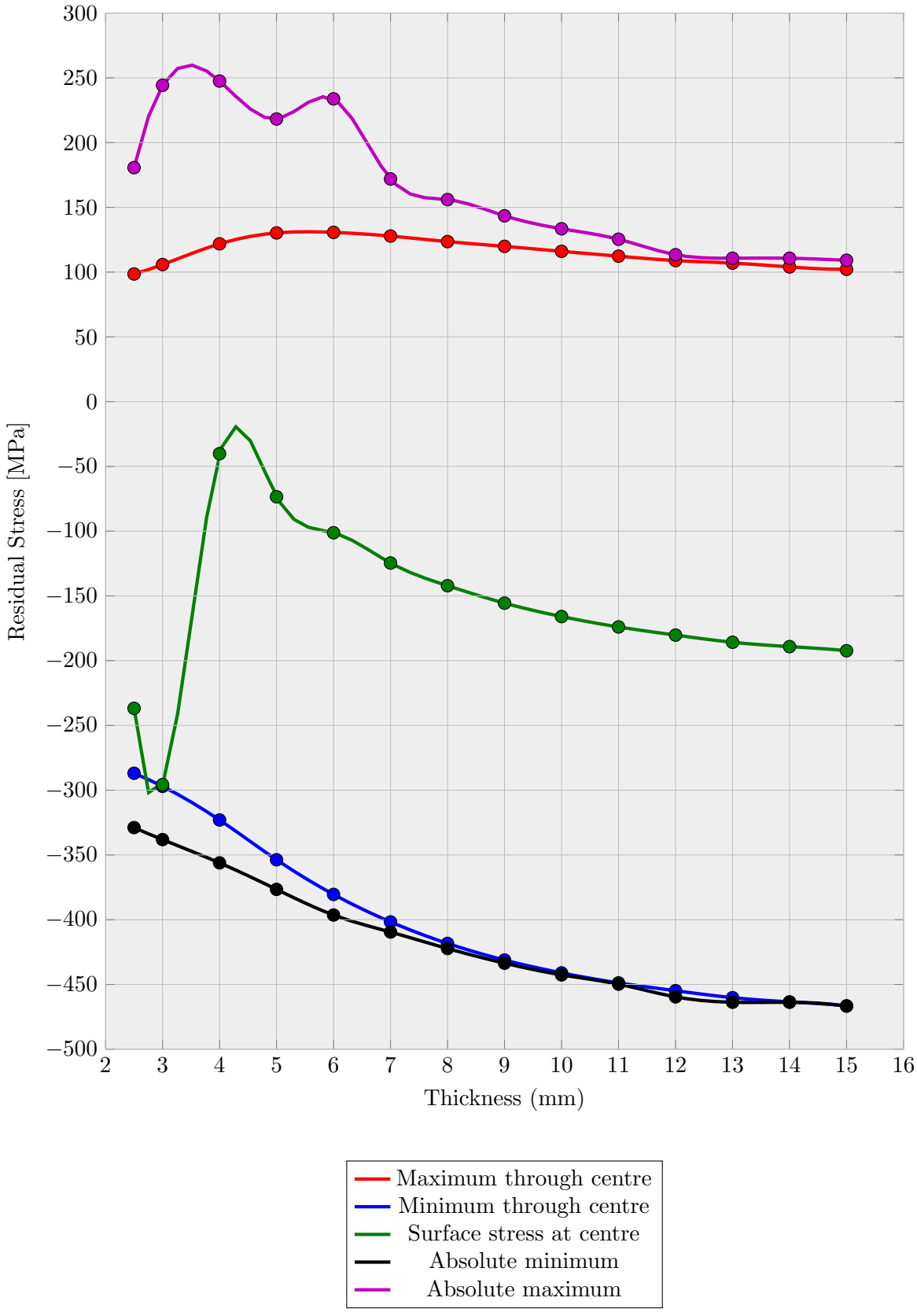

Figure 4.7: *Variation of some critical stresses with respect to thickness – x direction*

3 Effect of Size of Peened Area

Another geometric parameter that can be varied and has an effect on the residual stress field is the size of the peened square. Before commencing with the study, a question naturally arises. Does the residual stress field vary with the absolute size of the peened area, or with the relative size? In other words, do a samples with different peened areas but identical relative peened areas, have the same residual stress field? To investigate this, a study was done on a sample whose scale was reduced by half, except in the z direction (the thickness was kept the same).

The comparison between the original sample and the reduced sample is depicted in Figure 4.8. It is clear that the residual stress fields are not the same in both cases. In the reduced model, the stresses within the peened region are less compressive than in the the full-sized model. The maximum tensile stress is also much lower in the reduced model. The only similarity between the two is the pattern of the residual stress field; the stress values at equivalent locations are disparate. The conclusion is that the residual stresses due to peened area are not independent of sample size. Thus, the independent variable cannot be defined as the percentage of total area that is peened, but rather as the absolute area at a fixed thickness and sample size.

A number of models were created with square peened areas of varying size. All the other variables, including thickness and sample size, were kept the same as Sample B15. Line plots of residual stress in the x direction, through the centre of the sample are shown in Figure 4.9. Near the surface of the sample, the curves tend to shift downwards as the size of the peened region increases. However, at higher depths, the order changes and the curves tend to shift upwards as the size of peened region increases. In summary, the magnitude of the both the compressive stresses near the surface, and tensile stresses deeper in the material seem to increase with increasing size of the peened area. Beyond the peened depth, where the curve transitions to a line, the steepness of the lines varies according to the size of the peened region. The preponderant pattern governing this variation seems to be that the higher the maximum tensile stress, the steeper the curve. For example, it can clearly be seen that the model with a $5\,\text{mm}\times5\,\text{mm}$ peened square, which has the lowest tensile stress also has the least steep line. The curves with higher tensile stresses have steeper lines.

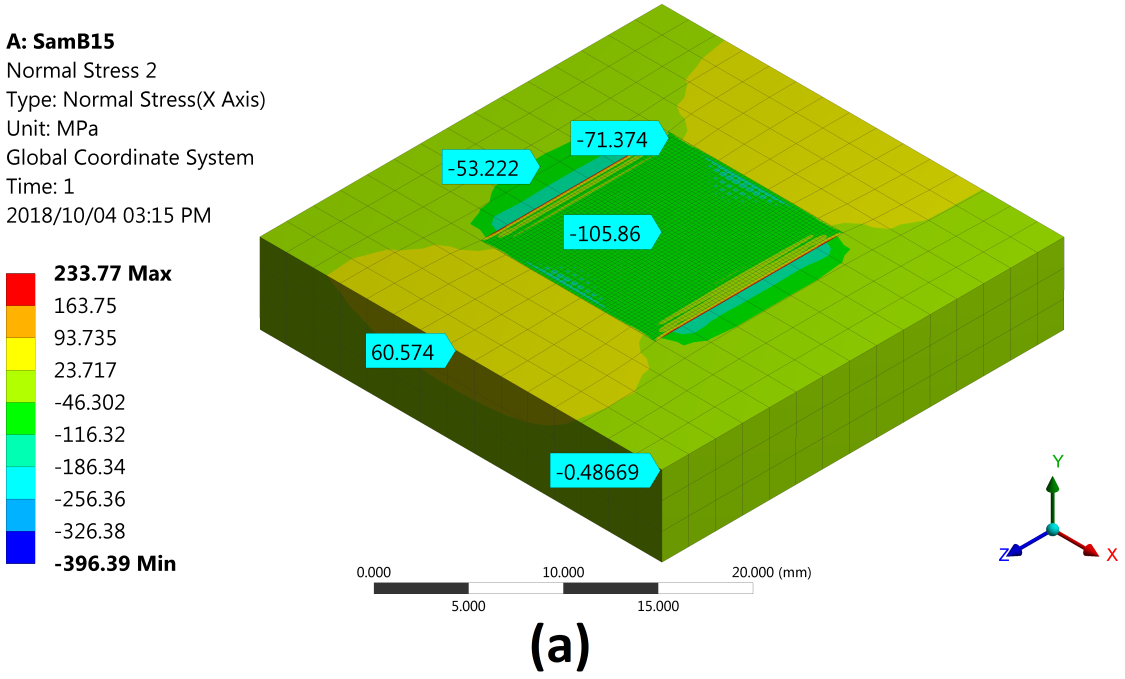

(a)

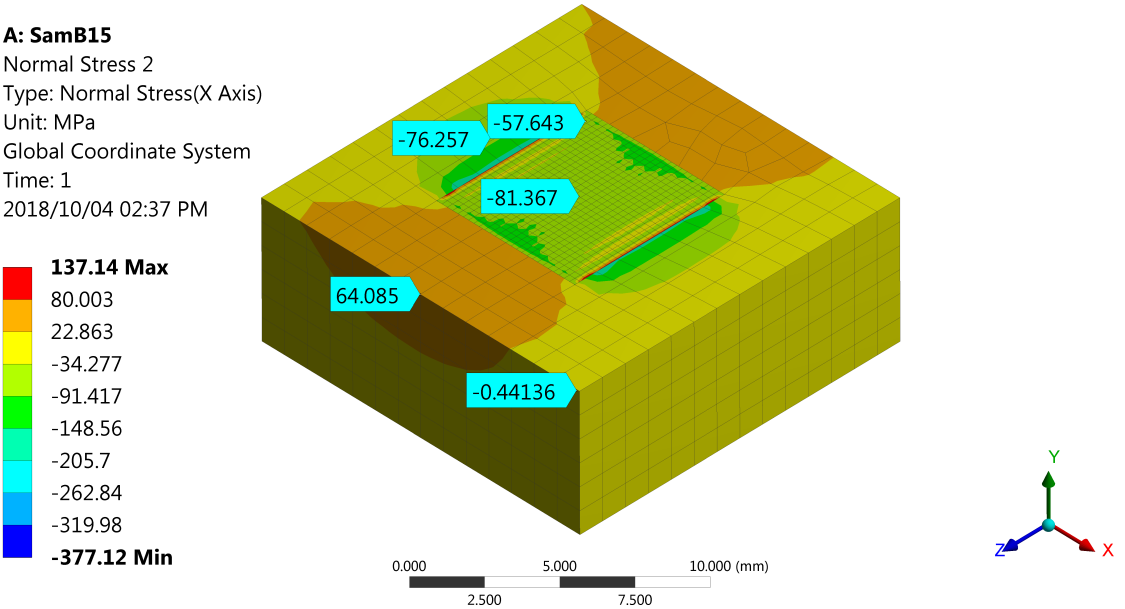

(b)

Figure 4.8: *Effect of scale on residual stresses: (a) Original size, (b) Half size*

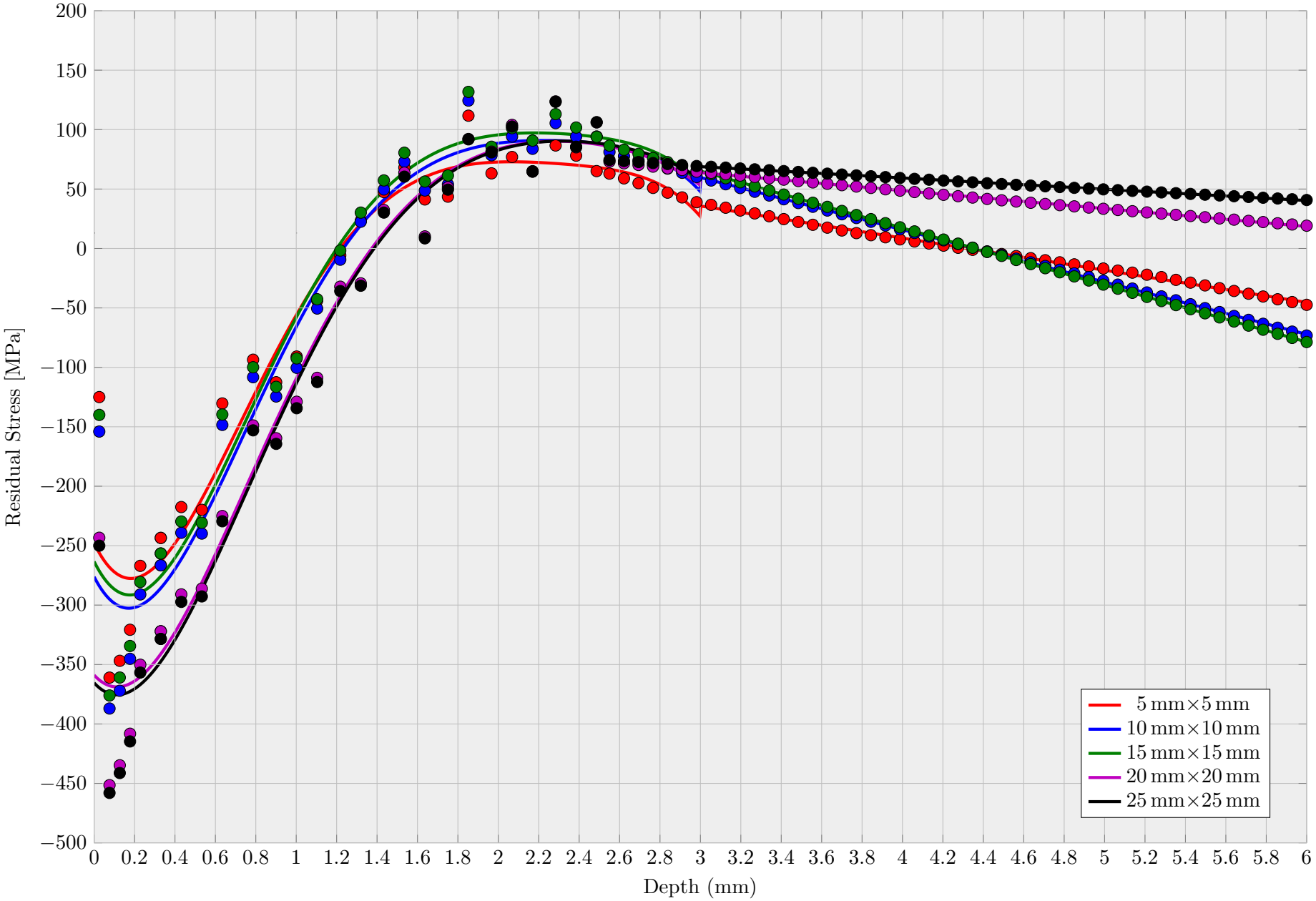

Figure 4.9: *Residual stress distributions in samples with varying peened squares – x direction*

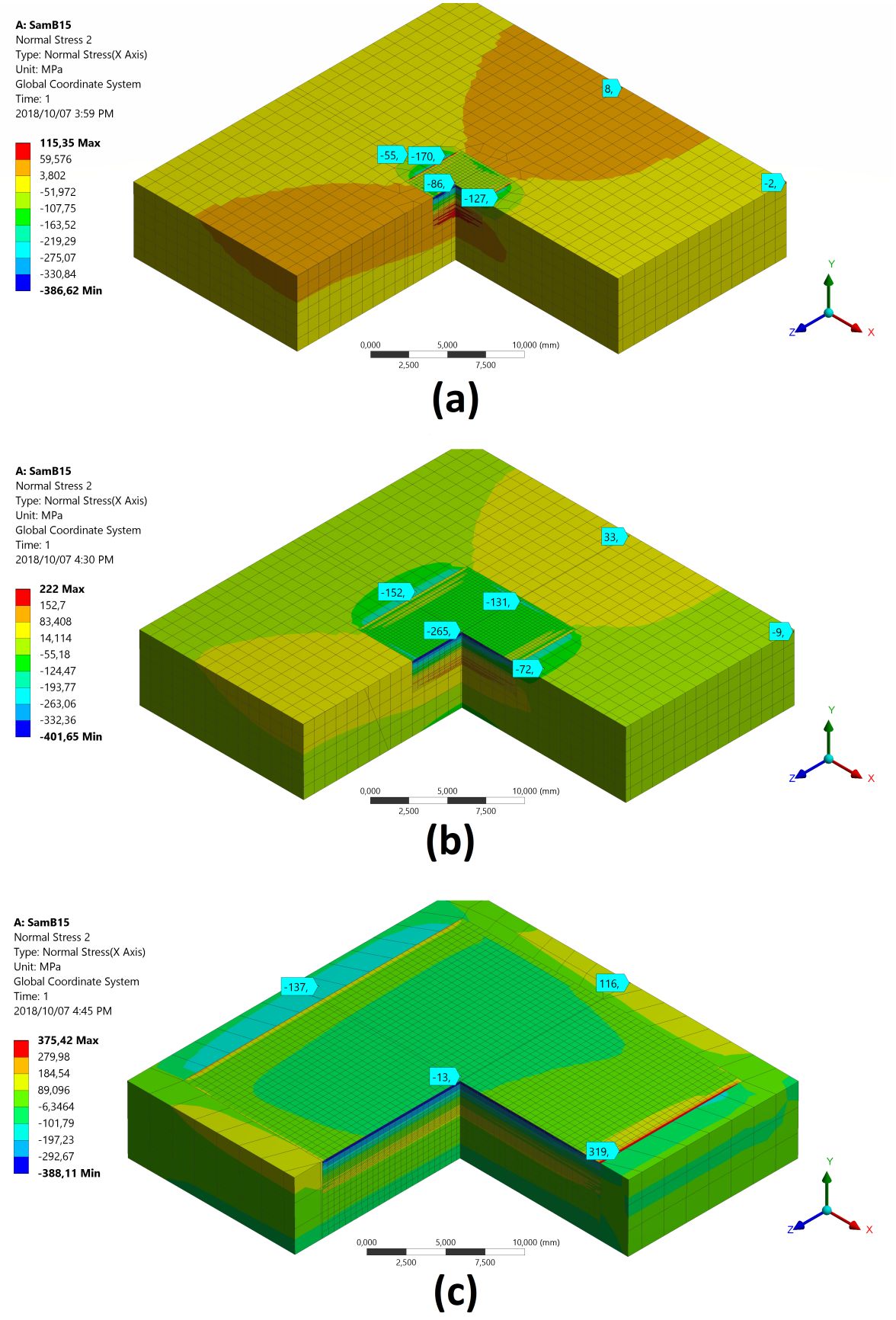

Figure 4.10: *Comparison between residual stress fields in samples with various peened areas: (a)* 5 mm×5 mm *(b)* 15 mm×15 mm *(c)* 25 mm×25 mm

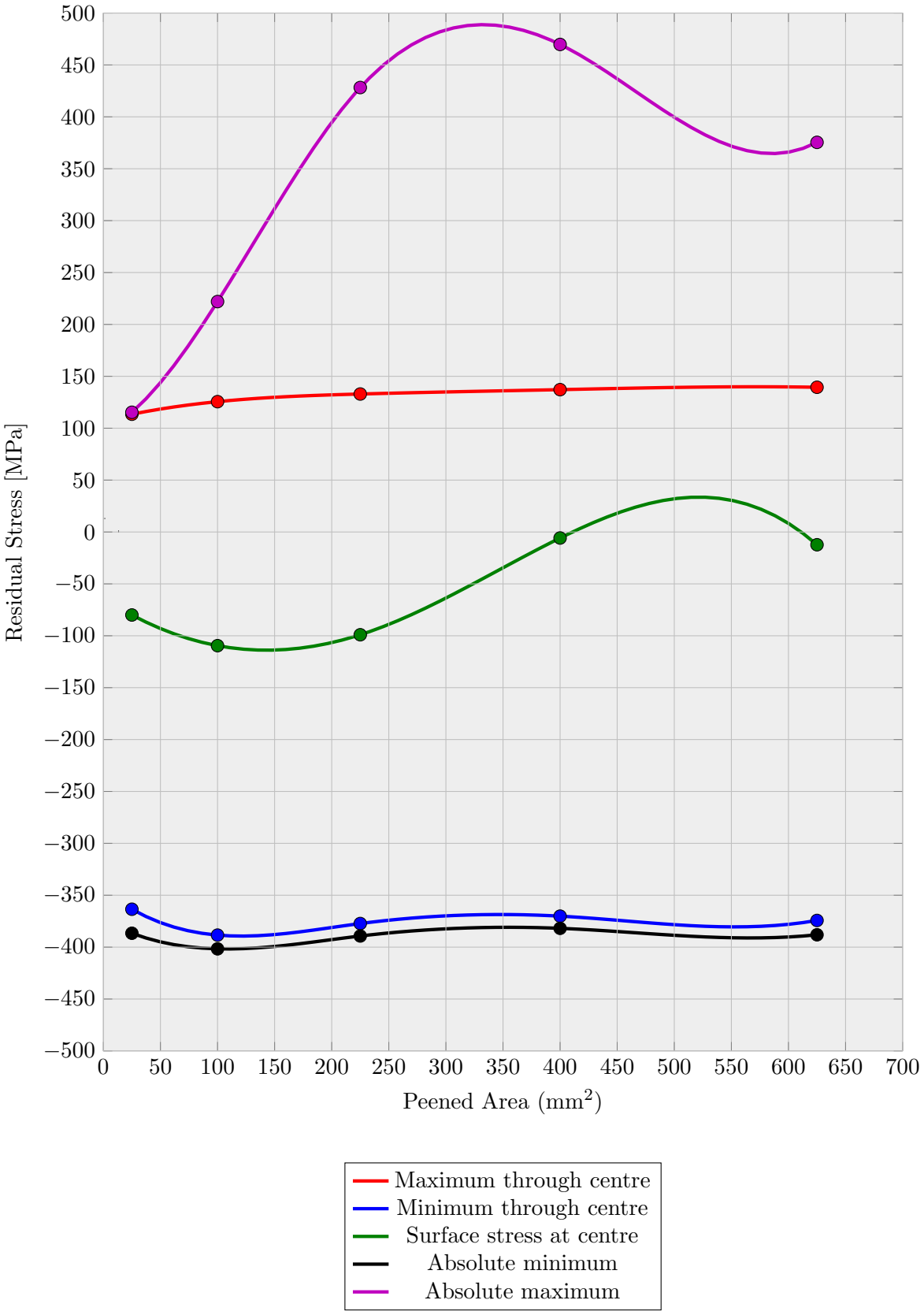

Figure 4.11: *Variation of some critical stresses with respect to peened area – x direction*

4 Effect of Sample Size

Figure 4.8 shows that for a given thickness, the variation of residual stresses cannot be studied with respect to relative size of the peened zone. Instead, the study had to be conducted keeping the sample size and thickness fixed at a certain value and varying only the size of the peened area. This means that the variation of residual stresses with respect to sample size can be studied separately from the size of the peened area.

To conduct this study, the size of Sample B15 was varied, while retaining all other parameters as the same. Figure 4.12 shows the residual stress distributions, in the x direction, through the centres of the various samples (The location from which the original measurements were taken in Sample B15). It should be noted that the sizes listed in the legend refer to the full size of the model, whereas the FEM was applied to a quarter of the model due to the symmetry condition. Thus, a sample size of $30\,\text{mm}\times30\,\text{mm}$ corresponds to a quarter-model size of $15\,\text{mm}\times15\,\text{mm}$.

The residual stress distribution through the centre does not change much as sample size increases. However, it can clearly be seen that the stresses within the peened depth generally decrease with increasing sample size. Beyond the peened depth, the linear portion of the curve generally becomes less steep with increasing sample size. Also, the change in the residual stress profile becomes less marked as sample size increases, which seems to indicate that the results converge to a residual stress distribution in a theoretically infinite sample.

Contour plots of the residual stress fields in the x direction are depicted in Figure 4.13. Once again, it should be borne in mind that the models are quarter-sized models, so the features should be viewed as symmetric over two axes. As the sample becomes larger, the stresses at the extremities of the sample tend towards zero. This is expected because of Saint Venant's Principle. Once again the tendency for the results to converge is evident from the different samples.

Figure 4.14 shows the variation of five location-specific stresses in the x direction, with respect to the area of the sample. The most obviously apparent feature is that all the stresses seem to level off, after which the change in stresses becomes minimal with increasing sample size. This confirms the observations made above that the results seem to be converging. The maximum stress through the centre changes the least and seems to reach a steady value most quickly. The absolute maximum changes the most with increasing sample size, though it does eventually settle down towards a steady value.

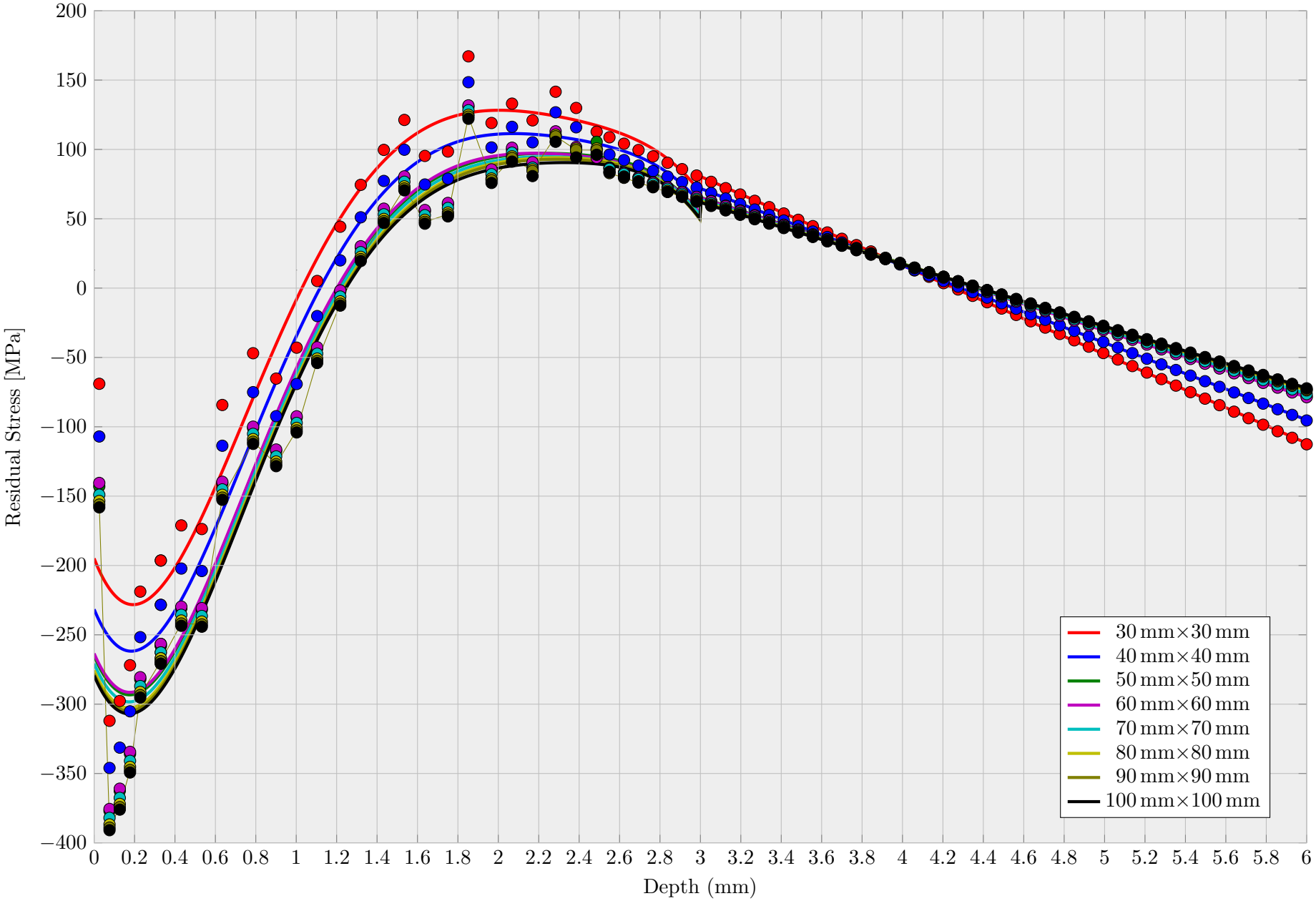

Figure 4.12: *Residual stress distributions in various sample sizes – x direction*

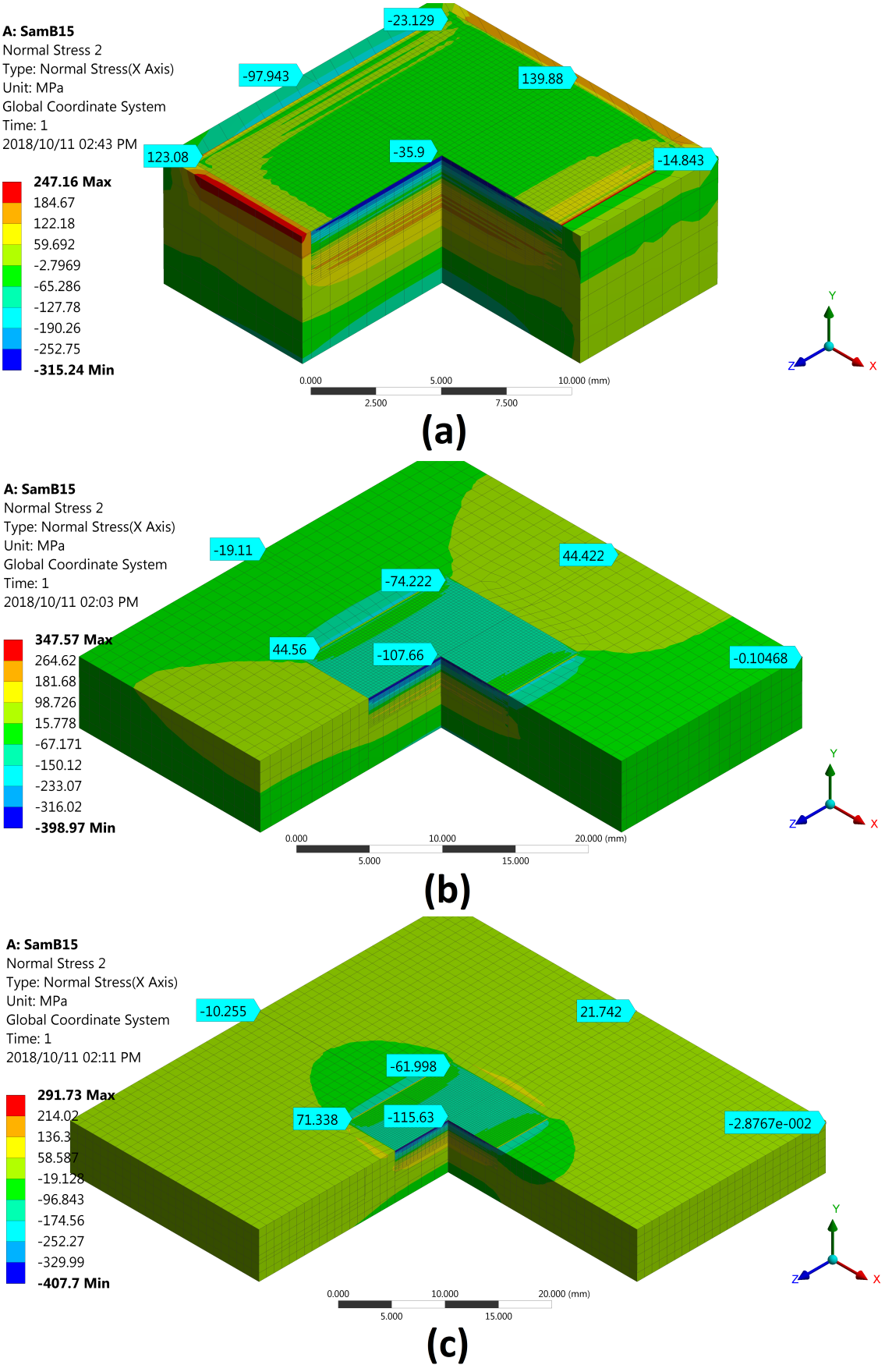

Figure 4.13: *Comparison between residual stress fields in samples of various sizes: (a)* 30 mm×30 mm *(b)* 70 mm×70 mm *(c)* 100 mm×100 mm

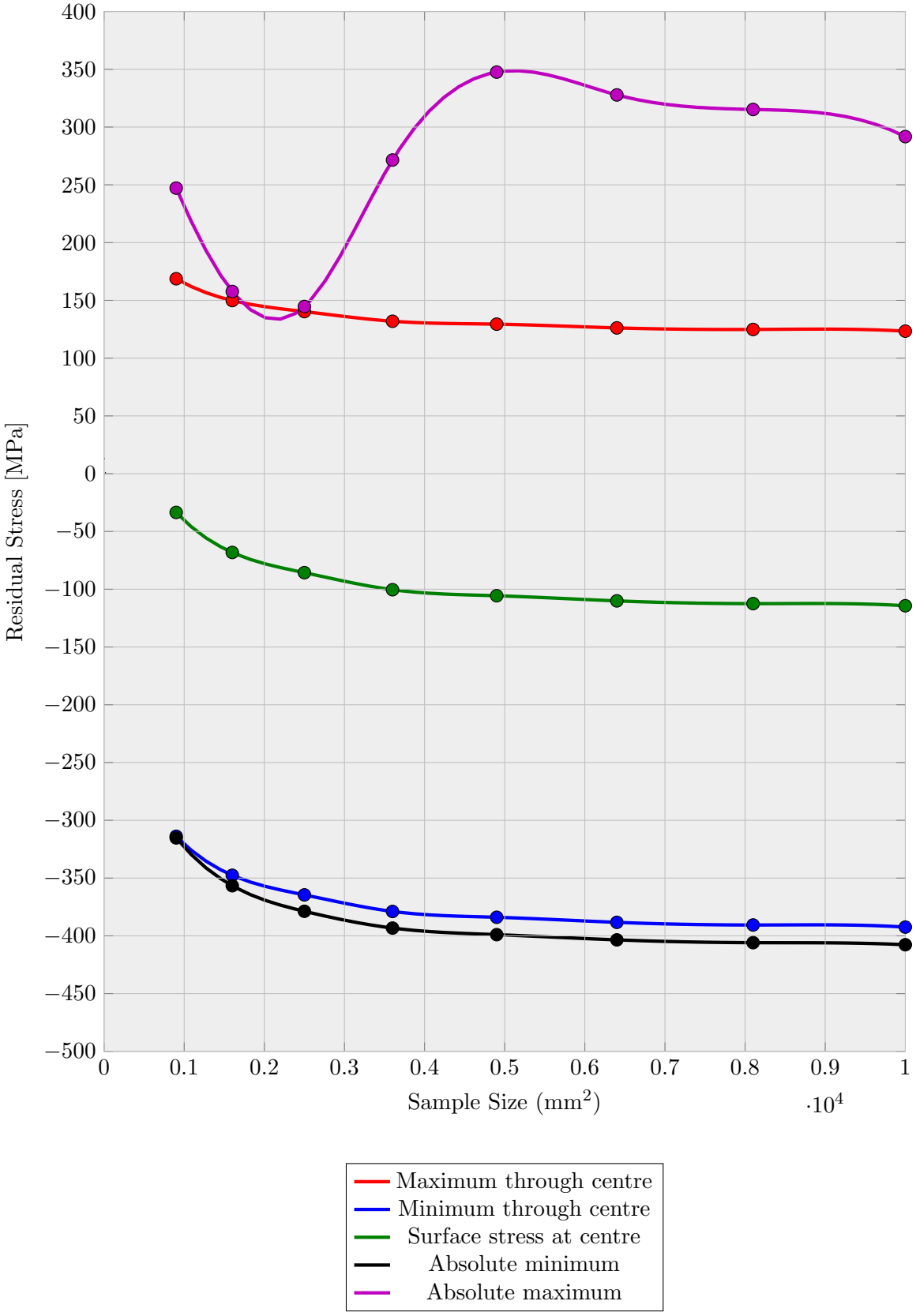

Figure 4.14: *Variation of some critical stresses with respect to sample size area – x direction*

5 Discussion

The aim of this chapter was to study the effect of thickness, size, and peened area of cuboid samples, on residual stresses due to LSP. Given the residual stresses in a cuboid sample, like Sample B15, a question that naturally arises is, "What would the residual stresses be like if the thickness, or size, or peened area are changed"? This question motivated the study in this chapter. The study was performed using only FEM models of cuboid samples and eigenstrain data measured from an actual sample. Because the data was predicted and not measured, it is subject to some uncertainty regarding the veracity of the results.

A critical assumption made in the study, was that the geometric parameters studied did not have any effect on the eigenstrains. This assumption allows one to apply the same eigenstrains to the different models and hold that these are the results that would occur in a physically identical sample subjected to the same peening process as Sample B15.

This assumption of insensitivity of eigenstrains to geometry is based on what is termed in the literature as "Principle of Transferability of Eigenstrain" (See section 9 of chapter 2). Numerous studies have been conducted to confirm this principle. However, a study by De Wald[23] has found that thickness does affect eigenstrains to an extent. De Wald attributes this to the effect of thickness on attenuation of the shock wave. If this is the case, then it can be hypothesised that the effect of thickness on eigenstrains is strongest in thin samples and diminishes in thicker samples. In thinner samples, shock reflection might occur, modifying the eigenstrains (See subsection 9.1 of chapter 2).

Considering the above, it may be that some or all of the results of the thickness study do not represent residual stresses arising from the same LSP process. Regardless, what the results of the thickness study definitely do represent, is residual stresses arising from the same eigenstrain distribution. The dispute is whether that eigenstrain really is the same eigenstrain that would occur in a sample subjected to the pertinent LSP process. Given De Wald's finding, what can definitely be stated is that for thicknesses that are close in magnitude to the depth of peening, the results would be spurious due to shock reflection. In any case, the method used cannot predict residual stresses in thicknesses smaller than the peened depth.

Regarding the effect of other parameters on eigenstrain, it does not seem likely that the size would affect the eigenstrains in the current context, as the size is much larger than the peening spot size and also does not affect the attenuation of the shock wave. The change in size occurs transversely to the direction of propagation of the shock wave. Similar sentiments apply to the peened area.

Line plots of residual stress through the centres of the cuboid samples were extracted for each parameter. The main information gleaned from this, is the behaviour of the stresses beyond the peened zone. With increasing thickness, the slopes of the lines beyond the peened region decrease. This is expected because the stresses beyond the peened region are essentially balancing forces to ensure that the net stress over the cross-section is zero. Increasing the thickness increases the cross section available to balance out the compressive stresses near the surface. The same effect is seen with increasing size.

The variation of five critical stresses with respect to each of the parameters was studied. A common feature between the parameters is the fact that the stresses seem to vary much with small values of the parameters, but seem to reach steady values, as the parameter size increases. This seems to indicate that geometry only affects the residual stresses in cuboid samples with relatively small dimensions compared to the depth of peening. In samples that are larger overall, the geometry does not have a significant impact on the residual stresses. The surface stress is compressive for all parameter variations.

6 Conclusions

- The effect of thickness, size and peened area of cuboid peened samples on residual stresses arising from a specific eigenstrain distribution, were studied.
- The results represent the effect of the aforementioned parameters on LSP-induced residual stresses, if the assumption of insensitivity of eigenstrain to geometry holds.
- In samples that are relatively thin compared to the depth of peening, the thickness of the sample may affect the eigenstrain distribution, due to shock reflection. Thus, the results for thin samples may not be accurate.
- It is unlikely that the size of the sample and size of the peened region affect the eigenstrain distributions induced by LSP.
- Increasing thickness or size of sample causes a decrease in the slope of the line beyond the peened region.
- The effect of geometry on residual stresses is more apparent in smaller samples than larger samples.
- The surface stress is always compressive.

Chapter 5 Effect of Curvilinear Geometric Parameters on Residual Stresses in Cylinders and Spheres

This chapter deals with the third objective. It explores the relationships between curvature and residual stresses induced by LSP, by studying residual stresses in spheres and cylinders. This study hinges on the Principle of Transferability of Eigenstrain. Eigenstrains that were extracted from Sample B15 are used to predict the residual stresses in spheres and cylinders subjected to the same peening process as Sample B15. The relationships between geometric parameters and residual stresses arising from LSP are then studied.

1 Residual Stresses in Spheres

This section studies residual stresses in spheres of various radii.

1.1 Base Model

Unlike chapter 4, there was no physical base model of the sphere. Instead, a CAD model of the sphere was created and the eigenstrain distribution from Sample B15 was imposed on the model to create a virtual peened model of the sphere. The CAD model of the sphere is shown in Figure 5.1. The diameter of the base model is 15mm. The study was conducted for spheres whose entire surface was peened. With the entire surface peened, it was noted that the problem was symmetric about the $x-y$, $x-z$, and $y-z$ planes. The FEM model of the sphere was thus reduced to one-eighth of its original size, as shown in Figure 5.2. The sphere was split into layers near the surface, corresponding to the depths of known eigenstrains. The thickness of the layers has to be consistent throughout the sphere. In this instance, the thickness of the layers created corresponded to the layers created for the analysis of Sample B15.

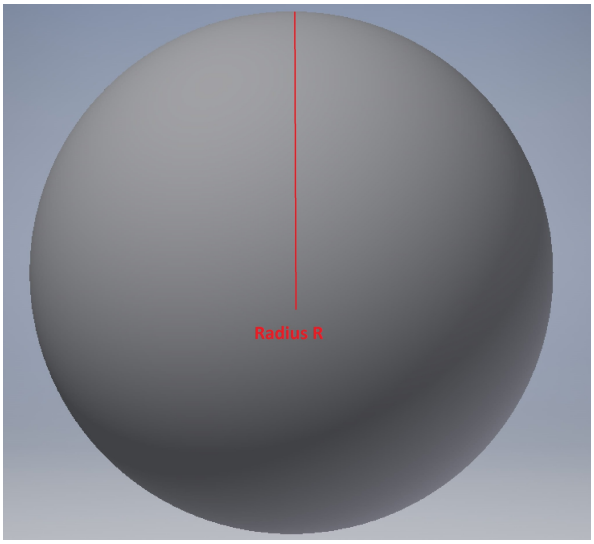

Figure 5.1: *Base CAD model of the sphere*

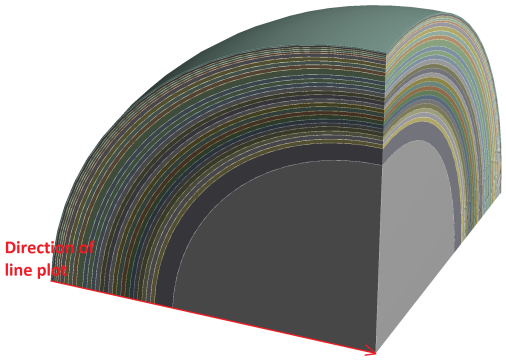

Figure 5.2: *FEM model of the base sphere*

An important consideration in conducting the eigenstrain analysis for curved objects, is the co-ordinate system used to introduce the eigenstrains. For a flat plate, it is easy to see that the appropriate co-ordinate system is Cartesian. However, for a curved object, introducing the eigenstrains in the directions of the Cartesian system leads to spurious results. The peening always takes place normal to the surface, and so a co-ordinate system with a consistent normal over the entire peened surface is required.

For a sphere, the correct co-ordinate system is obviously the spherical co-ordinate system. Figure 5.3 compares the Cartesian co-ordinate system used in the cuboid samples, to the spherical co-ordinate system used in spherical models. In the spherical co-ordinate system, the R axis is normal to the surface, which corresponds to the z axis in the Cartesian co-ordinate system. The x and y axes in the Cartesian system correspond to the θ and ϕ co-ordinates in the spherical system. The x axis is in the step direction and y in the scan direction (Refer to Figure 3.2 of chapter 3, Figure 3.1). Due to the uniformity of the curvature of the sphere, the θ and ϕ axes are indistinguishable from each other in terms of the shape

of the sphere. Thus, it does not matter which of these axes is chosen as the step or scan direction. What is important is that the z direction corresponds to the R axis, which is normal to the surface of the sphere.

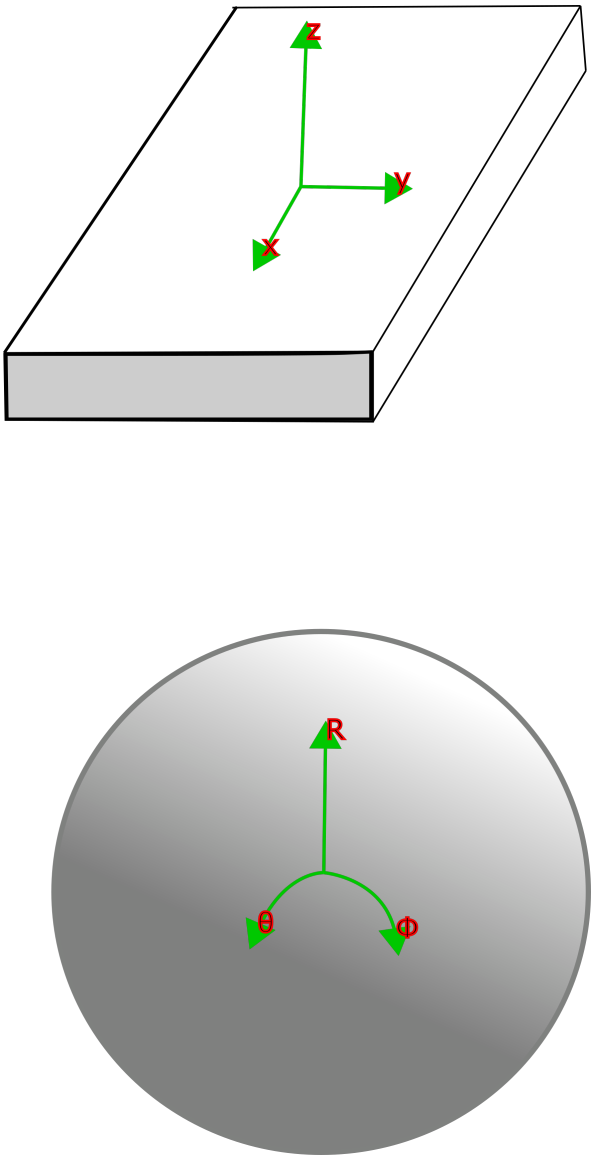

Figure 5.3: *Comparing spherical co-ordinate system to spherical*

Having established the correct co-ordinate system, the next step was to ensure that eigen-strains (which were imposed as orthotropic thermal coefficients of expansion under a temperature variation of 1°C) were imposed using the spherical co-ordinate system in ANSYS, rather than the default Cartesian global co-ordinate system. Firstly, a named selection was created, which encompassed all parts of the model. This named selection was dubbed "Everything". An APDL command snippet was then included under the analysis branch (Static Structural), which performs the following tasks:

1. Enter the preprocessing environment.

2. Select the named selection “Everything”.
3. Create a local co-ordinate system with ‘co-ordinate system type’ = 2 (spherical or spheroidal system).
4. Modify all selected elements to have the above co-ordinate system as its element co-ordinate system (ESYS).
5. Select all bodies.
6. Enter the Solution processor.

The origin of the spherical system was made to coincide with the centre of the sphere. This is important to ensure the eigenstrains in the θ and ϕ directions are applied tangential to the surface of the sphere.

Figure 5.4 depicts the residual stress field in the base sample after applying the eigenstrains from Sample B15. There is a noticeable symmetry between the stresses in the $x-z$ and $y-z$ planes (In the global co-ordinate system depicted). However, this symmetry is not shared with the $x-y$ plane. The stresses along the global z axis are slightly different to the stresses along other directions. This is surprising, as spheres are radially symmetric and the eigenstrain distribution is applied uniformly throughout the sphere. The stresses along any radial direction of the sphere should not be distinguishable from the stresses along any other radial direction. Perhaps this anomaly is due to discretisation errors and the mesh itself not being symmetric.

Besides the above issue, the results are as expected. The stresses are compressive near the surface and gradually become tensile. The maximum tensile stresses occur in the core of the sphere. The maximum compressive stresses occur along the global z axis. The maximum depth of compression also occurs along the global z axis.

1.2 Varying Radius

Residual stress distributions for spheres with different diameters are shown in Figure 5.5. The line along which the stresses were extracted is shown in Figure 5.2 as a red line. The shapes of the distributions are similar to those found in section 2 of chapter 4 for cuboid samples of varying thickness. As the radius of the sphere increases, the curves tend to shift downward, increasing the maximum compressive residual stress and decreasing the maximum tensile residual stress. Increasing the radius also has the effect of decreasing the slope of the stresses beyond the peened zone.

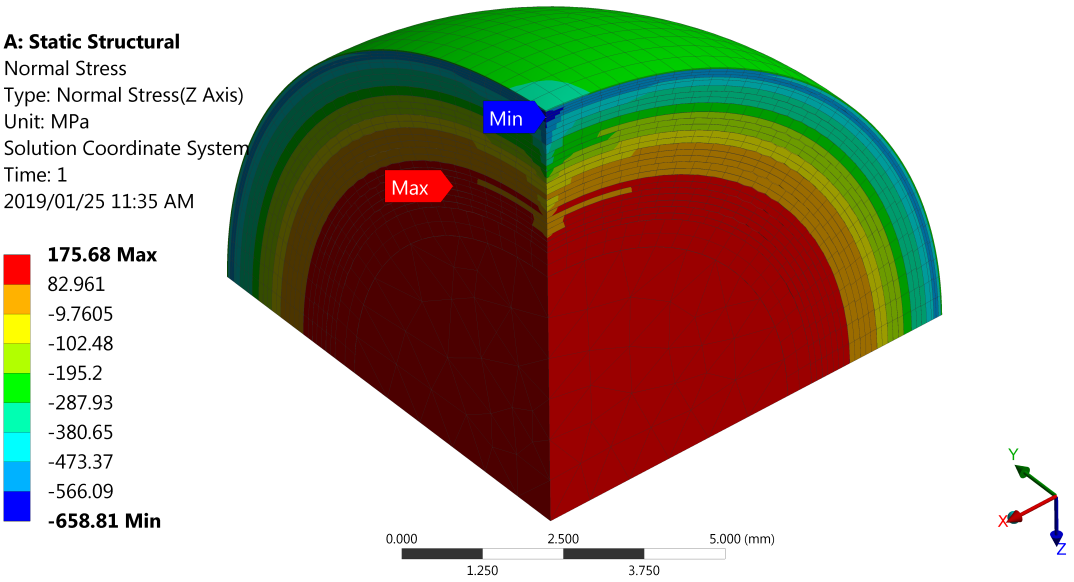

Figure 5.4: *Residual stresses in base sphere*

Beyond the peened zone, the curves are not completely linear. For each sphere diameter, the stresses beyond the peened zone tend to converge to specific values. It should be borne in mind that due to the symmetry of the problem, the residual stress distributions beyond the centres of the spheres mirror the curves of Figure 5.5. This may be the reason for the stress distributions not continuing in a linear fashion through the centre of the sphere. By tapering off, the distributions transition smoothly across the axes of symmetry.

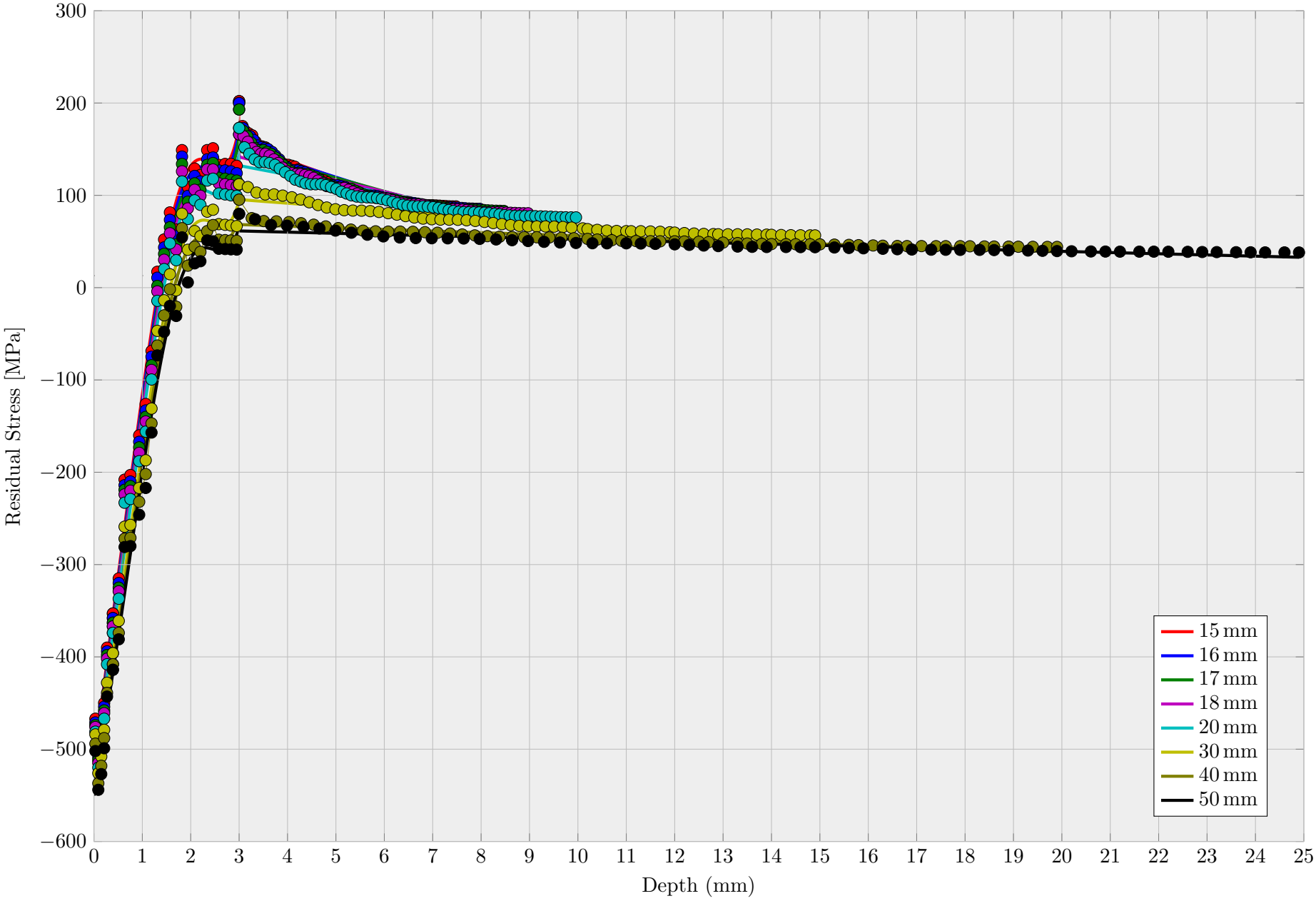

Figure 5.5: *Residual stress distributions in spheres of varying radius – x direction*

Figure 5.6 shows the variation of different stresses with respect to the diameter of the sphere. The common feature between all of these stresses is the fact that they all decrease fairly rapidly with increasing radius in small spheres. In larger spheres, increasing the diameter does not seem to have a great effect on any of the stresses. The stresses tend to converge to specific values.

The absolute maximum stress mostly seems to occur through the centre of the sample, particularly for large spheres. The values of the absolute maximum tensile stresses along the line plot of the sphere range from 175 MPa for small radii, to just over 30 MPa for large radii. This is a decrease of around 145 MPa for a difference in diameter of 85 mm. The maximum along the line plot starts at 150MPa, also converging towards a value of 30 MPa. The surface stress through the centre of the model, ranges from -240 MPa to just above -290 MPa, a difference of approximately 50 MPa.

The Absolute minimum (or maximum compressive) stresses do not occur along the line plot, and are of a much higher magnitude than the maximum compressive stress along the line plot. The curve for absolute minimum declines and reaches a minimum at a diameter of 40 mm before increasing slightly and reaching a plateau. The curve for the minimum along the line plot, on the other hand, declines steadily. This means that the magnitude of the absolute maximum compressive stress generally decreases, while the absolute maximum compressive stress along the line plot generally increases in magnitude. The absolute maximum compressive residual stress ranges between 700 MPa and 630 MPa. The minimum stress along the line plot ranges from around 500 MPa to 560 MPa.

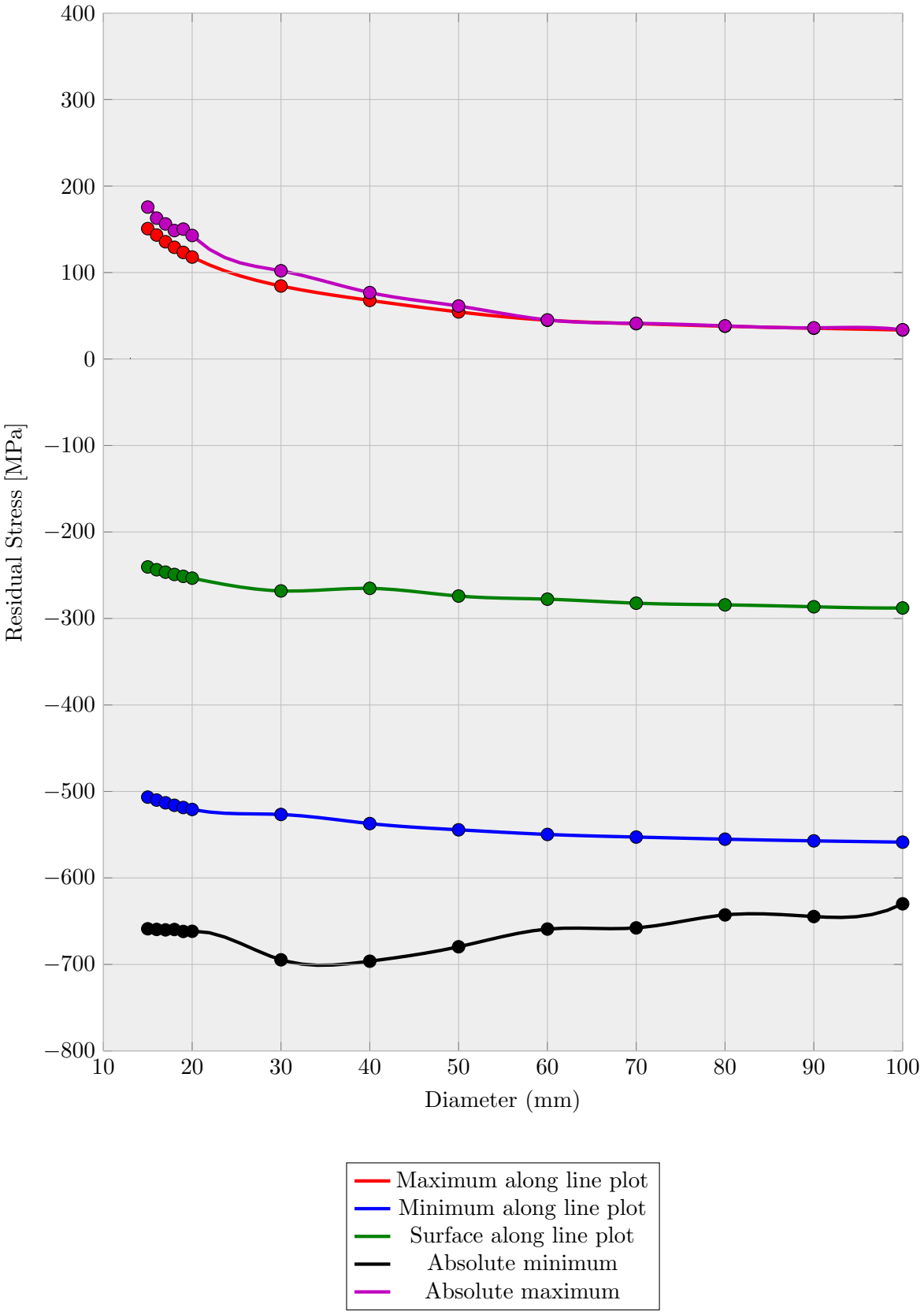

Figure 5.6: *Variation of some critical stresses with respect to diameter of sphere – x direction*

2 Residual Stresses in Cylinders

This section studies residual stresses in cylinders of various radii and lengths.

2.1 Base Model

A base model of the cylinder was created, with a diameter of 10mm and length of 10mm, as shown in Figure 5.7. The study was conducted for a cylinder with the entire curved surface peened. The peening on the cylinder was assumed to be in a raster pattern, as was the case for Sample B15. The step direction of peening was set as the longitudinal axis of the cylinder, while the transverse direction was set as the scan direction. The FEM model of the sphere was reduced to an eighth of the original size by utilising 3 planes of symmetry ($x-y$, $x-z$, and $y-z$). The FEM model is shown in Figure 5.8, where the layers in the direction of peening can be seen.

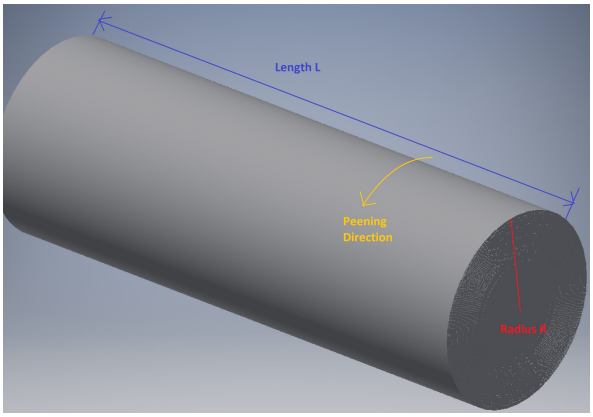

Figure 5.7: *Base CAD model of the cylinder*

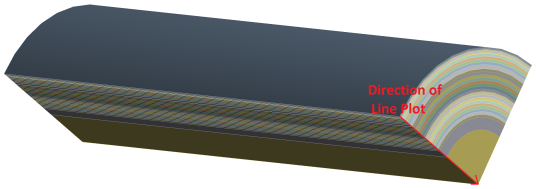

Figure 5.8: *FEM model of the base cylinder*

For cylinders, the appropriate co-ordinate system to introduce the eigenstrains is the cylindrical co-ordinate system. Figure 5.9 compares the Cartesian co-ordinate system used in the cuboid samples to cylindrical co-ordinate system used in cylindrical models. In the cylindrical system, the R axis is normal to the curved surface of the cylinder. This corresponds to the z axis in the Cartesian co-ordinate system. The z axis is in the step direction of

peening and corresponds to the x axis in the Cartesian system. The θ axis is in the scan direction of peening and corresponds to the y axis in the Cartesian system.

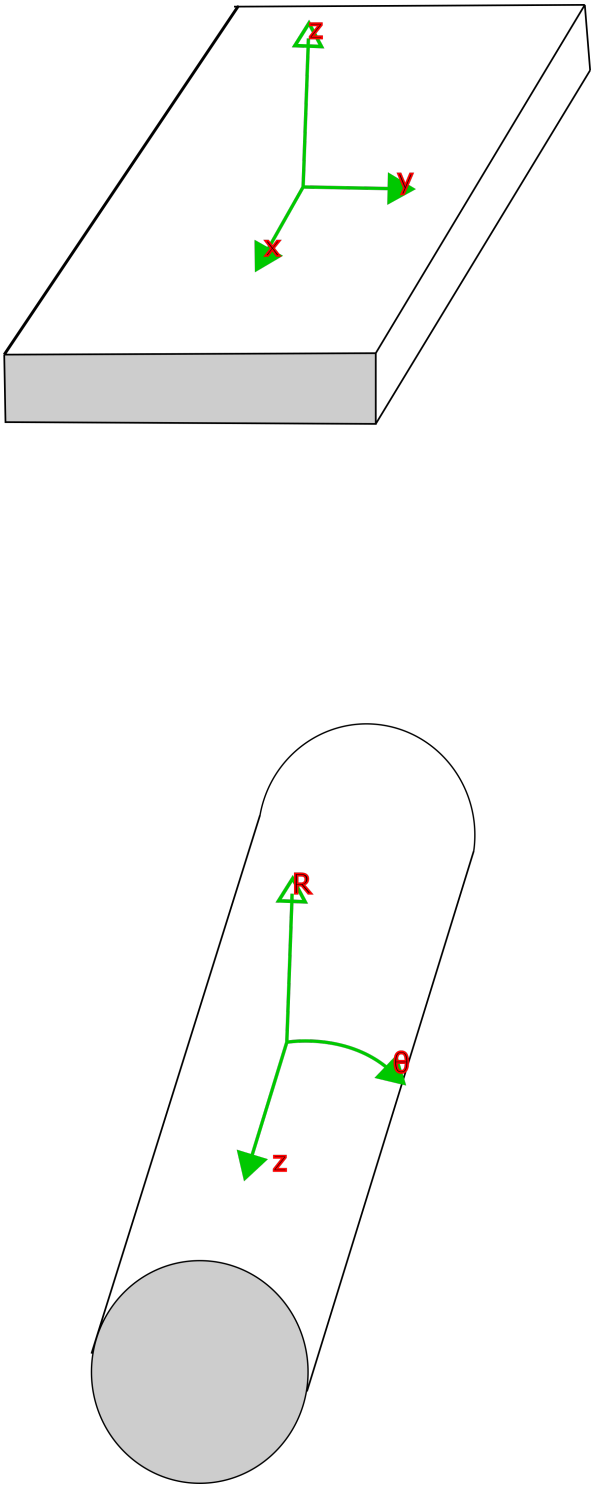

Figure 5.9: *Comparing cylindrical co-ordinate system to Cartesian*

To implement the cylindrical co-ordinate system, a local cylindrical co-ordinate system was created under the co-ordinate systems branch. The co-ordinate systems branch allows the creation of Cartesian and cylindrical co-ordinate systems. The co-ordinate system was given

an ID to be referenced in the APDL code snippet. The origin of the co-ordinate system was placed at the centre of the cylinder, which was an important step to ensure the eigenstrains were imposed in the correct directions. A named selection including all parts of the model was named "Everything". An APDL Commands object was placed under the analysis branch to change the element co-ordinate system to cylindrical before imposing the eigenstrains. The routine was as follows:

1. Enter the preprocessing environment.
2. Select named selection "Everything".
3. Modify all selected elements to have the local cylindrical co-ordinate system previously created.
4. Select all elements.
5. Enter solution processor.

The two parameters required to fully define a cylinder are radius and length. The variation of residual stress with each of these parameters was studied, keeping the other parameter constant.

Figure 5.10 depicts the residual stress field in the base cylinder after applying the eigenstrains from Sample B15. It should be borne in mind that the front cross section shown in the image is actually the cross section through the centre of the cylinder. The residual stresses vary across the length of the cylinder. While the stresses near the surface are strongly compressive towards the centre of the sample, they become less compressive towards the ends of the cylinder. The surface stresses actually become tensile towards the ends of the cylinder. On the other hand, the tensile stresses in the core of the cylinder become less tensile towards the ends of the cylinder.

The maximum compressive stress occurs through the centre of the cylinder. The maximum tensile stress occurs at the surface near the end of the cylinder.

2.2 Varying Radius

Residual stress distributions for cylinders with different diameters are shown in Figure 5.11. The line along which the stresses were extracted is shown in Figure 5.8 as a red line. The length of the cylinders was kept constant at 10 mm. The shape of the distributions is similar to what was seen in Figure 5.5. Like the sphere study, it should be borne in mind that the

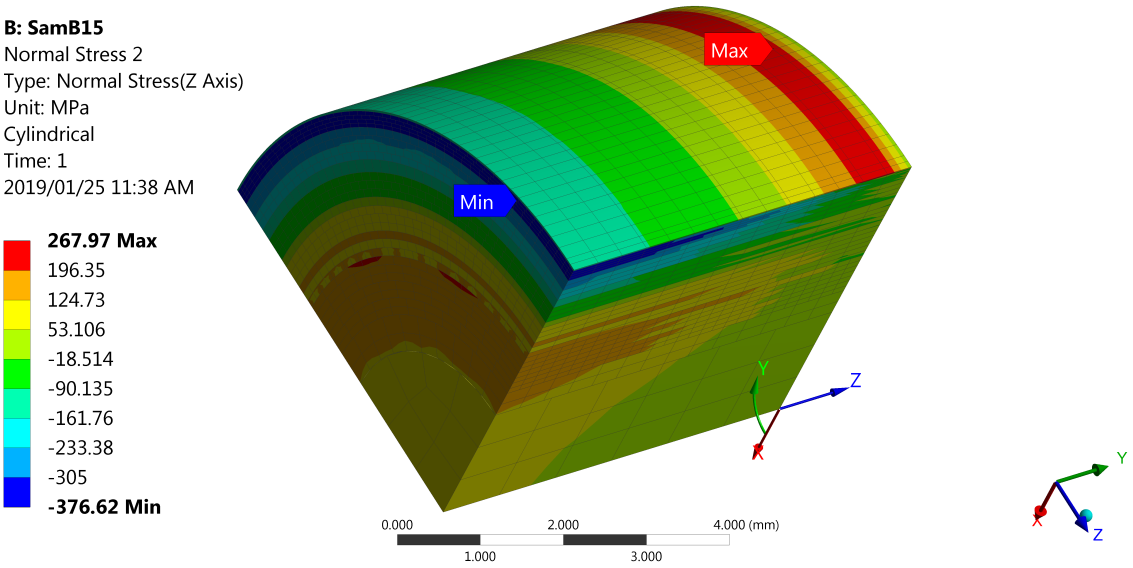

Figure 5.10: *Residual stresses in base cylinder*

symmetry of the problem means that each distribution continues beyond the centre of the cylinder, mirroring the distribution seen in Figure 5.11. The symmetry could explain why the distributions taper off, rather than continuing in a linear fashion.

Within the peened region, the stress curves do not change much at different diameters. Unlike Figure 5.5, the stresses beyond the peened region do not consistently decrease with increasing cylinder diameter. Instead, the stresses seem to decrease with increasing diameter for smaller diameters, and increase for diameters above 16 mm.

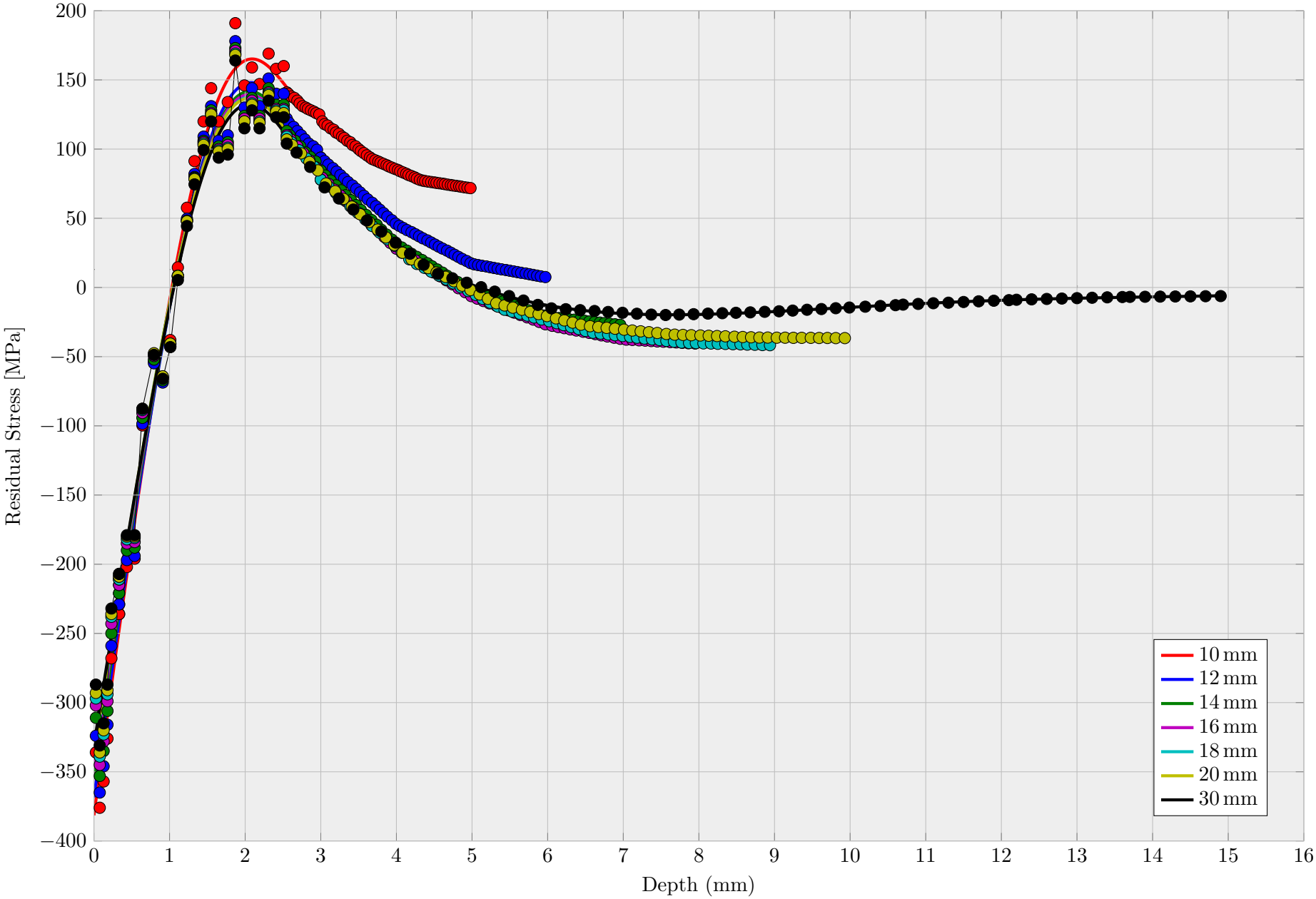

Figure 5.11: *Residual stress distributions in cylinders of varying radius – x direction*

Figure 5.12 shows the variation of different stresses with respect to the diameter of the cylinder. The most striking congruity between all the stresses, is that they all seem to be relatively constant for diameters greater than 20 mm. Increasing the diameter of the cylinder beyond 20 mm does not change these stresses very much. The stresses reach stable values and do not oscillate between different diameters.

The absolute maximum stress is very stable, even for small diameters. That being said, the general trend seems to be a slight decline in absolute maximum stress as diameter increases, beyond a diameter of 20 mm. It varies between around 270 MPa at 10 mm diameter, to 250 MPa at 50 mm – a variation of only 20 MPa. The maximum tensile stress along the line plot gradually decreases with increasing diameter. The values of the maximum tensile stresses along the line plot range from around 200 MPa for a diameter of 10 mm to around 160 MPa for diameter of 50 mm. The surface stress along the line plot increases slightly for diameters smaller than 20 mm, before stabilising to a magnitude of around 50 MPa. At a diameter of 10 mm, the surface stress is approximately 110 MPa.

The absolute minimum stress occurs along the line plot for all diameters. The magnitude of the minimum stress decreases with increasing diameter, below a diameter of 20 mm. The minimum stress stabilises to a magnitude of about 330 MPa. At 10 mm diameter, the magnitude of the minimum stress is around 380 MPa.

2.3 Varying Length

Residual stress distributions for cylinders with different lengths are shown in Figure 5.13. The diameter of the cylinders was kept constant at 10 mm. It is apparent that length does not affect the residual stresses that much. Excluding the 10 mm length, the other curves are almost identical, and indeed, some of the curves are barely visible due to the overlap between the curves. Beyond the peened region, the slopes of the graphs for lengths greater than 10 mm tend to zero. This implies that for long cylinders, the residual stresses around the core of the cylinder are almost constant.

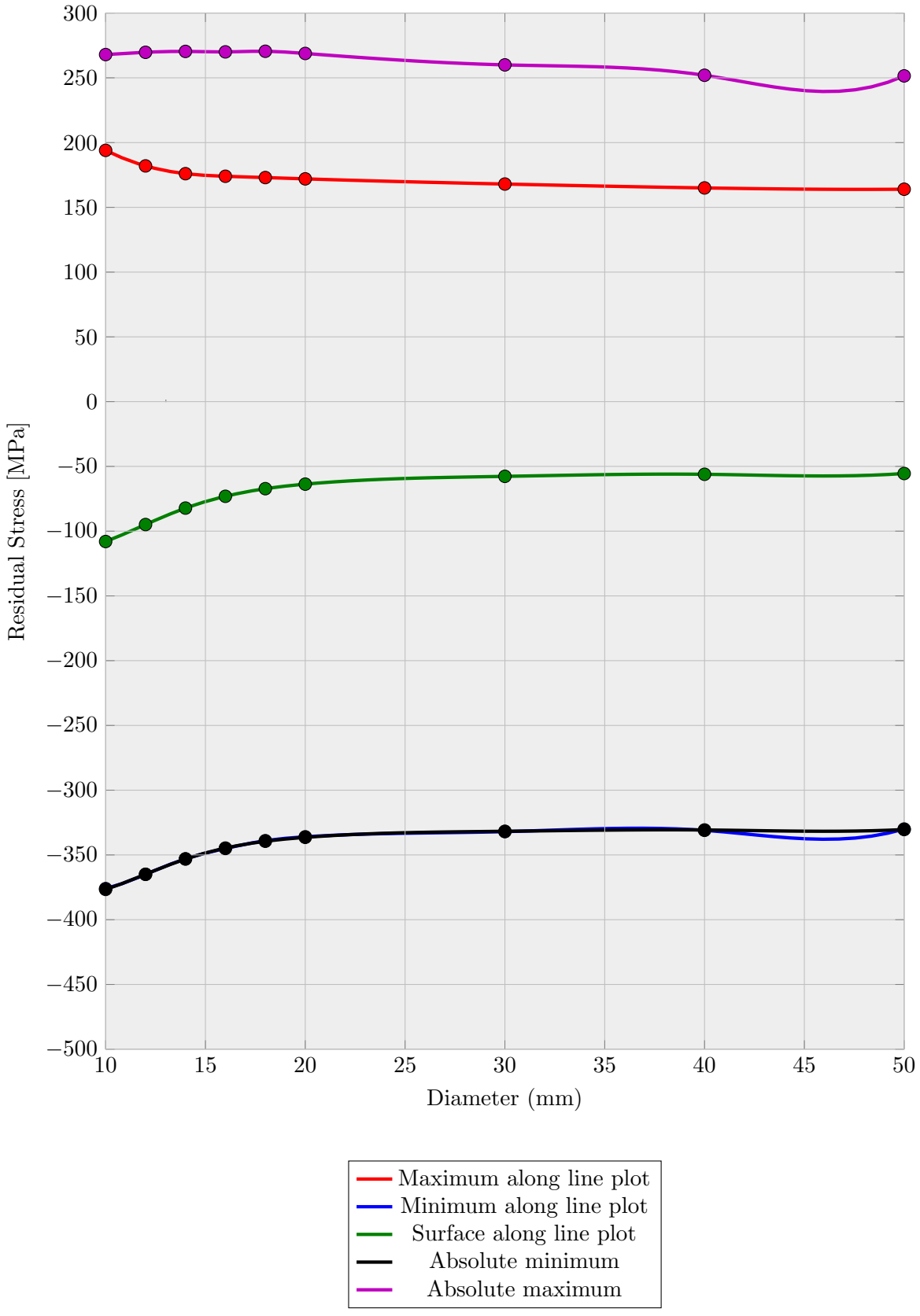

Figure 5.12: *Variation of some critical stresses with respect to diameter of cylinder – x direction*

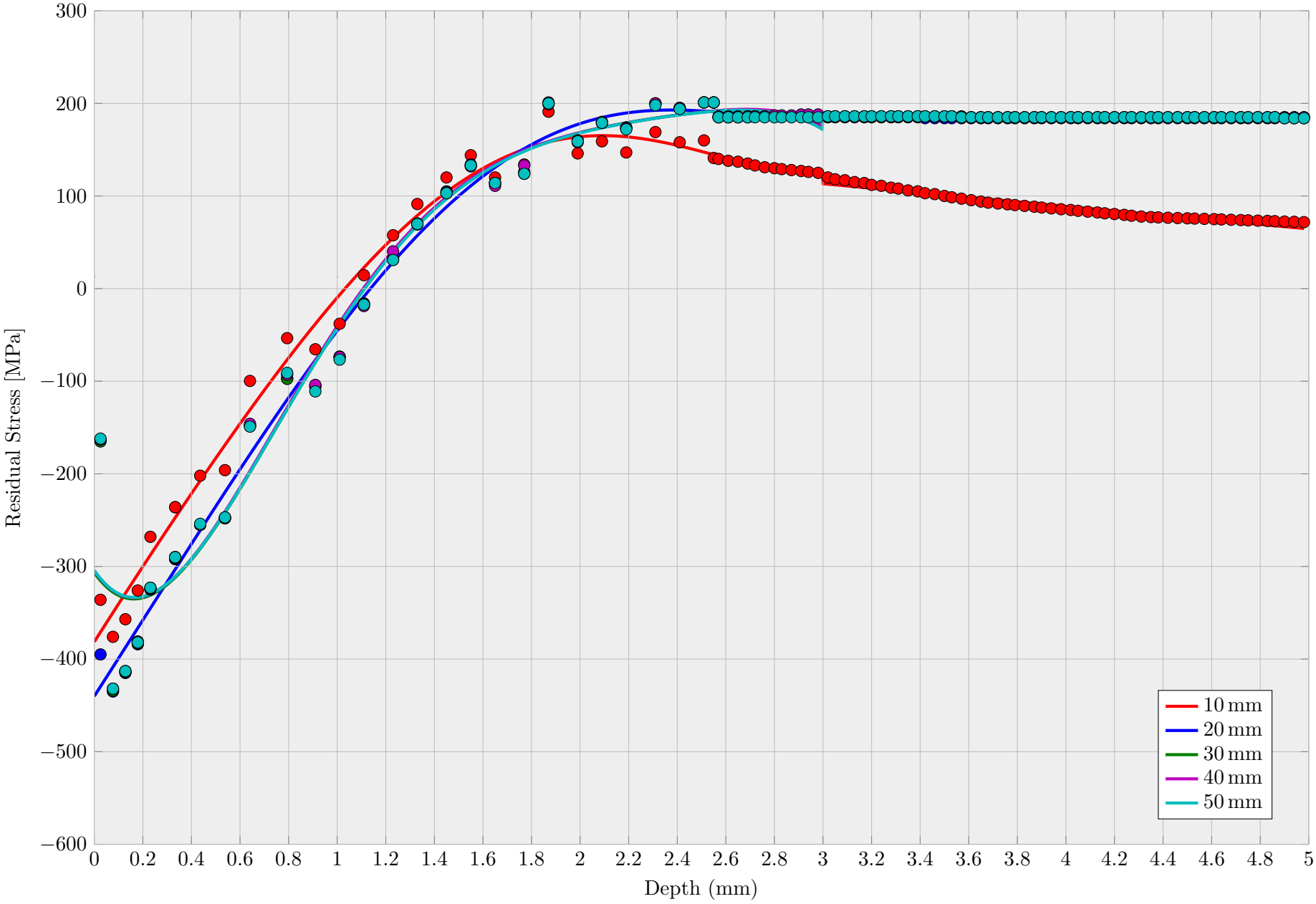

Figure 5.13: *Residual stress distributions in cylinders of varying lengths – x direction*

Figure 5.14 shows the variation of different stresses with respect to the length of the cylinder. The graphs confirm that in the current context, length does not affect the residual stresses much. Besides the surface stresses, the other stresses are almost constant beyond a length of 10 mm.

The absolute maximum stress stabilises to about 240 MPa, while the maximum along the line plot is almost constant at around 200 MPa. The absolute maximum at 10 mm length is around 270 MPa. The surface stress varies in magnitude between 100 MPa and 400 MPa. There is a drastic increase in the magnitude of surface stress between 30 mm and 40 mm.

The absolute minimum stress occurs along the line plot for all lengths. It varies between 380 MPa and 430 MPa, mainly increasing in magnitude between 10 mm and 20 mm.

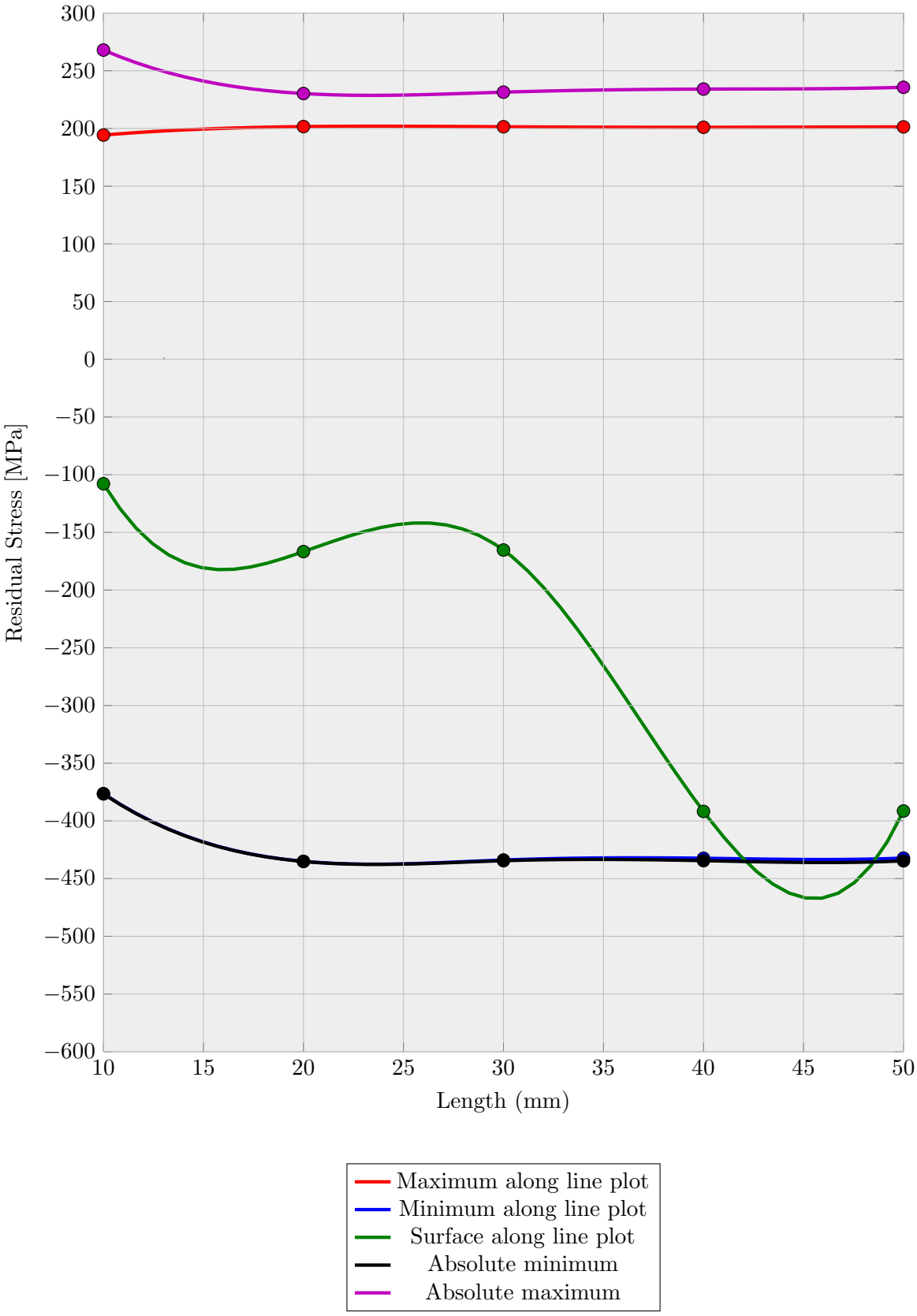

Figure 5.14: *Variation of some critical stresses with respect to length of cylinder – x direction*

3 Discussion

The aim of this chapter was to extend the study of chapter 4 to spheres and cylinders. The effect of radius on residual stresses in spheres subjected to LSP, and radius and length on residual stresses in cylinders subjected to LSP, was studied. The study was conducted using only FEM models and eigenstrain data from Sample B15. The results are subject to uncertainty due to assumptions made. The question motivating this study is, "Given the eigenstrain distribution in a laser peened cuboid sample, what is the residual stress distribution in spheres of varying radius, and cylinders of varying radius and length, subject to the same LSP process?"

Like chapter 4, the basic assumption of this study was the insensitivity of eigenstrains to geometry (See section 9). Just as eigenstrains are not fully independent of thickness, due to the effect thickness has on attenuation of the shock wave, they may not be fully independent of radius in spheres and cylinders. It is presumed that the radius of spheres and cylinders might cause shock reflection in relatively small spheres and cylinders, just as thin cuboid samples cause shock reflection. It is reiterated here that relative size in this context refers to the size of the peened sample relative to the size of the peened zone. Another potential modifier of eigenstrains when peening a curved object, is shock focussing, when peening over convex curves, like spheres and cylinders. However, this should only be an issue when the radius of curvature is comparable in scale to the shock wave. In relatively large radii of curvature, the shock wave experiences the curved surface as if it is an almost flat surface. Thus, residual stresses calculated in small cylinders and spheres using this method may not be an accurate reflection of the results in a physically peened geometry. That being said, the study conducted in section 6 of chapter 3 lends some weight to the results, along with the numerous similar studies conducted in literature.

The length of the cylinder is analogous to the size of the sample in chapter 4. It changes in a direction transverse to the direction of propagation of the shock wave, so it is not envisaged to affect the eigenstrain distribution.

Line plots of residual stress through the centres of the spheres and cylinders were extracted for each parameter. Unlike the distributions of chapter 4, the distributions for both spheres and cylinders are not linear beyond the peened region. Rather, they decline steeply at first, before flattening out towards the centres of the spheres and cylinders. The reason proposed for this phenomenon is that the spheres and cylinders are symmetrical and were peened over the entire curved surface. Unlike the cuboid samples, which were peened on a single side, the residual stress distributions are mirrored across the centres of the spheres and cylinders. The

slope of the distribution at the centre has to be zero, so that symmetry can be preserved. The residual stresses on both sides of the centre form in such a way as to preserve this symmetry.

The variation of five critical stresses with respect to each of the parameters was studied. The surface stress along the line plot is compressive for all parameter combinations in spheres and cylinders. The tensile stresses in both spheres and cylinders tends to decrease with increasing radius. The tensile stresses in cylinders also decreases with increasing length of the cylinder. This seems to indicate that increasing the gross size of spheres and cylinders leads to a decrease in maximum tensile stress. The general trend for compressive residual stresses is to increase in magnitude with increasing size. The exception to this is increasing the radius of cylinders, which decreases the magnitude of compressive residual stresses up to a point.

It is quite apparent that for large values of the parameters, for both spheres and cylinders, the stresses stabilise and do not change much. The residual stresses are only sensitive to geometry for relatively small geometries. For large geometries, the residual stresses converge to steady values.

4 Conclusions

- The effect of radius of spheres on residual stresses arising from a specific eigenstrain distribution was studied.
- The results represent the residual stresses that would arise if the sphere was laser peened with the same process used on Sample B15, provided the assumption of insensitivity of eigenstrain to geometry holds.
- The effects of radius and length of cylinders on residual stresses arising from a specific eigenstrain distribution were studied.
- If the assumption of insensitivity of eigenstrain to geometry holds, the results represent the residual stresses that would arise if the cylinder was laser peened with the same process as Sample B15.
- In small spheres and cylinders, the shock wave arising from LSP may reflect, modifying the eigenstrains. Thus, the results for small spheres and cylinders may be inaccurate.
- The length of the cylinder should not affect eigenstrain distribution. Thus, the results for length of cylinder should be accurate.
- The tensile stresses seem to decrease with increasing gross size of both cylinders and spheres.

- The surface residual stress along the line plot is compressive in spheres and cylinders of all sizes.
- The compressive stresses tend to decrease with increasing radius of cylinders and increase with increasing radius of spheres and increasing length of cylinders.
- The general shape of the residual stress line plots resemble those found in cuboid samples.

Chapter 6 Residual Stresses in Common Engineering Geometries

This chapter deals with the fourth objective. The studies conducted in the previous two chapters are extended to include some common engineering geometries. Ultimately, if this method is used to make predictions in industry, it will have to be able to deal with geometries which are more complex than those dealt with in the previous two chapters.

1 Residual Stresses in Fillets

1.1 Base Model

Figure 6.1 depicts the base model of the filleted bar. It is a square bar with a circular fillet at one corner. The base model has a size of 20 mm×20 mm, fillet radius of 3 mm, and length of 10 mm. In this model, only the fillet and the two adjoining surfaces were peened. The scan direction of peening was set along the curvature of the fillet, with the step direction being transverse to it. With this setup, the model was identified as being symmetric about two planes. The FEM model was thus reduced to a quarter of its original size, as is apparent from Figure 6.2. The FEM model was created with three major divisions in mind:

- The "core" of the model, in which the eigenstrains are zero
- The volume beneath the fillet, which is part of the peened region
- The volume beneath the flat surface adjoining the fillet, which is part of the peened region

The latter two divisions were further subdivided into the layers necessary to impose the eigenstrains on the model. The two divisions and the layers can be identified in Figure 6.2.

The reason for dividing the model in this way, was to facilitate the creation of the correct co-ordinate systems for the imposition of the eigenstrains.

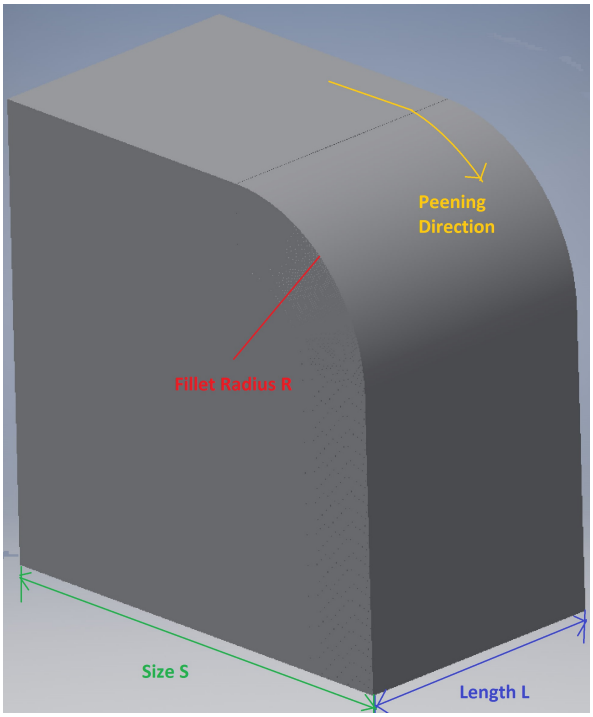

Figure 6.1: *Base CAD model of the filleted bar*

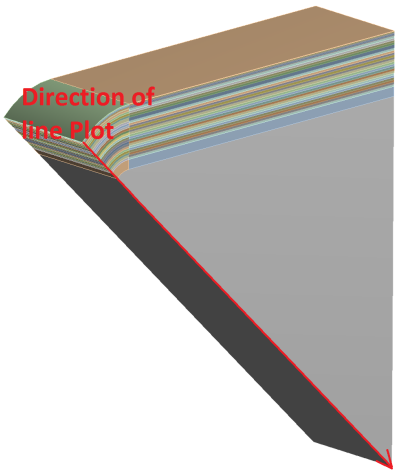

Figure 6.2: *FEM model of the base filleted bar*

For this model, two local co-ordinate systems had to be created to ensure the eigenstrains were applied in the correct direction. The two co-ordinate systems have to meet two requirements:

- They both require one axis to be consistently normal to the peened surface.
- The directions of the axes have to be consistent across both co-ordinate systems.

To meet these requirements, a local Cartesian co-ordinate system, with ID of 110, was created under the co-ordinate systems branch, for the volume beneath the peened flat surface adjoining the fillet. A local cylindrical co-ordinate system, with ID of 100, was created for the volume beneath the fillet. The origin of the cylindrical system was placed at the centre-point of the fillet. The co-ordinate systems created are depicted in Figure 6.3. It can be seen that the axes are consistent across both co-ordinate systems. The x axes of both systems are normal to the surface and correspond to the z axis of the Cartesian system used for Sample B15. The y (scan) and z (step) axes of both co-ordinate systems correspond to the y and x axes, respectively, of the co-ordinate system used in Sample B15.

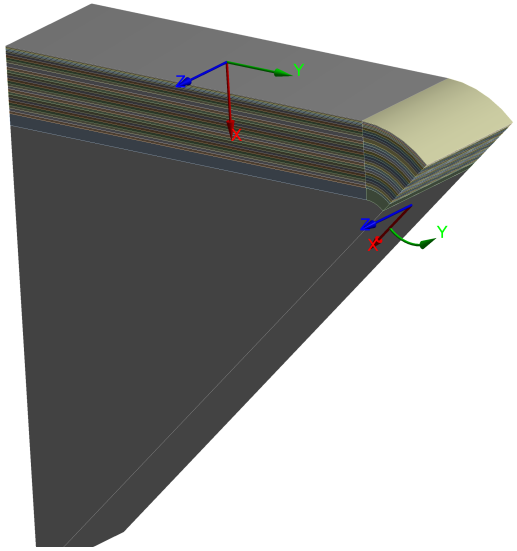

Figure 6.3: *Co-ordinate systems used to implement eigenstrains in filleted bar*

A named selection, incorporating all the layers of the volume beneath the fillet, was created and called "Curve". Another named selection incorporating all the layers beneath the peened flat surface, was dubbed "Top". An APDL Commands object was added under the analysis branch, to perform the following tasks, ensuring that the eigenstrains are imposed in the correct directions:

1. Enter the preprocessing environment.
2. Select the named selection "Top".
3. Modify all selected elements to have the local Cartesian co-ordinate system (ID 110) as the element system.
4. Select named selection "Curve".
5. Modify all selected elements to have the local cylindrical co-ordinate system (ID 100) as the element system.

6. Select all bodies

7. Enter the Solution processor.

Figure 6.4 depicts the residual stress field in the base cylinder after applying the eigenstrains from Sample B15. It should be remembered that the front cross section shown in the figure is through the centre of the filleted bar. The stresses vary along the length and width of the filleted bar. Through the centre of the bar, the stresses near the surface are highly compressive and transition to relatively high tensile stresses. As one progresses towards the ends of the filleted bar, the residual stresses become less compressive near the surface and less tensile deeper into the material. The surface stresses become very tensile towards the length-end of the bar. At the side-end of the bar, the surface stresses do also become tensile, but not to the degree of the length-end of the bar.

The degree and depth of compression seem slightly lower in the fillet itself than in the non-filleted part immediately adjacent to the fillet. The maximum depth of compression and maximum compressive stress occur near the filleted part of the bar. The maximum tensile stress occurs near the far corner of the bar (the intersection between the side edge and long edge). The residual stresses in the bulk of the material are zero.

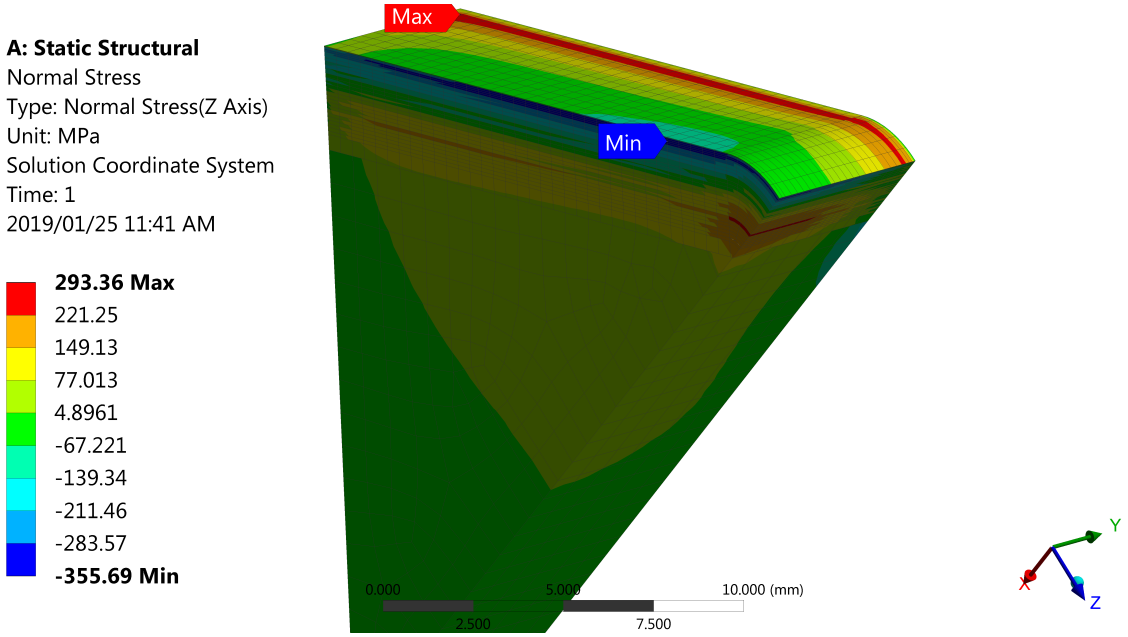

Figure 6.4: *Residual stresses in base filleted bar*

1.2 Varying Radius of Fillet

Residual stress distributions for fillets with varying radius are shown in Figure 6.5. The line along which the stresses were extracted is shown in Figure 6.2 as a red line. The length

of the filleted bars was kept constant at 10 mm, while the size was kept at 20 mm×20 mm. The stresses near the surface are highly compressive and rise steeply to a peak tensile stress, before sharply dropping. Thereafter, the stress appears to reduce in an exponential manner, converging on zero stress.

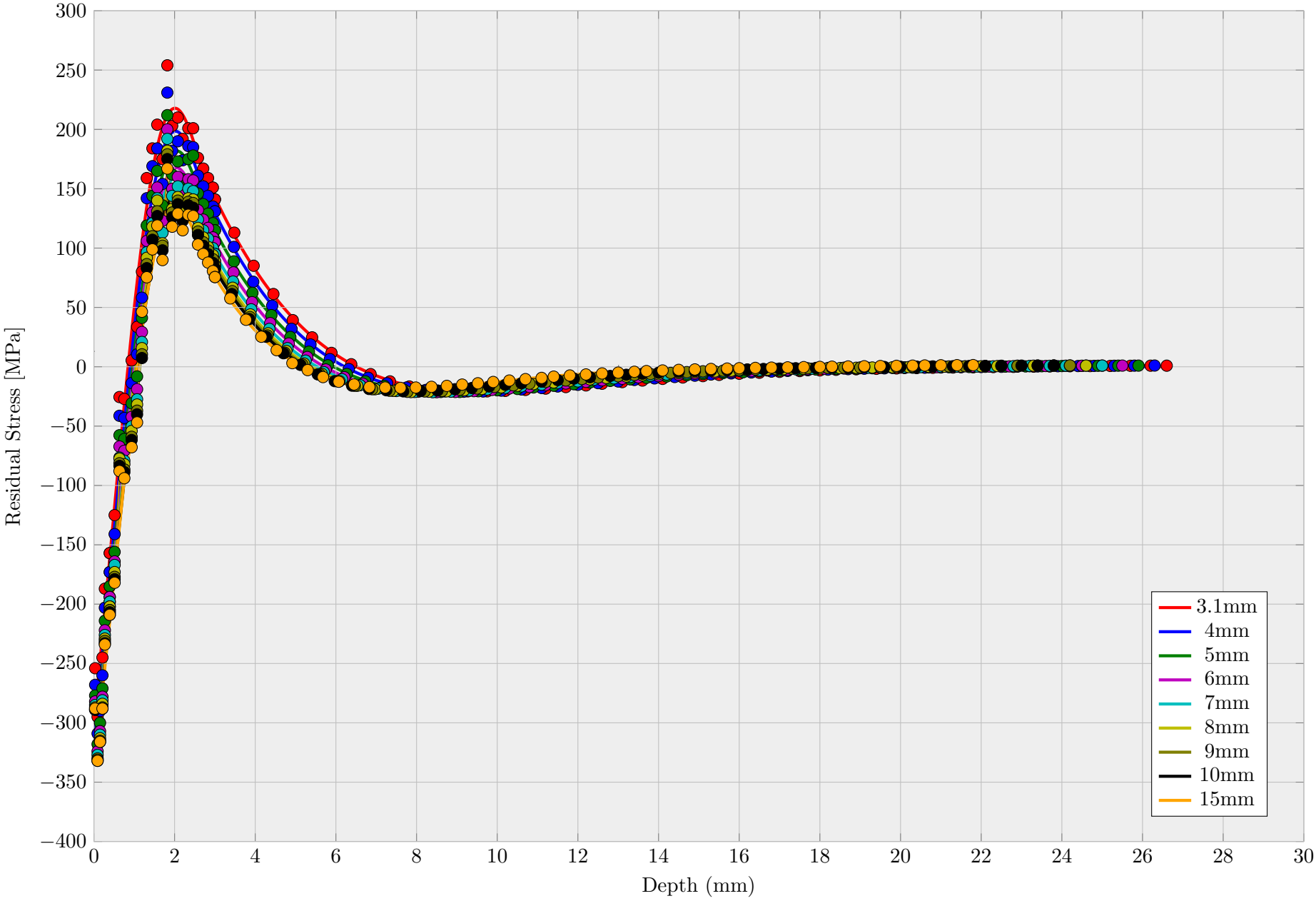

Figure 6.5: *Residual stress distributions in fillets of varying radius – x direction*

Figure 6.6 shows the variation of different stresses with respect to the fillet radius. The variation of most of the stresses seems to be fairly stable over the range of fillet radii. The absolute maximum stress, in particular, is constant over the entire range of radii, with a value of just under 300 MPa. The maximum stress on the line plot varies the most from all these stresses. It decreases with increasing fillet radius. The values range between around 270 MPa – at fillet radius of 3 mm, to around 200 MPa at 15 mm. It seems to converge to a value of 200 MPa. The surface stress does not vary much over the range of radii. At a fillet radius of 3 mm, the surface stress is about 20 MPa. It gradually decreases to 50 MPa as fillet radius increases.

The magnitude of the absolute minimum increases slightly as fillet radius increases. It varies between around 360 MPa to 330 MPa. The minimum stress on the line plot varies in a more complex manner. It decreases in magnitude between radii of 3 mm and 4 mm and thereafter increases in magnitude, eventually converging on the absolute minimum stress. The magnitude varies between 260 MPa (at 4 mm radius) and 330 MPa.

1.3 Varying Size of Filleted Bar

Residual stress distributions for fillets with varying size are shown in Figure 6.7. The line along which the stresses were extracted is shown in Figure 6.2 as a red line. The length of the filleted bars was kept constant at 10 mm, while the radius was kept at 3 mm. The shape of the curves match those in Figure 6.5. It is apparent that size of the filleted bar does not affect the residual stresses much. The residual stress curves are very close to each other and there is a significant amount of overlap between the curves. This is especially the case beyond the peened region, where the graphs seem to converge onto a single line.

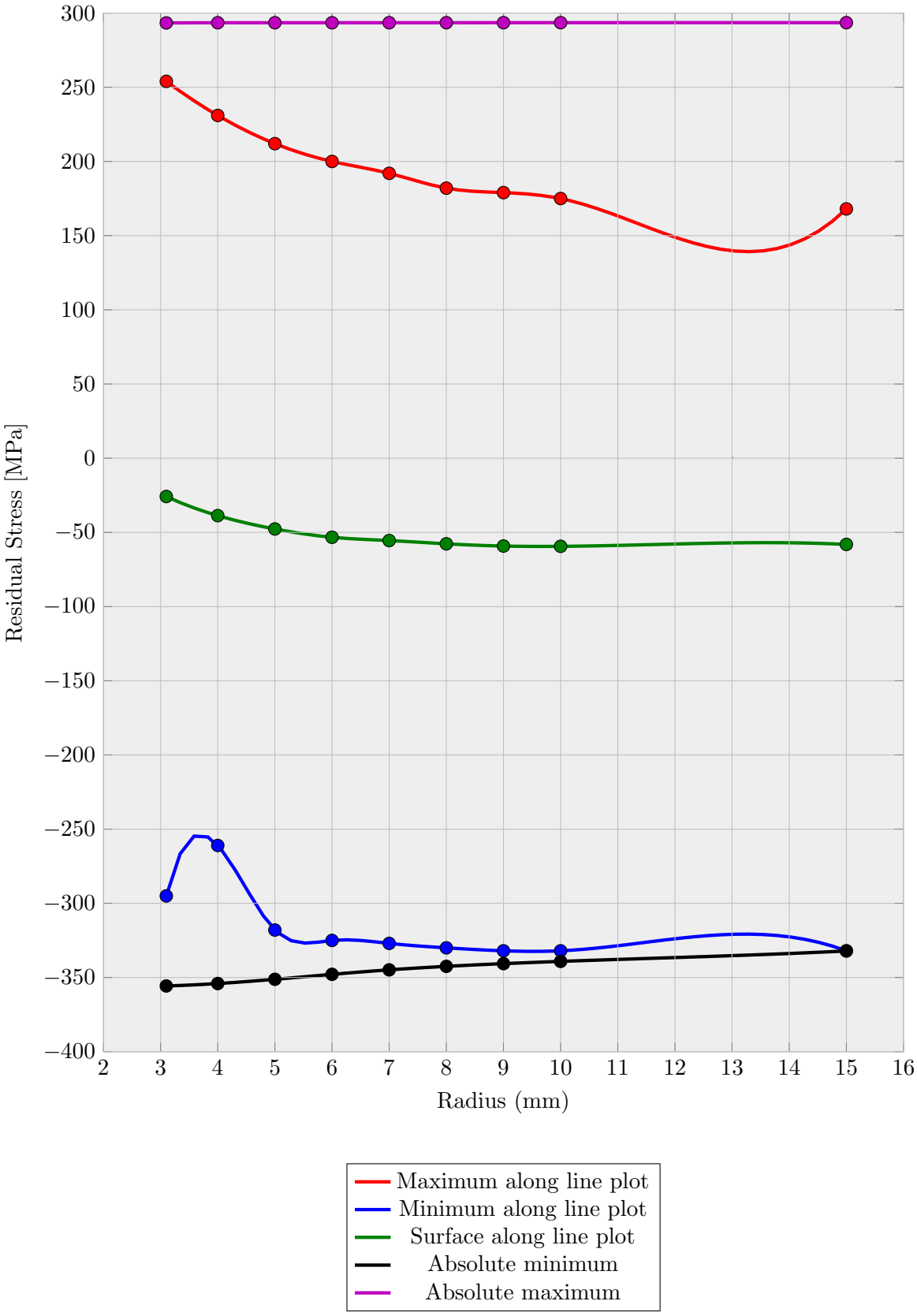

Figure 6.6: *Variation of some critical stresses with respect to radius of fillet – x direction*

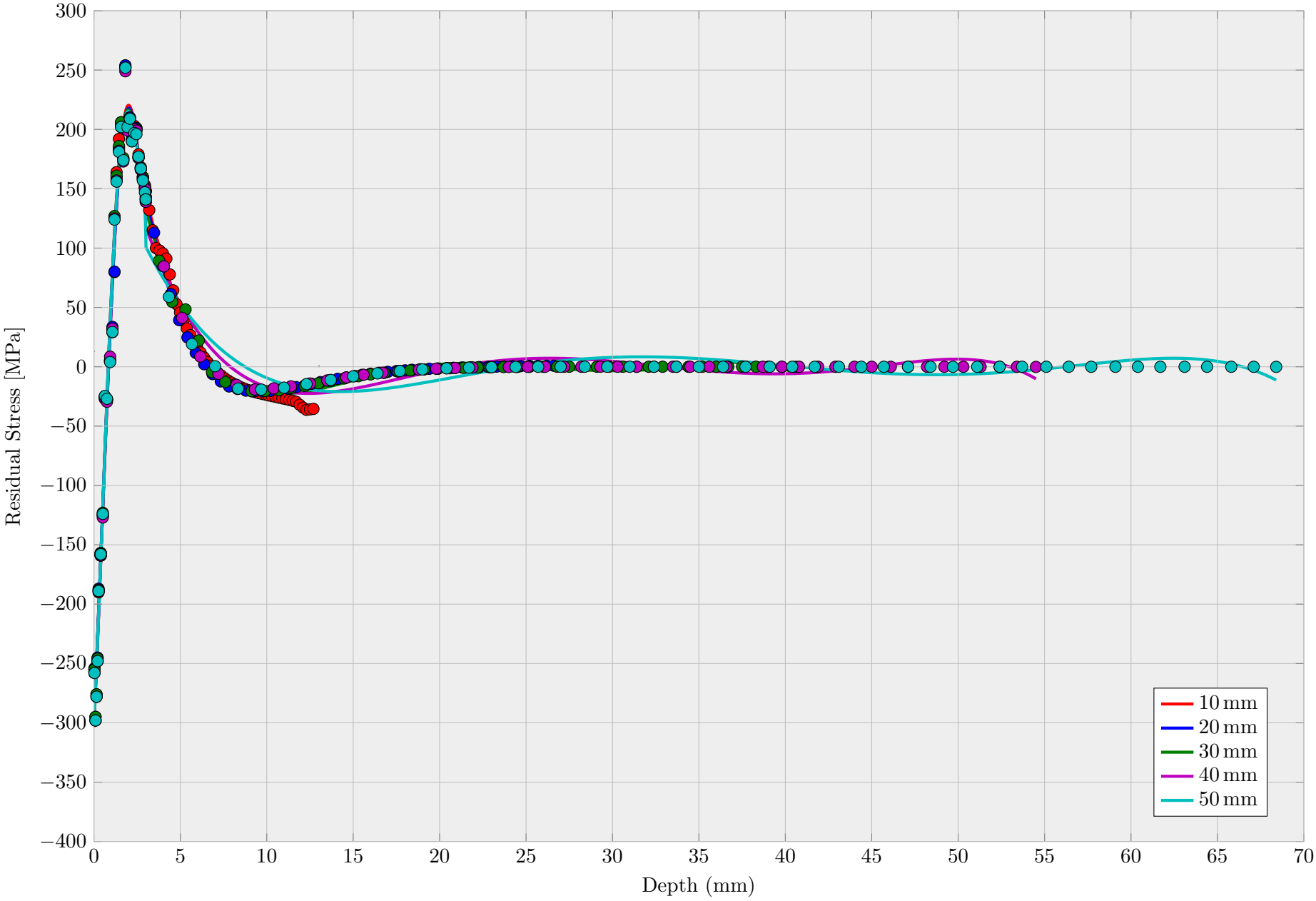

Figure 6.7: *Residual stress distributions in filleted bars of varying size – x direction*

Figure 6.8 shows the variation of different stresses with respect to size of the filleted bar. Most of the stresses do not seem to vary very much. This reinforces the statement made about Figure 6.7, that size does not seem to affect the residual stresses much. Only the absolute stresses seem to vary slightly. The stresses on the line plot are constant for all sizes.

The absolute maximum stress decreases from around 300 MPa – at 20 mm size, to a low of 250 MPa – at 50 mm size. The absolute maximum coincides with the maximum on the line plot for sizes above 30 mm. The surface stress is constant, with a magnitude of about 290 MPa for all sizes.

The absolute minimum varies very little for sizes below 30 mm, with a magnitude of around 350 MPa. The magnitude decreases slightly for sizes above 30 mm – to about 330 MPa. This is closer to the magnitude of the minimum on the line plot, which is 300 MPa for all sizes.

1.4 Varying Length of Filleted Bar

Residual stress distributions for fillets with varying length are shown in Figure 6.9. The line along which the stresses were extracted is shown in Figure 6.2 as a red line. The size of the filleted bars was kept constant at 20 mm, while the radius was kept at 3 mm. It is clear that the length of the filleted bar has a significant effect on residual stresses. For small lengths, the graphs are similar to those of Figure 6.5 and Figure 6.7, with the graphs varying in an exponential manner beyond the peened region. However, as length increases, the rate of exponential decay decreases and the curve approaches a straight line. It is apparent from this that the unexpected non-linear variation of stresses beyond the peened region in Figure 6.5 and Figure 6.7, is due to the small length of the base filleted bar.

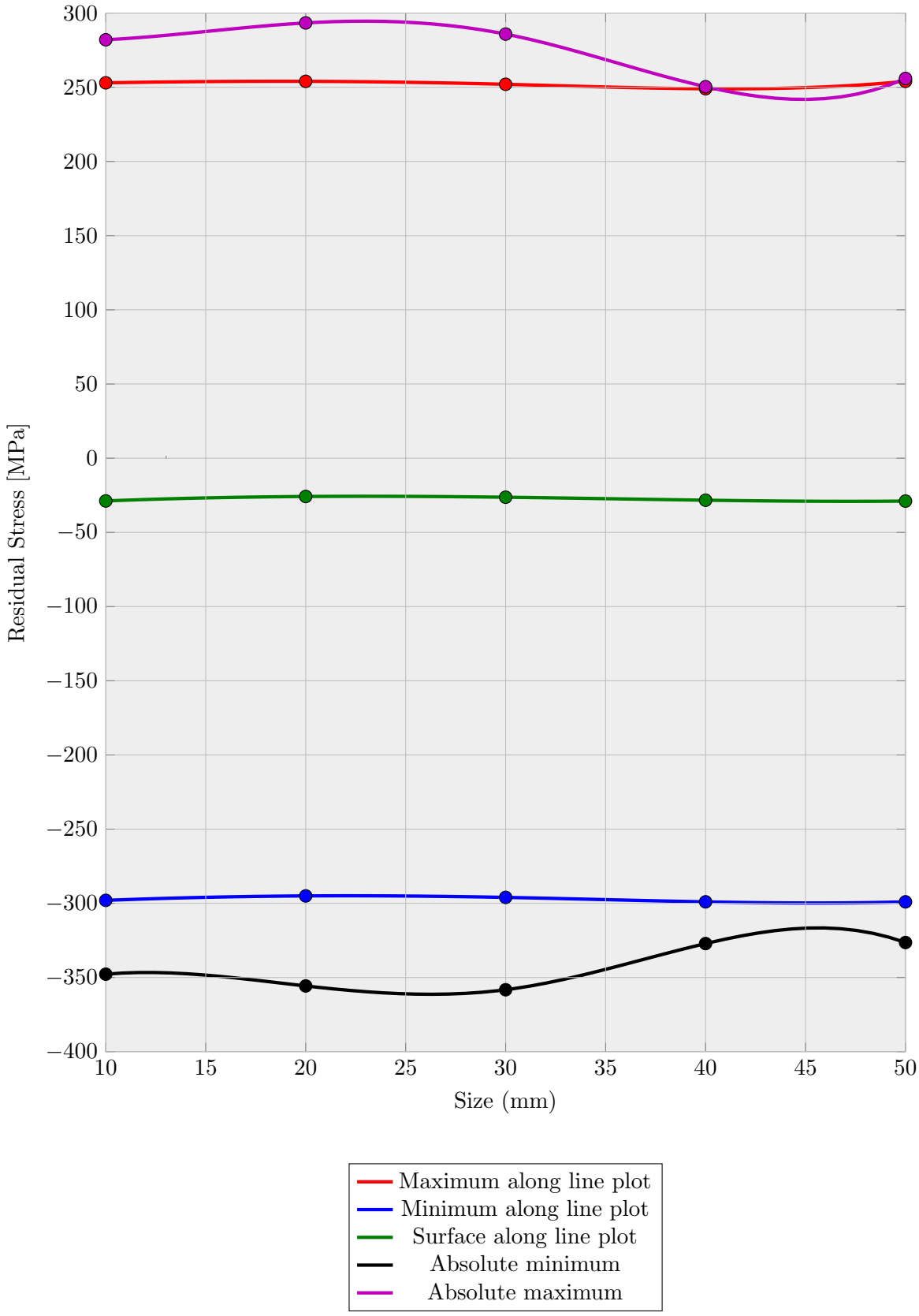

Figure 6.8: *Variation of some critical stresses with respect to size of filleted bars – x direction*

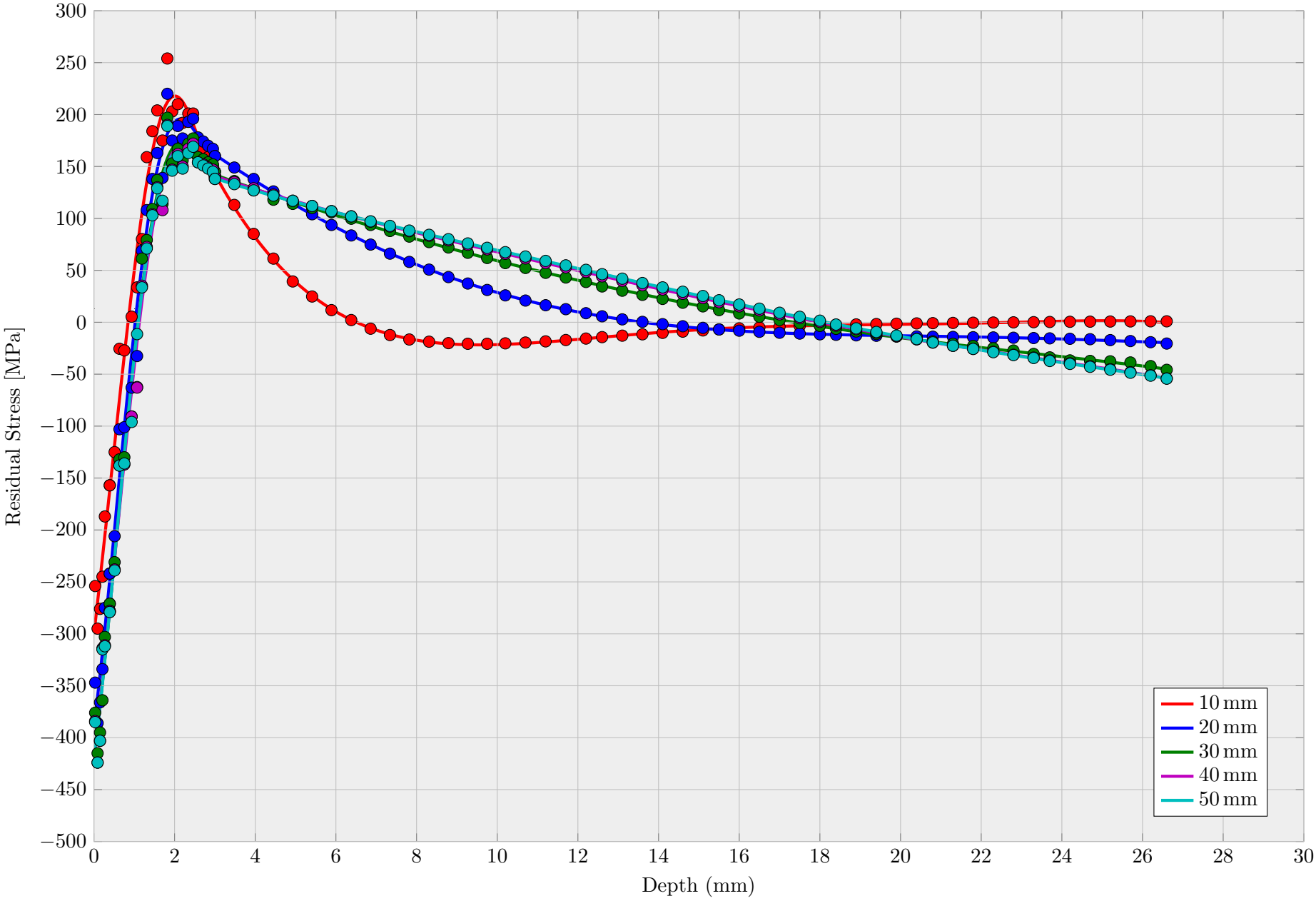

Figure 6.9: *Residual stress distributions in filleted bars of varying lengths – x direction*

Figure 6.10 shows the variation of different stresses with respect to length of the filleted bar. Although the stresses do not vary much, they vary more than they do with size and thickness.

The absolute maximum stress decreases from around 300 MPa – at 20 mm size, to a low of 250 MPa –at 50 mm size. The absolute maximum coincides with the maximum on the line plot for sizes above 30 mm. The surface stress is constant, with a magnitude of about 290 MPa for all sizes. The absolute maximum and absolute minimum do not vary monotonously, but oscillate gently over the range of lengths. The stresses along the line plot vary monotonously, with a maximum at 10 mm length. The stresses decrease to stable values, thereafter.

The absolute maximum varies between 300 MPa – at 10 mm length, and 240 MPa – at 10 mm length. The maximum along the line plot is 250 MPa at 10 mm length and stabilises to around 190 MPa. The surface stress has a magnitude of 25 MPa and stabilises to a magnitude of around 150 MPa.

The absolute minimum varies between a maximum magnitude of around 450 MPa – for a length of 20 mm, to a minimum magnitude of around 350 MPa – for a length of 10 mm. The minimum along the line plot has a maximum magnitude about 430 MPa and minimum magnitude of 300 MPa. The minimum along the line plot and absolute minimum converge towards each other, but remain distinct, as length increases.

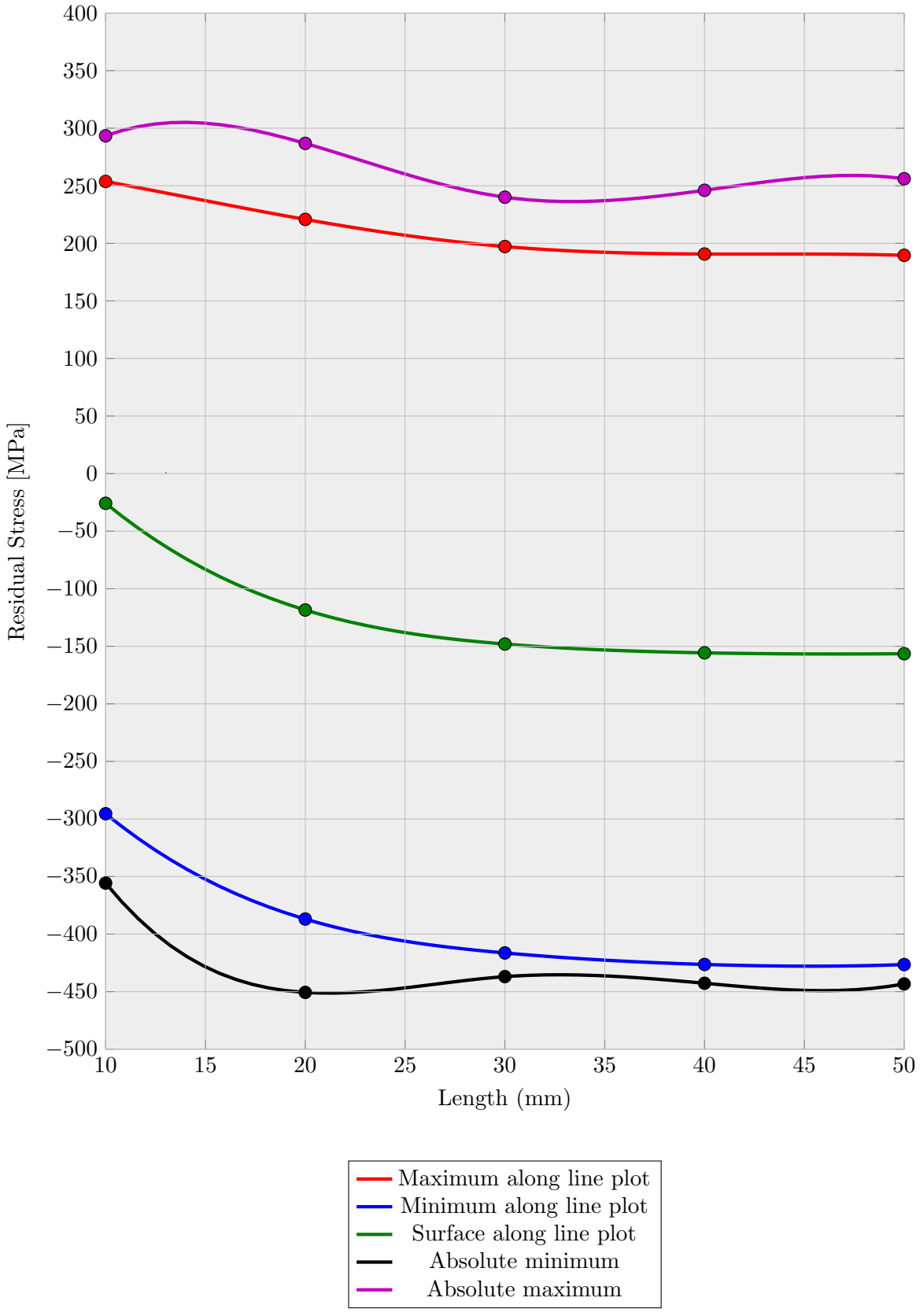

Figure 6.10: *Variation of some critical stresses with respect to length of filleted bar – x direction*

2 Residual Stresses in Equal Angles

2.1 Base Models

This section deals with residual stresses in standard equal angles. The parameters of the angles were varied according to IS 808-1957 standards for equal angles. There are three parameters required to fully define an equal angle:

- Size, which is the length of the legs
- Thickness, which is the thickness of the legs
- Length, which is the length of the equal angle

All other parameters, such as radii of fillets, depend on these three parameters. This standard was chosen because it has a good variety of thickness for each size, which is advantageous for the parameter study. However, one problem is that the thickness available for each size of angle are not consistent across all sizes. For larger sizes, only thicker legs are available, while for smaller angles, only thinner legs are available. It was decided that two separate parameter studies would be conducted for small and large equal angles. Thus, two base models were required; one for large equal angles and one for small equal angles. Figure 6.11 depicts the base models. The small angle has a size of 50 mm, a thickness of 5 mm, and length of 60 mm. The large angle has a size of 150 mm, thickness of 12 mm, and length of 60 mm.

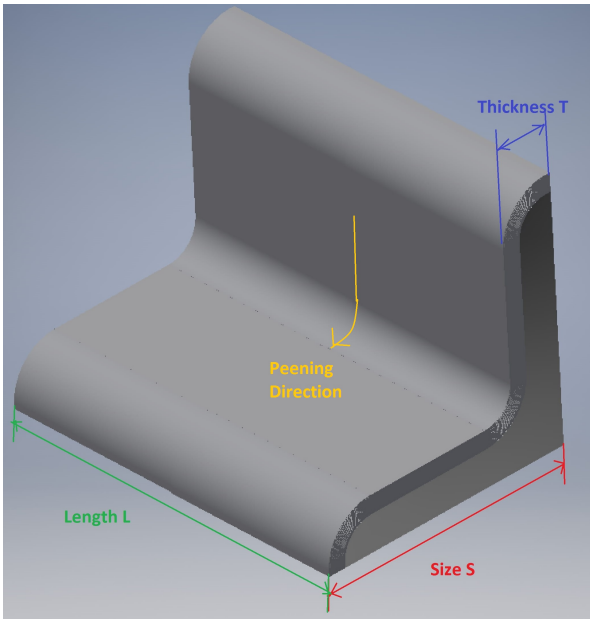

Figure 6.11: *Base CAD model of the equal angle*

Other than the parameter combinations being different, there was no real difference between the analysis of small and large angles. The peened surface included the inner part of the legs (adjoining the concave fillet) and the concave fillet. The convex fillets were not included under the peened region. The scan direction of peening was along the curvature of the concave fillet, with the step direction in the transverse direction. Noting that the model was symmetric about two planes, (one bisecting the length and the other bisecting the cross section) the model was reduced to a quarter of its original size, as shown in Figure 6.12.

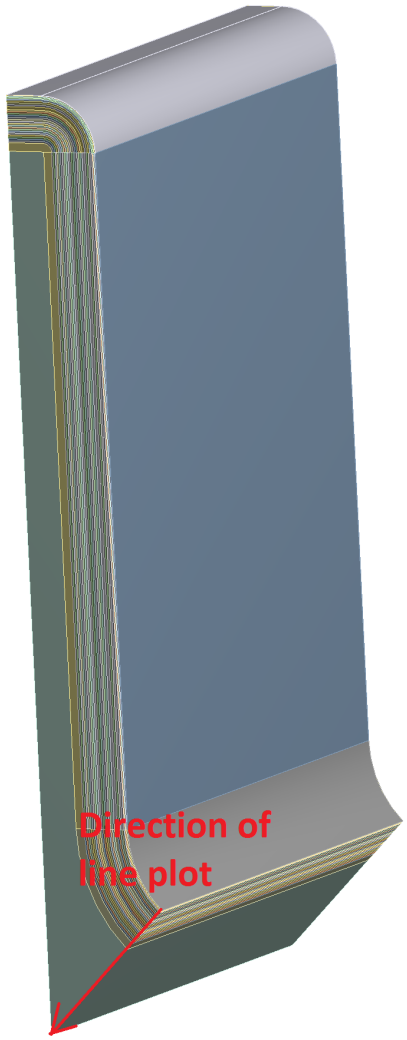

Figure 6.12: *FEM model of the base equal angle*

The model was divided into four major parts:

- The "core" of the model, in which the eigenstrains are zero
- The volume beneath the concave fillet, which is part of the peened region
- The volume beneath the flat surface adjoining the concave fillet, which is part of the peened region

- The volume beneath the convex fillet, in which the eigenstrains are zero.

The latter three divisions were further subdivided into the necessary layers to impose the eigenstrains. It should be noted that the volume under the convex fillet could have been included in the "core" of the model, as it was not part of the peened zone. However, this division was created anticipating that it would be included under the peened zone. Subsequently, it was decided to exclude it in order to simplify the analysis.

Two local co-ordinate systems were created: a cylindrical co-ordinate system for the concave fillet with an ID of 100, and a Cartesian co-ordinate system with an ID of 110 for the peened part of the leg. The origin of the cylindrical co-ordinate system was placed at the centre of the concave fillet to ensure correct imposition of the eigenstrains. The co-ordinate systems are depicted in Figure 6.13.

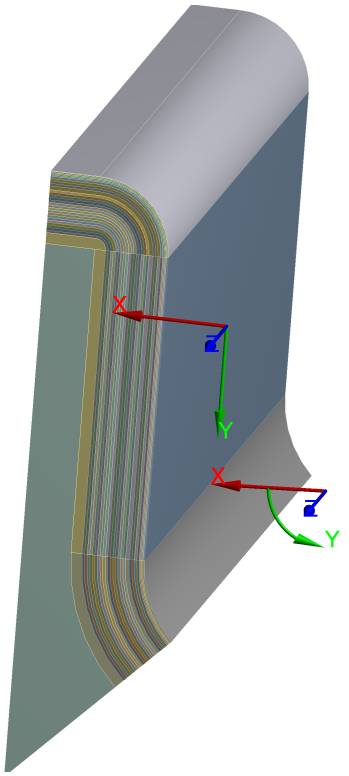

Figure 6.13: *Co-ordinate systems used to implement eigenstrains in equal angles*

The directions of the co-ordinate systems are similar to those used for the fillet study. The x axis is normal to the surface, corresponding to the z axis of Sample B15 co-ordinate system. The y axis is in the scan direction, corresponding to the y axis of Sample B15 co-ordinate system. The z axis is in the step direction, corresponding to the x axis in Sample B15 co-ordinate system.

A named selection, incorporating all the layers of the volume beneath the concave fillet, was created and called "Curve". Another named selection incorporating all the layers beneath the peened flat surface, was dubbed "Side". An APDL Commands object was added under the analysis branch, to perform the following tasks, ensuring that the eigenstrains are imposed in the correct directions:

1. Enter the preprocessing environment.
2. Select the named selection "Side".
3. Modify all selected elements to have the local Cartesian co-ordinate system (ID 110) as the element system.
4. Select named selection "Curve".
5. Modify all selected elements to have the local cylindrical co-ordinate system (ID 100) as the element system.
6. Select all bodies
7. Enter the Solution processor.

Figure 6.14 depicts the residual stress field in the small base equal angle after applying the eigenstrains from Sample B15. It should be borne in mind that the front cross-section shown is actually the central cross section of the angle, due to the symmetrical reduction of the model. The surface stresses are strongly compressive towards the middle of the angle and in the vicinity of the concave fillet. The surface stresses gradually transition to strongly tensile stresses as one progresses towards the ends of the angle. The maximum compressive stresses near the ends of the angle are also lower than those in the middle.

The surface stresses in the legs are compressive through most of the peened region, but the magnitude of compression decreases away from the concave fillet. The tips of the legs, including the convex fillet, were not subjected to peening. It can be seen that the residual stresses in the non-peened region are tensile.

The maximum compressive stress occurs beneath the centre of the concave fillet at the centre of the equal angle. The maximum tensile stress occurs at the end of the angle, also on the concave fillet.

Figure 6.15 depicts the residual stress field in the large base equal angle after applying the eigenstrains from Sample B15. The residual stress field is similar to that found in the small angle, Figure 6.14. The same features identified in Figure 6.14 also exist here. A notable

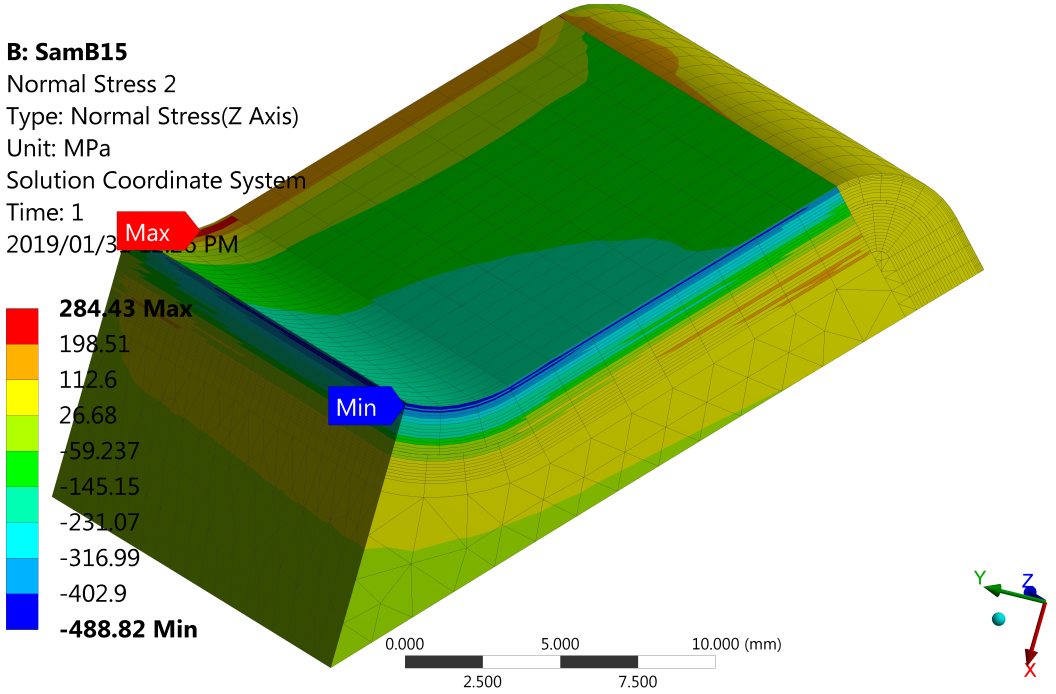

Figure 6.14: *Residual stresses in small base equal angle*

difference is the fact that the maximum tensile stress does not occur on the concave fillet, but at the juncture between the peened and non-peened parts of the leg.

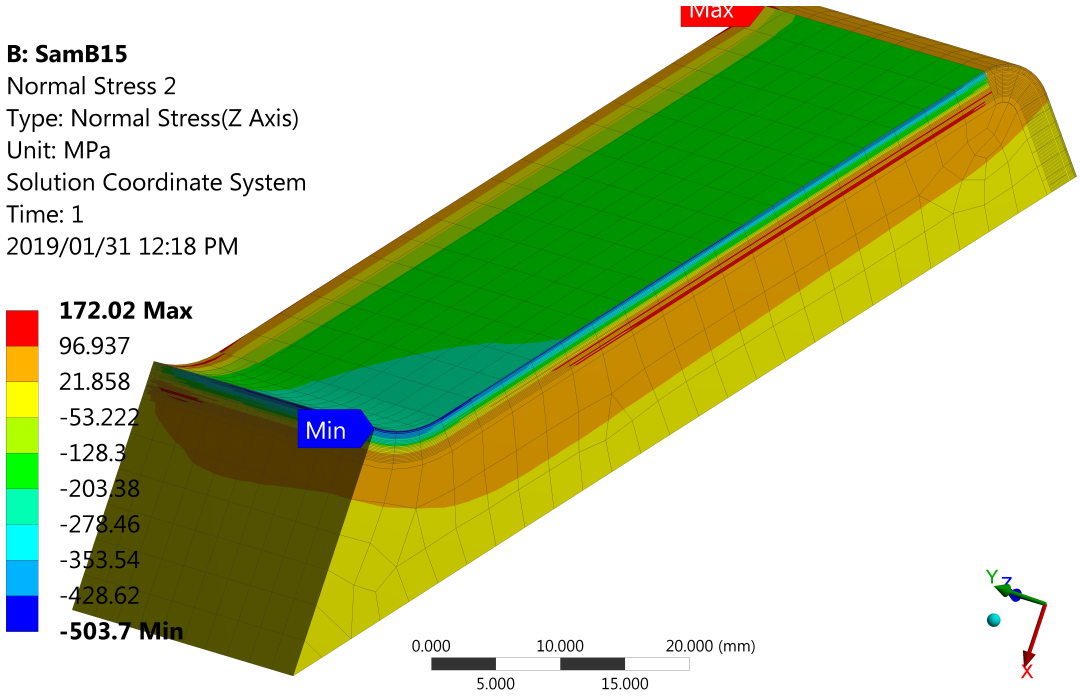

Figure 6.15: *Residual stresses in large base equal angle*

2.2 Small Angles

2.2.1 Varying Thickness of Small Equal Angles

Residual stress distributions for small equal angles with varying leg thickness are shown in Figure 6.16. The line along which the stresses were extracted is shown in Figure 6.12 as a red line. The size of the small equal angles was kept constant at 50 mm, while the length of the angle was kept constant at 60 mm. The shape of the curves is similar to those encountered in the cuboid samples, as well as the spheres and cylinders. However, compared to the curves for those models, the stress in the non-peened zone drops very little from the peak stress. Thus, the peak is not well defined. The slopes of the lines beyond the peened zone do not seem to change much as thickness of the leg increases. However, the stresses beyond the peened region decrease with increasing thickness.

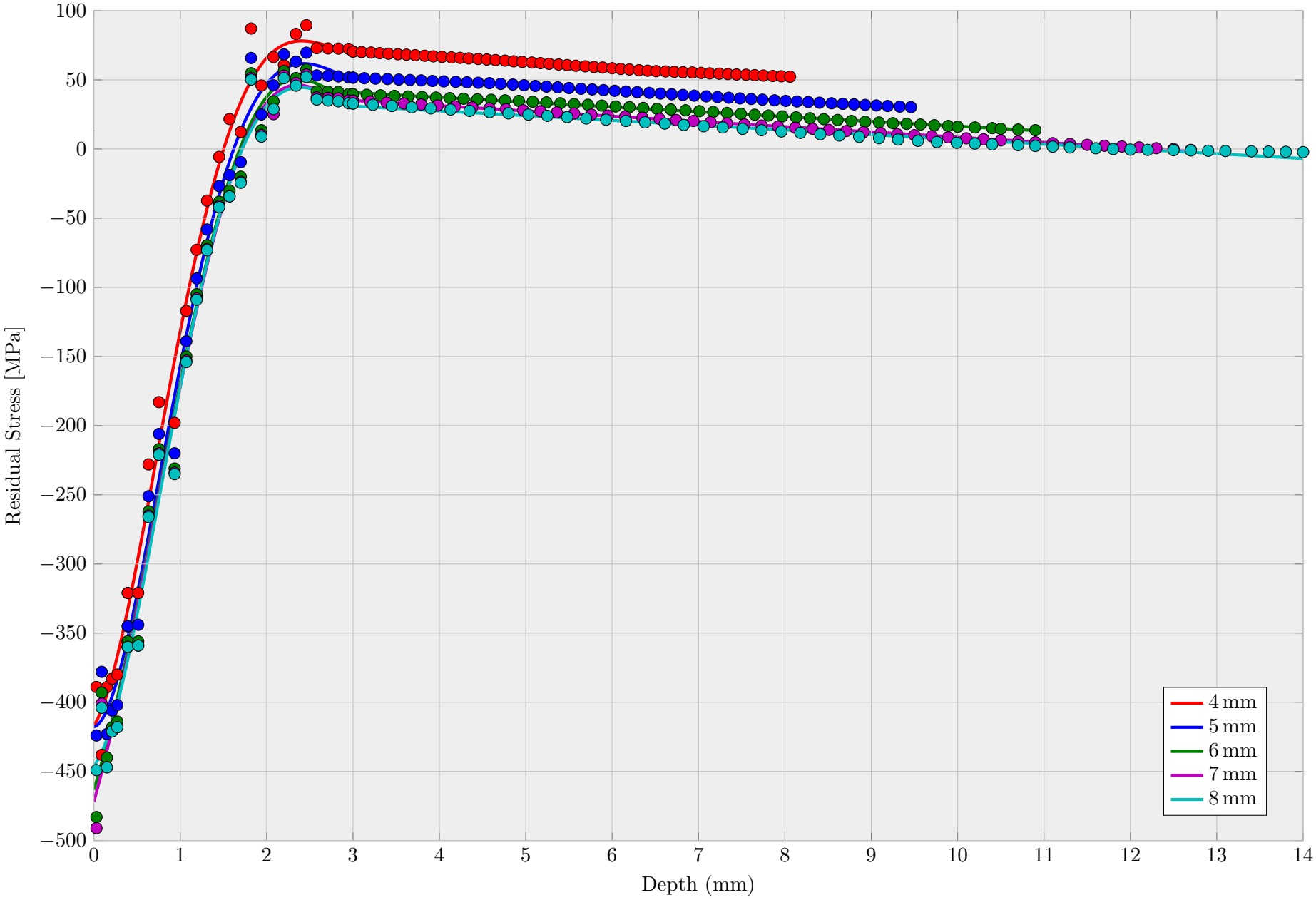

Figure 6.16: *Residual stress distributions in small equal angles of varying thickness – x direction*

Figure 6.17 shows the variation of different stresses with respect to thickness of the equal angle. All the stresses appear to gently decrease with increasing thickness, before stabilising to constant values.

The absolute maximum stress decreases from around 200 MPa – at 4 mm thickness, to a low of around 160 MPa – at a thickness of 7 mm. The maximum along the line plot varies between 90MPa and 50MPa, varying monotonously across the range of thickness. The surface stress also varies monotonously from a magnitude of 390 MPa to a magnitude of 450 MPa. The surface stresses are highly compressive compared to the surface stresses in spheres, cylinders, and fillets.

The minimum along the line plot converges to the absolute minimum for large thickness. The magnitude of the absolute minimum varies between 450 MPa – at 4 mm thickness, and 500 MPa – at 8 mm thickness. The magnitude of the minimum along the line plot is around 430 MPa at 4 mm.

2.2.2 Varying Size of Small Equal Angles

Residual stress distributions for small equal angles with varying size are shown in Figure 6.18. The line along which the stresses were extracted is shown in Figure 6.12 as a red line. The thickness of the small equal angles was kept constant at 5 mm, while the length of the angle was kept constant at 60 mm. The shapes of the curves are similar to those in Figure 6.16. However, in this case, the stresses beyond the peened zone generally increase with increasing size. This is the inverse of what was seen in Figure 6.16. It should be borne in mind that while increasing the size of the angle increases the cross-sectional area of the entire angle, the thickness of the leg relative to the size of the angle decreases (If it is kept constant). This may explain why the aforementioned inversion of relationships occurs.

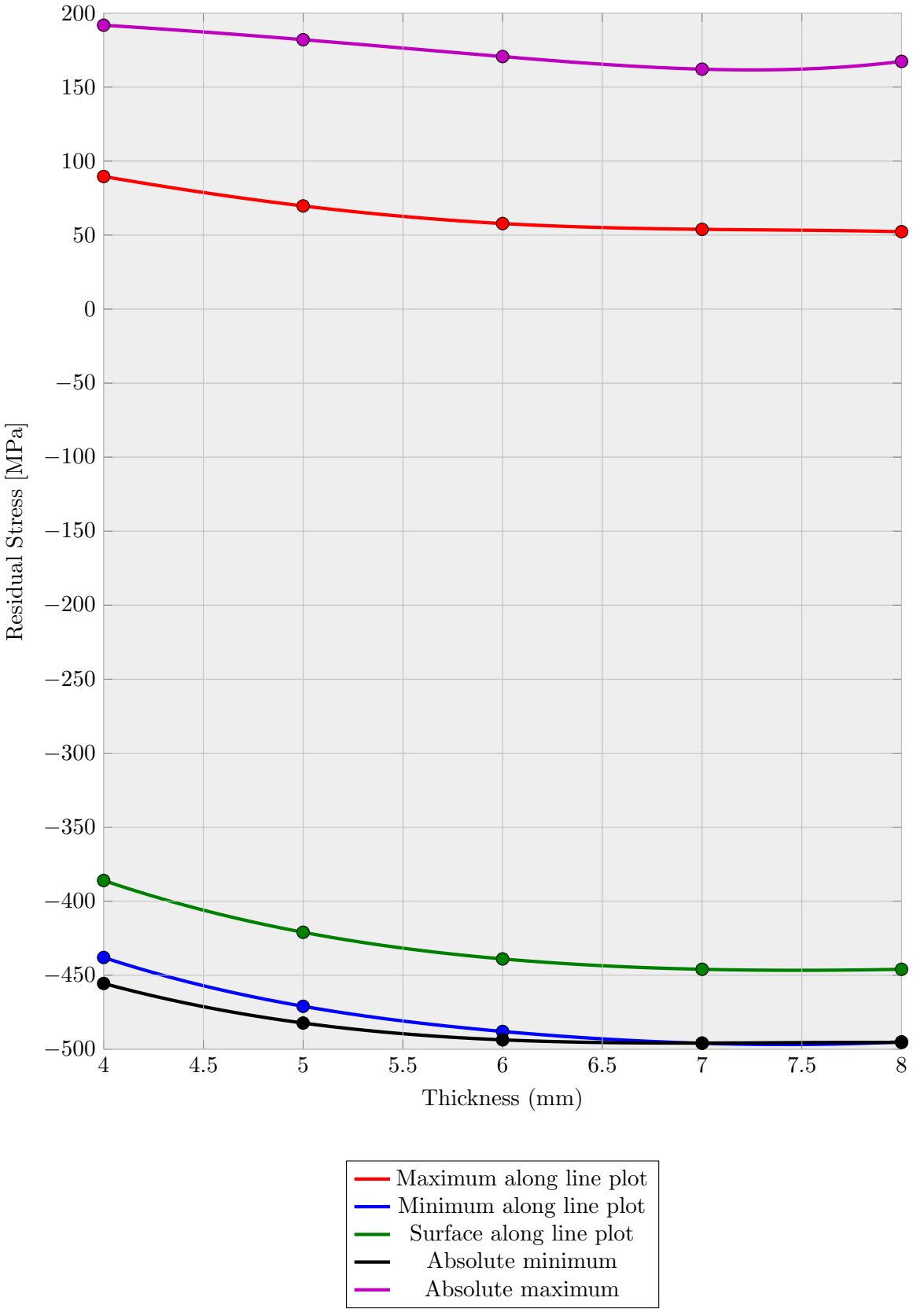

Figure 6.17: *Variation of some critical stresses with respect to thickness of small equal angles – x direction*

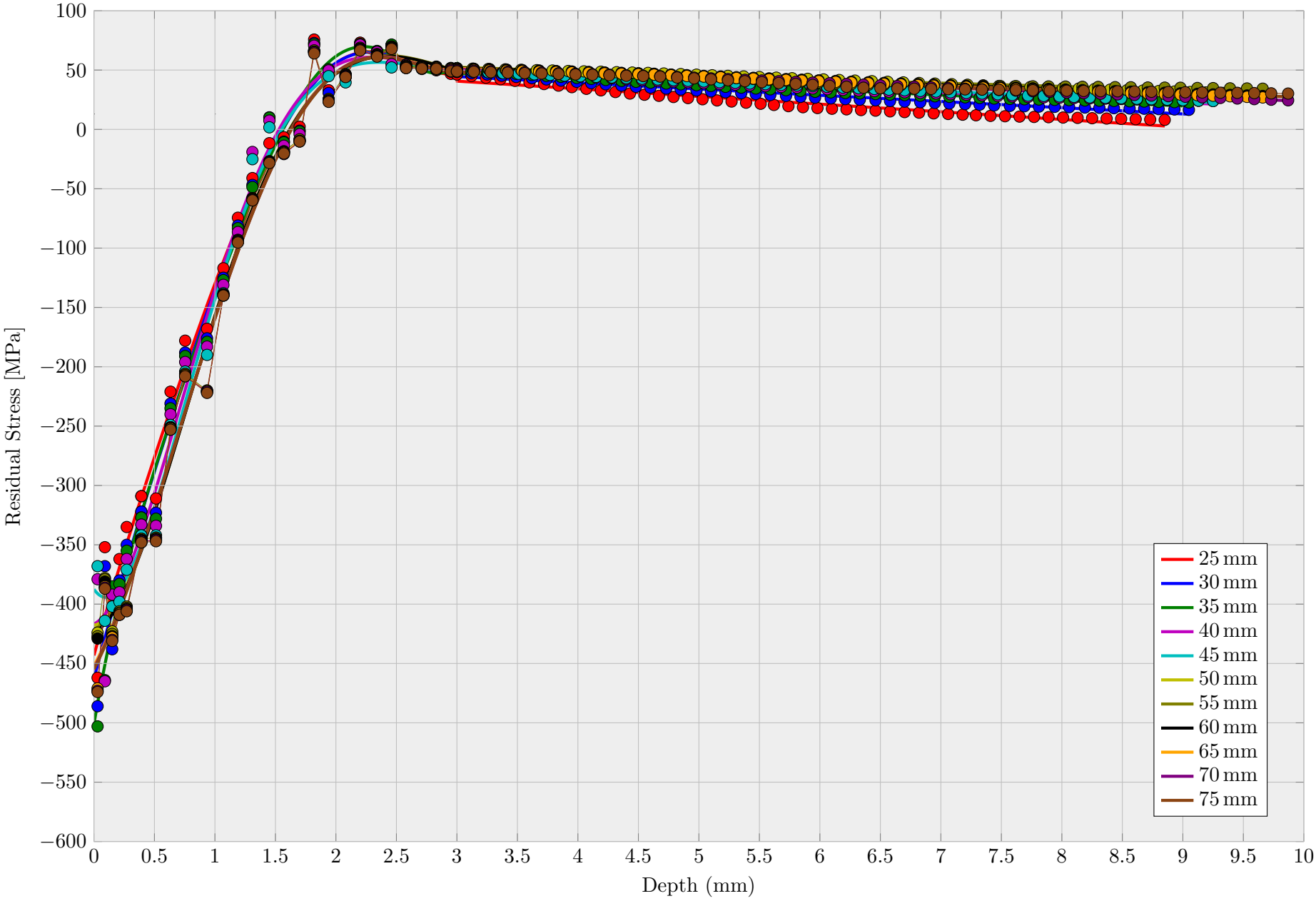

Figure 6.18: *Residual stress distributions in small equal angles of varying size – x direction*

Figure 6.19 shows the variation of different stresses with respect to the size of the equal angle. The stresses have one thing in common. They are all constant beyond a size of 50 mm.

The absolute maximum stress is almost constant at just below 300 MPa for sizes below 40 mm. It then gradually decreases to around 150 MPa – at a size of 55 mm, and remains constant thereafter. The maximum along the line plot remains almost constant, at around 70 MPa, across all sizes. The magnitude of the surface stress increases from around 400 MPa to a maximum of about 500 MPa, at a size of 40 mm. Thereafter, it gradually decreases to about 430 MPa and remains constant.

The curves for minimum along the line plot and absolute minimum for large thickness are very close to each other, but still distinct. They both start at a magnitude of around 480 MPa and increase to a magnitude of around 520 MPa, at a size of 40 mm. They then decrease in magnitude to about 480 MPa, remaining relatively constant thereafter.

2.2.3 Varying Length of Small Equal Angles

Residual stress distributions for small equal angles with varying length are shown in Figure 6.20. The line along which the stresses were extracted is shown in Figure 6.12 as a red line. The thickness of the small equal angles was kept constant at 5 mm, while the size of the angle was kept constant at 50 mm. The shapes of the curves are similar to those in Figure 6.16. It was mentioned in the thickness study that, relative to the curves for those models, the stress in the non-peened zone drops very little from the peak stress, leading to an ill-defined tensile peak. It is apparent here that this quality is due to the large length (60 mm) of the base sample. For large lengths, the slope of the line beyond the peened zone is low, and the peak ill-defined. However, at smaller lengths, the slope is greater in magnitude, and the tensile peak is better defined. This is clear from the graph for 10 mm length. The 20 mm graph is quite distinct from the others. The 40 mm graph is distinct beyond the peened region. The graphs for other lengths are not very distinct from each other.

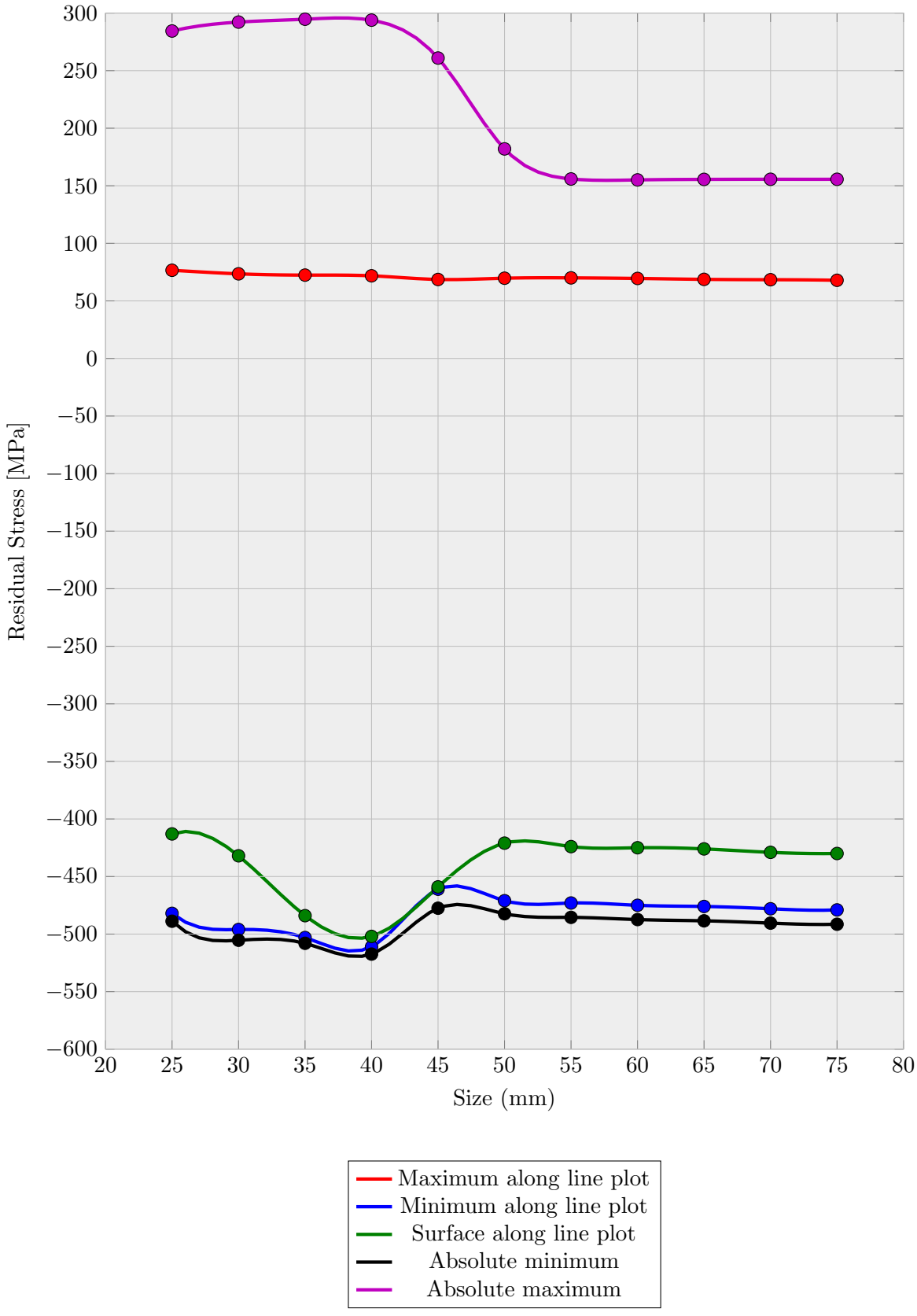

Figure 6.19: *Variation of some critical stresses with respect to size of small equal angles – x direction*

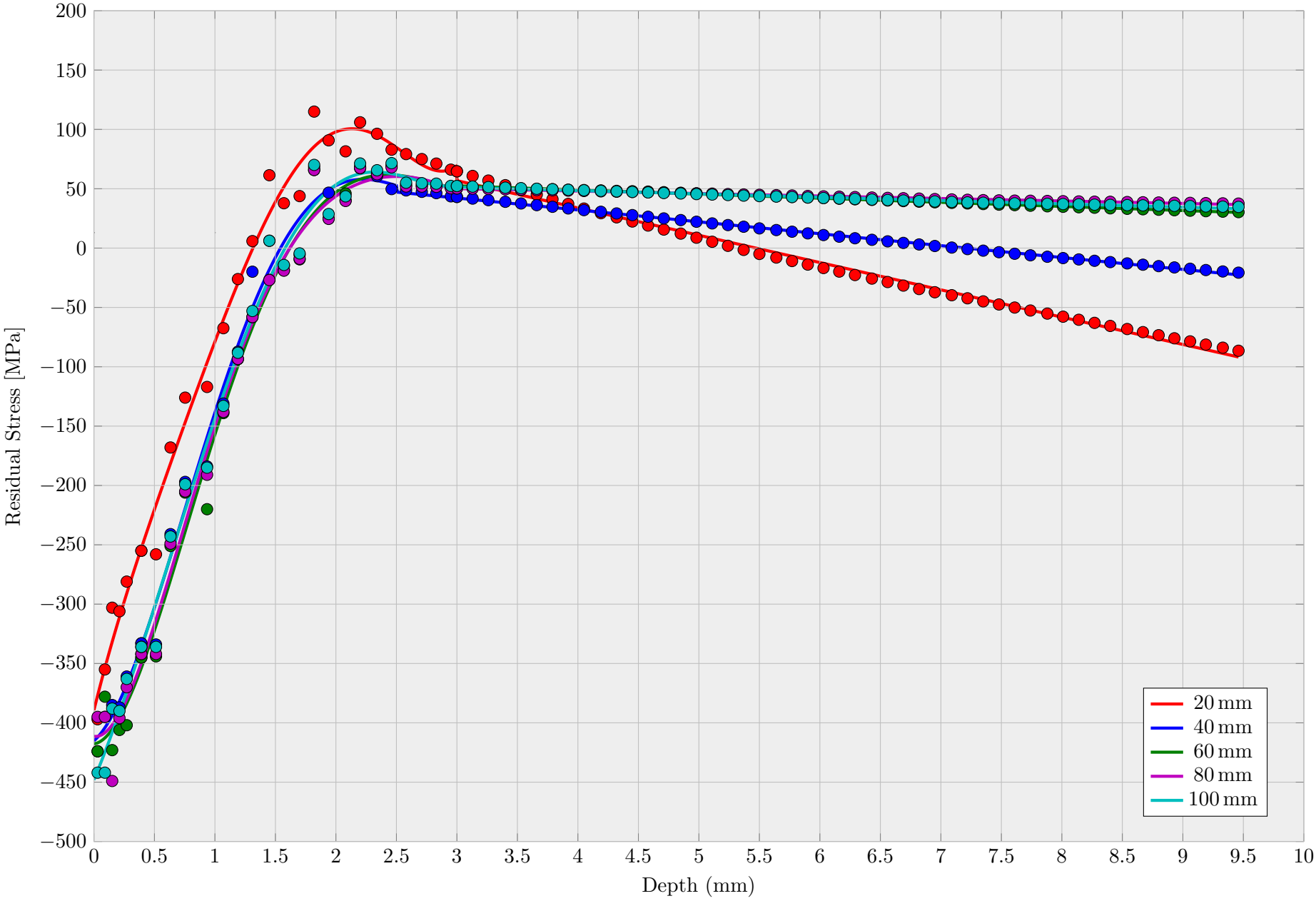

Figure 6.20: *Residual stress distributions in small equal angles of varying lengths – x direction*

Figure 6.21 shows the variation of different stresses with respect to length of the equal angle. The absolute stresses vary quite a bit, while the stresses along the line plot vary less.

The absolute maximum stress decreases with increasing length, from around 280 MPa to 160 MPa. The maximum along the line plot starts at 120 MPa stabilising to 70 MPa. The magnitude of the surface stress oscillates between 400 MPa and 450 MPa.

The curve for minimum along the line plot coincides with the curve for surface stress for most lengths, the exception being the length of the base sample (60 mm). The absolute minimum stresses also coincide with the minimum stresses along the line plot, up to a length of 60 mm. They diverge thereafter. The magnitude of absolute minimum increases from 400 MPa to nearly 600 MPa.

2.3 Large Angles

2.3.1 Varying Thickness of Large Equal Angles

Residual stress distributions for large equal angles with varying thickness are shown in Figure 6.22. The line along which the stresses were extracted is shown in Figure 6.12 as a red line. The size of the large equal angles was kept constant at 150 mm, while the length of the angle was kept constant at 60 mm. The shapes of the curves are similar to those in Figure 6.16. The graphs for the different thicknesses are very close to each other and barely distinguishable from one another. As was the case for small angles, the line beyond the peened region is very shallow in slope.

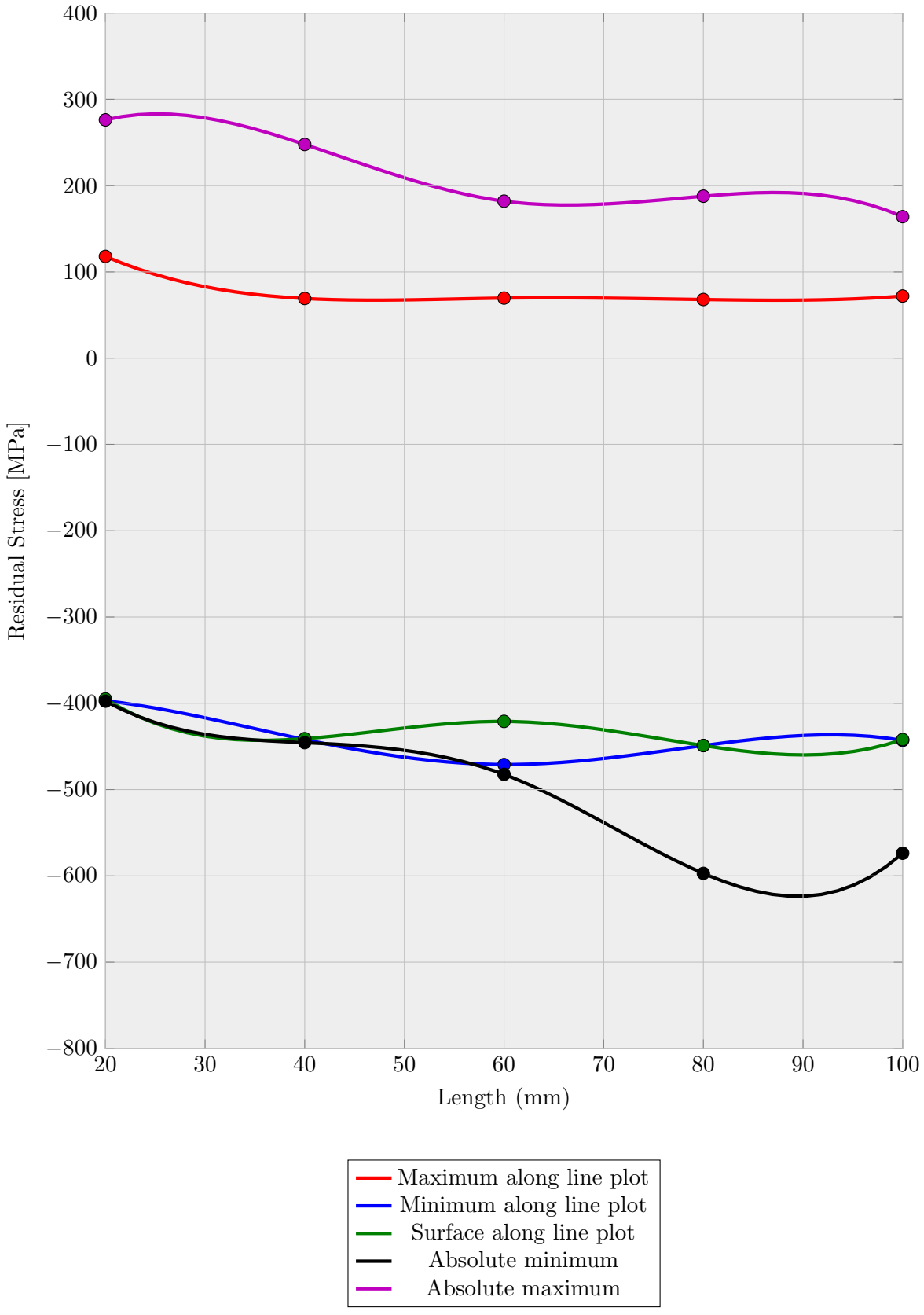

Figure 6.21: *Variation of some critical stresses with respect to length of small equal angles – x direction*

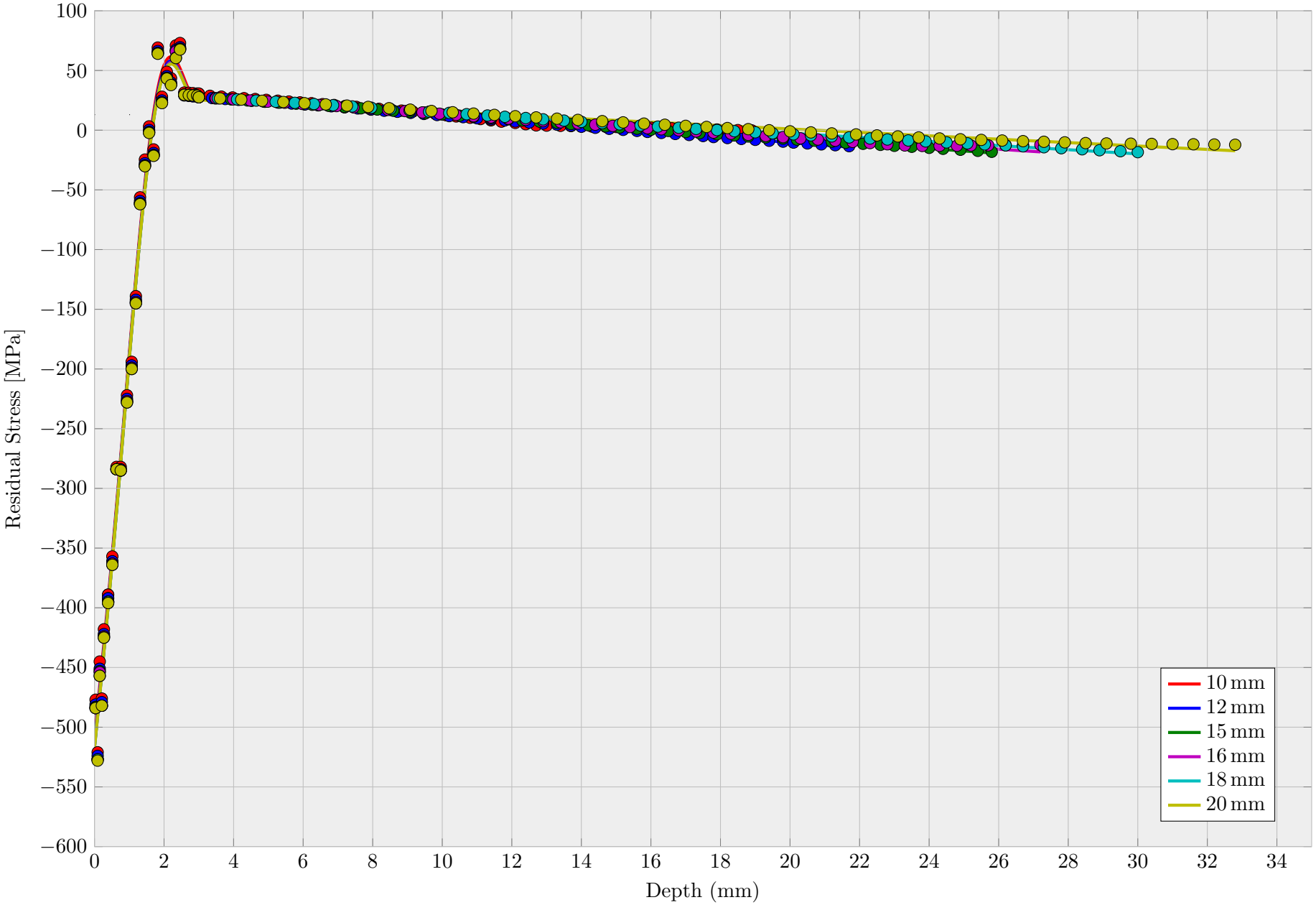

Figure 6.22: *Residual stress distributions in large equal angles of varying thickness – x direction*

Figure 6.23 shows the variation of different stresses with respect to thickness of the equal angle. The stresses are remarkably steady across the range of thickness, with the exception of the surface stress, which decreases in magnitude between 10 mm and 12 mm thickness.

The absolute maximum stress is steady at around 160 MPa. The maximum along the line plot is around 70 MPa for all thicknesses. The magnitudes of the absolute minimum and minimum along the line plot are both around 525MPa for all thickness.

The magnitude of the surface residual stress rises sharply from around 420 MPa to around 270 MPa, after which it remains steadily around that value.

2.3.2 Varying Size of Large Equal Angles

Residual stress distributions for large equal angles with varying size are shown in Figure 6.24. The line along which the stresses were extracted is shown in Figure 6.12 as a red line. The thickness of the large equal angles was kept constant at 12 mm, while the length of the angle was kept constant at 60 mm. The shapes of the curves are similar to those in Figure 6.22. Once again, the graphs for the different sizes are very close to each other and barely distinguishable from one another. As was the case for small angles, the lines beyond the peened regions are very shallow in slope. The slope generally decreases with increasing size.

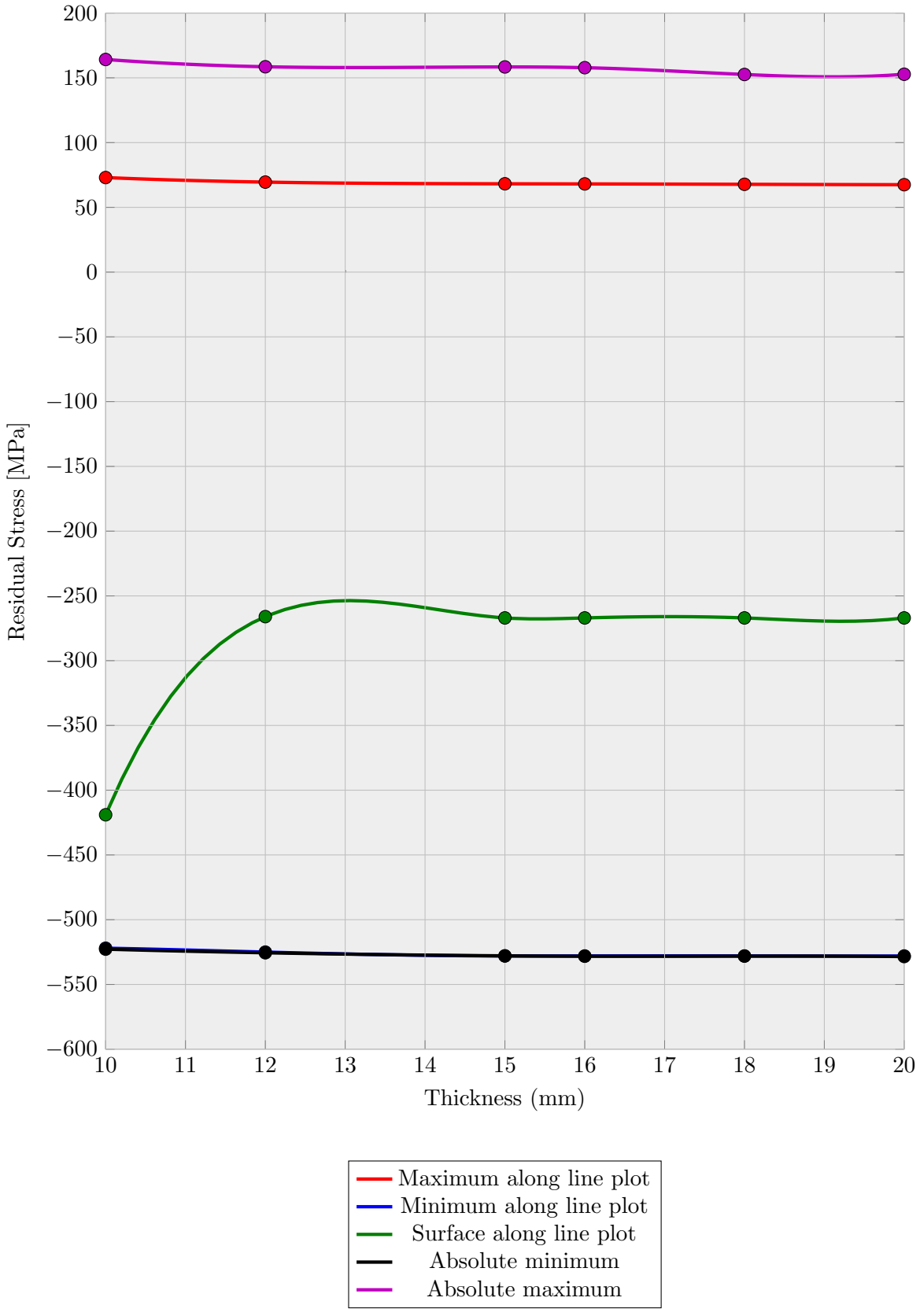

Figure 6.23: *Variation of some critical stresses with respect to thickness of large equal angles – x direction*

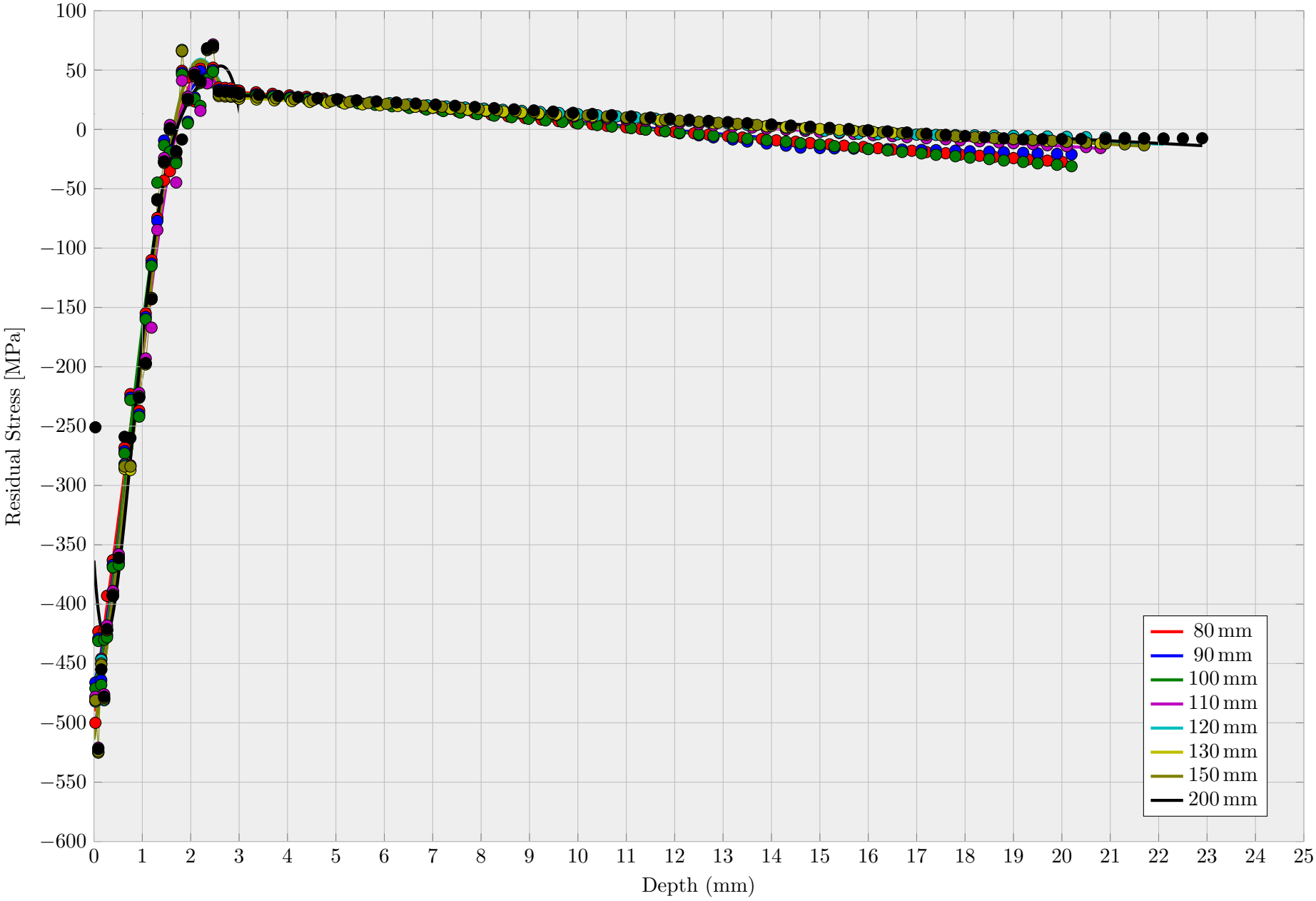

Figure 6.24: *Residual stress distributions in large equal angles of varying size – x direction*

Figure 6.25 shows the variation of different stresses with respect to size of the equal angle. The stresses do not vary much across the range of sizes, with the exception of the surface stress, which oscillates quite significantly over the range of sizes.

The absolute maximum stress varies between 170 MPa and 160 MPa, decreasing slightly with increasing size. The maximum along the line plot, on the other hand, increases slightly from 50 MPa to 70 MPa, with increasing size.

The absolute minimum residual stress occurs along the line plot for all sizes. The magnitude of the minimum residual stress increases slightly from around 500 MPa to 520 MPa.

The magnitude of the surface residual stress oscillates between a maximum of 470 MPa and a minimum of 260 MPa.

2.3.3 Varying Length of Large Equal Angles

Residual stress distributions for large equal angles with varying length are shown in Figure 6.26. The line along which the stresses were extracted is shown in Figure 6.12 as a red line. The size of the large equal angles was kept constant at 150 mm, while the thickness of the angle was kept constant at 12 mm. The shapes of the curves are similar to those in Figure 6.22. Once again, the graphs for the different lengths are very close to each other, but are more distinguishable than in Figure 6.24 and Figure 6.22. As was the case for small angles, the lines beyond the peened regions decrease in slope, as length increases.

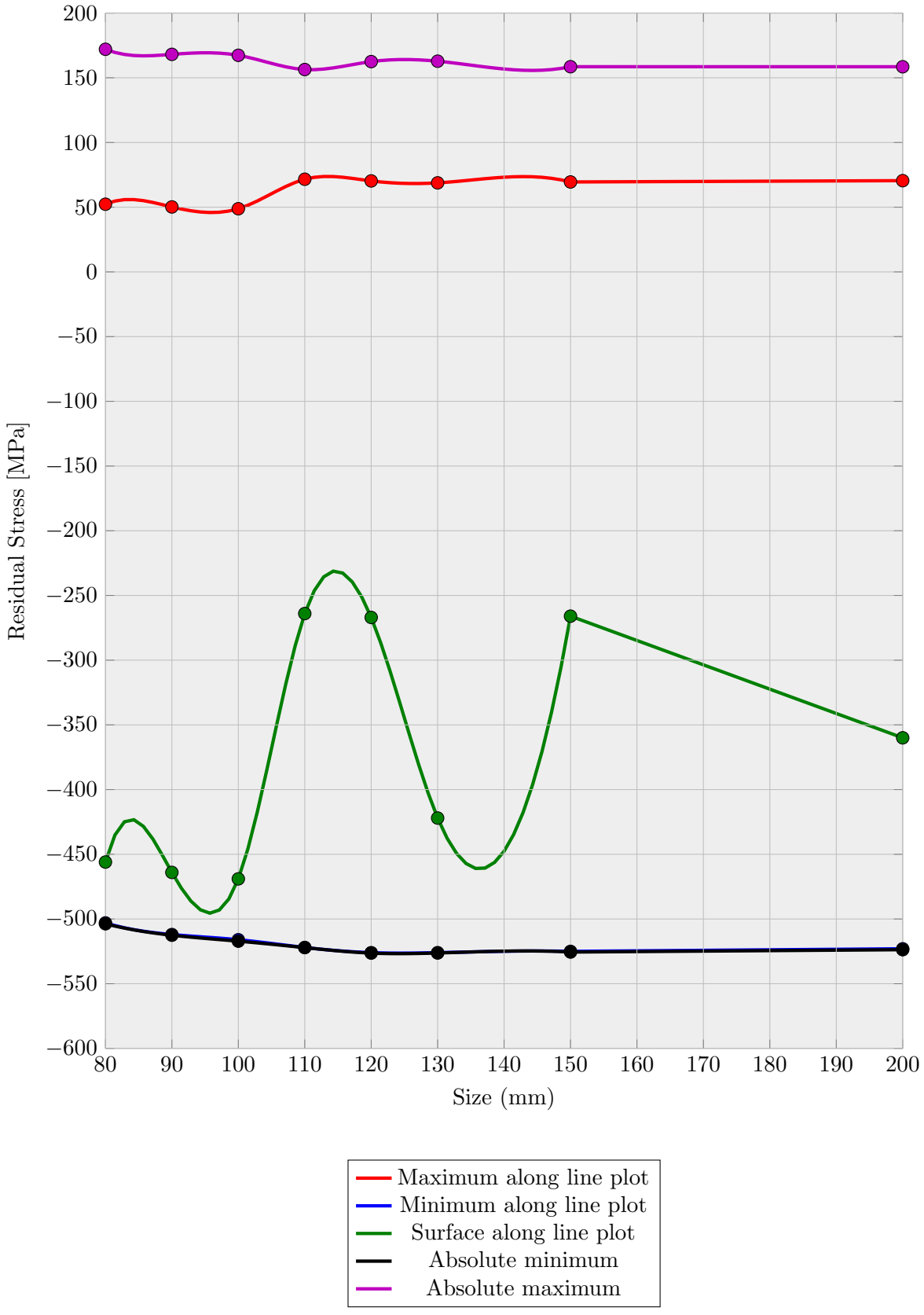

Figure 6.25: *Variation of some critical stresses with respect to size of large equal angles – x direction*

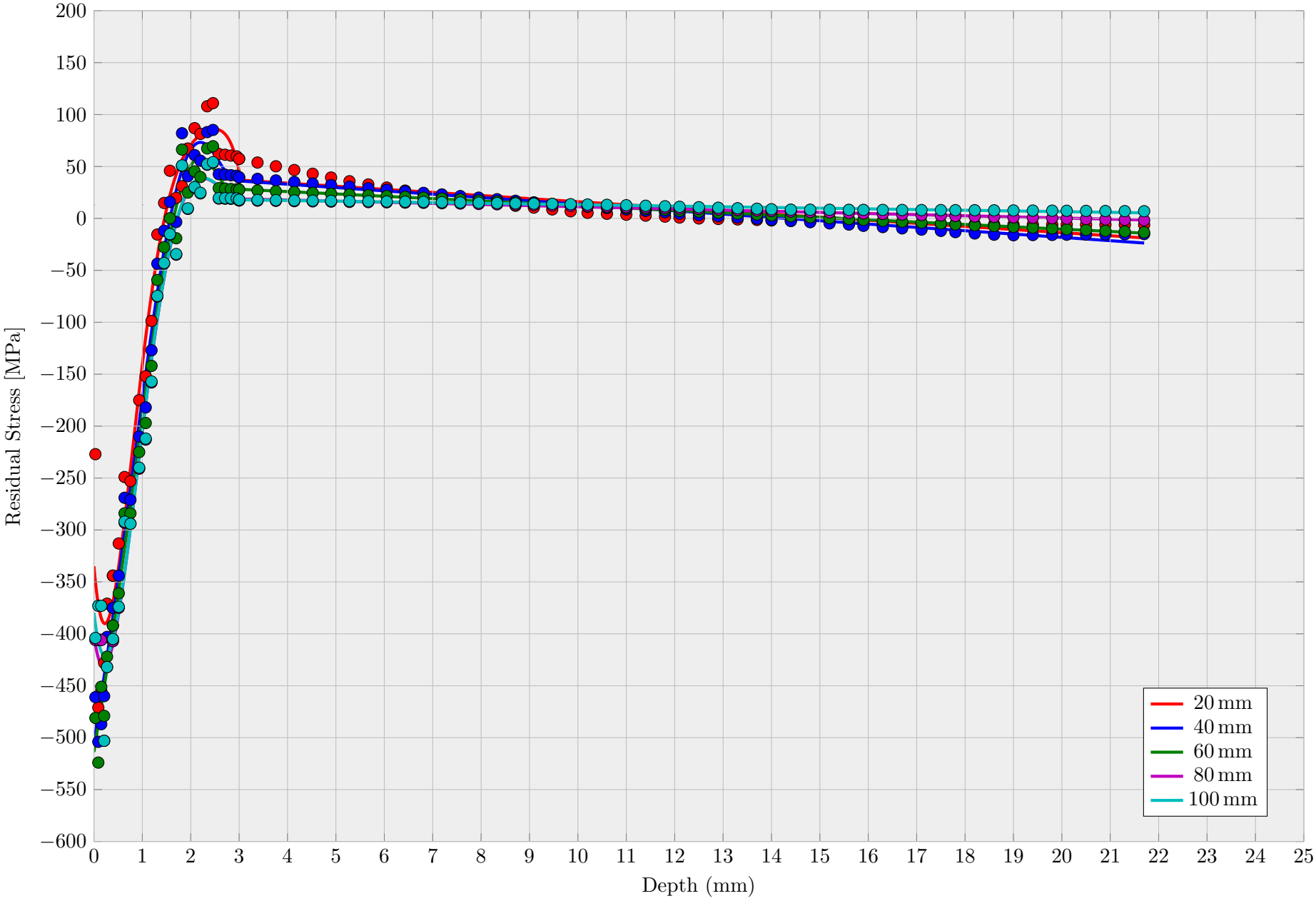

Figure 6.26: *Residual stress distributions in large equal angles of varying lengths – x direction*

Figure 6.27 shows the variation of different stresses with respect to length of the equal angle. The variation of stresses is more marked than it is for thickness or size.

The absolute maximum stress varies between 170 MPa and 150 MPa, decreasing with increasing size. The maximum along the line plot decreases quite significantly from around 110 MPa to 50 MPa.

The absolute minimum residual stress occurs along the line plot for lengths less than 80 mm. For lengths greater than 80 mm, the absolute minimum diverges from the minimum along the line plot. The magnitude of the minimum residual stress is around 480 MPa at a length of 20 mm. The magnitude of the absolute minimum then increases to about 580 MPa, while the magnitude of the minimum along the line plot increases to around 500 MPa.

The magnitude of the surface residual stress oscillates between a maximum of 400 MPa and a minimum of 220 MPa.

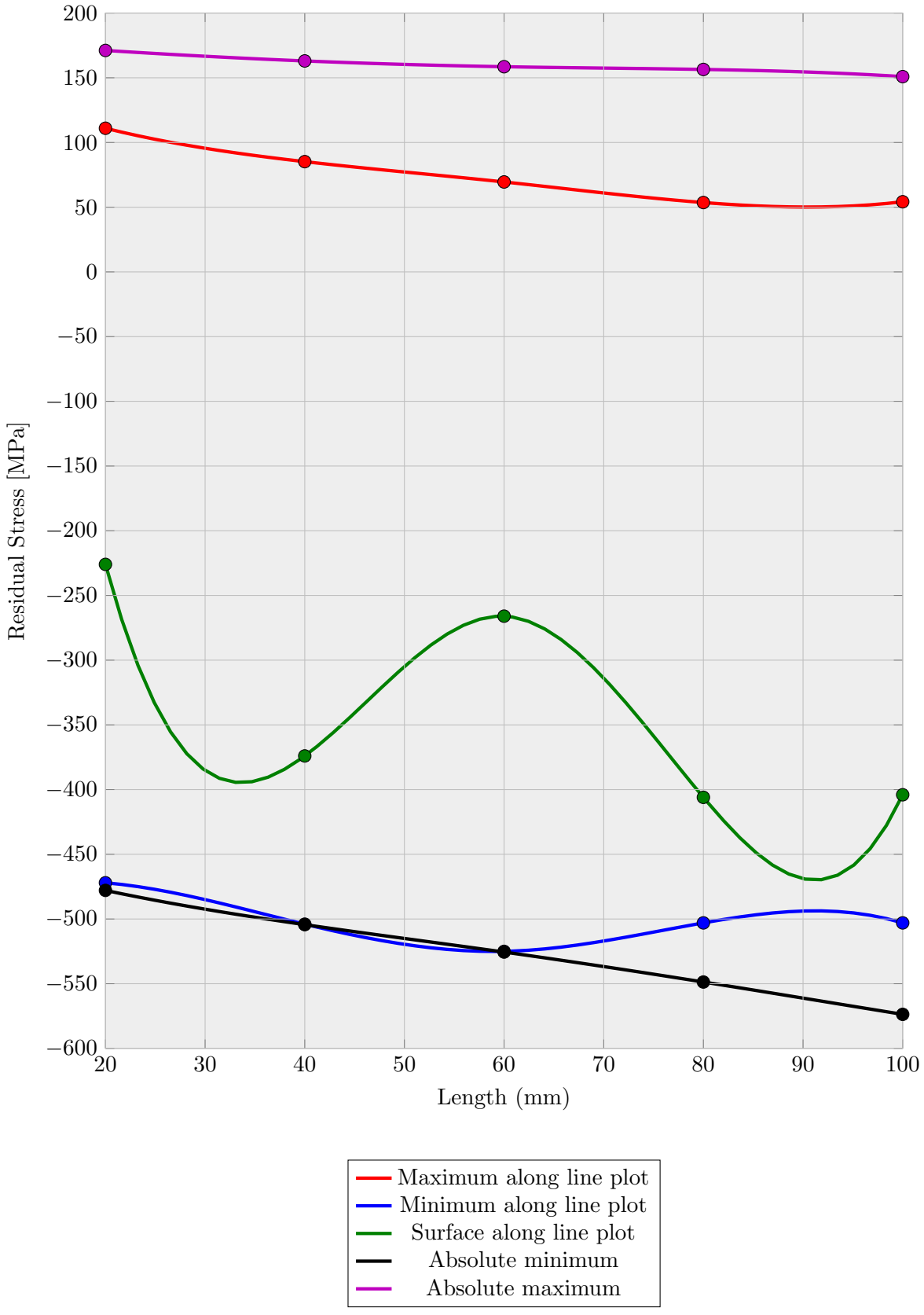

Figure 6.27: *Variation of some critical stresses with respect to length of large equal angles – x direction*

3 Residual Stresses in Channels

3.1 Base Models

This section deals with residual stresses in standard C-channels. The parameters of the angles were varied according to ISO 657/11-1980(E) standards. A channel is fully defined by its height and length. The base model has a height of 80 mm and length of 30 mm and is depicted in Figure 6.28.

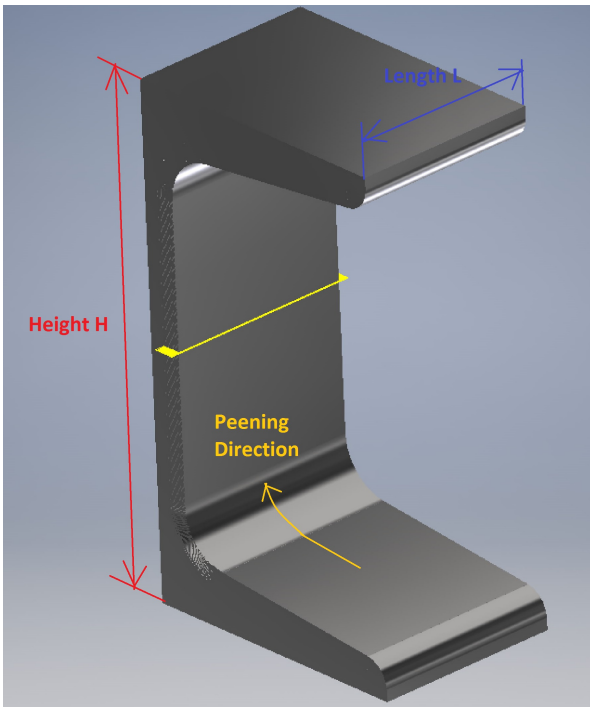

Figure 6.28: *Base CAD model of the c-channel*

Similar to the angle study, the scan direction of peening was along the curvature of the concave fillet, with the step direction in the transverse direction. Noting that the model was symmetric about two planes (one bisecting the length and the other bisecting the cross section), the model was reduced to a quarter of its original size, as shown in Figure 6.29.

The model was divided into four major parts:

- The "core" of the model, in which the eigenstrains are zero, including the convex fillets at the ends of the legs
- The volume beneath the concave fillet, which is part of the peened region
- The volume beneath the flat surface of the web, which is part of the peened region

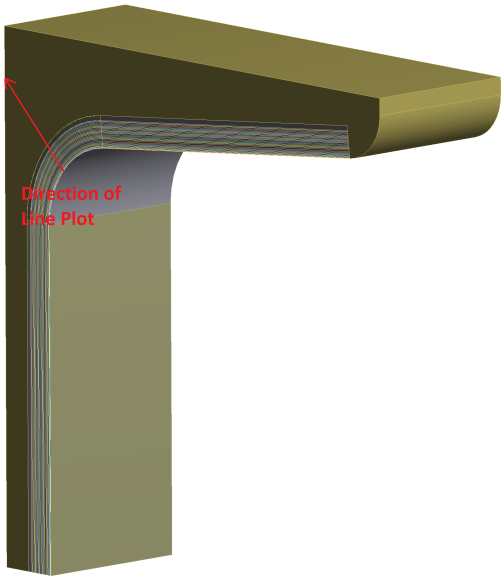

Figure 6.29: *FEM model of the base channel*

- The volume beneath the skew surface of the flange, which is part of the peened region

The latter three divisions were further subdivided into the necessary layers to impose the eigenstrains. Three local co-ordinate systems were created. A cylindrical co-ordinate system for the concave fillet with an ID of 100, a Cartesian co-ordinate system with an ID of 110 for the peened part of the web, and another with an ID of 120 for the peened part of the flange. The origin of the cylindrical co-ordinate system was placed at the centre of the concave fillet to ensure correct imposition of the eigenstrains. The co-ordinate systems are depicted in Figure 6.30. As is apparent from Figure 6.30, the co-ordinate system for the flange was oriented with the principal axis normal to the surface.

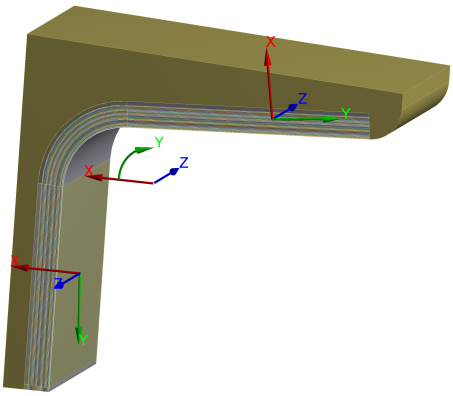

Figure 6.30: *Co-ordinate systems used to implement eigenstrains in channels*

The directions of the co-ordinate systems are similar to those used for the fillet study. The x axis is normal to the surface, corresponding to the z axis of Sample B15 co-ordinate system.

The y axis is in the scan direction, corresponding to the y axis of Sample B15 co-ordinate system. The z axis is in the step direction, corresponding to the x axis in Sample B15 co-ordinate system.

A named selection for each of the peened regions was created. These were called "Top", "Side", and "Curve" for the flange, web, and concave fillet, respectively. The tasks of the APDL script included under the analysis branch is outlined below.

1. Enter the preprocessing environment.
2. Select the named selection "Top".
3. Modify all selected elements to have the local Cartesian co-ordinate system (ID 120) as the element system.
4. Select the named selection "Side".
5. Modify all selected elements to have the local Cartesian co-ordinate system (ID 110) as the element system.
6. Select named selection "Curve".
7. Modify all selected elements to have the local cylindrical co-ordinate system (ID 100) as the element system.
8. Select all bodies
9. Enter the Solution processor.

Figure 6.31 depicts the residual stress field in the base channel after applying the eigenstrains from Sample B15. The front cross-section represents the central cross section of the channel. The residual stress field is quite uniform throughout the peened region, with the exception of the ends of the channel, which have tensile surface stresses and lower compressive residual stresses near the surface. The tensile stresses on the concave fillet are especially high, compared to the stresses in the rest of the channel.

The stresses in the non-peened region – including the convex fillet at the tip of the flange – are tensile. The maximum tensile stress occurs at the junction between the peened and non-peened regions.

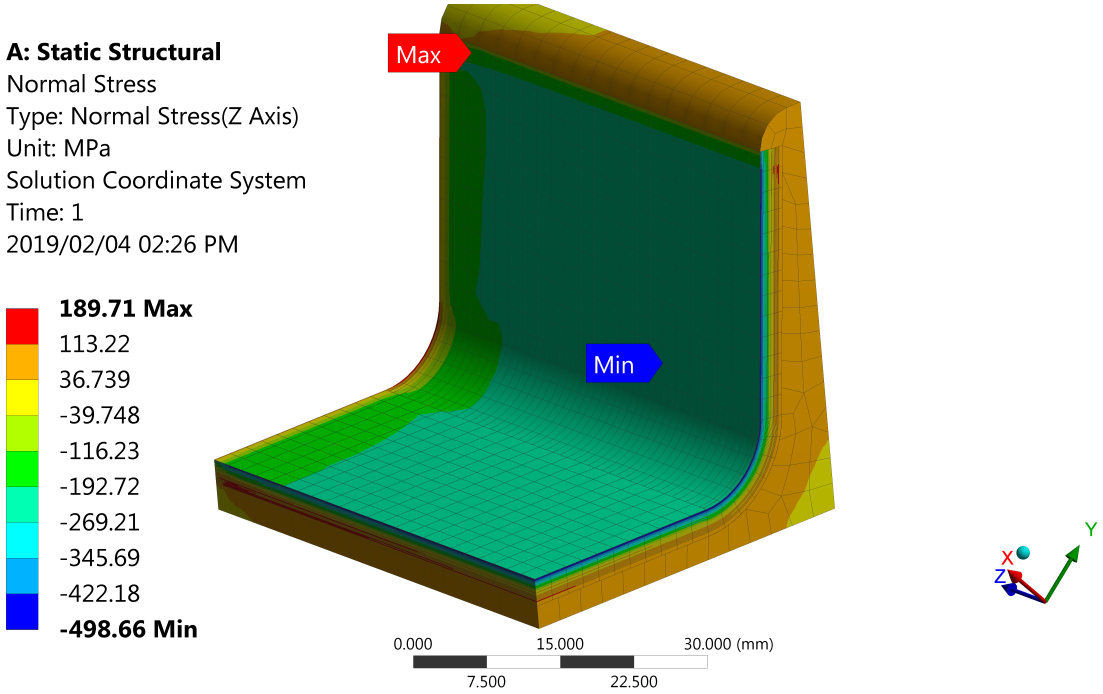

Figure 6.31: *Residual stresses in base channel*

3.2 Varying Size of Channel

Residual stress distributions for channels with varying sizes are shown in Figure 6.32. The line along which the stresses were extracted is shown in Figure 6.29 as a red line. The length of the channels was kept constant at 30 mm. The shapes of the curves are similar to the those of the structural angles. The slopes of the lines beyond the peened region tend to decrease with increasing height of the channel. However, the slopes do not increase very much, and overall, the height of the channel does not seem to have a great impact on the residual stresses.

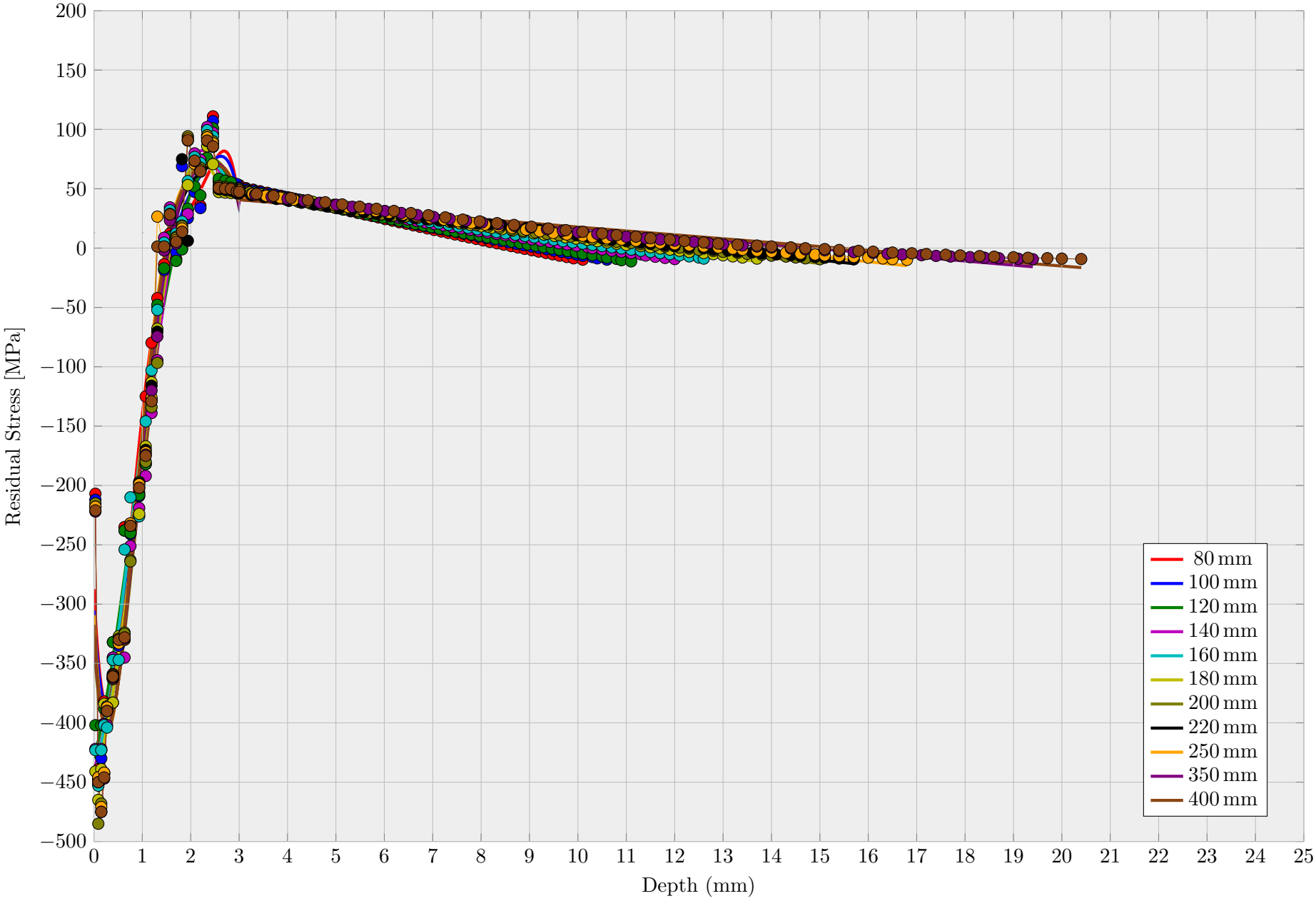

Figure 6.32: *Residual stress distributions in channels of varying size – x direction*

Figure 6.33 shows the variation of different stresses with respect to size of the channel. The absolute maximum stress and surface stress vary quite bit, but the other stresses are quite steady over the range of sizes.

The absolute maximum stress increases from a stress of approximately 190 MPa to a stress of about 265 MPa – at a size of 120 mm. It decreases, thereafter, to a value of around 160 MPa. The maximum along the line plot decreases slightly from around 110 MPa to 90 MPa.

For channel sizes greater than 160 mm, the absolute minimum and minimum along the line plot are coincident. The magnitude of both increases to around 500 MPa. For lengths greater than 80 mm, the absolute minimum diverges from the minimum along the line plot. The magnitude of the minimum residual stress is around 480 MPa at a length of 20 mm. The magnitude of the absolute minimum then increases to about 580 MPa, while the magnitude of the minimum along the line plot increases to around 500 MPa. The absolute minimum has a minimum magnitude of around 470 MPa, while the minimum along the line plot has a minimum of around 440 MPa.

The magnitude of the surface residual stress oscillates between a maximum of 475 MPa at a channel size of 220 mm, and a minimum of 200 MPa at a channel size of 80 mm.

3.3 Varying Length of Channel

Residual stress distributions for channels with varying lengths are shown in Figure 6.34. The line along which the stresses were extracted is shown in Figure 6.29 as a red line. The size of the channels was kept constant at 80 mm. The shapes of the curves are similar to what has been seen previously. It is apparent that the length of the channel has a significant effect on the residual stresses, at least for small lengths. The slopes of the lines beyond the peened region tend to decrease with increasing length of the channel. In the peened region, the curves tend to shift downwards with increasing length.

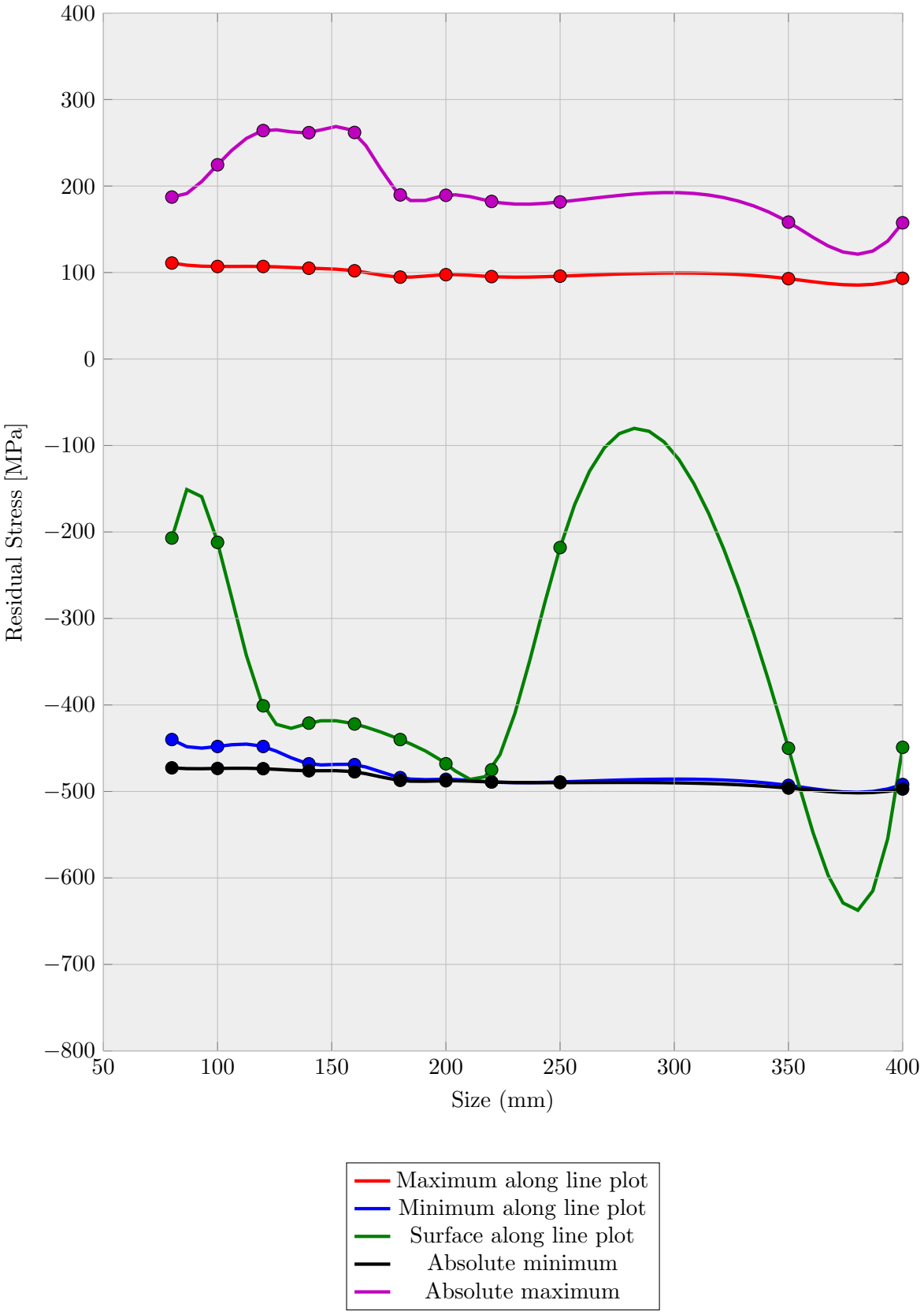

Figure 6.33: *Variation of some critical stresses with respect to size of channels – x direction*

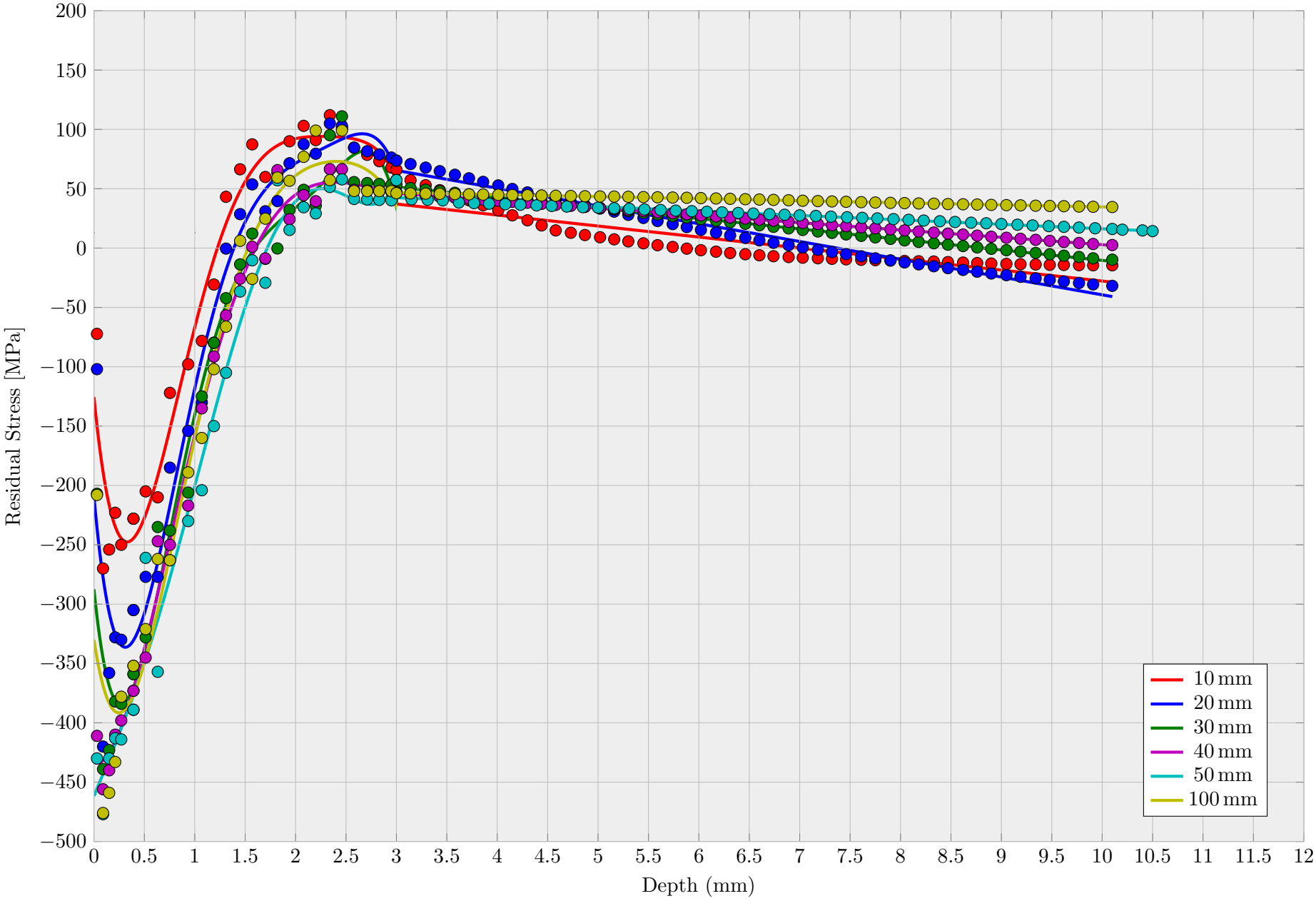

Figure 6.34: *Residual stress distributions in channels of varying lengths – x direction*

Figure 6.35 shows the variation of different stresses with respect to length of the channel. The stresses vary significantly with changing length.

The absolute maximum stress oscillates between 180 MPa and 380 MPa. The maximum along the line plot decreases from about 130 MPa to about 60 MPa – at a length of 50 mm. It then increases to 100 MPa at 100 mm

Between lengths of 10 mm and 50 mm, the magnitude of the absolute minimum varies between 280 MPa and 540 MPa. It then declines slightly to around 500 MPa at 100 mm. The minimum along the line plot varies between 270 MPa and 480 MPa, across the entire range of lengths.

The magnitude of the surface residual stress oscillates between a maximum of 460 MPa at a length of 100 mm, and a minimum of 200 MPa at a length of 30 mm.

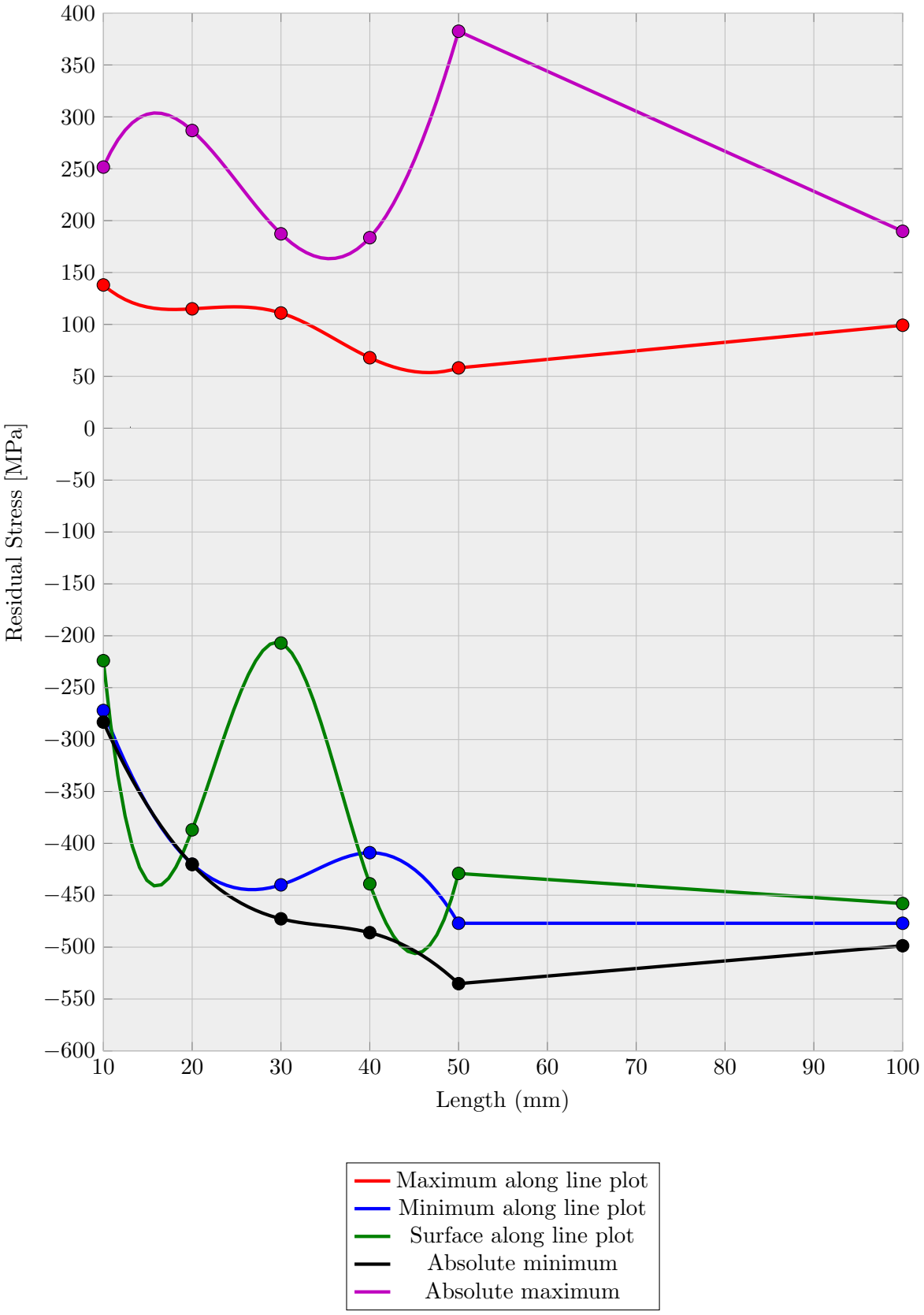

Figure 6.35: *Variation of some critical stresses with respect to length of channels – x direction*

4 Discussion

The aim of this chapter was to extend the study of chapter 4 to some geometries commonly encountered in engineering practice. The question motivating this study is, "Given the eigenstrain distribution in a laser peened cuboid sample; what is the residual stress distribution in some common engineering geometries?" The geometries studied, along with the specific parameters, are recounted below. All the studies were conducted using FEM models and eigenstrain data from Sample B15.

1. The effect of fillet radius, length, and size on residual stresses in a filleted square bar subjected to LSP was studied.
2. The effect of leg thickness, length, and size on residual stresses in small and large standard structural angles subjected to LSP was studied.
3. The effect of length and size on residual stresses in standard C-channels subjected to LSP was studied.

Like in chapter 4, the Principle of Transferability of Eigenstrains formed the basis of this study (See section 9 of chapter 2). The accuracy of the results depends on whether this principle holds for each individual geometry, or not. For the fillet study, the fillet radius and size could conceivably affect the eigenstrains by focussing the shock waves. However, in this context, the bulk of the filleted bars are so much larger than the peened depth, that it seems safe to assume that no shock wave reflection occurs, even for smaller specimens. A similar argument could be made with regards to the size of channels.

In structural angles, the thickness of the legs may conceivably affect the attenuation of shock waves, thereby affecting eigenstrain distribution. For the large angles, this is unlikely due to the large leg thickness. The size parameter of angles mostly affects the length of the legs and the size of the concave fillet. The length of the angles changes transversely to the direction of propagation of the shock waves, and should not affect the attenuation of the shock wave. The concave fillet does affect the dimension of the material in the direction of propagation of the shock wave, but the effect is small. A more substantial potential modifier of eigenstrains in concave geometries is shock dispersal, due to the divergence of the peened geometry in the direction of propagation of the shock wave. Overall, the size of the angles should not affect the attenuation of shock waves much. In all the geometries, length is transverse to the direction of propagation of the shock wave and should not affect the eigenstrain distribution. In summary, the only concern with regards to the Principle of Transferability of Eigenstrain holding, is for structural angles with small thickness.

For each parameter, line plots of residual stresses were extracted. The locations of the line plots were chosen to study the stress distributions through the most interesting features of each geometry. The line plots for the fillet study do not vary linearly beyond the peened region, as expected. They seem to vary in an exponentially decaying manner, dropping sharply to a value and then changing very little. This was attributed to the small length of the base sample, as it is quite clear from Figure 6.9 that the distribution beyond the peened region approaches a straight line for larger lengths. The channels and angles have distributions similar to what has previously been seen.

The variation of five critical stresses with respect to each of the parameters was studied. The surface stress along the line plot is compressive for all parameter combinations of all geometries. The maximum tensile stresses tend to decrease with increasing size, if they are not constant. The relationship between the maximum compressive residual stresses and size seems to be a bit more nuanced. However, one consistency is that the maximum compressive stresses appear to increase in magnitude with increasing lengths, across all geometries.

It is quite apparent that as the values of the parameters increase for all geometries, the stresses tend to converge towards stable values. In fact, in some cases, particularly the large angles, the residual stresses are almost constant across the range of the parameter.

5 Conclusions

- The effects of fillet radius, length, and size of filleted square bars on residual stresses arising from a specific eigenstrain distribution were studied.
- The effects of leg thickness, length, and size of structural angles on residual stresses arising from a specific eigenstrain distribution were studied.
- The effects of length and size of C-channels on residual stresses arising from a specific eigenstrain distribution were studied.
- If the assumption of insensitivity of eigenstrain to geometry holds, the results represent the residual stresses that would arise if the aforementioned components were laser peened with the same process as Sample B15.
- In small angles with small leg thickness, the geometry may affect the attenuation of shock waves, thereby affecting eigenstrain distribution.
- The tensile stresses in the geometries studied seem to decrease with increasing gross size.
- The surface residual stress along the line plot is compressive in geometries of all sizes.

- The maximum compressive stresses tend to increase with increasing length, for all the geometries studied.
- The general shape of the residual stress line plots resemble those found in cuboid samples, except for the fillets, which exhibit exponentially decaying behaviour for small lengths.

Chapter 7 Discussion

The first objective of this project was to validate and compare various eigenstrain models on their ability to predict residual stresses in components subjected to LSP. A benchmark sample (Sample B15) was chosen to validate the methods against. Five methods were tested, but only three yielded results. Although none of these methods were categorically proven to be better than the others, Coratella's method was eventually chosen as the best, due to its simplicity.

The method requires a line plot of residual stress to extract the eigenstrain distribution. The eigenstrain distribution is then imposed on an FEM model of the desired geometry, yielding the full residual stress fields in that geometry. ANSYS Workbench was used for this project. The more accurate the measured residual stress data is, the better the prediction will be. Using a variety of measurement techniques is recommended, as each measurement technique has different advantages and disadvantages, which can be used to complement and offset each other.

The method of imposing eigenstrains in this project was to separate the model into layers near the surface, and impose the relevant eigenstrains as orthotropic thermal coefficients of expansion, subject to temperature change of $1°C$, at the correct depth. This method obviously is subject to discretisation error. The greater the number of layers, the lower this error will be, but greater computational resources will be required. An alternative method of imposing eigenstrains is to use the equation of the eigenstrain distribution to impose the coefficients of expansion directly to the nodes. However, this is more difficult to achieve and requires a good grasp of the APDL language. This latter method may be more accurate than the method used in this project.

The remaining objectives were to study the effects of geometry on residual stress in cuboid samples, spheres, cylinders, fillets, structural angles, and C-channels, subjected to the same LSP process. Coratella's method was used to achieve this part of the project. The eigenstrains extracted from the benchmark sample were imposed on various parameter combinations of these geometries, varying one parameter at a time. The critical assumption in all these

studies is that the eigenstrains are not dependent on geometry. This allowed the usage of the same eigenstrain distribution for all the parameter combinations of the geometries. This assumption is based on the Principle of Transferability of Eigenstrain.

A common concern in all the geometries studied, is regarding whether the Principle of Transferability of Eigenstrain holds or not. It was postulated that if the geometric parameter affects the attenuation of the shock wave, it would affect the eigenstrain distribution, modifying it from what is expected. The phenomenon of shock wave reflection, which manifests in thin samples, was identified as a potential modifier of the eigenstrain distribution. Similarly, shock focussing in convex geometries and shock dispersal in concave geometries might modify the eigenstrains from expected values. This could impact the accuracy of predictions in thin/small samples. If it is determined in a particular parameter study that the aforementioned assumption does not hold, then the study merely represents the effect of the particular parameter on residual stresses arising from a constant eigenstrain distribution. In the context of this project, the Principle of Transferability of Eigenstrain provides the vital link between a specific eigenstrain and a specific peening process. The study in section 6 of chapter 3, along with similar studies in the literature, somewhat justifies the assumption of insensitivity of eigenstrain to geometric parameters.

A weakness of the current method, revealed in section 6 of chapter 3, is in predicting residual stresses through peened sharp edges. The reason is that peening over a sharp edge leads to overlapping peened regions, which creates a more complex eigenstrain distribution than anticipated. Due to the non-linearity of plastic strain, it is difficult to accurately predict the resultant eigenstrain distribution using available data. This weakness can only be overcome by creating a strategy to easily and efficiently predict the complex eigenstrain distribution in such situations.

A common thread found in all the geometries studied is the tendency for the residual stresses to converge on specific values as the gross size of the models increase. This means that residual stresses due to LSP are only dependent on size in samples which are small relative to the peened depth. In larger geometries, the size of the sample does not affect the residual stresses that arise from LSP.

Another common thread is that the maximum tensile stresses tend to decrease with increasing size. Generally, the maximum compressive stress tends to increase in magnitude with increasing size, though this is not always the case. Given that the aim of LSP is to enhance fatigue life of components, the goal should be to increase the magnitude of compressive stresses near the surface and decrease the maximum tensile residual stress. Based on the two leading statements of this paragraph, it may tentatively be stated that LSP has a more positive effect on larger components than on smaller ones.

Compared to process modelling, which models the physical processes involved in the laser peening process, this method is simpler, less computationally demanding and less time-consuming. The drawback is that it requires the line plot of residual stresses in a sample, which has to be measured. In practice, the best way to make use of this method as a predictive tool in industry, would be to laser peen flat plates with a variety of thickness, extract the eigenstrains and apply them to a more complex geometry in which it is desired to know the residual stress field. However, more empirical information on the relationship between geometry and eigenstrains is required to make this a reality. On a cautionary note, the flat plates have to be made from the same material and be subject to the same peening parameters as the geometry of interest.

In chapter 1, it was mentioned that a tool for optimising the LSP process parameters is required to realise the full potential of this technology in industry. This in turn, requires a predictive tool that can be integrated into the optimisation framework. The predictive tool should be able to take the relevant parameters as an input and predict the resulting residual stress field. As it stands, eigenstrain methods do not meet this requirement. The reason for this is that this method does not take the peening and material parameters directly as an input, but requires measured data. To be integrated into an optimisation algorithm, a model for predicting eigenstrains given material and process parameters needs to be developed. If this is done, the aforementioned model can be used to predict eigenstrains and the eigenstrains can then be imposed on a model of the prospective peened sample to predict the residual stress field.

Chapter 8 Conclusions

- Five Eigenstrain models were validated and compared to each other, in terms of predictive performance.
- Coratella's method was chosen as the best because it is simple without compromising on accuracy.
- A better prediction results from eigenstrains extracted from more accurately measured residual stresses.
- Use of a variety of residual stress measurement techniques can enhance accuracy.
- The Principle of Transferability of Eigenstrain was tested and found to hold generally.
- As it stands, the method used has a weakness in predicting residual stresses through peened sharp edges.
- The parameter variation of residual stresses in cuboid samples, spheres, cylinders, fillets, structural angles, and channels was studied.
- For all geometries, residual stresses are insensitive to changes in size for larger geometries.
- For smaller geometric parameters, the attenuation of the shock wave might be affected by the geometry, leading to a different eigenstrain distribution than expected.
- It appears that there is a tendency for LSP to have a more positive impact on larger samples.

Chapter 9 Recommendations

The residual stresses in spheres, cylinders, and common engineering geometries was predicted on the assumption that geometry does not affect the eigenstrain distribution. As pointed out in the discussion, there are times when this assumption is called into question. Thus, the accuracy of those results is uncertain. Validating the results against empirical data, as was done for the cuboid samples, would grant more clarity on the accuracy of the results. Conducting this study, one could easily go a step further, and study the effect of geometry on eigenstrains and the limits of the Principle of Transferability of Eigenstrain. This knowledge is imperative if this method is to be used in industry.

As mentioned in chapter 7, a method for predicting eigenstrains given process and material parameters is required to use eigenstrain methods to optimise LSP process parameters. One way of achieving this may be to use process modelling to predict the eigenstrains. The obvious question that this elicits is: Can't process modelling just be used to predict the residual stresses directly, without eigenstrain methods? While this is a legitimate question, the eigenstrain method has one advantage, which may warrant its inclusion in such a model: it can be used to predict residual stresses across various geometries. The major disadvantage of process modelling, though, is that it is computationally expensive and time consuming, especially when the peening involves multiple overlapping shots, as was the case for the samples used in this research.

Another solution may be to use statistical methods to predict what the eigenstrains should be given a parameter set. However, for this to work in reality would require a very extensive database, spanning various materials, laser power densities, spot sizes, etc. To compile such a database would prove to be very expensive. If simple analytical or empirical formulae for estimating the relationships between eigenstrains and some parameters is developed, this may make the above task easier.

Chapter 10 Research Contributions

As mentioned in the acknowledgments, this project was funded by the Centre of Excellence in Strong Materials (CoE-SM). The CoE-SM holds an annual workshop, in which each funded student is required to present a poster. Parts of this work were presented in the form of a poster at the Annual CoE-SM/AMSEN Student Presentation Workshop. The poster is included in Appendix E.

Parts of this work were accepted for oral presentation at the 7th International Conference on Laser Peening and Related Phenomena, held in Singapore from the 17th to 22nd of June 2018. However, due to a lack of funding, the author could not personally present the work. A poster was instead prepared, which was presented on behalf of the author. The Acceptance letter, abstract, and presented poster are included in Appendix E. The details of the posters are summarised below:

- R. Omar and C. Polese, "Prediction of Residual Stresses Due to Laser Shock Peening Using Eigenstrain Methods". Poster Presentation at *Annual CoE-SM/AMSEN Student Presentation Workshop*. Johannesburg. 2018
- R. Omar and C. Polese, "Prediction of Residual Stresses in AA7075 Due to Laser Shock Peening Using Eigenstrain Methods". Poster Presentation at *7th International Conference on Laser Peening and Related Phenomena*. Singapore. 2018

A paper based on the work in this dissertation is currently under preparation for submission to an international journal.

References

[1] K. Ding and L. Ye. *Laser Shock Peening: Performance and Process Simulation*. Woodhead Publishing Ltd, 2006. ISBN: 13: 978-1-84569-109-7.

[2] S. Coratella et al. 'Application of the eigenstrain approach to predict the residual stress distribution in laser shock peened AA7050-T7451 samples'. In: *Surface and Coatings Technology* 273 (2015), pp. 39–49.

[3] H. Kamkarrad, S. Narayanswamy and X. Tao. 'Feasibility Study of High Repetition Rate Laser Shock Peening of Biodegradable Magnesium Alloys'. In: *International Journal of Manufacturing Technology* (2014).

[4] LSP Technologies. *Transparent Overlay for Laser Peening*. Date Accessed: 20/02/2018. URL: https://www.lsptechnologies.com/transparent-overlay-for-laser-peening/.

[5] I. Altenberger and B. Scholtes. 'Improvement of Fatigue Lifetime of Mechanically Surface Treated Materials in the Low Cycle Fatigue Regime'. In: *Surface Treatments IV*. Ed. by C. Brebbia and J. Kenny. WIT Press, Southampton, UK, 1999, pp. 281–290.

[6] P. Peyre and R. Fabbro. 'Laser shock processing: a review of the physics and applications'. In: *Optical and Quantum Electronics* (1995), pp. 1213–1229.

[7] L. Wagner and G. Lutjering. 'Influence of Shot Peening on the Fatigue Behaviour of Ti-Alloys'. In: *Shot Peening*. Pergamon Press, 1981, pp. 453–460.

[8] C. Rodopoulos et al. 'Effect of Controlled Shot Peening and Laser Shock Peening on the Fatigue Performance of 2024-T351 AluminumAlloy'. In: *Journal of Materials Engineering and Performance* 12.4 (2003), pp. 414–419.

[9] A. Clauer. 'Laser Shock Peening For Fatigue Resistance'. In: *Surface Performance of Titanium* (1996), pp. 217–230.

[10] King et al. 'Effects of fatigue and fretting on residual stresses introduced by laser shock peening'. In: *Materials Science and Engineering A* (2006), pp. 12–18.

[11] M. Morales et al. 'Analysis of plasma thermal surface effects on the residual stress field induced by LSP in A12024-t351'. In: *Journal of Optoelectronics and Advanced Materials* 12 (2010).

[12] W. Steen and J. Mazumder. *Laser Material Processing*. Springer, 2010.

[13] R. Serway and J. Jewett. *Physics for Scientists and Engineers with Modern Physics*. Cengage Learning, 2014.

[14] P. Musler and D. Bauer. *High Power Laser-Matter Interaction*. Springer, 2010.

[15] L. Berthe et al. 'Shock waves from a water-confined laser-generated plasma'. In: *Journal of Applied Physics* 82.6 (1997), pp. 2826–2832.

[16] W. Benxin and CSYung. 'Laser pulse transmission through the water breakdown plasma in laser shock peening'. In: *Applied Physics Letters* 88.041116 041116 (2006).

[17] G. Elert. *Shock Waves*. Date Accessed: 20/02/2018. The Physics Hypertextbook. URL: https://physics.info/shock/.

[18] M. Boustie et al. 'Laser Shock Waves: Fundamentals and Applications'. In: *1st International Symposium on Laser Ultrasonics: Science, Technology and Applications*. July 16-18 2008, Montreal, Canada.

[19] R. Fabbro et al. 'Physics and applications of laser-shock processing'. In: *Laser Application* 10 (1998), pp. 265–279.

[20] P. Ballard et al. 'Residual stresses induced by laser-shocks'. In: *Journal de Physique IV* 1 (1991), pp. 487–494.

[21] R. Hibbeler. *Mechanics of Materials*. Eighth. Pearson, 2011.

[22] N. Rossini et al. 'Residual Stress Measurement'. In: *Applied Surface Science* (2000).

[23] A. DeWald and M. Hill. 'Eigenstrain-based model for prediction of laser peening residual stresses in arbitrary three-dimensional bodies'. In: *Journal of Strain Analysis for Engineering Design* 44 (2008). DOI: 10.1243/03093247JSA417.

[24] D. Askeland and P. Fulay. *Essentials of Materials Science and Engineering*. 2nd. Cengage Learning, 2010.

[25] Efunda. *The Definition of Stress*. Date Accessed: 20/02/2018. Efunda. URL: http://www.efunda.com/formulae/solid_mechanics/mat_mechanics/stress.cfm.

[26] Efunda. *Plane State of Stress*. Date Accessed: 20/02/2018. Efunda. URL: http://www.efunda.com/formulae/solid_mechanics/mat_mechanics/plane_stress.cfm.

[27] A. Korsunsky. 'Residual elastic strain due to laser shock peening: modelling by eigenstrain distribution'. In: *The Journal of Strain Analysis for Engineering Design* 41.3 (2006), pp. 195–204. DOI: DOI:10.1243/03093247JSA141.

[28] R. Budynas and J. Nisbett. *Shigleys Mechanical Engineering Design*. 10th. McGraw Hill, 2015.

[29] J. Johnson and R. Rohde. 'Dynamic deformation twining in shock-loaded iron'. In: *Journal of Applied Physics* 42.11 (1971), pp. 4171–4182.

[30] Peyre et al. 'Laser-shock processing of aluminium-coated 55C1 steel in water-confinement regime, characterization and application to high-cycle fatigue behaviour'. In: *Materials Science* 33 (1998), pp. 1421–1429.

[31] A. Korsunsky, G. Regino and D. Nowell. 'Variational determination of eigenstrain sources of residual stress'. In: *International Conference on Computational and Experimatnal Engineering and Science*. 2004.

[32] T. Jun. 'Development of the Eigenstrain Reconstruction Method for the Interpretation of Diffraction Stress Measurements in Engineering Components'. PhD thesis. Department of Engineering Science, University of Oxford, 2009.

[33] P. Withers and H. Bhadeshia. 'Residual stress Part 1 Measurement Techniques'. In: *Materials Science and Technology* 17.4 (2001), pp. 355–365. DOI: 10.1179/026708301101509980.

[34] P. Withers and H. Bhadeshia. 'Residual stress Part 2 Nature and Origins'. In: *Materials Science and Technology* 17.4 (2001), pp. 366–375.

[35] T. Jun and A. Korsunsky. 'Evaluation of residual stresses and strains using the Eigenstrain Reconstruction Method'. In: *International Journal of Solids and Structures* 47 (2010), pp. 1678–1686.

[36] A. G. Ramm. *Inverse Problems: Mathematical and Analytical Techniques With Applications to Engineering*. Springer, 2005. ISBN: 0-387-23218-4.

[37] A. Tarantola. *Inverse Problem Theory and Methods for Model Parameter Estimation*. Society for Industrial and Applied Mathematics, 2005. ISBN: 0-89871-572-5.

[38] S. Kabanikhin. 'Definitions and examples of inverse and ill-posed problems'. In: *Journal of Inverse and Ill-Posed Problems* (2008).

[39] S. Wright. *Optimization*. Encyclopaedia Britannica. 2018. URL: https://www.britannica.com/science/optimization.

[40] P. Ngatchou, A. Zarei and M. El-Sharkawi. *Pareto Multi Objective Optimization*. Date Accessed: 23/02/2018. IEEE. 2018. URL: http://ieeexplore.ieee.org/stamp/stamp.jsp?arnumber=1599245.

[41] *Types of Optimization Problems*. Date Accessed: 23/02/2018. University of Wisconsin - Madison. 2017. URL: https://neos-guide.org/optimization-tree.

[42] S.Singer and J.Nelder. *Nelder-Mead algorithm*. Date Accessed: 25/02/2018. Scholarpedia. 2009. URL: http://www.scholarpedia.org/article/Nelder-Mead_algorithm.

[43] J. Mathews and K. Fink. *Numerical Methods Using Matlab*. Fourth. Prentice-Hall, 2004. ISBN: 0-13-065248-2.

[44] R. Dehghani, M. Hosseini and N. Bidabadi. 'The Modified quasi-Newton method for solving unconstrained optimisation problems'. In: *International Journal of Numerical Modelling* 32.e2459 (2018).

[45] Synergy Software. *The KaleidaGraph Guide to Curve Fitting*. pdf. Date Accessed: 19/04/2018. www.synergycom/Tools/curvefitting.pdf.

[46] J. Kiusalaas. *Numerical Methods in Engineering with Python 3*. Cambridge University Press, 2013. ISBN: 978-1-107-03385-6.

[47] S. Carroll and C. Hursey. *Efficient Curve Fitting Techniques*. slides. Date Accessed: 23/04/2018. 2011.

[48] A. Goncalves. *Linear Regression: Goodness of Fit and Model Selection*. Slides. Date Accessed: 10/05/2018.

[49] J. Vandekerckhove, D. Matzke and E. Wagenmakers. 'The Oxford Handbook of Computational and Mathematical Psychology'. In: ed. by J. Busemeyer et al. Oxford Library of Psychology. Oxford University Press, 2015. Chap. Model Comparison and the Principle of Parsimony, pp. 300–319.

[50] C. Hagquist and M. Stenbeck. 'Goodness of Fit in Regression Analysis: R^2 and G^2 Reconsidered'. In: *Quality and Quantity* 32 (1998), pp. 229–245.

[51] S. Coratella. 'Evaluation of Residual Stress Fields after Laser Shock Peening Treatment of Aerospace Components'. PhD thesis. Coventry University, 2014.

[52] A. DeWald and M. Hill. 'Eigenstrain-based model for prediction of laser peening residual stresses in arbitrary three-dimensional bodies. Part 2: model verification'. In: *Journal of Strain Analysis for Engineering Design* 44 (2008). DOI: 10.1243/03093247JSA417.

[53] M. Achintha and D. Nowell. 'Residual stress in geometric features subjected to laser shock peening'. In: *Proceedings of the Institution of Mechanical Engineers, Part C: Journal of Mechanical Engineering Science* (2014).

[54] M. Achintha and D. Nowell. 'Eigenstrain modelling of residual stresses generated by arrays of LSP shots'. In: *Procedia Engineering* (2011).

[55] A. Vasu and R. Grandhi. 'Effects of curved geometry on residual stress in laser peening'. In: *Surface & Coatings Technology* 218 (2013), pp. 71–79.

[56] S. van Staden. 'Residual Stress Measurement and Parametric Analysis of Laser Shock Peening of Aluminium Alloy 7075 with Different Thicknesses'. MSc thesis. University of the Witwatersrand, Johannesburg, 2018.

[57] S. Coratella et al. 'Evaluation of Residual Stresses Generated by Laser Shock Peening in Non-uniform Geometries'. In: *7th Laser Shock Peening and Related Phenomena Conference, NUT, Singapore, 17-22 June*. 2018.

Appendix A Benchmark Sample Parameters

Table A.1: Key to Table A.2

E	Elettra (Synchrotron XRD)
IHD	Incremental Hole Drilling
APS	Advanced Photon Source (Synchrotron XRD)
N	NECSA
X	Laboratory XRD - CSIR

Table A.2: Parameters of benchmark samples

Sample Number	**Size** [mm]	**Thickness**	**Number of areas peened**	**Power Intensity** [GW/cm^2]	**Spot Size [mm]**	**Coverage [spots/**mm^2**]**	**IPS [spots]**	**1**	**2**	**3**	**4**
B1	60x60	1.6	4	3	1.5	5	11.25				E, APS, N
B15	60x60	6	4	3	1.5	5	11.25	E, APS, N			
5	28x28	10	1	3	0.5	45	11.25	APS, X	x	x	x
38	28x28	10	1	3	1.5	5	11.25	APS, X	x	x	x
70	28x28	10	1	3	2	2.8125	11.25	APS, X	x	x	x

Appendix B Extra Results

1 Coratella's Method

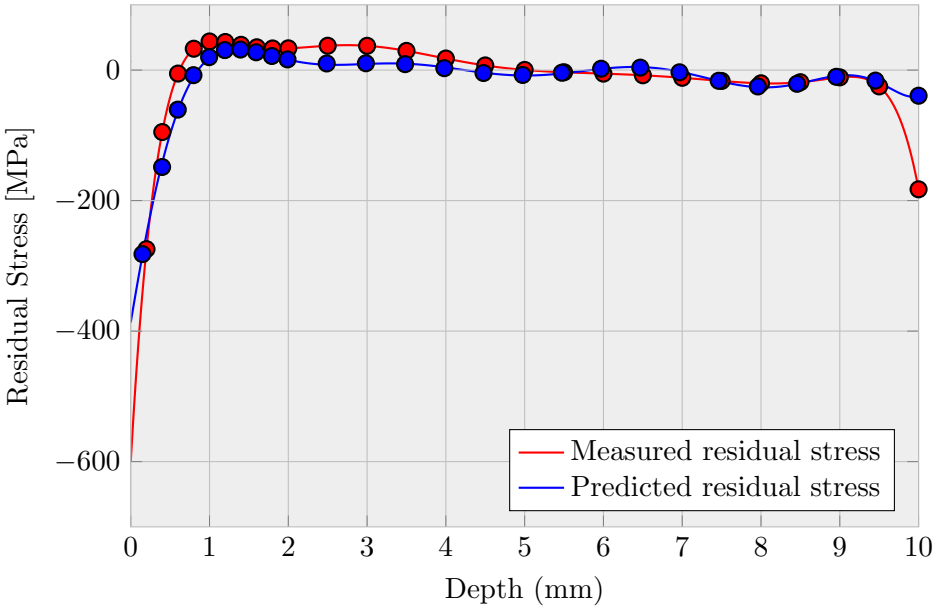

Figure B.1: *Coratella's Method: Prediction vs measured residual stress in sample 05 - x direction*

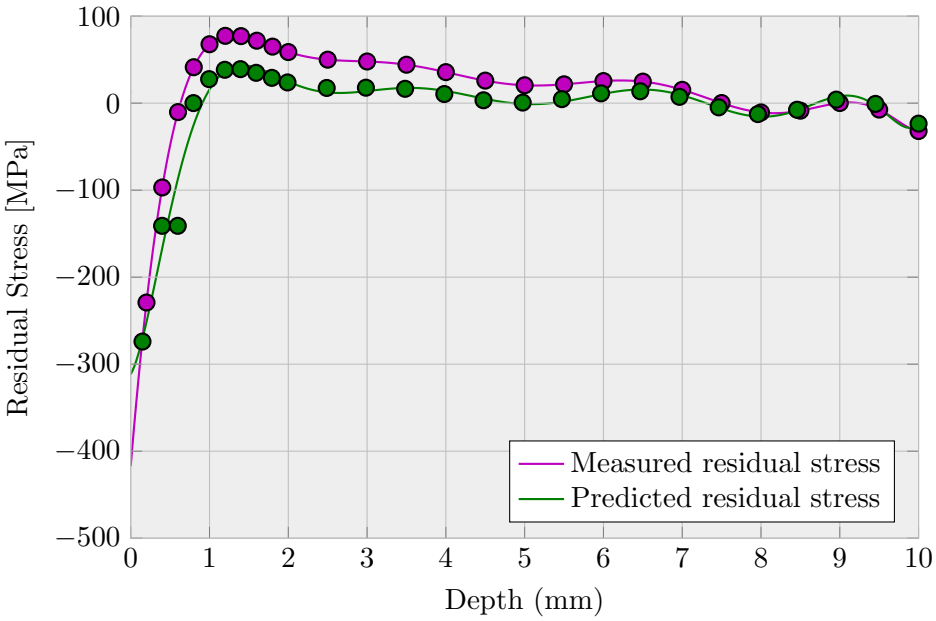

Figure B.2: *Coratella's Method: Prediction vs measured residual stress in sample 05 - y direction*

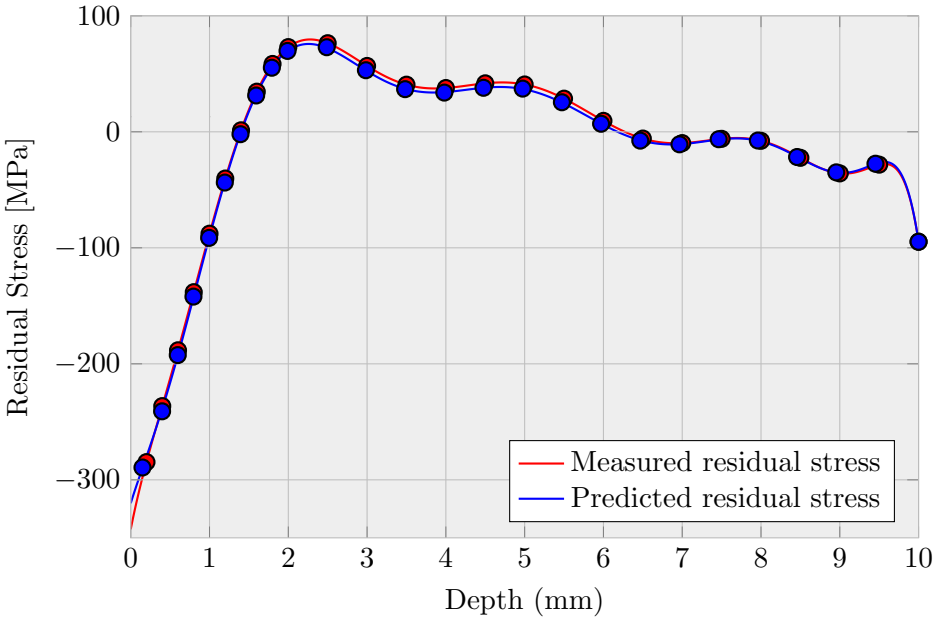

Figure B.3: *Coratella's Method: Prediction vs measured residual stress in sample 38 - x direction*

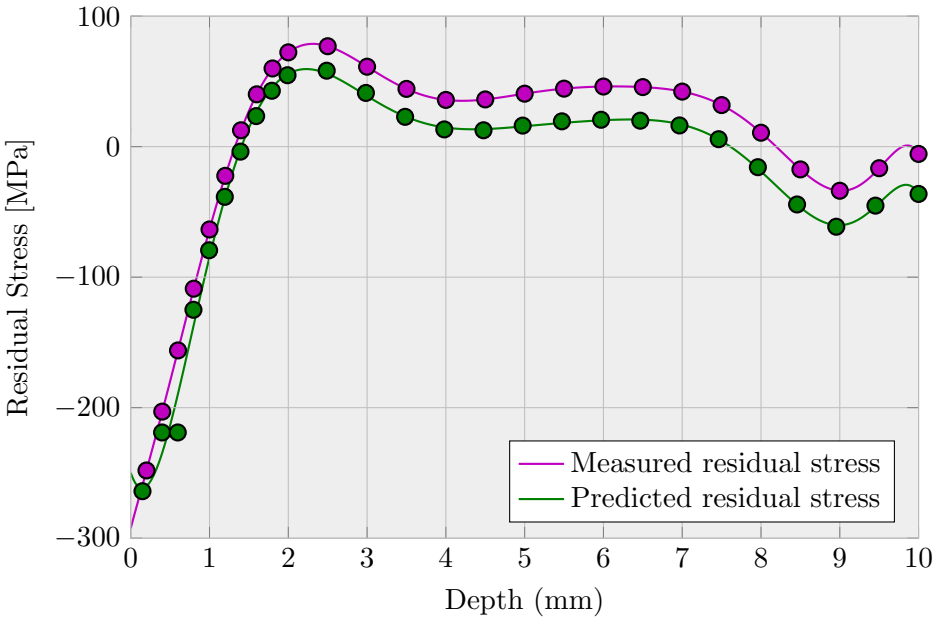

Figure B.4: *Coratella's Method: Prediction vs measured residual stress in sample 38 - y direction*

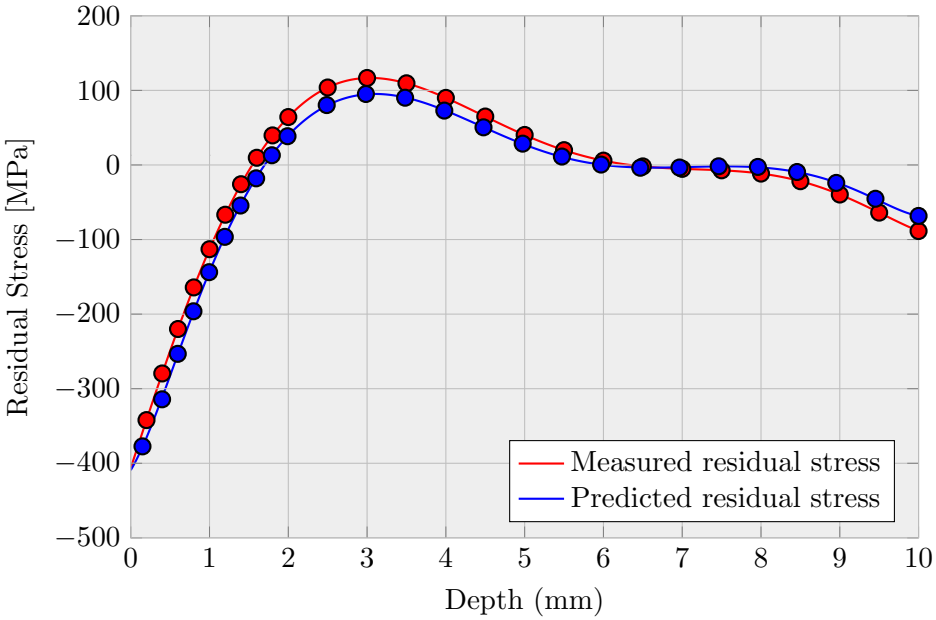

Figure B.5: *Coratella's Method: Prediction vs measured residual stress in sample 70 - x direction*

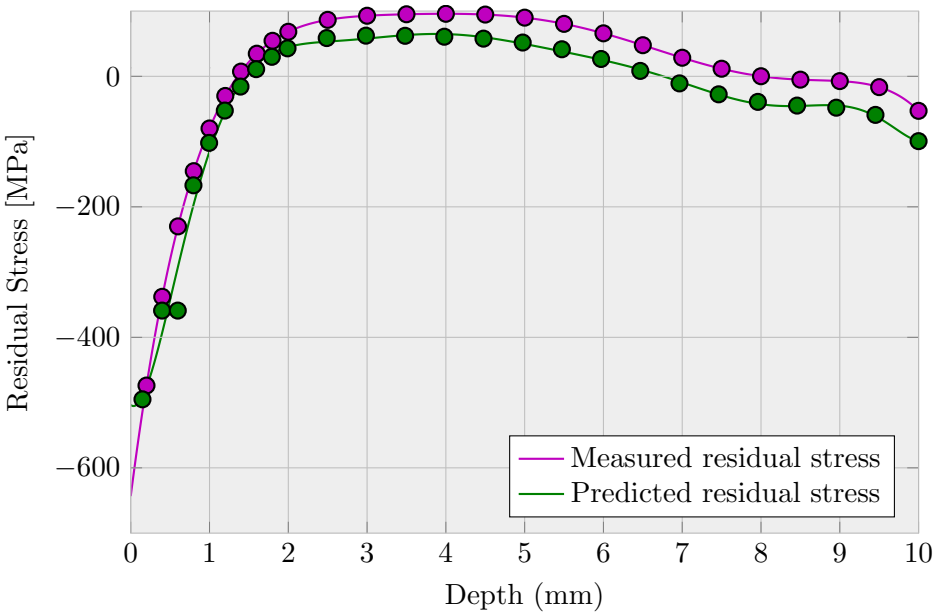

Figure B.6: *Coratella's Method: Prediction vs measured residual stress in sample 70 - y direction*

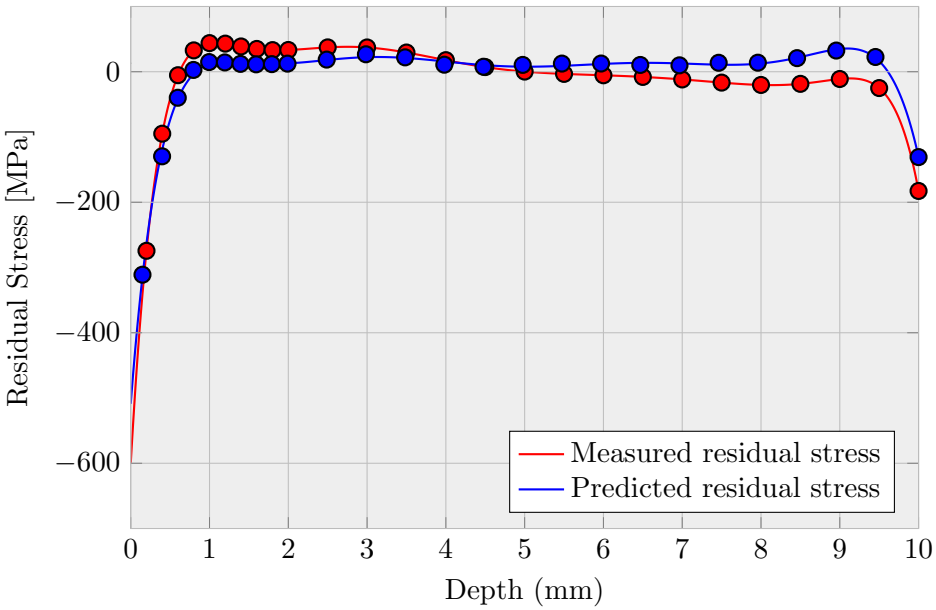

Figure B.7: *Korsunsky's Method: Prediction vs measured residual stress in sample 05 - x direction*

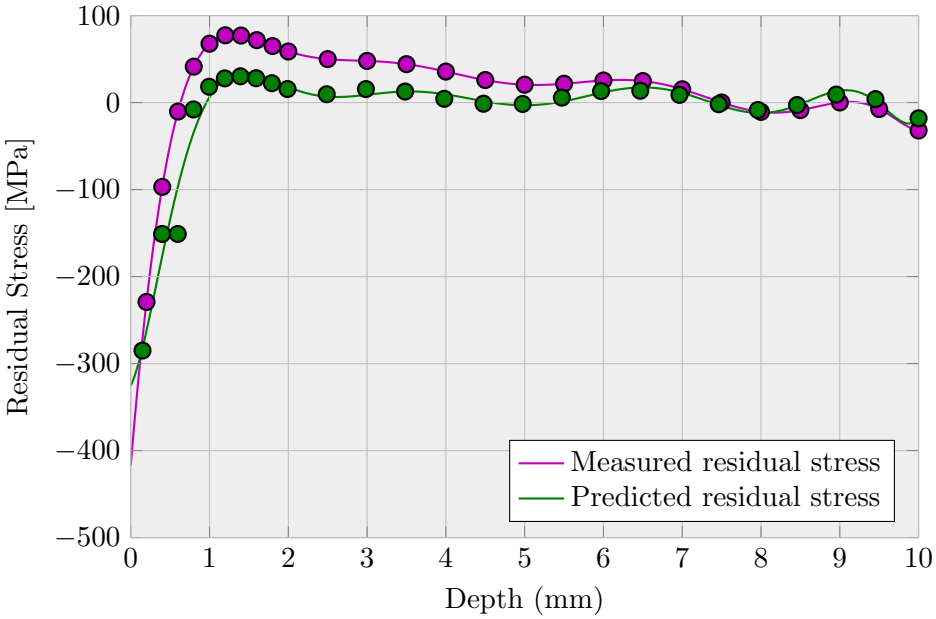

Figure B.8: *Korsunsky's Method: Prediction vs measured residual stress in sample 05 - y direction*

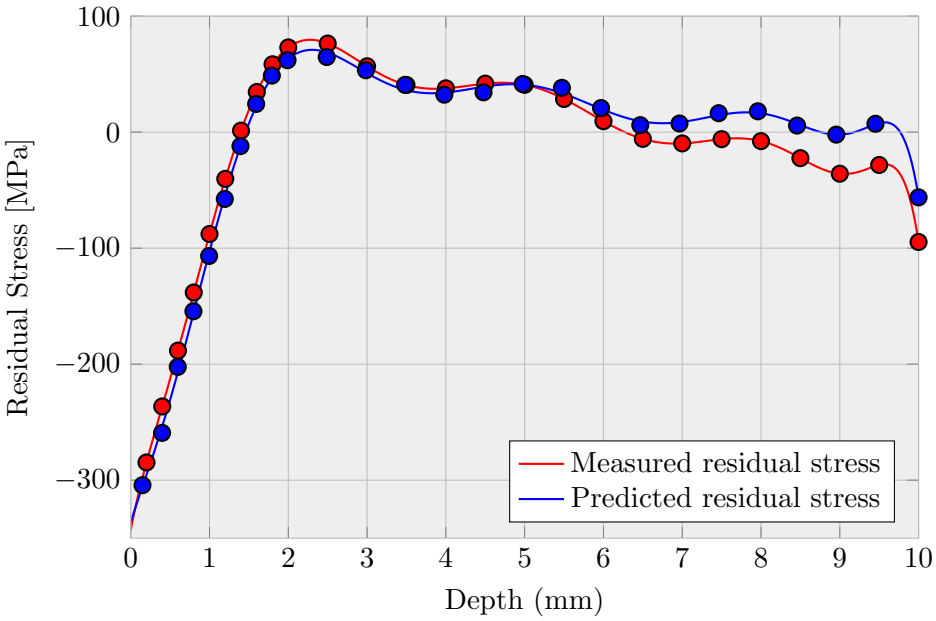

Figure B.9: *Korsunsky's Method: Prediction vs measured residual stress in sample 38 - x direction*

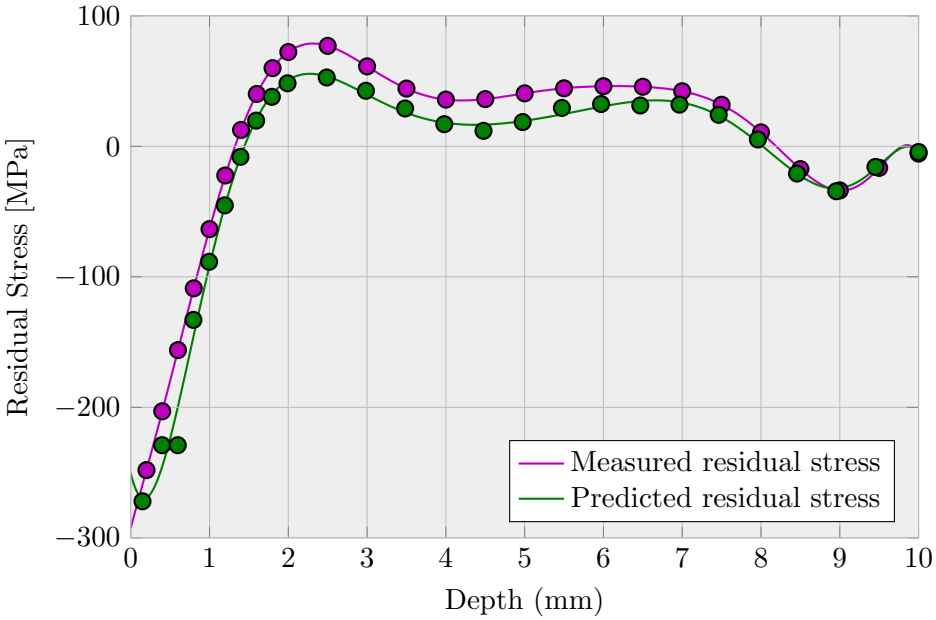

Figure B.10: *Korsunsky's Method: Prediction vs measured residual stress in sample 38 - y direction*

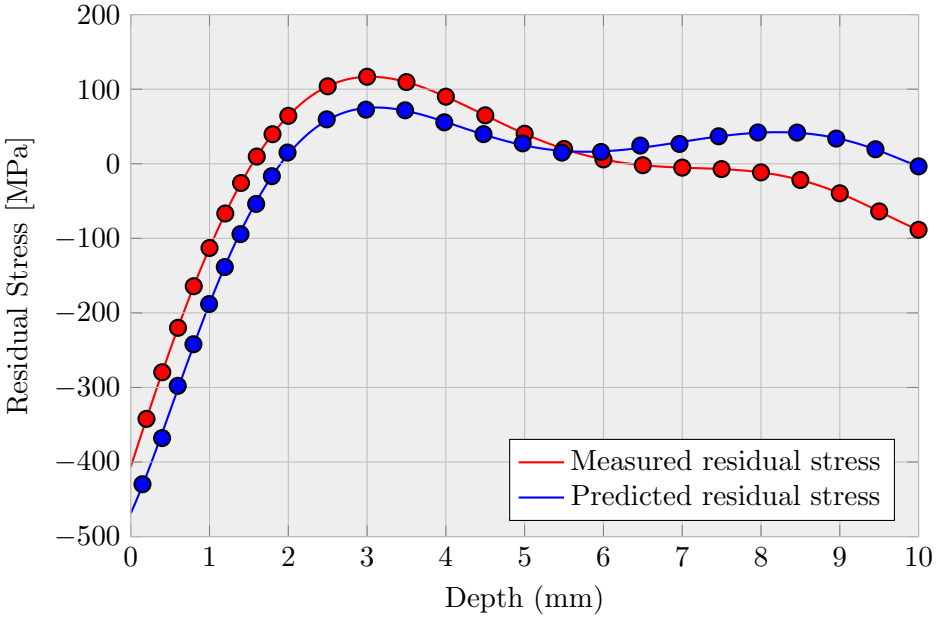

Figure B.11: *Korsunsky's Method: Prediction vs measured residual stress in sample 70 - x direction*

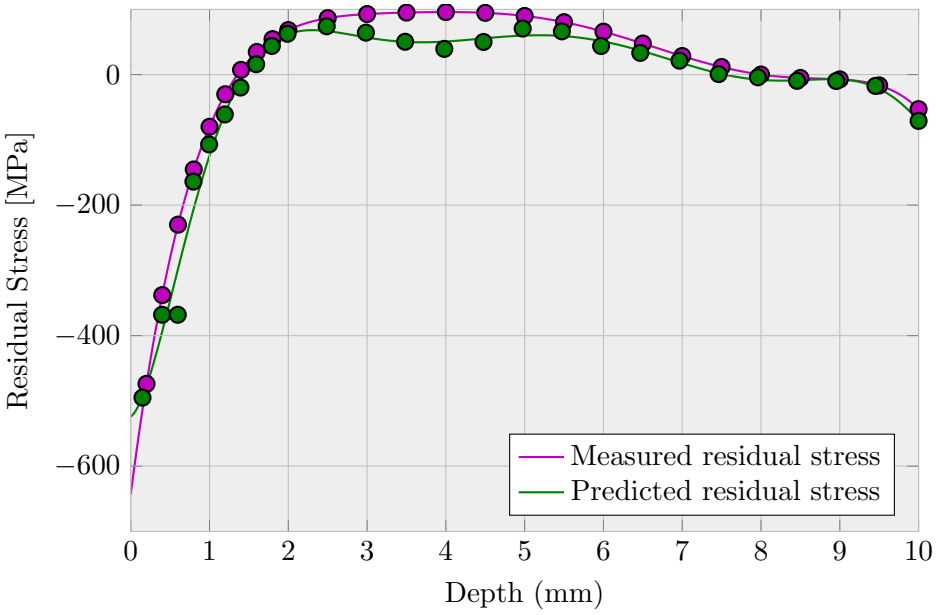

Figure B.12: *Korsunsky's Method: Prediction vs measured residual stress in sample 70 - y direction*

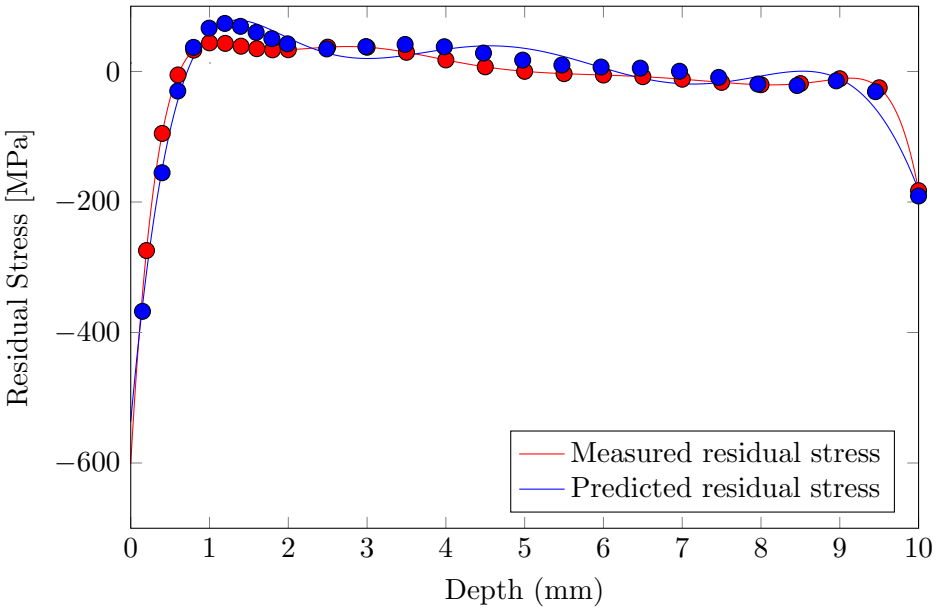

Figure B.13: *Korsunsky's Method with FEM to Generate Elastic Strain Matrix: Prediction vs measured residual stress in sample 05 - x direction*

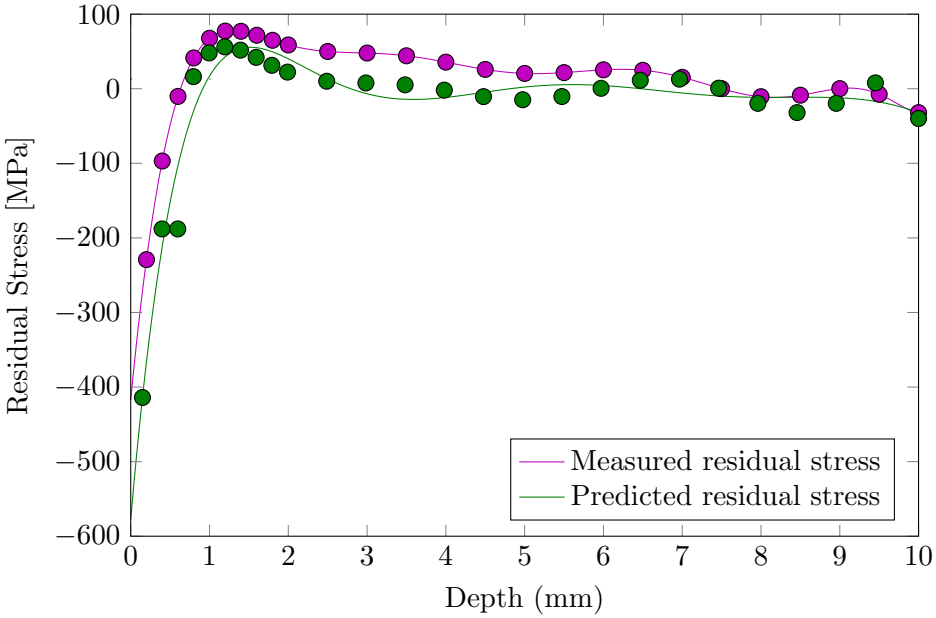

Figure B.14: *Korsunsky's Method with FEM to Generate Elastic Strain Matrix: Prediction vs measured residual stress in sample 05 - y direction*

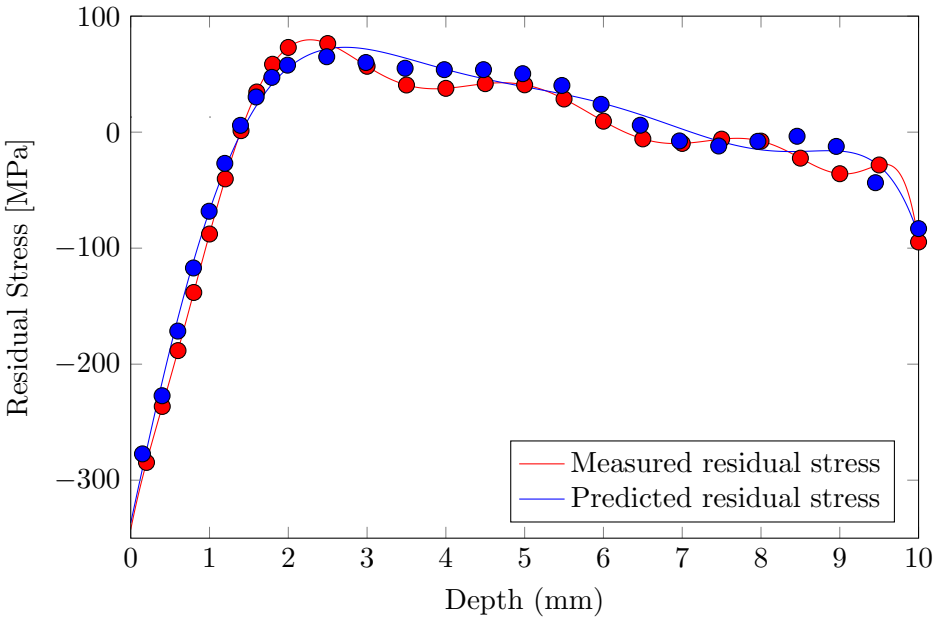

Figure B.15: *Korsunsky's Method with FEM to Generate Elastic Strain Matrix: Prediction vs measured residual stress in sample 38 - x direction*

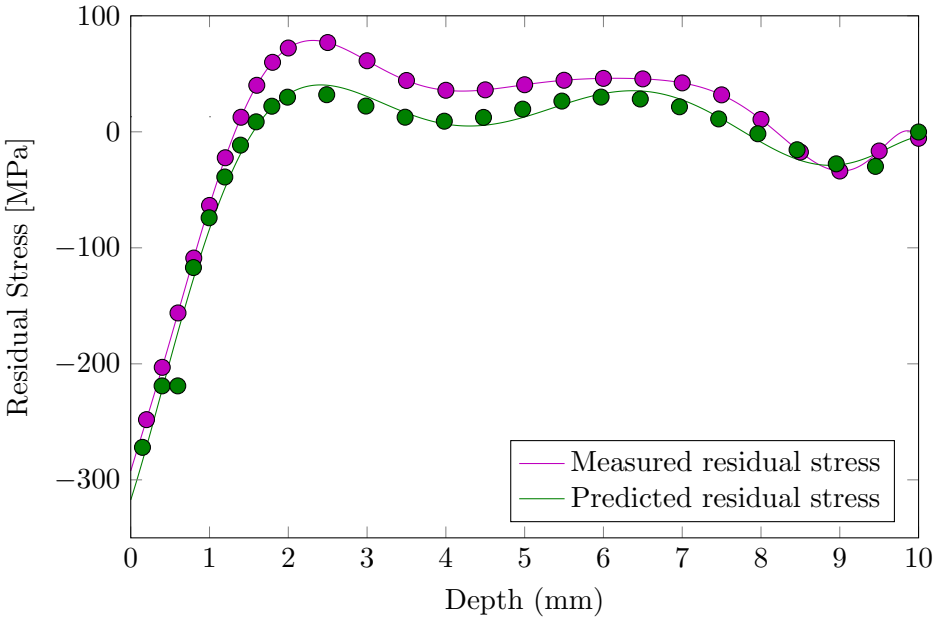

Figure B.16: *Korsunsky's Method with FEM to Generate Elastic Strain Matrix: Prediction vs measured residual stress in sample 38 - y direction*

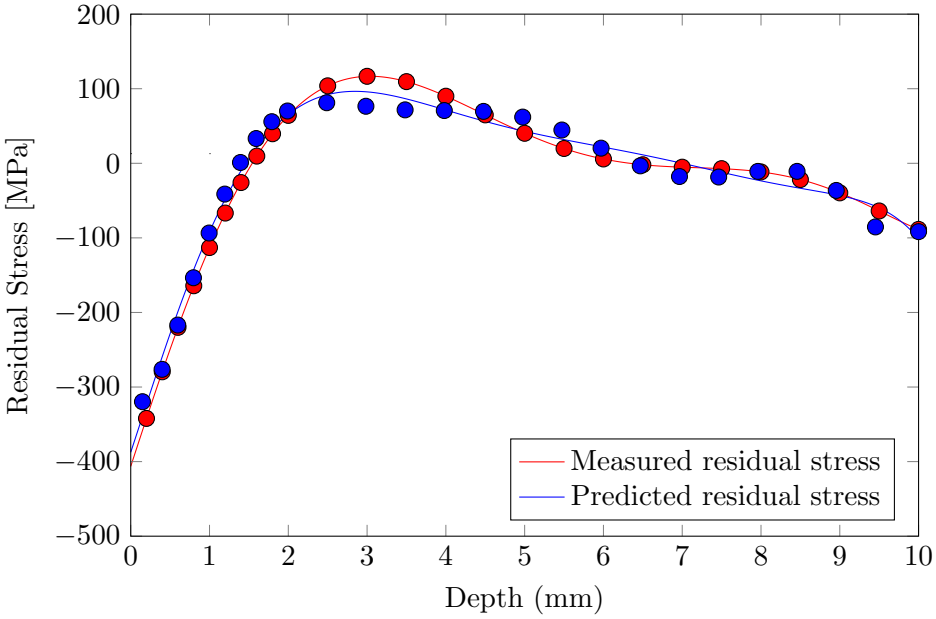

Figure B.17: *Korsunsky's Method with FEM to Generate Elastic Strain Matrix: Prediction vs measured residual stress in sample 70 - x direction*

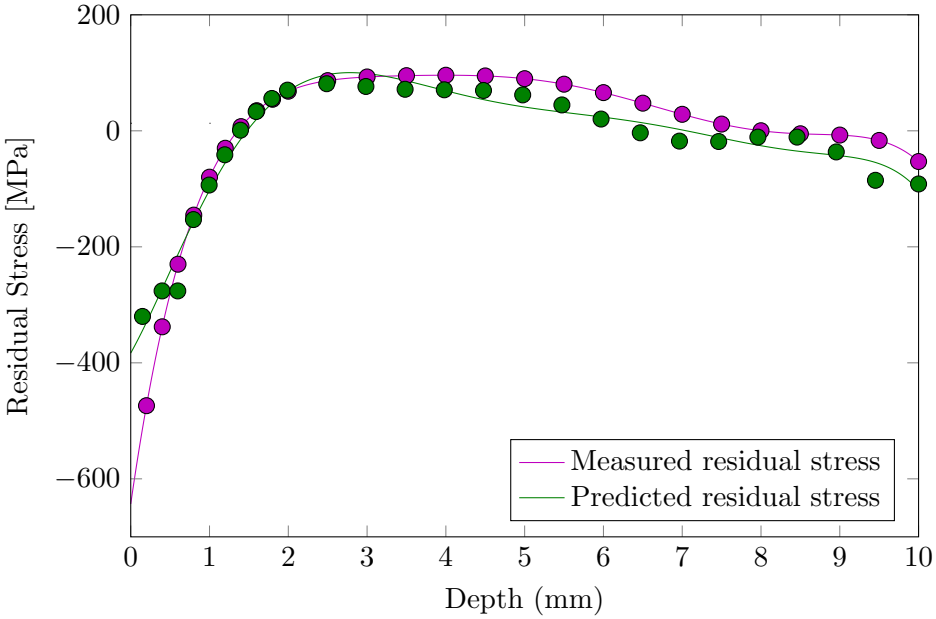

Figure B.18: *Korsunsky's Method with FEM to Generate Elastic Strain Matrix: Prediction vs measured residual stress in sample 70 - y direction*

Appendix C Scripts

1 Korsunsky's Method Script

```
"""
Created on Tue Jan 30 11:33:04 2018
Implements Korsunsky's method using basis functions zeta_i of the
    form (x - x0)^(i+a)
@author: Ridwaan Omar
"""
import numpy as np
import csv
import pylab as pl
import copy as cp
from scipy.optimize import minimize
from datetime import datetime
#
    ##############################################################################
     Functions
    ##############################################################################


def zeta(x,N,x0,a):             # Define the basis functions which
    output the values at given x value. Truncate at N. Output is a
    list of N basis functions
     Zeta = []
     for i in range(N):
         i = float(i)
         zetai = (x - x0)**(i+a)
         Zeta.append(zetai)
```

```
    return Zeta

def gamma(xr,xl,x0,N,a):        # Defines gamma as an integral
    parameter involving the basis functions. Output is a list of N
    parameters related to the N basis functions respectively.
    Obtained from force balance
    h = xr - xl
    Gamma = []
    for i in range(N):
        i = float(i)
        gammai = (1/(h*(i+a+1)))*((xr-x0)**(i+a+1)-(xl-x0)**(i+a+1)
            )
        Gamma.append(gammai)

    return Gamma

def gamma1(xr,xl,x0,N,a):       # Defines gamma as an integral
    parameter involving the basis functions. Output is a list of N
    values related to the N basis functions respectively. Obtained
    from moment balance.
    h = xr - xl
    Gamma1 = []
    for i in range(N):
        i = float(i)
        gamma1i = (1/((h**2)*(i+a+1)))*(xr*(xr-x0)**(i+a+1)-xl*(xl-
            x0)**(i+a+1) + (1/(i+a+2))*((xl-x0)**(i+a+2) - (xr-x0)
            **(i+a+2)))
        Gamma1.append(gamma1i)

    return Gamma1

def RESMatrix(x,x0,N,a,t):      # Constructs transposed residual
    elastic strain matrix
    Eij = []
    for j in range(len(x)):
        Ei = []
        xl = x[0]
        xr = t
```

```
            Zeta = zeta(x[j],N,x0,a)
            Gamma = gamma(xr,xl,x0,N,a)
            Gamma1 = gamma1(xr,xl,x0,N,a)

            for i in range(len(Zeta)):
                i = int(i)
                ei = (1/(xr-xl)**2)*(6*Gamma1[i]*(xr-xl)*(2*x[j]-xr-xl)
                    + 2*Gamma[i]*((xr**2+xr*xl+xl**2) - 3*x[j]*(xr+xl))
                    ) - Zeta[i]
                Ei.append(ei)

            Eij.append(Ei)

        return Eij

def csv_reader(file_obj,i):        # Obtains raw data
    x = []
    y = []
    reader = csv.reader(file_obj)
    counter = 0
    for row in reader:
        if counter > 0:
            x.append(float(row[0]))
            y.append(float(row[i]))
        counter += 1

    return [x,y]


def linsolve(x,x0,N,y,a,t):                    # Solves the linear
    optimisation problem. Returns list of basis coefficients
    E = np.matrix(RESMatrix(x,x0,N,a,t))       # Returns
       transposed elastic matrix
    y = np.matrix(y)
    ET =   E.T
    A = ET*E
    b = ET*y.T

    c =  np.matrix.tolist(A.I*b)
```

```
    C = []
    for each in c:
        each = each[0]
        C.append(each)

    return C

def Estrain(c,N,x,x0,a):                    # Calculates
    eigenstrains.
    Eigenstrains = []
    for i in x:
        Basis = []
        Zeta = zeta(i,N,x0,a)
        for j in range(N):
            basis = c[j]*Zeta[j]
            Basis.append(basis)
        eigenstrain = sum(Basis)
        Eigenstrains.append(eigenstrain)
    return Eigenstrains

def REstrains(c,x,x0,N,a,t):                # Calculates the
    Residual elastic strains at the measured depths
    Eij = RESMatrix(x,x0,N,a,t)
    RES = []
    for n in Eij:
        Ej = []
        for i in range(len(c)):
            ej = c[i]*n[i]
            Ej.append(ej)
        RES.append(sum(Ej))

    return RES

def GV(y,RES):                              # Returns sum of
    squared residuals
    Deviations = []
    for i in range(len(y)):
        Deviations.append((y[i] - RES[i])**2)
    return sum(Deviations)
```

```
def Opti(x0,N,a,y,x1,t):                                    # Locally
    optimise x0, N, and a with respect to least squares criterion.
    Requires initial guesses.

     def GVOP(x,y,x1,t):                                    # Define least
         squares criterion for optimisation
          x0 = x[0]
          N = int(x[1])
          a = int(x[2])

          c = linsolve(x1,x0,N,y,a,t)
          RES = REstrains(c,x1,x0,N,a,t)
          G = GV(y,RES)
          return G

     x00 = np.array([x0,N,a])                                #
         Optimize parameters
     Args = tuple([y,x1,t])
     res = minimize(GVOP, x00, args = Args, method='BFGS', options={
         'xtol': 1e-10, 'disp': True,'ftol':1e-10})
     sol = res.x

     return sol

def Opopti(x0,N,y,x1,t):                                    # Gloabally
    optimise a given N and x0. Calls Opti
     Goodness = []
     Sol = []
     for i in range(5,15):
          try:
               sol =  Opti(x0,N,i,y,x1,t)
               Sol.append(sol)

               x0 = sol[0]
               N = int(sol[1])
               a = int(sol[2])

               c = linsolve(x1,x0,N,y,a,t)
```

```
            RES = REstrains(c,x1,x0,N,a,t)
            goodness = GV(y,RES)
            Goodness.append(goodness)
        except:
            pass
    try:
        min_index = Goodness.index(min(Goodness))
        sol1 = Sol[min_index]
    except ValueError:
        pass
    return sol1

def Opopopti(x0,y,x1,t):                                    # Gloabally
    optimise N and a given x0. Calls Opopti
    Goodness = []
    Sol = []
    for i in range(10,30,2):
        try:
            sol =  Opopti(x0,i,y,x1,t)
            Sol.append(sol)

            x0 = sol[0]
            N = int(sol[1])
            a = int(sol[2])

            c = linsolve(x1,x0,N,y,a,t)
            RES = REstrains(c,x1,x0,N,a,t)
            goodness = GV(y,RES)
            Goodness.append(goodness)
        except:
            pass
    try:
        min_index = Goodness.index(min(Goodness))
        sol2 = Sol[min_index]
    except ValueError:
        pass
    return sol2
```

```
def Optiall(y,x1,t):                                    # Gloabally
    optimise all paramters. Calls Opopopti
    Goodness = []
    Sol = []
    i = 1.5
    while i <= int(x1[-1]):
        try:
            sol =  Opopopti(i,y,x1,t)
            Sol.append(sol)

            x0 = sol[0]
            N = int(sol[1])
            a = int(sol[2])

            c = linsolve(x1,x0,N,y,a,t)
            RES = REstrains(c,x1,x0,N,a,t)
            goodness = GV(y,RES)
            Goodness.append(goodness)
        except:
            pass
        i = i + 0.5
    try:
        min_index = Goodness.index(min(Goodness))
        sol3 = Sol[min_index]
    except ValueError:
        pass
    return sol3

################################################################ MAIN

    ##########################################################################

startTime = datetime.now()

Eigenstrainsii = []                                     # Store
    eigenstrains of each direction (x,y,z)
J = []
x0s = []
Ns = []
```

```
As = []

filnm = raw_input("Input file name: ")

t = input("Input thickness of sample: ")

for i in range(1,4):                                    #For
    eigenstrains in x, y, and z directions
     csv_path = "F:/Ridwaan/Spreadsheets/Residual strain data/
        Processed/%s_processed.csv" %filnm              # Obtains
        measured data
     with open(csv_path, "rb") as f_obj:
         data = csv_reader(f_obj,i)

     x1 = cp.deepcopy(data[0])                          #
        Processes data to obtain outputs
     y = cp.deepcopy(data[1])



     sol = Optiall(y,x1,t)
     #sol = Opti(x0,N,a,y,x1,t)
     x0 = sol[0]
     N = int(sol[1])
     a = int(sol[2])

     c = linsolve(x1,x0,N,y,a,t)
     Eigenstrains = Estrain(c,N,x1,x0,a)
     RES = REstrains(c,x1,x0,N,a,t)
     Goodness = GV(y,RES)

     Eigenstrainsii.append(Eigenstrains)
     J.append(Goodness)
     x0s.append(x0)
     Ns.append(N)
     As.append(a)
```

```
#################################################################
    Write to file
    #################################################################

with open("F:/Ridwaan/Spreadsheets/Eigenstrain data/Korsunsky/%
    s_Eigenstrains.csv" %filnm,"wb") as csvfile:
     writer = csv.writer(csvfile)
     writer.writerow(["Depth","Eigenstrainxx","Eigenstrainyy","
         Eigenstrainzz"])
     for i in range(len(x1)):
          writer.writerow([x1[i],Eigenstrainsii[0][i],Eigenstrainsii
              [1][i],Eigenstrainsii[2][i]])
with open("F:/Ridwaan/Spreadsheets/Eigenstrain data/Korsunsky/
    Parameters/%s_params.csv" %filnm,"wb") as csvfile:
     writer = csv.writer(csvfile)
     writer.writerow([J[0],J[1],J[2]])
     writer.writerow([x0s[0],x0s[1],x0s[2]])
     writer.writerow([Ns[0],Ns[1],Ns[2]])
     writer.writerow([As[0],As[1],As[2]])

################################################################# Plot
    Results
    #################################################################

     plot1 = pl.plot(x1,y,'ko')
     p = np.poly1d(np.polyfit(x1,RES,10))
     xp = np.linspace(0,x1[-1],1000)
     plot2 = pl.plot(xp,p(xp),'b')
     pl.title('Predicted vs Measured RES')
     pl.xlabel('Depth (mm)')
     pl.ylabel('RES')
     pl.legend([plot1,plot2],('Measured' , 'Predicted'),'best',
         numpoints = 1)
     pl.show()

print datetime.now() - startTime
```

2 Korsunsky's Method With FEM: Main Script

```
# -*- coding: utf-8 -*-
"""
Created on Mon Mar 12 14:59:09 2018

@author: Ridwaan
"""

import numpy as np
import csv
import pylab as pl
import copy as cp
from scipy.optimize import minimize
from datetime import datetime
import os

#
    ##############################################################################
     Functions
    ##############################################################################

def Estrain(c,N,x,x0,a):                                    # Calculates
    eigenstrains.
     Eigenstrains = []
     modcoeff =  Modcoeff(N,x,x0,a)
     for i in x:
         Basis = []
         for j in range(N):
             basis = c[j]*zeta(i,j,x0,a,modcoeff)
             Basis.append(basis)
         eigenstrain = sum(Basis)
         Eigenstrains.append(eigenstrain)

     return Eigenstrains

def linsolve(x,x0,N,y,a,matrix):                            # Solves the
    linear optimisation problem. Returns list of basis coefficients
     E = np.matrix(matrix)                                  # Returns
         transposed elastic matrix
```

```
    y = np.matrix(y)
    ET =    E.T
    A = E*ET
    b = E*y.T

    c =  np.matrix.tolist(A.I*b)
    C = []
    for each in c:
        each = each[0]
        C.append(each)

    return C

def RESMatrix(x0,N,a,sam,lenx):        # Constructs transposed
    residual elastic strain matrix
    with open("C:/Users/Ridwaan/Desktop/Masters/Scripts/
        Korsunsky_Mod_Method/RES.csv", "rb") as f_obj:
        reader = csv.reader(f_obj)

        Ex = []
        Ey = []
        Ez = []

        for row in reader:
            Ex.append(float(row[0]))
            Ey.append(float(row[1]))
            Ez.append(float(row[2]))

    Eijx = []
    Eijy = []
    Eijz = []

    for i in range(N):
        Ejx = []
        Ejy = []
        Ejz = []
        for j in range(lenx):
            Ejx.append(Ex[j + i*lenx])
            Ejy.append(Ex[j + i*lenx])
```

```
            Ejz.append(Ex[j + i*lenx])
        Eijx.append(Ejx)
        Eijy.append(Ejy)
        Eijz.append(Ejz)

    return [Eijx,Eijy,Eijz]

def zeta(x,i,x0,a,Modcoeff):            # Define the basis functions
    which output the values at given x value.
    zeta = (x - x0)**(i+a)
    Zeta = Modcoeff*zeta

    return Zeta

def Modcoeff(N,x,x0,a):          # Generates a moderating coefficient
    for a given zeta value (that ensures zeta is a reasonable value
   )
    coeff = 1
    if abs((x[-1] - x0)) > abs((x[0] - x0)):
        x1 = x[-1]
    else:
        x1 = x[0]
    zeta = (x1 - x0)**(N+a)
    Zetavalue = cp.deepcopy(zeta)
    while abs(Zetavalue) > 0.01:
        coeff = coeff*0.01
        Zetavalue = coeff*zeta

    return coeff

def REstrains(Eigenstrains,sam):                    # Calculates the
    Residual elastic strains at the measured depths
    Eigenstrains = str(Eigenstrains)
    directory = 'C:/Users/Ridwaan/Desktop/Masters/Scripts/
       Korsunsky_Mod_Method'
    with open(os.path.join(directory, 'FinalScript.bat'), 'w') as
       OPATH:
```

```
        OPATH.write('@echo off\ncd C:\Program Files\ANSYS Inc\\v180
            \Framework\\bin\Win64\nrunwb2 -B -F"C:\Users\Ridwaan\
            Desktop\Masters\FEA Models\Korsunsky_Mod\Korsunsky_Mod(%
            s).wbpj" -E "Eigenstrains = %s" -R "C:\Users\Ridwaan\
            Desktop\Masters\FEA Models\Korsunsky_Mod\Korsunsky_Mod(%
            s)_files\session_files\FinalScript.wbjn"' % (sam,
            Eigenstrains,sam))
    os.system('FinalScript.bat')
    [RESx,RESy,RESz] = ResultReader(sam)

    return [RESx,RESy,RESz]

def ResultReader(sam):
    with open("C:/Users/Ridwaan/Desktop/Masters/FEA Models/
        Korsunsky_Mod/Korsunsky_Mod(%s)_files/user_files/export.csv"
        %sam,"rb") as csvfile:
        reader = csv.reader(csvfile)
        xdata = []
        ydata = []
        zdata = []
        for row in reader:
            try:
                xdata.append(row[0])
                ydata.append(row[1])
                zdata.append(row[2])
            except IndexError:
                pass
        Ejx = []
        Ejy = []
        Ejz = []
        for i in range(4,len(xdata),5):
            ejx = xdata[i]
            Ejx.append(float(ejx))

        for i in range(1,len(ydata),2):
            ejy = ydata[i]
            Ejy.append(float(ejy))
```

```
        for i in range(1,len(zdata),2):
            ejz = zdata[i]
            Ejz.append(float(ejz))

        return [Ejx,Ejy,Ejz]

def GV(y,RES):                                  # Returns sum of
    squared residuals
    Deviations = []
    for i in range(len(y)):
        Deviations.append((y[i] - RES[i])**2)

    return sum(Deviations)

def xreader(file_obj):
    x = []
    reader = csv.reader(file_obj)
    counter = 0
    for row in reader:
        if counter > 0:
            x.append(float(row[0]))
        counter += 1

    return x

def csv_reader(file_obj,i):       # Obtains raw data
    y = []
    reader = csv.reader(file_obj)
    counter = 0
    for row in reader:
        if counter > 0:
            y.append(float(row[i]))
        counter += 1

    return y
```

```
########################################################################## MAIN
    ##############################################################################

startTime = datetime.now()

Eigenstrainsii = []                                                    # Store
    eigenstrains of each direction (x,y,z)
J = []

x0s = []
Ns = []
As = []

x0 = input("Input x0: ")
N = input("Input N: ")
a = input("Input a: ")

sam = raw_input("Input sample name: ")

directory = 'C:/Users/Ridwaan/Desktop/Masters/Scripts/Korsunsky_Mod
    _Method'
with open(os.path.join(directory, 'Batch_Commands.bat'), 'w') as
    OPATH:
     OPATH.write('@echo off\ncd C:\Program Files\ANSYS Inc\\v180\
         Framework\\bin\Win64\nrunwb2 -B -F"C:\Users\Ridwaan\Desktop\
         Masters\FEA Models\Korsunsky_Mod\Korsunsky_Mod(%s).wbpj" -E
         "a=%d; N=%d; x0=%r" -R"C:\Users\Ridwaan\Desktop\Masters\FEA
         Models\Korsunsky_Mod\Korsunsky_Mod(%s)_files\session_files\
         Korsunsky_Mod.wbjn"' % (sam,a,N,x0,sam))

os.system('Batch_Commands.bat')

csv_path = "C:/Users/Ridwaan/Desktop/Masters/Spreadsheets/Residual
    strain data/Processed/%s_processed.csv" %sam

with open(csv_path, "rb") as f_obj:
      x1 = xreader(f_obj)
```

```
lenx = len(x1)
RESMatrix = RESMatrix(x0,N,a,sam,lenx)

for i in range(1,4):                                    #For
    eigenstrains in x, y, and z direction
     with open(csv_path, "rb") as f_obj:
         y = csv_reader(f_obj,i)

     matrix =  RESMatrix[i-1]
     c = linsolve(x1,x0,N,y,a,matrix)
     Eigenstrains = Estrain(c,N,x1,x0,a)

     Eigenstrainsii.append(Eigenstrains)
     x0s.append(x0)
     Ns.append(N)
     As.append(a)

RES = REstrains(Eigenstrainsii,sam)
for i in RES:
     Goodness = GV(y,i)
     J.append(Goodness)


#####################################################################
    Write to file
   ###################################################################

with open("C:/Users/Ridwaan/Desktop/Masters/Spreadsheets/
    Eigenstrain_data/Korsunsky_Mod/%s_Eigenstrains.csv" %sam,"wb")
    as csvfile:
     writer = csv.writer(csvfile)
     writer.writerow(["Depth","Eigenstrainxx","Eigenstrainyy","
         Eigenstrainzz"])
     for i in range(len(x1)):
          writer.writerow([x1[i],Eigenstrainsii[0][i],Eigenstrainsii
              [1][i],Eigenstrainsii[2][i]])
with open("C:/Users/Ridwaan/Desktop/Masters/Spreadsheets/
    Eigenstrain_data/Korsunsky_Mod/Parameters/%s_params.csv" %sam,"
    wb") as csvfile:
```

```
    writer = csv.writer(csvfile)
    writer.writerow([J[0],J[1],J[2]])
    writer.writerow([x0s[0],x0s[1],x0s[2]])
    writer.writerow([Ns[0],Ns[1],Ns[2]])
    writer.writerow([As[0],As[1],As[2]])

import winsound
frequency = 700  # Set Frequency To 2500 Hertz
duration = 3000  # Set Duration To 1000 ms == 1 second
winsound.Beep(frequency, duration)


print datetime.now() - startTime
```

3 Korsunsky's Method With FEM: ANSYS Journal File Script

```
# encoding: utf-8
# Release 18.0
SetScriptVersion(Version="18.0.351")
import csv
import copy as cp

def RESMatrix(x,x0,N,a,sam):        # Constructs transposed residual
    elastic strain matrices
    Eijx = []
    Eijy = []
    Eijz = []
    modcoeff = Modcoeff(N,x,x0,a)
    for i in range(N):
        for j in range(len(x)):
            Zeta = zeta(x[j],i,x0,a,modcoeff)
            ZetaWrite(j+1,Zeta)
        Update()
        ResultWriter()
        Ej = ResultReader(sam)
        Ejx = Ej[0]
        Ejy = Ej[1]
        Ejz = Ej[2]
```

```
            Eijx.append(Ejx)
            Eijy.append(Ejy)
            Eijz.append(Ejz)

        return [Eijx,Eijy,Eijz]

def zeta(x,i,x0,a,Modcoeff):            # Define the basis functions
    which output the values at given x value.
    zeta = (x - x0)**(i+a)
    Zeta = Modcoeff*zeta

    return Zeta

def Modcoeff(N,x,x0,a):          # Generates a moderating coefficient
    for a given zeta value (that ensures zeta is a reasonable value
   )
    coeff = 1
    if abs((x[-1] - x0)) > abs((x[0] - x0)):
        x1 = x[-1]
    else:
        x1 = x[0]
    zeta = (x1 - x0)**(N+a)
    Zetavalue = cp.deepcopy(zeta)
    while abs(Zetavalue) > 0.01:
        coeff = coeff*0.01
        Zetavalue = coeff*zeta

    return coeff

def ZetaWrite(layer,value):
    system1 = GetSystem(Name="SYS")
    engineeringData1 = system1.GetContainer(ComponentName="
        Engineering Data")
    material1 = engineeringData1.GetMaterial(Name="Layer %d" %layer
        )
    matlProp1 = material1.GetProperty(Name="Coefficient of Thermal
        Expansion")
    matlProp1.SetData(
```

```
        Variables=["Coefficient of Thermal Expansion X direction"],
        Values=[["%r [C^-1]" % value]])
    matlProp1.SetData(
        Variables=["Coefficient of Thermal Expansion Y direction"],
        Values=[["%r [C^-1]" % value]])
    matlProp1.SetData(
        Variables=["Coefficient of Thermal Expansion Z direction"],
        Values=[["%r [C^-1]" % value]])

def ResultWriter():
    system1 = GetSystem(Name="Post")
    results1 = system1.GetContainer(ComponentName="Results")
    results1.SendCommand(Command="""EXPORT:
    ANSYS Export Data = Element Heat Flux
    ANSYS File Format = ANSYS
    ANSYS Reference Temperature = 0.0 [K]
    ANSYS Specify Reference Temperature = Off
    ANSYS Supplemental HTC = 0.0 [W mm^-2 K^-1]
    Additional Variable List =
    BC Profile Type = Inlet Velocity
    Export Connectivity = Off
    Export Coord Frame = Global
    Export File = F:/Ridwaan/FEA Models/Korsunsky_Mod/Korsunsky_Mod
        (SamB15)_files/user_files/export.csv
    Export Geometry = Off
    Export Location Aliases =
    Export Node Numbers = Off
    Export Null Data = On
    Export Type = Generic
    Export Units System = Current
    Export Variable Type = Current
    External Export Data = None
    Include File Information = Off
    Include Header = On
    Location = Default Boundary
```

```
    Location List = /POINT:Point A,/POINT:Point B,/POINT:Point C,/
       POINT:Point D,/POINT:Point E,/POINT:Point F,/POINT:Point G,/
       POINT:Point H,/POINT:Point I,/POINT:Point J,/POINT:Point K,/
       POINT:Point L,/POINT:Point M,/POINT:Point N,/POINT:Point O,/
       POINT:Point P,/POINT:Point Q,/POINT:Point R
    Null Token = null
    Overwrite = On
    Precision = 8
    Separator = \", \"
    Spatial Variables = X,Y,Z
    Variable List = Normal Elastic Strain X, Normal Elastic Strain
       Y, Normal Elastic Strain Z, Y
    Vector Brackets = ()
    Vector Display = Scalar
    END
    >export""")
    results1.Exit()

def ResultReader(filnm):
    with open("F:/Ridwaan/FEA_Models/Korsunsky_Mod/Korsunsky_Mod(%s
       )_files/user_files/export.csv" %sam,"rb") as csvfile:
        reader = csv.reader(csvfile)
        xdata = []
        ydata = []
        zdata = []
        for row in reader:
            try:
                xdata.append(row[0])
                ydata.append(row[1])
                zdata.append(row[2])
            except IndexError:
                pass
        Ejx = []
        Ejy = []
        Ejz = []
        for i in range(4,len(xdata),5):
            ejx = xdata[i]
            Ejx.append(ejx)
```

```
        for i in range(1,len(ydata),2):
            ejy = ydata[i]
            Ejy.append(ejy)


        for i in range(1,len(zdata),2):
            ejz = zdata[i]
            Ejz.append(ejz)

        return [Ejx,Ejy,Ejz]

def xreader(file_obj):
    x = []
    reader = csv.reader(file_obj)
    counter = 0
    for row in reader:
        if counter > 0:
            x.append(float(row[0]))
        counter += 1

    return x

sam = 'SamB15'


csv_path = "F:/Ridwaan/Spreadsheets/Residual_strain_data/Processed
   /%s_processed.csv" %sam

with open(csv_path, "rb") as f_obj:
     x = xreader(f_obj)


RESMatrix = RESMatrix(x,x0,N,a,sam)

Eijx = RESMatrix[0]
Eijy = RESMatrix[1]
Eijz = RESMatrix[2]
```

```
with open("F:/Ridwaan/Scripts/Korsunsky_Mod_Method/RES.csv" ,"wb")
    as csvfile:
     writer = csv.writer(csvfile)
     for i in range(len(Eijx)):
         for j in range(len(Eijx[i])):
             writer.writerow([Eijx[i][j],Eijy[i][j],Eijz[i][j]])
```

Appendix D Thickness Study – Results in y Direction

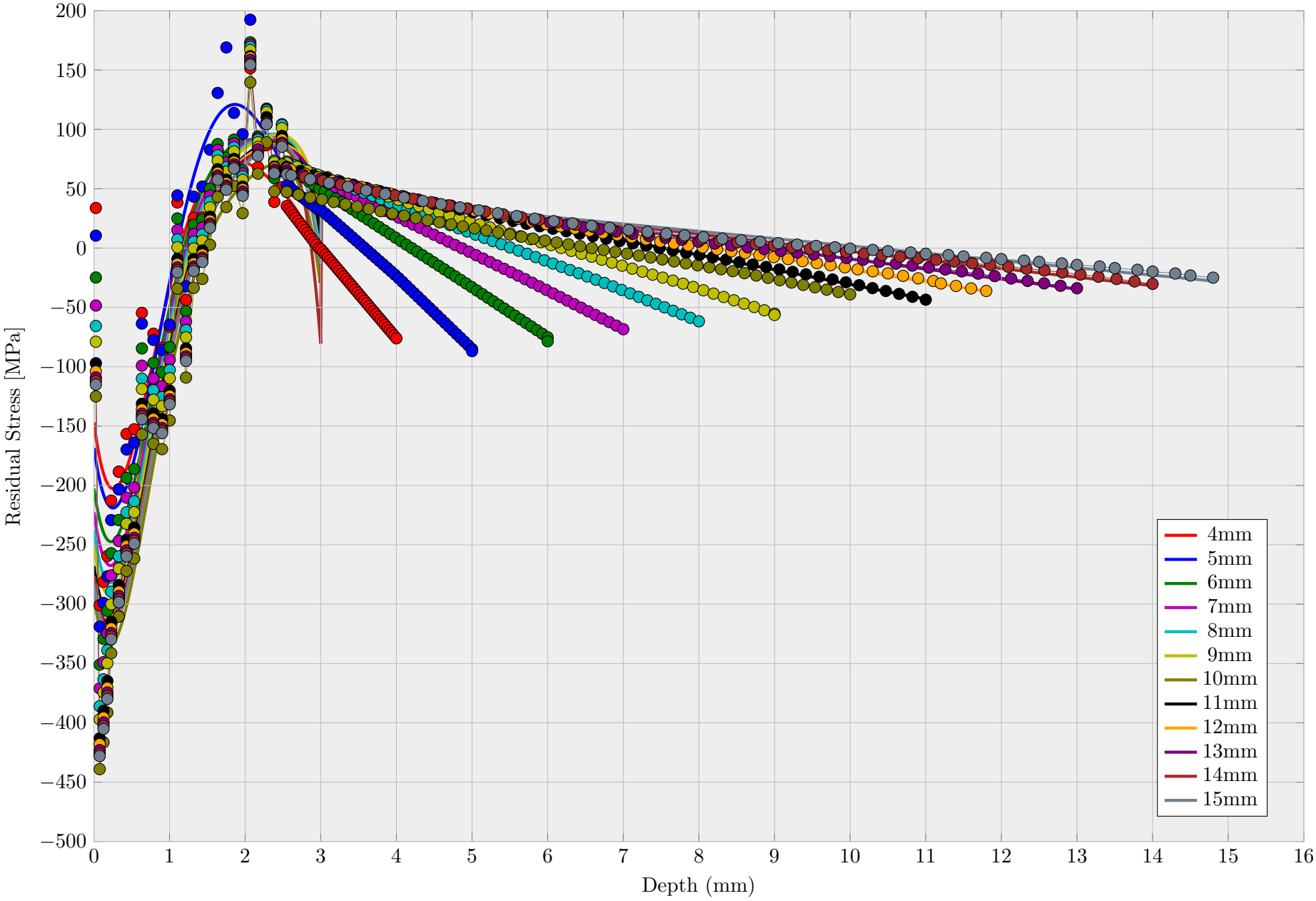

Figure D.1: *Residual stress distributions in samples with varying thickness – y - direction*

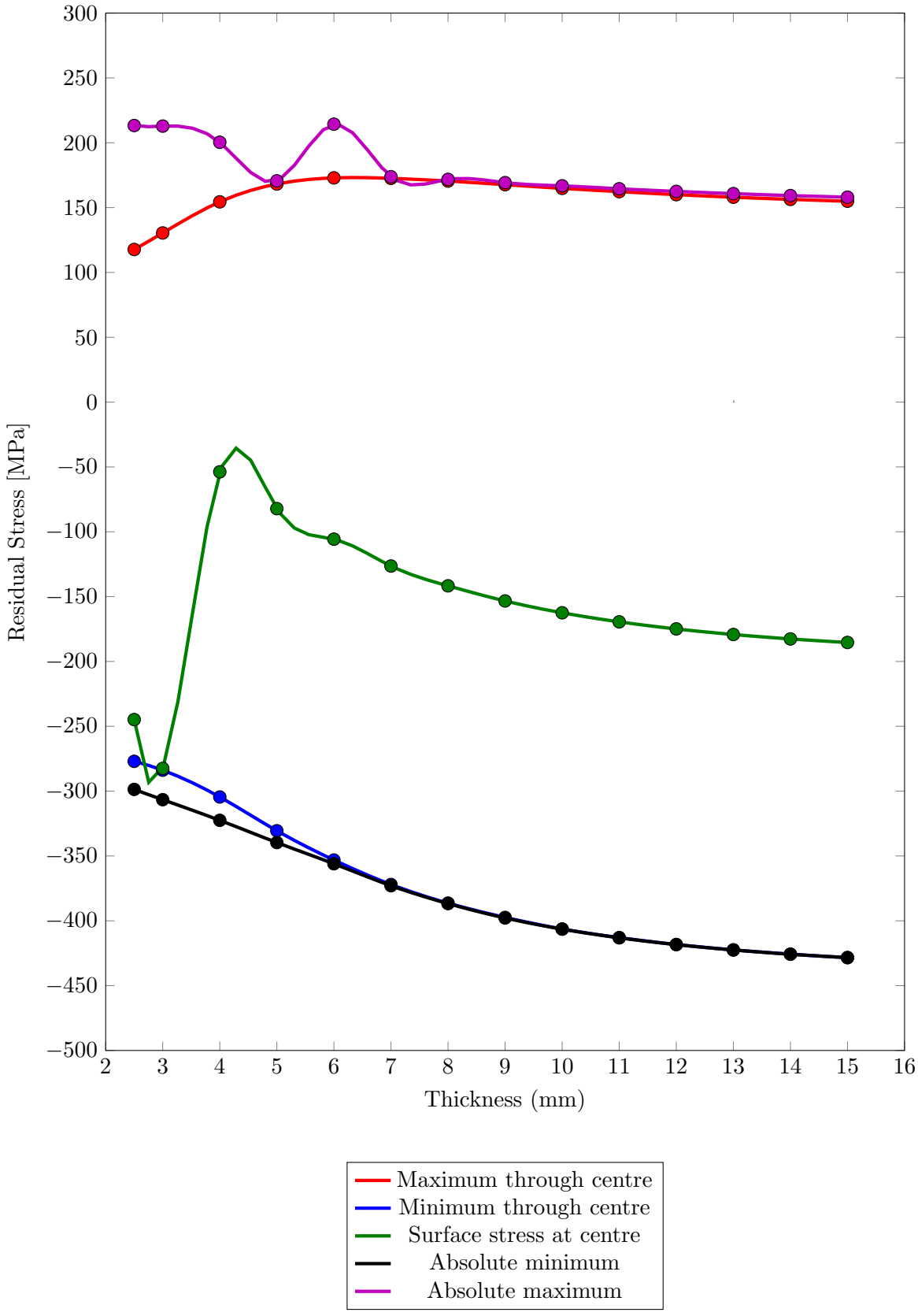

Figure D.2: *Variation of some critical stresses with respect to thickness – y - direction*

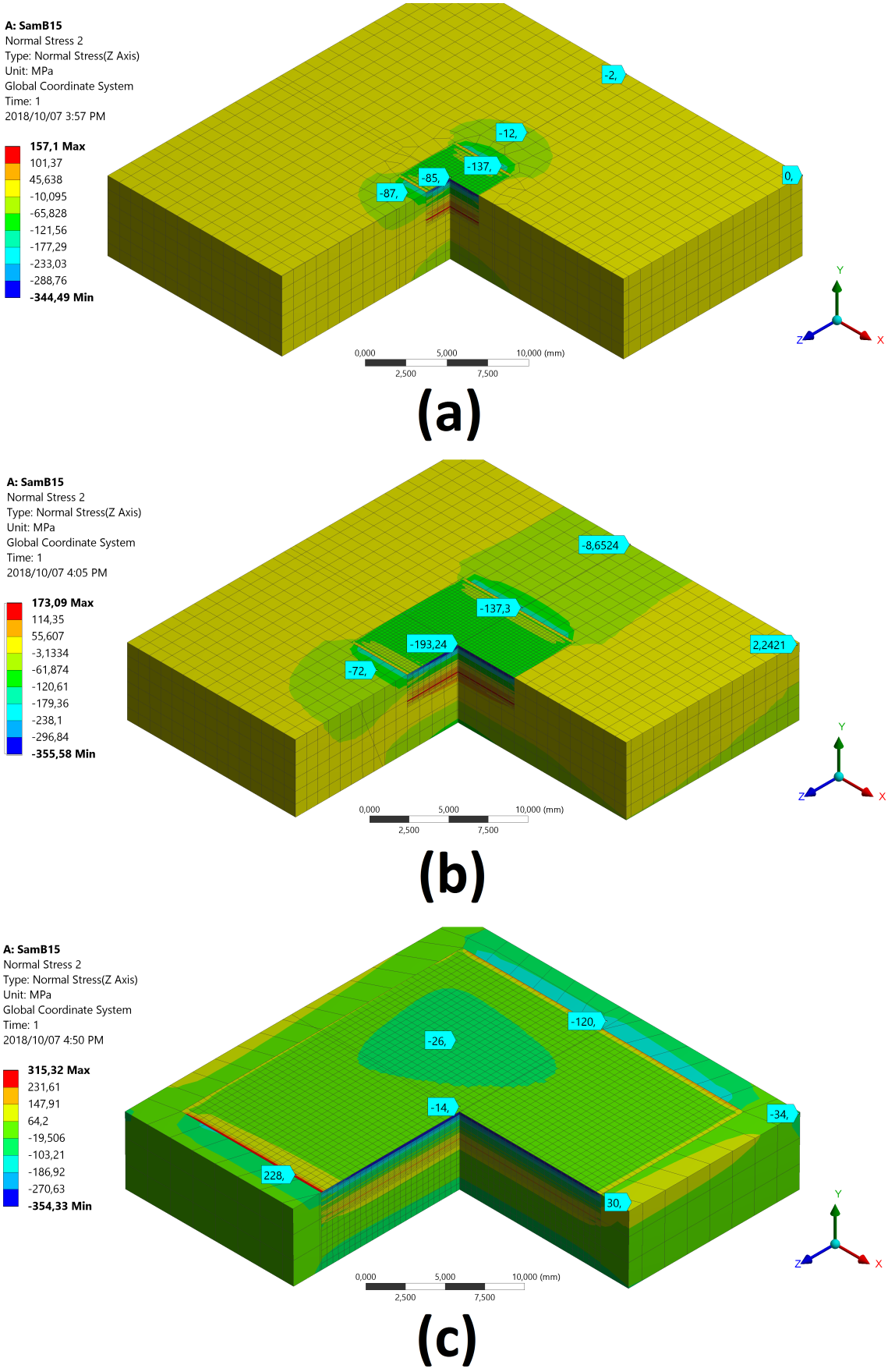

Figure D.3: *Comparison between residual stress fields in samples with various peened areas: (a)* $5 \times 5mm$ *(b)* $15 \times 15mm$ *(c)* $25 \times 25mm$

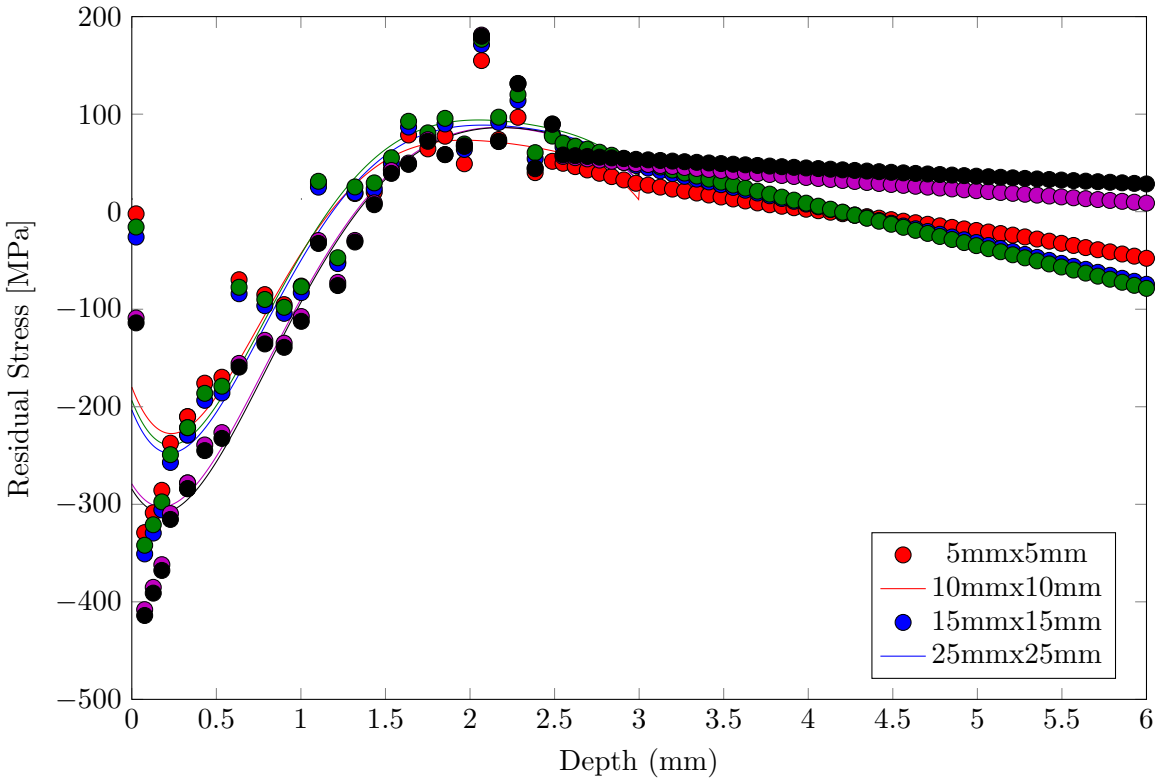

Figure D.4: *Variation of some critical stresses with respect to thickness – y - direction*

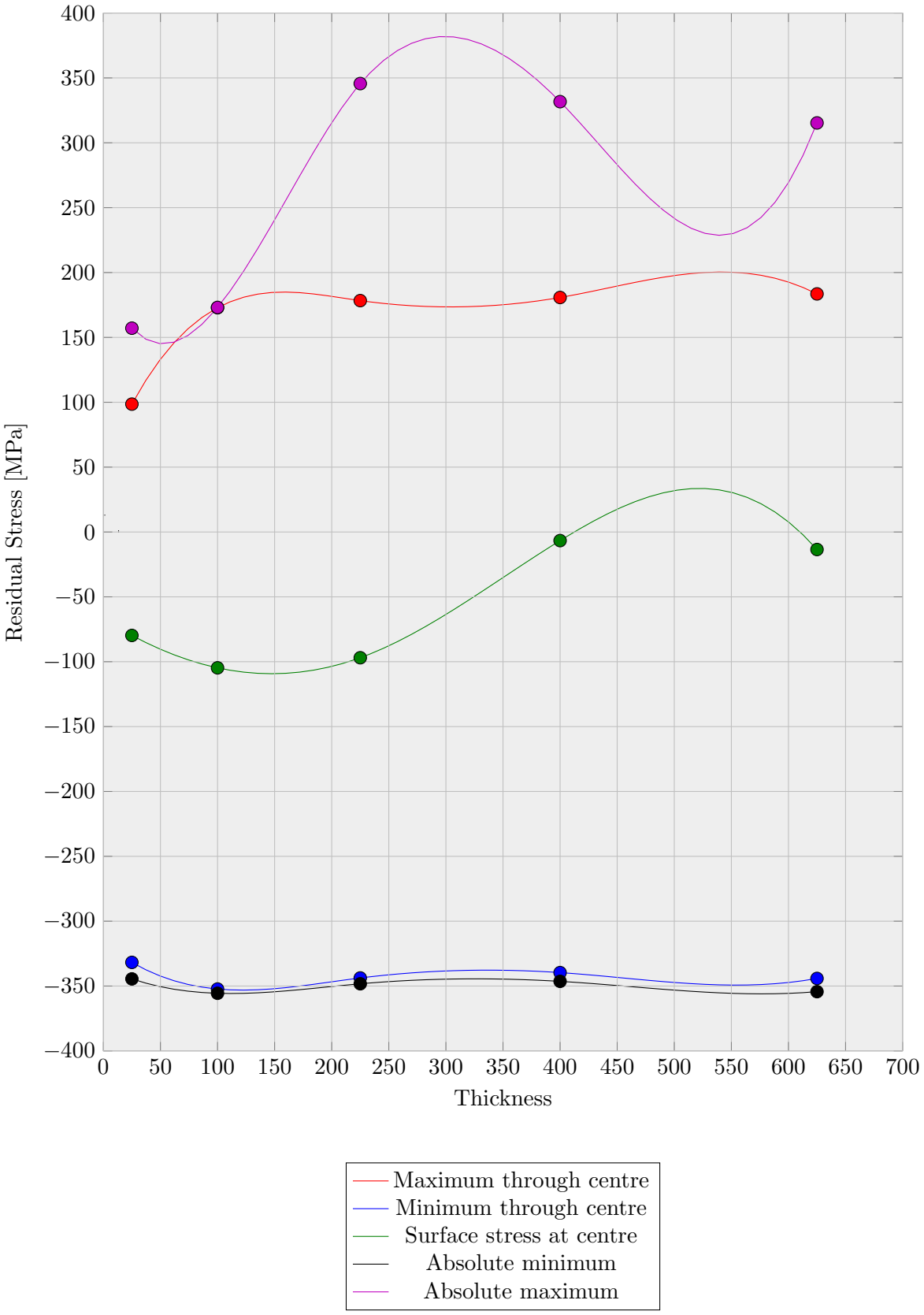

Figure D.5: *Variation of some critical stresses with respect to peened area – y - direction*

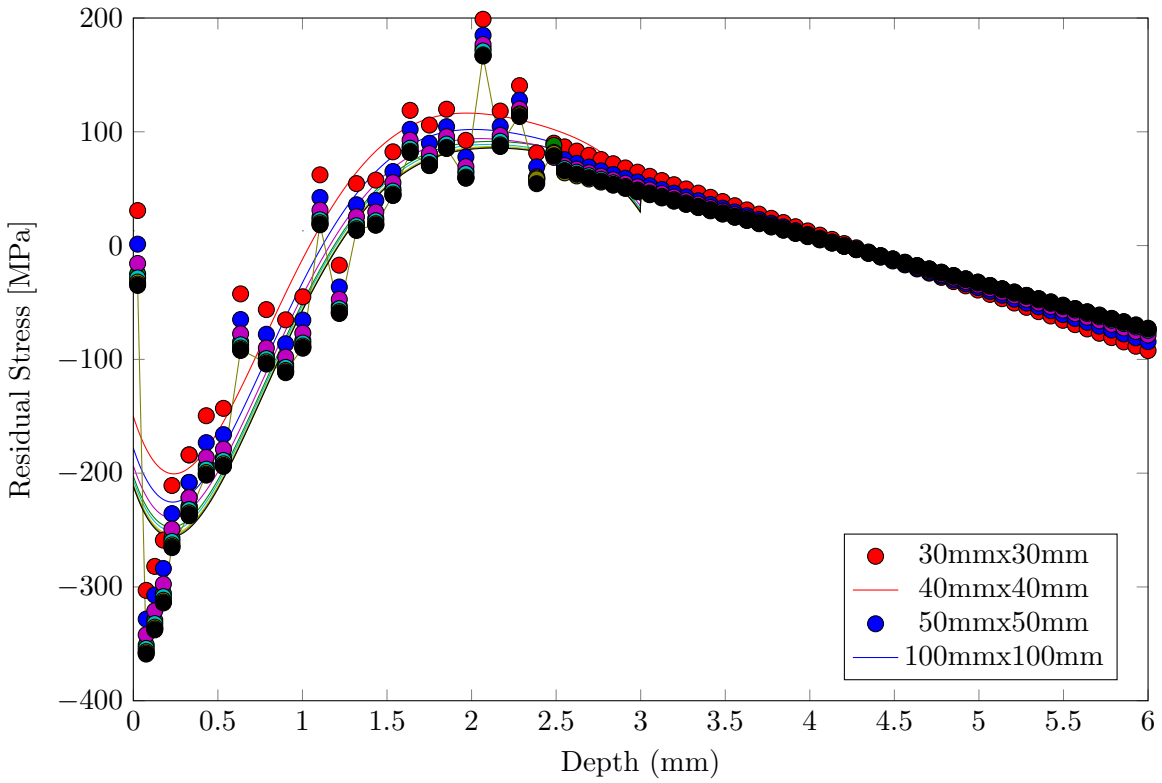

Figure D.6: *Residual stress distributions in various sample sizes – y - direction*

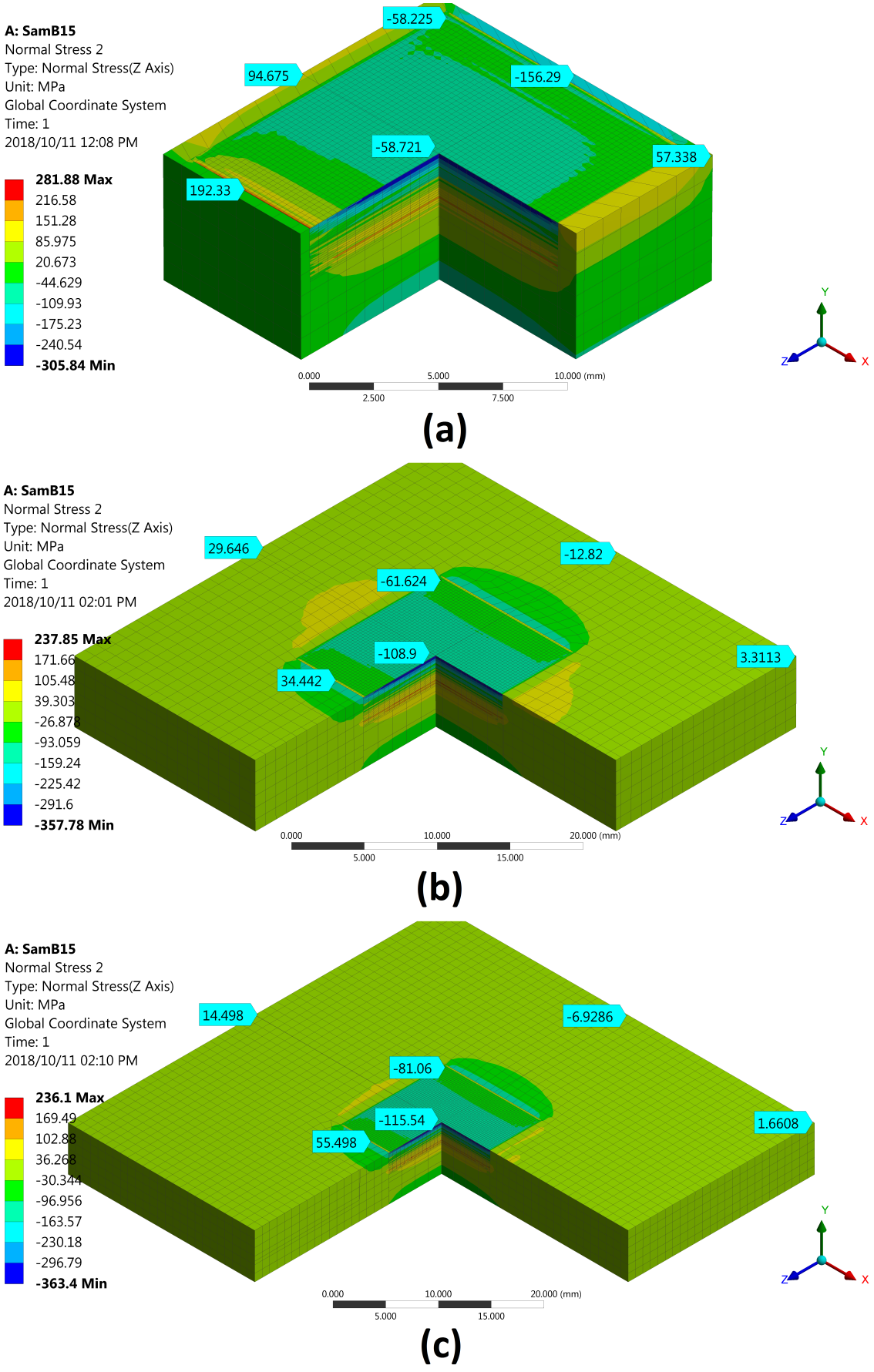

Figure D.7: *Comparison between residual stress fields in samples of various sizes: (a)* $30 \times 30mm$ *(b)* $70 \times 70mm$ *(c)* $100 \times 100mm$

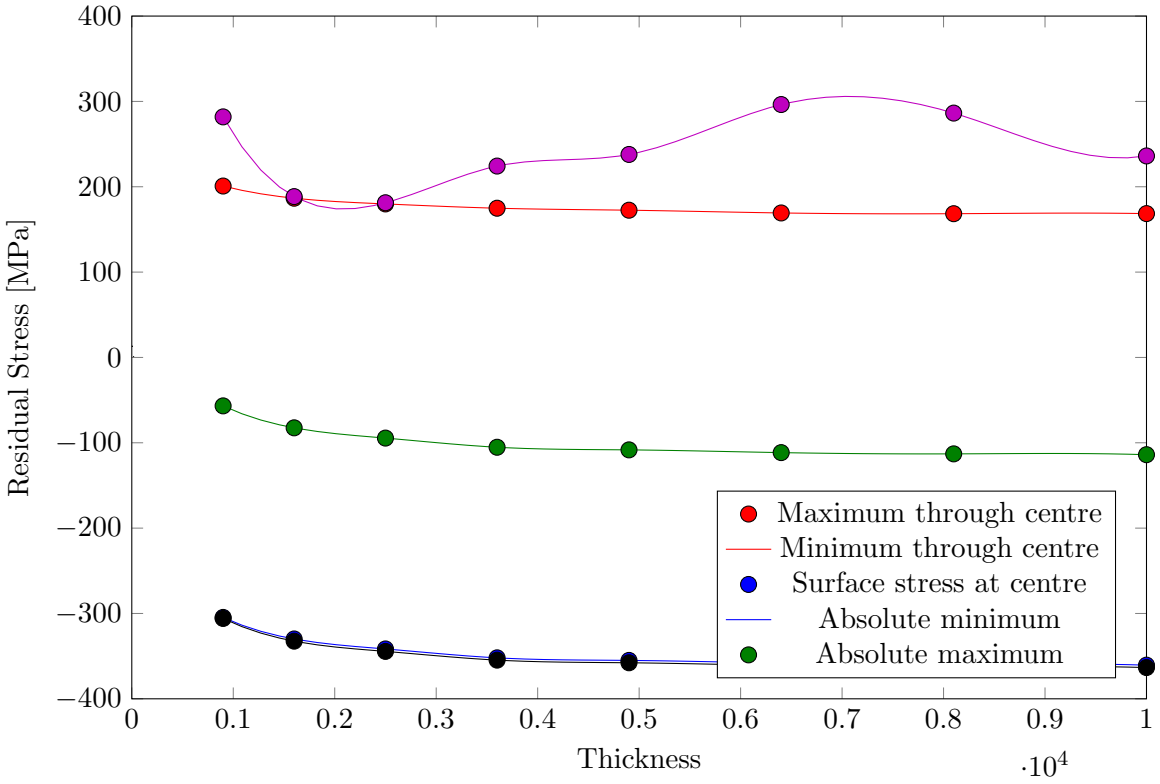

Figure D.8: *Variation of some critical stresses with respect to sample size area – y - direction*

Appendix E Research Contributions

Prediction of Residual Stresses Due to Laser Shock Peening Using Eigenstrain Methods

Ridwaan Omar, Prof. Claudia Polese

Introduction

Laser Shock Peening (LSP) works as follows:

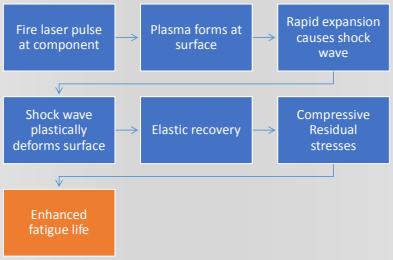

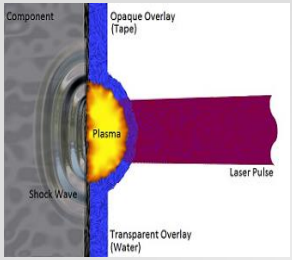

We want to achieve greater fatigue life.
→ *requires* Optimise LSP parameters.
→ *requires* Tool to Predict residual stress.

- Eigenstrain Methods meet this requirement in a computationally inexpensive way.
- In the context of LSP, eigenstrain is equivalent to plastic strain.
- Plastic strain can be imposed on FEA model and solved to yield residual stress/strain.
- But how do we get plastic strain? Using measured residual stress data.
- *Principle of Transferability of Eigenstrain*: Eigenstrains are insensitive to geometry.

Principle of Transferability of Eigenstrain allows one to determine residual stresses in a complex geometry using data from a simple geometry.

Laser Peen a selected area of a simple sample
↓
Measure the residual stresses
↓
Calculate the eigenstrains
↓
Impose eigenstrains on a complex geometry and solve for equilibrium
↓
Compressive Residual stresses in complex geometry can be obtained.

Objectives

- To evaluate the accuracy of various eigenstrain models available in literature, by comparing their predictions to experimentally determined residual stress.
- To identify important parameters in each model in order to optimise the accuracy of models.
- To determine the relationship between thickness and residual stresses induced by laser peening in cuboid samples.
- To determine relationship between curvature and residual stresses induced by laser peening in cylindrical and spherical samples.

The reason for using both cylinders and spheres is that cylinders have one dimension of curvature, whereas spheres have two.

Method

A previous student has collected residual stress profiles in cuboid samples, which are being used as benchmark data. Two methods based on literature were applied to this sample.

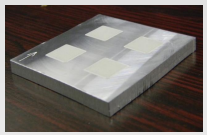

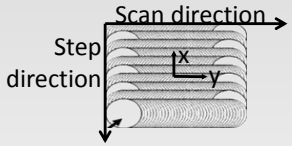

Coratella's Method: The graph on the left is the residual stress profile (measured using neutron diffraction) in the above sample. Residual stress can be separated into two components:

$$\sigma = \sigma_{el}(\varepsilon_{el}) + \sigma_{pl}(\varepsilon_{pl})$$

Linear portion of the graph was extrapolated and constitutive relations used to obtain eigenstrains.

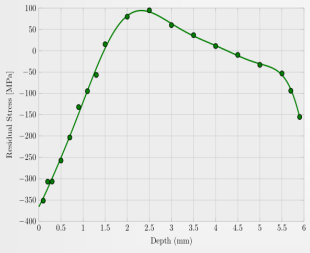

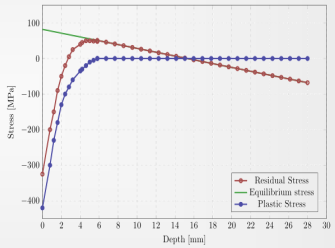

The eigenstrain distribution was imposed on an FEA model of the above sample, by splitting the peened zones into layers, as shown in the figure below.

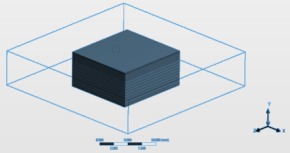

Korsunsky's Method: Eigenstrain distribution was assumed to be equivalent to a set of basis functions with parameters a, N, and x_0:

$$\varepsilon^*(x) = \sum_{i=1}^{N} c_i (x - x_0)^{i+a}$$

Needed to determine c_i → Set them as the values which lead to the best prediction of residual stress.
This required the following:

- Method to determine ε_{el} from eigenstrain. An analytical bending formulation was used.

$$\varepsilon_{el}(x) = f(\varepsilon^*)$$

- A criterion, J, to determine the goodness of the prediction. A least squares criterion was used.

$$J = \sum_{i=1}^{m} (\varepsilon_{predicted} - \varepsilon_{measured})^2$$

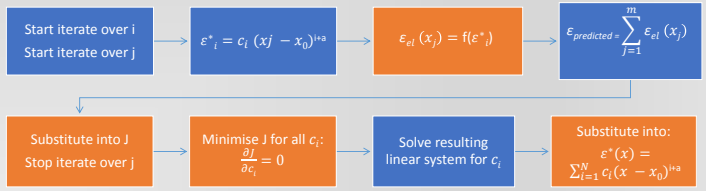

- The above algorithm was implemented into Python.
- A BFGS optimisation algorithm was incorporated to optimise the parameters a, N, and x_0.
- The resulting eigenstrains were imposed on an FEA model, in the same manner as Coratella's method.

Results

Results in the x direction are shown below. Both predicted curves match the general shape of measured curves, which is quite heartening.

Coratella's Method

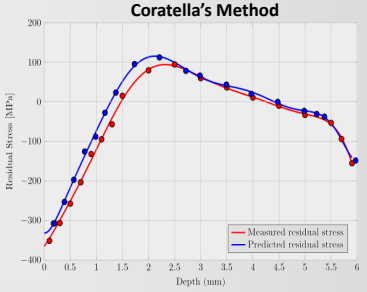

Korsunsky's Method

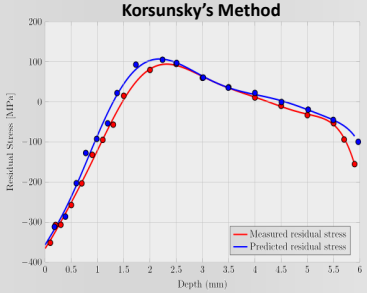

Overall, Korsunsky's method seems to give a better prediction, except near the bottom of the sample. It is especially more accurate than Coratella's method near the peened surface of the sample.

Conclusions and Future Work

- Both of the methods tested to date are capable of predicting residual stress to a reasonable extent.
- Korsunsky's Method seems to be more accurate overall.
- There are more methods that will still be tested and modified.
- Once all methods have been tested, the best model will be used to study the effect of sample thickness on residual stresses.
- The same eigenstrains will then be imposed on spheres and cylinders of different curvatures, to study the effect of curvature on residual stress.

WITS UNIVERSITY
DST-NRF CENTRE OF EXCELLENCE IN STRONG MATERIALS
science & technology Department: Science and Technology REPUBLIC OF SOUTH AFRICA
NRF National Research Foundation

7th International Conference on Laser Peening and Related Phenomena

June 17th – 22nd 2018
National University of Singapore

Letter of Acceptance

Dear **Mr. Ridwaan Omar**,

On behalf of the LSP 2018 Organising Committee, we are delighted to inform you that the following submission has been accepted for **Oral Presentation**.

Paper ID: **94: Prediction of Residual Stresses in AA7075 Due to Laser Shock Peening Using Eigenstrain Methods**

Please note that at least one of the authors of the accepted paper has to register and present their paper at the conference. Any paper without registration will not be included in the Conference Booklet. Please visit the conference websites, http://www.lsp2018.com/ , for more information such as registration, hotel booking, visa applications etc.

Congratulations again on your excellent work. If you have any enquiries or need any assistance, please feel free to contact us at secretariat@lsp2018.com . We look forward to seeing you in Singapore in June, 2018.

Sincerely,

Prof. Michael Fitzpatrick
Coventry University
Conference co-Chairs

Prof. Minghui Hong
National University of Singapore
Conference co-Chairs

Prediction of Residual Stresses in AA7075 Due to Laser Shock Peening Using Eigenstrain Methods

R. Omar[1,2] and C. Polese[1,2]
[1]School of Mechanical, Industrial and Aeronautical Engineering, University of the Witwatersrand, 1 Jan Smuts Avenue, Johannesburg, 2000, South Africa
[2]DST-NRF Centre of Excellence in Strong Materials, University of the Witwatersrand, 1 Jan Smuts Avenue, Johannesburg, 2000, South Africa

601525@students.wits.ac.za

Laser Shock Peening (LSP) is a surface treatment that enhances fatigue properties of a component by introducing compressive residual stresses near the processed surface. In order to realise the full potential of LSP, the process parameters need to be optimised. This in turn requires a model that can accurately predict residual stresses due to LSP. There are two types of models that are generally used to achieve this prediction. Process models are physics-based models and are complex and computationally expensive. Eigenstrain methods are comparatively simpler and less computationally expensive [1].

Eigenstrain methods allow the prediction of the residual stress field in a sample, given residual stress measurements at a few discrete locations. They also allow one to predict the residual stresses in a complex geometry, given residual stress data from a simple geometry [2]. This is significant because measuring residual stresses in components with a complex geometry is usually a very difficult task.

There is a variety of eigenstrain methods available in literature, all with different levels of simplicity and predictive capabilities. This paper compares the accuracy of different eigenstrain-based models in predicting residual stresses.

Residual stress data on AA7075 samples have been experimentally determined previously by the South African LSP Group [3]. These are used in the present study as benchmark data in order to compare the predictive capabilities of different models. Important parameters in each model will be identified and optimised in order to enhance the accuracy of these models.

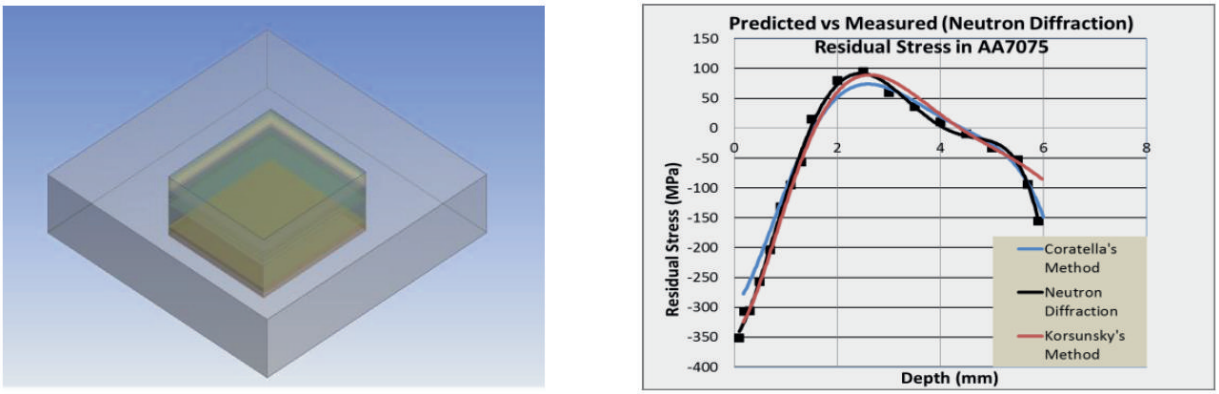

(a) (b)

Fig.1. (a) Finite Element Model of sample. (b) Preliminary results showing predictive capabilities of two models.

[1] A. Korsunsky, "Residual Elastic Strain Due to Laser Shock Peening: Modelling by Eigenstrain Distribution", The Journal of Strain Analysis for Engineering Design, vol. 41, 198-204 (2006)
[2] S. Coratella et al., "Application of the Eigenstrain Approach to Predict the Residual Stress Distribution in Laser Shock Peened AA7050-T7451 Samples", Surface and Coatings Technology, vol. 273, 39-49 (2015).
[3] S.N. Van Staden, C. Polese, and D. Glaser, "Effect of Varying Laser Shock Peening Parameters on Residual Stresses in Different Thicknesses of Aluminium Alloy Samples", 9th International Conference on Mechanical Stress Evaluation by Neutron and Synchrotron Radiation, 19-21 September 2017, Skukuza, South Africa.

Prediction of Residual Stresses in AA7075 Due to Laser Shock Peening Using Eigenstrain Methods

Ridwaan Omar, Prof. Claudia Polese

Introduction

Laser Shock Peening (LSP) is a surface treatment that can enhance the fatigue life of a component. Here is how it works:

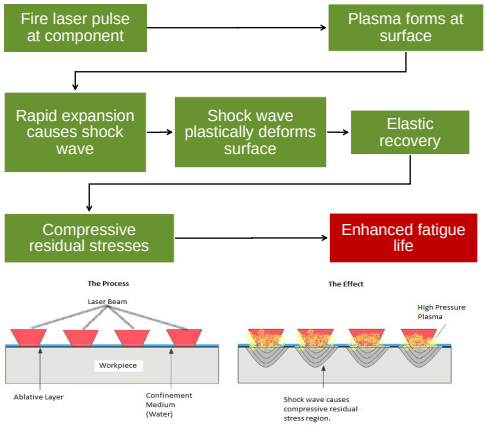

Enhanced fatigue life is due to compressive residual stresses.

We want to achieve greater fatigue life using LSP.
→ *requires* Optimisation of LSP parameters.
→ *requires* Tool to predict residual stress.

- Eigenstrain Methods meet this requirement in a computationally inexpensive way.
- In this context, eigenstrain is equivalent to plastic strain.
- Plastic strain can be used to yield residual stress/strain. This is *Direct Problem of Eigenstrain*.
- But how do we get plastic strain? Using measured residual stress data. This is *Inverse Problem of Eigenstrain*.

Eigenstrains are insensitive to geometry. This allows one to obtain residual stress in complex geometry, using data from simple geometry

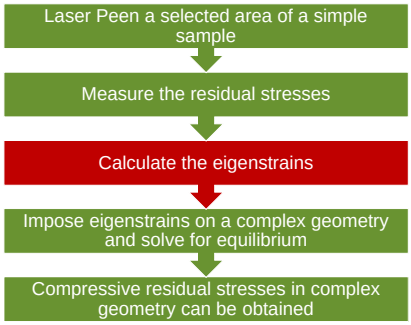

Significance: obtaining residual stresses in complex geometries is difficult using measurements or process modelling.

Objectives

- To evaluate the accuracy of various eigenstrain models available in literature, by comparing their predictions to experimentally determined residual stress.
- To identify important parameters in each model in order to optimise the accuracy of models.
- To determine the relationship between thickness and residual stresses induced by laser peening in cuboid samples.
- To determine relationship between curvature and residual stresses induced by laser peening in cylindrical and spherical samples.

The reason for using both cylinders and spheres is that cylinders have one dimension of curvature, whereas spheres have two

Benchmark Data

A previous student has compiled a residual stress database for cuboid AA7075 samples. This is being used to validate the models.



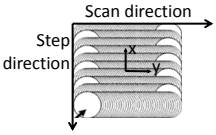

Inverse Problem of Eigenstrain

This is the essence of the problem. There are many ways to solve this problem. Three methods have been tested.

Coratella's Method: This method is illustrated by the graph below. Total strain can be written as:

$$\varepsilon = \varepsilon_{el} + \varepsilon_{pl} \quad \dots (1)$$

Linear portion is purely elastic. Extrapolate the line and subtract from total residual stress. Use elastic properties to convert resulting stress to eigenstrain.

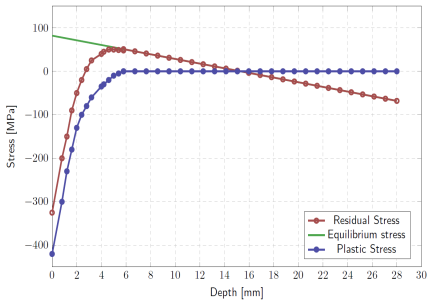

Korsunsky's Method: Eigenstrain distribution is a set of basis functions with parameters a, N, and x_0:

$$\varepsilon^*(x) = \sum_{i=1}^{N} c_i (x - x_0)^{i+a} \quad \dots (2)$$

Need to determine c_i → Set them as the values which lead to the best prediction of residual stress.
This requires the following:

- Method to determine ε_{el} from eigenstrain. An analytical bending formulation is used.

$$\varepsilon_{el}(x) = f(\varepsilon^*) \dots (3)$$

- A criterion, J, to determine the goodness of the prediction. A least squares criterion is used.

$$J = \sum_{i=1}^{m} (\varepsilon_{predicted} - \varepsilon_{measured})^2 \dots (4)$$

$$\frac{\partial J}{\partial c_i} = 0 \quad \dots (5)$$

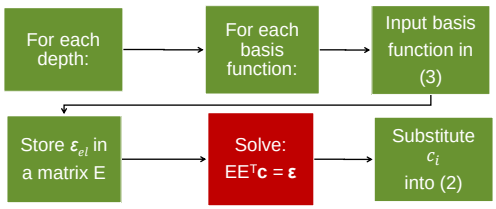

- The above algorithm was written as a Python script.
- A BFGS optimisation algorithm was incorporated to optimise the parameters a, N, and x_0.

Korsunsky's Method with FEM to Generate E:

- This method is the same as above, but instead of using Equation (3) to predict residual stresses, Finite Element Method is used.
- The BFGS optimisation algorithm was not included here, due to time constraints.
- The method used to introduce eigenstrains into FEM model is outlined in the next section.

Direct Problem of Eigenstrain

This was done in the same way for all methods.

The eigenstrain distribution was imposed on an FEA model of the above sample, by splitting the peened zones into layers, as shown in the figure below.

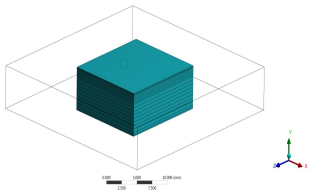

The eigenstrains were introduced as coefficients of thermal expansion in each layer.

Results

Results in the x direction for different spot sizes are shown below. All predicted curves match the general shape of measured curves.

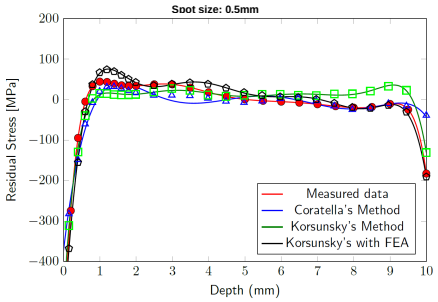

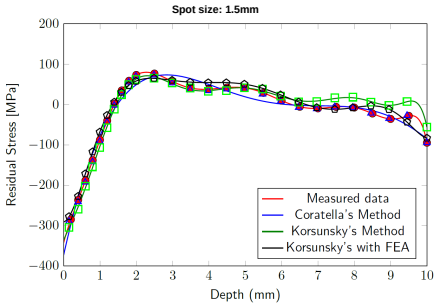

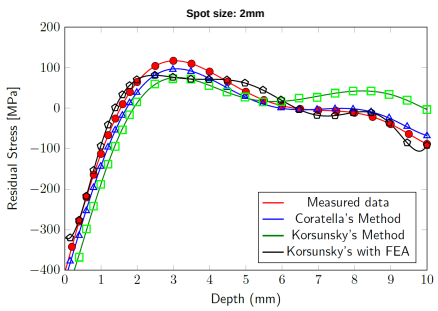

No single method seems consistently better than the others. Korsunsky's Method tends to diverge towards the bottom of the sample.

Conclusions and Future Work

- All methods are capable of reasonable predictions.
- The methods need to be applied to more samples to better compare the methods.
- There are more methods that will still be tested and modified.
- The best model will be used to study the effect of sample thickness and curvature on residual stresses.

Acknowledgements

Acknowledgements are due to the DST-NRF Centre of Excellence in Strong Materials and the CSIR National Laser Centre Rental Pool Programme.

Contact Details
601525@students.wits.ac.za
ridwaanomar7@gmail.com